DEPARTMENT OF PHARMACOLOGY
Medical Sciences Division

An investigation of the relationship between transcriptomic signals and functional phenotypes across atrial physiology and pharmacology

Alexander Grassam-Rowe

Thesis for the title of Doctor of Philosophy (D.Phil) in Pharmacology

Hilary Term 2024

Supervised by Assoc. Prof. M. Lei and Prof. A. Galione

Corpus Christi College

Department of Pharmacology

University of Oxford

Word count: 49,859 excluding references & tables

Corpus Christi
College Oxford

An investigation of the relationship between transcriptomic signals and functional phenotypes across atrial physiology and pharmacology

Abstract

Cardiovascular disease is the leading global cause of mortality and morbidity. Cardiac disease is a major contributor, including diseases of abnormal rhythm or rate. The most common dysrhythmia is atrial fibrillation (AF). Despite progress in our understanding of the cellular- and tissue-level remodelling that contributes to AF, and in our clinical treatments of AF, there remains a need for novel pharmacological therapies to treat and prevent AF. Here, I use single-cell and spatially-resolved transcriptomics alongside structural imaging and ex vivo Langendorff perfusion to reveal a novel catecholaminergic population of cardiomyocytes (CMs). I then go on to use hiPSC-CM differentiation and RNA sequencing to examine maturation-associated transcriptomic networks and calcium handling networks. Finally, I also further characterise novel atrial-like hiPSC-CMs' pharmacology and their ability to model both inherited and acquired cardiac disease. My work provides multiple exciting avenues for further research to examine how transcriptomic signals in both mouse and hiPSC-CM models relate to both basic and translational atrial science.

Key words: iPSCs, transcriptomics, atria, iPSC-derived cardiomyocytes, 4-aminopyridine, calcium handling.

Acknowledgements

Rome was not built in a day and iPSCs are not grown in a day.

For helping me to contribute my small part to the corpus of human knowledge, I would like to thank Prof. Ming Lei for his guidance over the years and his ever-insightful advice alongside Prof. Galione. I would like to thank the rest of the Lei group, with particular note to Dr.'s Bae, Mu-u-min, Sun, & He. I would also like the thank the other members of the unofficial 'integrated cardiovascular institute' from the Tammaro group: the eponymous Paolo, Claire, Rachel, Rumaitha, & Zeki. For their friendship, guidance, and support – I would like to thank the other members of the Pharmacology Department with Dr. Charalampos & Mr. Hofer standing out in particular.

For providing me a home, in many ways, over the best part of a decade, I would like to thank Corpus Christi and our College community for keeping my spark of learning alive – with particular thanks to our Bursar Mr. Melhuish, without whom I would not have been able to complete my earlier studies. From the JCR, to the MCR, and to the SCR and back again, a Corpuscle I will always be. May our little hive continue its buzz forever.

For teaching me how to think, I would like to thank my tutors, with Prof.'s Akerman and Swietach of particular note for laying bare the very elements that make up the complexities of life and for taking a chance on the unpolished 18 year old who came and interviewed with them on a cold December nearly a decade ago. In addition, my other tutors who will particularly remain with me are Dr.'s Murray, Rowan-Hull, and Lear, who respectively taught me how to write, the principles of embryology I used in this thesis, and how to use language as a tool of information transfer.

For getting me here, I would like to thank my parents Dawn and David, who have fought their own battles, for giving me the values and love of learning that has carried me to each and every success in my life. I would also like to thank my siblings Rachel & Lucy for bearing with me along the way. To those who helped me get on the right track – I would like to thank my teachers: Mr. Sumption, Mr. Davies, & Mr. Anstey. I also must thank Dr. Brunskill for acting as a role model of what being a doctor meant.

Finally, and most importantly, those who put up with me. All the feeding cells, writing code, and overnight electrophysiology, I could not have done it without the support of those nearest to me. Jana - my darling wife, I could not have done this without you and I am forever grateful that you allowed me to prioritise these cells for a while. I look forward to making it up to you for the rest of our lives. For supporting me, two names need mention above all: Lilya and Alex. However, many more that go unmentioned.

The final person to thank is me: Alex. You never would have believed it would happen but you got here through hard work, determination, and sheer stubbornness. The work isn't done, but you did a good job so far – well done and never forget: "οὐδ ἐν τοῖς θαρροῦσ ιν ἀν ἁλωτον".

None of this would have been possible without the people who support the British Heart Foundation through their donations, physical exertion, and giving up their time - thank you all.

List of contents

List of Figures

List of Tables

Statement of authorship

All work presented within this thesis was authored by Alexander Grassam-Rowe, unless stated otherwise. Alexander Grassam-Rowe worked across a number of highly collaborative projects and highlights any contribution by others – including work where Alexander Grassam-Rowe had a significant contribution in the conception or interpretation. Each methods subsection and Figure highlights where any work was not exclusively performed by Alexander Grassam-Rowe. However, in the case of the collection of sequencing data by co-authors, this is typically only highlighted the first time the data is presented in the thesis.

Chapter 1. Introduction

This chapter is in part adapted from Ahmad, Jin, Grassam-Rowe et al.[1] and Sun, Grassam-Rowe et al.[2], He, Grassam-Rowe et al, and, Grassam-Rowe et al.[3]

a. The heart in health and disease

i. The cardiovascular system enables complex multi-cellular life

The heart serves to maintain the extracellular milieu of cells across the body. Eukaryotic cells rely primarily on oxidative phosphorylation to translate chemical energy from diverse nutritive sources into a universal form of readily utilisable but rapidly recycled short-term chemical energy

stores – ATP. The essentiality of this discovery to life has been recognised by two Nobel Prizes – first in 1978 for Peter Mitchell's pioneering suggestion of the chemiosmotic theory[4,5], and then in 1997 Boyer and Walker were awarded theirs for their work on the enzyme ATP synthase that performs the final step in producing ATP[6,7]. This process is essential for both the specialised functions of the cells that give rise to the functional behaviour their respective tissues, and for the requisite processes of cellular life – such as maintaining specific ion gradients across their cellular membranes. Oxidative phosphorylation consumes oxygen and emits carbon dioxide. These oxidative processes originally likely evolved in simple unicellular lifeforms that were surrounded by our oxygen-rich and carbon dioxide-poor atmospheric air, and could similarly consume nutrients from their immediate surroundings. However, as multi-cellular life evolved with increasingly specialised tissues, it mandated a mass transport system to supply tissues and cells that were not exposed to the atmosphere, and had no ready access to the nutrients and ions needed to maintain cellular life. This mass transport system is most complex life forms is described as the cardiovascular system – a series of functionally and anatomically distinct vessels that supply and drain the extracellular milieu of cells around the entire body, with pressure generated by the rhythmic contractions of the heart. The double circulatory system present in humans describes that the vessels that connect to the heart form two distinct circulations, that unite through the heart[8-12]. The pulmonary circulation facilitates gas exchange between the blood and the atmosphere. The systemic circulation then circulates this oxygenated blood to distal tissues, where the microvascular structure facilitates efficient gas exchange and equilibration of the extracellular fluid with the plasma in terms of ions and nutrients. In tandem with the pulmonary, digestive, and renal systems, the cardiovascular system maintains the extracellular ion and nutrient concentrations and partial pressures of oxygen and carbon dioxide – to facilitate normal cellular function.

Initial conjecture about the physiology of the cardiovascular system took millennia to be examined robustly. From early work by the Greeks to purport on the contents and connections of the cardiovascular system, through to the work of Galen – primarily anatomical and hypothetical work established the idea that the heart provided some source of energy, which was distributed across the body through blood vessels[13,14]. The work of Medieval and Renaissance era anatomists, such as Vesalius and Colombo[10,15,16], produced the first suggestions of the closed and dual circulations based on human cadaveric anatomy. However, it was Harvey who first robustly identified the role of the heart as the central pump, through experiments on fish and snakes demonstrating the uptake of venous blood by the heart, and its forced pumping into the aorta and through the arteriovenous system[13]. At a similar time, Malpighi and Van Leeuwenhoek were identifying the anatomical basis of the microvasculature as the site of confluence between the arteries and the veins [8,17]. Yet, the cellular basis of the microvasculature, and its role as the site of gas exchange and general diffusion took several hundred more years, and the development of better histological techniques – including the silver nitrate staining approaches used by His[18,19].

Nonetheless, a different body of work identified how blood coursed through these vessels. Whilst the early anatomists such as Galen identified that the heart was central to the passage of blood, Harvey is arguably the first to robustly identify the role of the heart beat in producing the movement of blood through its contractions[13,20]. The work of Stephen Hales, notably in large animals such as horses, was the first to directly measure the arterial pressure evolved from these contractions[21]. However, the next major developments in our understanding of the heart as a pump developed primarily through isolated heart preparations, either with or without lungs attached. The work of physiologists such as Howell & Donaldson, first robustly identified that

the heart's pumping function dynamically responded to changes in venous and arterial pressure, through changes in stroke volume and heart rate to modulate their product of cardiac output[22,23]. It then took the seminal studies of Frank, with step-wise filling of frog atria and ventricles, to identify that some of this dynamism was related to the distension of the cardiac muscle during filling[24]. Subsequently, Starling's work on dog hearts, with alterations in preload and afterload, was used to build his eponymous law that relates the venous filling of the heart with end diastolic volume, contractile effort, and the arterial pressure that this contraction must overcome in terms of pressuring the luminal blood[25,26]. These scientists had taken us from the heart being a source of "heat" for peripheral organs, to being a dynamic pump that pressurised the blood to pass through the vasculature to supply end organs.

The generation of cardiac rhythm, its modulation, and intra-cardiac propagation required a different corpus of work to understand. The continuous beating of the heart has been acknowledged for millennia. However, it took Galen and Harvey to note that that this continued even following excision for some time and thus must arise from within the heart[11-14,27]. However, Harvey believed that this arose from the stimulating effect of blood entering the heart and this continued to be perpetuated as the cause of spontaneous cardiac activity by later physiologists such as Haller[14,27,28]. However, Thomas Willis, famed for his anatomical descriptions of the brain, suggested that the contractions of the heart were stimulated by neural input[27]. This was then supported by range of histology, nerve stimulation studies, and spinal cord destruction studies that demonstrated that the rate and rhythm of the heart could be severely affected by its innervation[29-31]. Following on from Galvani's groundbreaking studies identifying the electrical stimulation of frog muscle could cause contractiony[32], and the founding of electrophysiology, this was applied in the cardiac field by Matteucci[33], Koelliker and Muller to identify that the contractions of the heart could stimulate neuro-muscular preparations to be excited just before cardiac systole, and that the electrical activity of the heart polarised between systole and diastole, and thus formed the basis for identifying that the same 'animal electricity' was involved in cardiac contractions[33,34]. Burdon-Sanderson then used novel electrical recording devices to measure the changes in potential difference across the frog heart during the cardiac cycle, and recorded the positive and negative deflections that described the depolarisation and repolarisation of the myocardium[35]. Others then built on this to describe, and name, the electrocardiogram across larger species, with Einthoven being the first the record the electrocardiogram from the human surface in 1903 using a series of leads connecting the limbs[36]. However, the myogenic vs neurogenic origin of the heartbeat required further work to resolve and mandated the examination of the tissues and cells that make up the heart – with the general biology of the cardiomyocyte to be established as well.

ii. Cardiac heterogeneity produces its pump-like action

Cardiac contractile effort arises from the concerted shortening of individual cells. The parenchymal cells of the myocardium (cardiomyocytes) contain highly organised bundles of actin and myosin (myofibrils) organised along the long axis of the cell. The basic unit of the myofibrils is a sarcomere, where structural proteins bind together filaments of actin or myosin and keep these two in close approximation[37]. The regulatory troponin and tropomyosin complex tonically inhibits binding of actin and the myosin head, until calcium ions bind and induce a conformational shift that disinhibits acto-myosin cross-bridge cycling that causes the myofibrillar contraction and shortening of the cell. The role of calcium ions as master regulators of

contraction, alongside many other signalling cascades, mandates the tight regulation of cardiomyocyte cytosolic (sarcoplasmic) [Ca^{2+}_i] – which is held around 50-200 nM during diastole[38,39,40,41]. Ringer was the first to identify the importance of calcium ions, through the simple observation that upon use of distilled water, the beating of the heart ceased. Through a series of experiments, he determined that the ions responsible were calcium [42]. However, [Ca^{2+}_i] undergoes a 6-8 fold increase during systole in rat cardiomyocytes[38,39] and a 5-9 fold increase during systole in human cardiomyocytes up to 800 – 1650 nM [Ca^{2+}_i][40,41]. Whilst cardiomyocyte contraction is reliant on extracellular calcium[43,42], the influx of Ca^{2+} at the cardiomyocyte cell surface membrane (sarcolemma), only represents between 10-30% of the sarcoplasmic calcium influx[44], and $\Delta[Ca^{2+}_i]$ regularly exceeds the extracellular [Ca^{2+}]. The majority of cardiac $\Delta[Ca^{2+}_i]$ is released from intracellular stores – primarily the sarcoplasmic reticulum (SR), which can reach up to 80 μM [Ca^{2+}] in rat[45,46], and have been reported around 2.5-4 μM in humans[47,48]. This release of SR calcium arises from the opening of large conductance 100-200 pS cation channels (RyR2) on the SR surface that are activated by the local increase in [Ca^{2+}_i] from the sarcolemmal influx – called calcium-induced calcium release (CICR)[49,50,51,52]. The sarcolemmal calcium influx is mediated by voltage-gated calcium channels which are closely opposed to the RyR2 channels on the SR surface, in spatially restricted subsarcolemmal clefts around 3-4 x 10^5 nm^3 as the sarcolemma invaginates transversally across the cell (t-tubules), and the SR approximates and partially envelopes the t-tubules to create these clefts[53,54]. These structures are referred to as dyads, and they also correlate with the ultrastructural organisation of sarcomeres[51,54], releasing Ca^{2+} ions locally to sarcomeres from around the Z-discs that separate each sarcomere[51]. Thus, the spatiotemporal control of [Ca^{2+}_i] regulates and coordinates the activity of proteins to induce cardiomyocyte contraction upon sufficient depolarisation of the cell membrane. However, despite the progress made in understanding the basic subcellular components that contribute to this excitation-contraction coupling, it still remains unclear how cardiomyocytes balance and maintain the stoichiometry of their calcium handling machinery and thus fluxes and how this is maintained across species and individuals. Computational modelling has presented an opportunity to investigate the sources, interactions, and significance of this variation in emergent cardiac biology [55,56,57,58,59,60,61-63]. However, there has been only limited attempts to understand how the covariance of these individual components contributes to emergent activity [64,65], which would likely contribute to more accurate models capturing the impact of inter-individual variation and covariance. However, recent work[66], has used a series of linked experimental procedures to interrogate in turn each of the 5 major calcium fluxes in mouse ventricular cardiomyocytes (Figure 1-1). The calcium handling parameters were then used as input to a Bayesian inference approach that attempted to use these parameters to inform the posterior distribution of specific parameters within the Hinch model of the calcium transient [67]. Riabiz et al used a Markov Chain Monte Carlo approach with a novel Stein thinning approach to perform representative sampling from within the 3 million simulated samples[66]. Broadly, upon examining the inter-sample correlation between parameter posteriors, there were two major modules that had high degrees of inter-module correlation, which were assigned as 'purple' and 'blue'. They observed a negative correlation between fluxes handling sarcolemmal calcium transport against those handling intracellular calcium transport. Whilst similar relationships have been described between depolarising and repolarising currents[68,69], these relationships likely require further validation – despite the difficultly in acquiring single-cell information. Ultimately, this understanding of fundamental cardiomyocyte cellular biology became apparent only within the last 100 years or so, with most rapid advances following the successful isolation of intact rat cardiomyocytes by Harary and Farley in 1963[70]. However, this was built upon the initial

pioneering attempts of Carrel in 1912 to extract and culture tissue ex vivo – who built upon Galen and Harvey's observations of explanted hearts, to show that cardiac tissue could beat in culture for 3 months following extraction[71].

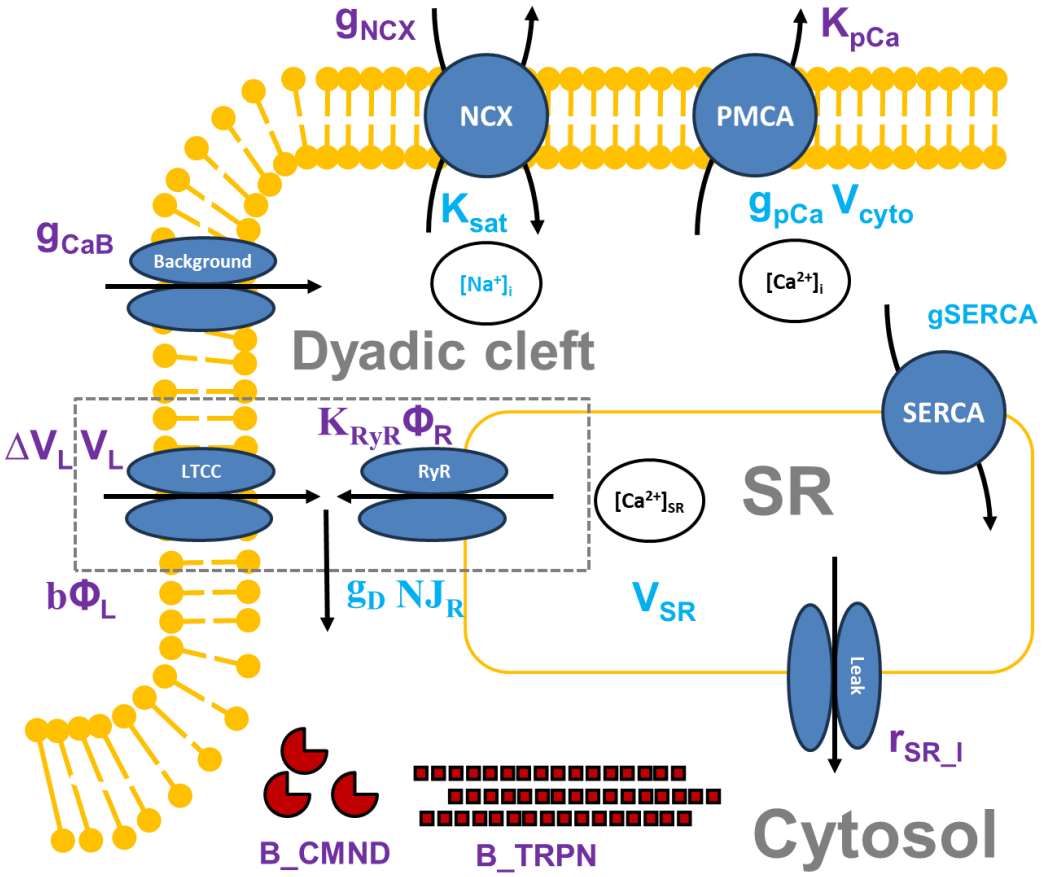

Figure 1-1. A diagrammatic representation of a subset of components of the Hinch model.

Different compartments are described in grey. Calcium transport proteins are in blue, with spheres as exchangers or pumps, and channels as paired ovals – associated names in white. Black arrows show the direction of ionic fluxes. Ion concentrations are shown in small white spheres. The major calcium fluxes are NCX, PMCA, SERCA, LTCC, & RYR. The cytosolic buffers of calmodulin and troponin are represented in dark red. All parameters shown in blue or purple are by respective grouping suggested by Riabiz et al. as highlighted in main text.

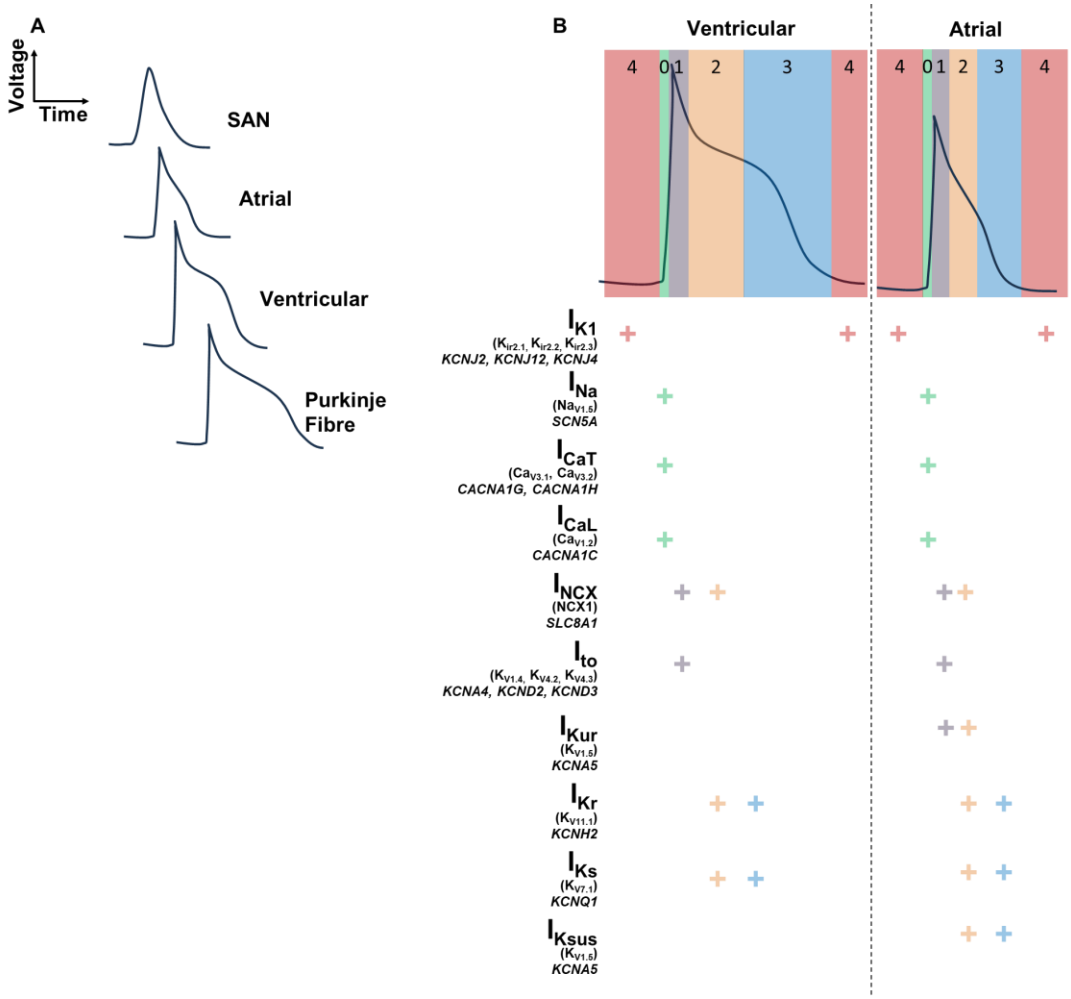

Figure 1-2. Different cardiomyocytes have different action potentials that arise from a given combination of ion currents.

A) Representative action potentials from different cardiomyocyte populations.
B) Action potentials from ventricular (left) and atrial (right) action potentials, coloured by respective action potential phases. Certain key ion currents are displayed below, with their respective associated transport proteins and their respective genes displayed under each current. For each current, a plus is shown on its respective row, under the specific phase(s) that the current exerts the most influence on the membrane potential. Pluses are coloured by their respective phase as above.

Cardiomyocyte heterogeneity enables coordinated cardiac output. Broadly, the heart is separated into 4 chambers: the atria and ventricles, which are separated into the right and left. The ventricles are the chambers specialised for powerful contractions that generate tension across their walls, which pressurises its incompressible luminal blood, which is then ejected, in part, from the ventricles through the valves of the heart into either the pulmonary or systemic circulation from the right and left ventricle respectively. Beyond the organ- and tissue-level anatomical specialisation of the ventricles: ventricular cardiomyocytes are particularly specialised for contractile effort. Ventricular cardiomyocytes have extensive myofibrils, and in humans express myosin isoforms, particularly the heavy chain, associated with more metabolically efficient tension generation and slower relaxation[72,73,74,75,76]. Beyond this, ventricular cardiomyocytes are specialised to maximise the calcium signal for contraction. Not only do ventricular cardiomyocytes have extensive t-tubules to facilitate rapid coupling of CICR to increased [Ca^{2+}] within sarcomeres[54,51] but they also have high amplitude calcium transients, that

liberate a large fraction of the SR calcium content, and these calcium transients decay slowly[77]. This specialisation for contraction is present even at the level of the transient depolarisations of the sarcolemma that trigger the initial opening of the voltage-gated calcium channels. The sarcolemma contains a number of ion transport systems that establish an electrochemical gradient, primarily through the active electrogenic extrusion of Na^+ coupled to K^+ uptake – which establishes a relatively more negative internal sarcolemmal charge[78,79,80,81]. Following initial depolarisation triggering rapid sodium and calcium influx through distinct voltage-gated channels, the membrane is repolarised by potassium efflux and calcium extrusion[82,83,84]. The duration and amplitude of the underlying currents that shape these action potentials influence the calcium transients and calcium loading of cells[84]. The longer action potential duration (APD) of ventricular cardiomyocytes contributes to loading the SR with Ca^{2+} and increased contractile force[85]. Thus, ventricular cardiomyocytes are specialised for their contractile contribution to cardiac output at each level of excitation-contraction coupling (ECC). However, ventricular cardiomyocytes are typically quiescent if without an external source to cause the initial depolarisation to trigger an action potential.

Thus, a great body of work has elaborated on the contractile mechanisms of the heart, and provided further insight into the basic nature of cardiomyocyte biology. However, much of the early work to identify the origin of the electrical activity in the heart actually preceded most of this fundamental cardiomyocyte biology work. The first description of the CCS was Purkinje's description of the subendocardial Purkinje fibre network in 1839[86,87]. However, it was Tawara and Aschoff who, through extensive histological examination, described the connection between these fibres and the atrioventricular node and supposed that their anatomy ontologically supported them being a specialised conduction pathway through the heart[87,88]. Gaskell's work in the 1880s was some of the first to robustly demonstrate that intrinsic cardiac activity did not rely on extrinsic neural input, or intrinsic ganglia; using tortoise heart, Gaskell observed contraction start within the sinus venous of the atria and spread across the atria and into the ventricles, and that ablation of particular portions of the atrioventricular junction lead to a greatly reduced ventricular rate[89-91]. His, working primarily in embryonic heart, firstly demonstrated further supporting evidence of the myogenic theory by describing the beating embryonic heart prior to the embryological development of the nervous system[92,93]. Secondly, His prepared the first robust anatomical description of the eponymous atrioventricular bundle that connects the atria and the ventricles – this was before Tawara had identified its connection with the Purkinje network, but His went on to demonstrate similar results as Gaskell's heart block studies upon severance of this bundle[87]. Despite all this evidence surrounding the nature of the sinus venosus as being one of the earliest sites of cardiac contraction, and of a specialised system for conducting this across the heart in an orderly fashion, and of its origination and propagation arising and persisting without neural input, the precise nature of the origin of the heartbeat remained elusive. Gaskell had also identified that the atrioventricular CCS and a region within the sinus venosus, were notably less striated compared to their surrounding cardiac tissue[87,89]. We now know that a number of cells in the heart spontaneously generate action potentials. These are most concentrated within the cardiac conduction system (CCS), and broadly referred to as non-working cardiomyocytes. The major pacemaker is typically the sinoatrial node (SAN), that sits within the intercaval right atrium[94], although some dispute that it is a single fixed site[95,96], and spontaneously depolarises at around a rate of 1 Hz in adult humans. The discovery of the SAN as the origin of the heartbeat again built upon initial anatomical descriptions. Keith, and then Flack under him, sought to build on the work of Gaskell and others, to more intimately describe the proposed pacemaker site in the sinus venosus. Flack, first in mole, described in greater detail

this same area of the sinus venosus with much less 'muscular' appearance[97,98], which was then later demonstrated by Lewis to be electrically distinct from the surrounding tissue as well[94,99]. Of note, recently, a number of groups have identified that the primary pacemaker, in certain conditions, may shift from being a single fixed site, to a collection of small non-nodal sites over which the role of primary pacemaker may 'wander'[100-102]. However, in most normal conditions a subset of cardiomyocytes within the SAN display spontaneous depolarisation during diastole, and likely mediate the role of primary pacemaker[103]. The automaticity was poorly understood for many years until the isolation of a particular depolarising current – the "funny" current I_f[104]. This current activates during diastole to depolarise these pacemaker cells, and was later isolated to being mediated through hyperpolarization-activated cyclic nucleotide-gated (HCN) channels – particularly HCN4[105]. This initial depolarisiation then triggers further depolarising currents such as T-, L-, and potentially even N-type Ca^{2+} currents, alongside Na^+ currents in pacemaker cells[106]. However, HCN4 knockout mice retain spontaneous cardiac rhythmogenesis and can be stimulated to faster heart rates[107,108]. This may be explained by a redundant pacemaker clock that interacts with funny current-led membrane clock to produce and coordinate spontaneous depolarisations. More recently, the interaction between intracellular calcium signalling and cAMP-mediated crosstalk with the membrane has been implicated as a second 'Calcium clock' acting in concert with the 'membrane' clock[106,109]. Spontaneous calcium release (SCR) from the sarcoplasmic reticulum during diastole may contribute to depolarising influx, primarily through the reverse action of the Sodium-Calcium exchanger NCX[106,110] – with a contribution from voltage-gated calcium channels as a signal contributing to calcium-induced calcium release synchrony with membrane depolarisation[111]. The network of interdependent cAMP-, cGMP-, and even-calcium sensitive phosphodiesterases and kinases contributes to the appropriate phosphorylation status of the relevant calcium-handling proteins, and may act to synchronise the membrane and calcium clocks as well[112-115]. The relative contribution of the membrane and calcium clocks across physiology and pathophysiology remains controversial – some redundancy across heterogenous mechanisms may be an essential part of pacemaking. Developing an understanding of their relative contributions, and how this may become dysregulated, or be targeted pharmacologically, is of immense interest to those seeking to understand cardiac rhythmogenesis.

These CCS cells are specialised to generate action potentials and propagate them rapidly across the heart to produce coordinated cardiac contraction (Figure 1-2). The cells of the SAN and the atrioventricular node (AVN) are similar structurally, in as much as they are not specialised for contraction, with a low density of poorly organised myofibrils in small spindle-shaped cells with poor SR organisation and no t-tubules[116,117]. Furthermore, they have no resting membrane potential, but regularly fire relatively shorter action potentials (Figure 2)[116] that are much more dependent on calcium for the initial upstroke than sodium[118,119]. Thus, whilst these nodal cells are not specialised to contract, they do possess a relatively unique cassette of interacting time-dependent membrane ion transporters coupled to the interactions of time-dependent subcellular calcium stores that produce two coordinated membrane and calcium 'clocks' that produce the rhythmic depolarisations[112,120,110] that are then transmitted to the rest of the myocardium to induce contraction. The action potentials of the pacemaker cells of the AVN differ only slightly from those of the SAN[121,122]. However, both the SAN and AVN contain further cellular heterogeneity, such as in the expression of different intercellular connexin isoforms, and this heterogeneity likely contributes to SAN pacemaking and the delaying function of the AVN between the atria and ventricles that ensures atria systole is complete before ventricular systole begins[122,121,123,124,125,126,117,127,128,129,130,131]. The non-nodal but rapid conducting cells of the CCS are

adapted to transmit these signals rapidly and in a coordinated fashion across the ventricular myocardium. From the proximal His-bundle, through to the bundle branches and distal Purkinje Fibre (PKJ) network, these cells share a similar cellular ultrastructure of elongated cells with low myofibril density[132,133]. However, in a similar fashion as the nodal components of the CCS: their adaptation to their particular role of rapid conduction becomes apparent at the electrophysiological and molecular level. For example, PKJs have a rapid upstroke velocity, high $Na_{v1.5}$ expression, and high expression of large conductance Cx40 gap junctions, which enable them to rapidly conduct action potentials[134,135,133,136,137,138,139,140]. Thus, the cardiomyocytes of the CCS are well-adapted to both generate and conduct the electrical activation signals across the myocardium.

Atrial cardiomyocytes are adapted to their intermediate role between the ventricles and the CCS. The atria contribute directly to cardiac haemodynamics, with atrial systole contributing to the last stages of ventricular filling, particularly at heart rates > 90/min[141], and then acting as a transient reservoir of afferent blood during ventricular systole, before passively allow the negative pressures of the ventricles to draw blood from them in early diastole[142,143]. However, the atria only generate around 5-10 mmHg of pressure difference from diastole to systole[142,144], compared to the ventricular c. 120 mmHg difference[144]. In fact, where the contractile effort of atrial systole is lost, the cardiac index only drops by around 20%[145,143,146]. Thus, whilst the atria's contractile function contributes to cardiac haemodynamics, it is through the filling of the ventricles in low-pressure settings, rather than through any contribution to directly overcome the resistances of the circulations. Atrial cardiomyocytes are adapted to produce a contractile effort and are working cardiomyocytes, albeit smaller than ventricular cardiomyocytes. Atrial cardiomyocytes have highly organised myobfibrils, and some may possess a rudimentary T-tubule system[147,148] although most rely more on centripetal calcium influx[149,150,151,152]. However, atrial cardiomyocytes are primarily adapted for rapid signal conductance, in a similar fashion as the CCS, alongside their small contractile effort. To ensure coordinated filling and systole between the atria and ventricles, the atria must rapidly propagate the electrical signal and then contract within the 200 ms between the activation of the SAN and the ventricles. The atria are adapted to this in a similar fashion as the conducting cells of the CCS, with expression of high-conductance connexins (Cx40)[153,154], a large amplitude I_{Na}, and a relatively depolarised resting membrane potential all contributing to rapid depolarisation and conduction velocity[155]. However, whereas the long APDs of the conducting cells in the CCS likely contribute to ensure unidirectional conduction towards the ventricles, the atrial action potential is relatively short as atrial cardiomyocytes have a high current density of repolarising potassium currents (Figure 1-2) – which may act as a repolarisation reserve given the high I_{Na} density. Thus, atrial cardiomyocytes are adapted for their intermediate role between contraction and conduction.

iii. Neuronal control of the heart

While the myogenic vs neurogenic origin of the heartbeat has been settled, the interactions of the heart and the nervous system remain a key regulator of cardiac function. The heart is richly innervated by both sympathetic and parasympathetic neurons, that act both to regulate the heart, and relay sensory signals back to the CNS[156]. This mixture of efferent and afferent innervation of the heart was demonstrated even during some of the earliest physiological work on the cardiac nervous system, with Von Bezold observing that cardiac vagal afferents could elicit vasodepressor effects upon stimulation[157,158] and Weber demonstrating that stimulating the vagus nerve could stop the heart completely[159]. However, the next large steps in understanding the innervation of the heart came from several key experiments and scientists, who came to describe

the quasi-antagonistic interactions of the autonomic nervous system with the heart, and the neurotransmitters and mechanisms through which this occurred. Following Schmiedeberg's observation that the cardioinhibitory effect of vagal nerve stimulation could be reversed into a cardioexcitatory response upon addition of nicotine[160], Gaskell and Langley separately determined the histological and pharmacological nature of the sympathetic nerves and their long post-ganglionic course to the heart, after a nicotinic synapse in the paravertebral sympathetic ganglia[161-164]. However, it was Langley's once student Dale, who with Loewi, would demonstrate the true neurotransmitter chemically-mediated mechanism by which the autonomic nerves were modulating cardiac activity – and would share their Nobel Prize for this in 1936[165]. With contributions from Elliot, to determine that noradrenaline secretion by the sympathetic neurons, and acetylcholine secretion by parasympathetic neurons were mediating their respective effects on the heart[166,167] (Figure 1-3).

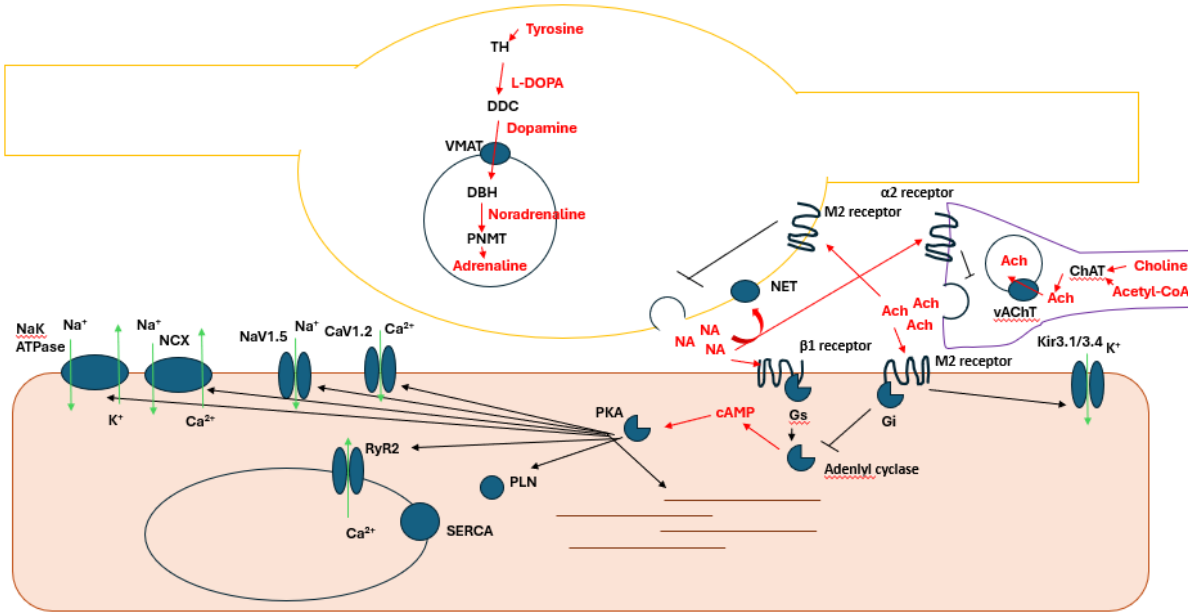

Figure 1-3. Noradrenergic and cholinergic neurons modulate cardiomyocyte behaviour

A diagrammatic representation of a noradrenergic neuron in yellow demonstrates the biosynthesis of catecholamines in sympathetic boutons. Following stimulation, vesicular fusion with the membrane leads to release of the readily diffusible noradrenaline to bathe the surrounding extracellular space. Upon ligation of B1 adrenoceptors on the surface of the cardiomyocyte, this leads to activation of G_s, which in turn recruits and activates adenlyl cylase to form cAMP. cAMP then goes on to activate protein kinase A, alongside its own direct binding stimulatory effect. PKA then phosphorylates a number of targets to produce the positive inotropic, chronotropic, lusiotropic, and dromotropic effects of noradrenaline on cardiomyocytes.

Shown in purple is a cholinergic neuron, with the simple biosynthetic pathway of Ach shown. The antagonistic interactions of cholinergic and noradrenergic neurons in the heart are shown here by the bidirectional inhibition of exocytotic activity mediated through M2 and α2 receptors on sympathetic and parasympathetic neurons respectively. Furthermore, shown is the M2 receptor on cardiomyocytes, which upon Ach ligation leads to G_i activation, and the inhibition of cAMP generation. Additionally, through other G proteins, the M2 receptor activates the I_{KACh} current to decrease cardiomyocyte excitability and contribute to ACh's negative dromotropic and chronotropic effects.

Abbreviations: TH – Tyrosine hydroxylase; DDC – Dopa decarboxylase; VMAT – vesicular monoamine transporter; DBH – Dopamine beta-hydroxylase; PNMT – Phentolamine-N-methyl transferase; NET – Norepinephrine transporter; NA – Noradrenaline; ACh – acetylcholine; ChAT – Acetyl-CoA Choline acetyltransferase; vAChT – Vesicular Acetylcholine Transporter; cAMP – Cyclic adenosine monophosphate; PKA –

Protein Kinase A; PLN – Phospholamban; SERCA – Sarcoplasmic/endoplasmic reticulum calcium ATPase; RyR2 – Ryanodine receptor 2; NCX – Sodium Calcium Exchanger.

Catecholamines are an essential regulator of cardiac function in the adult heart and development. The family of catecholamines are a family of related chemicals, with varying degrees of modification to their terminal amine or ethyl group connecting to a catechol ring. Catecholamines are highly bioactive, acting through a range of cell surface G-protein coupled receptors. The most cardiotropic effects of catecholamines are through noradrenaline and adrenaline, the two respective penultimate and ultimate molecules within the biosynthetic cascade of catecholamines, which act primarily through β_1-adrenoceptors on cardiomyocytes[168]. β_1-adrenoceptor signalling is G_s-coupled, and acts through cAMP and PKA signalling to stimulate a range of calcium handling and membrane ion flux-associated proteins to drive a positive chronotropic, dromotropic, inotropic, and lusiotropic response[168-171]. Cardiac catecholamines derive primarily from the sympathetic innervation of the heart, which release noradrenaline[172], or from the endocrine release of adrenaline by the Chromaffin cells of the adrenal medulla[173]. However, even since Axelrod's first identification of Pnmt[174], he observed intrinsic cardiac Pnmt activity across rabbit and monkey hearts, despite being lower than in the adrenal glands[174]. Later work identified that sympathetic neurons were not the only source of cardiac catecholamines[175,176]. Ignarro & Shideman used chick embryonic cardiac tissue homogenates to demonstrate a stage-specific change in the biosynthetic catecholamine enzymes and their respective products; this also was occurring prior to sympathetic innervation of the heart on the 6th day of incubation[176-178]. The heart also has notable catecholamine degradative enzyme activity, such as catechol-*O*-methyl transferase and monoamine oxidase in this pre-innervation period[176]. Additionally, Ignarro & Shideman identified that the uptake of noradrenaline persisted in non-innervated hearts, and that it was much less effected by reserpine and cocaine, which prevent NET-mediated reuptake and storage in sympathetic neurons—suggesting a non-neuronal source of noradrenaline uptake and storage in the heart[178]. Thus, even from early studies of catecholamines in the developing heart it became clear that there was some cellular source of both catecholamine production, degradation and storage that was not merely the sympathetic innervation. More recently, non-neuronal sources have been identified in the heart, including a neuroendocrine-like intrinsic cardiac adrenergic (ICA) cell type[179-182]. Beyond the regulatory role of cardiac catecholamines in the mature heart, they are also implicated in normal cardiac development, and non-neuronal sources in particular. The developing CCS, at E10.5 in rats before sympathetic innervation[180,182], is closely associated with catecholaminergic cells, putatively ICAs, particularly around the areas of the developing SAN and AVN[205]. However, at E16.5 in rats, these catecholaminergic signals appear also enriched in the atrioventricular and proximal ventricular CCS[203]. However, the function, if any, of this catecholaminergic signal in the developing heart remains poorly characterised. Cultured cardiomyocytes[183] and ex vivo cardiac preparations[184-186] producing conflicting evidence around a putative role for in utero catecholamines in maintaining normal beating rhythm. However, tyrosine hydroxylase-deficient[187] or dopamine beta-hydroxylase-deficient mice[188,189] die in utero with selective cardiac defects including poorly organised and atrophied cardiomyocytes. However, this can be rescued by exogenous catecholamines[190] or insertion of the deficient catecholaminergic gene from a different species[191] – confirming the catecholaminergic specificity of the phenotype.

Beyond the role of catecholamines in normal cardiac development and function, they are also implicated in disease. Catecholamine-mediated adrenergic signalling enables increased cardiac output in periods of acute cardiovascular demand. However, excess in either the acute or chronic setting contributes to pathology. Acutely, one of the main deleterious effects of catecholamines are their pro-arrhythmic nature[192,193]. Chronic catecholamine signalling, such as that seen in heart failure, is associated with pathological remodelling and hypertrophy[194-197]. Thus, there is a clear need to understand the sources of catecholamines within the heart.

iv. Cardiac dysfunction is a major contributor to mortality & morbidity

The study of cardiac biology attempts to understand, prevent, and treat cardiac disease. Where the heart is unable to provide the appropriate level of cardiac output, the function of all tissues is impaired and may result in cell and organism death. Cardiac output is typically measured in litres per minute, and depends on the product of the heart rate (beats per minute) and stroke volume (mL per beat). Stroke volume correlates strongly with heart volume[198]. However, inappropriately low stroke volumes tend to occur where the pumping of the heart is impaired, such as with pathological remodelling in heart failure[199] or with valvular incompetence[200]. With heart rate, whilst inappropriately low heart rates (bradycardia) can be pathological or physiological: inappropriately fast heart rates (tachycardia) are the more common acutely life-threatening problem[201] – with insufficient cardiac filling time leading to a quasi-paradoxical decrease in cardiac output above a certain threshold[202,203], or the risk of fibrillation where co-ordinated contractile effort is lost[204] and stroke volume decreases. Atrial fibrillation (AF) is the most prevalent form of chronic cardiac dysrhythmia[205]: AF affects up to 1 in 3 people over their lifetime[206] and is a major contributor to ischaemic stroke risk[205]. However, ventricular tachycardias (VT) and ventricular fibrillation (VF) are more typically associated with acute and sudden death, although they may be secondary to AF. Ultimately, cardiac dysrhythmias, and the arrhythmias within that, arise from the improper and deleterious conduction of the normal electrical activity across the heart, impeding its ability to pump. The two main heuristic and interacting mechanisms to describe arrhythmogenesis are that of 'trigger' and 'substrate'[207-211]. Trigger describes that any abnormal generation of an action potential, which is then propagated, may cause arrhythmia. This may arise from a single abnormal beat or short pulse of beats, or may arise from increased automaticity of either working or non-working cardiomyocytes. The underlying mechanisms for these are still debated depending on the cause. However, broadly some initial stimulus leads to membrane depolarisation and an action potential firing. For example, in the case of delayed after-depolarisation: the consensus is largely that calcium store overload leads to diastolic calcium release and calcium-induced calcium release, which mediated via NCX leads to membrane depolarisation and an action potential firing if the threshold is reached sufficient to activate voltage-gated sodium channels[212-214]. 'Substrate' refers to the arrhythmic conduction of an impulse, and is broadly referred to as either an anatomic or functional substrate. Anatomical substrates include abnormalities such as accessory conduction pathways through as seen in Wolff-Parkinson-White Syndrome[215], but may also include fibrotic tissue infiltration following myocardial infarctions[216-218]. Functional substrates may arise in situations where there is not a pure anatomical aberrance, but where the conductive nature of the cardiac tissue is altered, such as during myocardial ischaemia[219,220] or during late-stage AF-associated remodelling and shortened action potential duration that then allows re-entrant activity to propagate[221]. The autonomic nervous system can contribute greatly to both trigger and substrate mechanisms of arrhythmia: e.g. sympathetic activation increasing calcium overload and

the likelihood of delayed after-depolarisations[214], whilst also increasing conduction velocity and promoting re-entry – although response, and/or innervation heterogeneity may contribute to considerably increasing risk in infarcted and post-infarct hearts[222-224]. These mechanisms also provide us a heuristic platform upon which to integrate both the genetic and acquired causes of arrhythmia. For example, genetic mutations resulting in hyperexcitatory molecules, such as RyR2, leave cardiomyocytes as particularly prone to developing ectopic beats, particularly under acute proarrhythmic stress conditions[225-228]. However, despite our understanding of these basic mechanisms linking cellular and molecular dysfunction, through to tissue- and organ-level dysfunction, we still have a significant mortality burden from arrhythmia and lack robust understanding of why certain individuals fail to respond to surgical and/or medical treatments, despite progress at a population level[229,221,230,231]. For example, at least 30% of patients experience AF recurrence between 12 and 18 months following surgical ablation even in the most responsive early disease states or with patient-specific interventions[232,233,234]. Additionally, current pharmacological treatments are also limited in efficacy and may even be causes of proarrhythmic increased mortality without benefit on clinical outcomes[234,235,236].

b. The development of the heart

i. The heart arises primarily from two progenitor populations

Embryonic development involves the progressive restriction of gene expression. Cells derive their biological activity by the presence and interactions of the cassette of molecules that compose them. This particular cassette arises both from the environment of the cell, and the genes that are expressed by that cell; the expression of genes involves their transcription into mRNA, which is than translated into proteins that capture, store, and modify a range of lipids and saccharides to form the basis of the cell alongside structural and functional proteins. Humans, and most other complex multi-cellular organisms, develop from a small collection of cells which multiply and progressively restrict the portions of their genome that are available for expression[237]. This process results in the range of over 200 major cell types that make up the human body[237], each with their own unique, but overlapping, cassette of genes , in a particular anatomical arrangement. This process is driven, particularly so beyond the first stages, by cell-cell signalling through diffusible chemical signals that trigger cell surface and nuclear receptors that activate epigenetic mechanisms to promote specific transcriptional programs associated with each cell type[237].

This cardiomyocyte heterogeneity arises from the specification and differentiation of these cell subtypes during development. The heart develops from the anterolateral mesoderm[238,239], arising from two or more distinct progenitor populations that are specified by signalling from the endoderm, including BMP, and other population-specific signals[240-242]. These then give rise to the parenchymal cells in distinct regions of the heart (Figure 1-2).

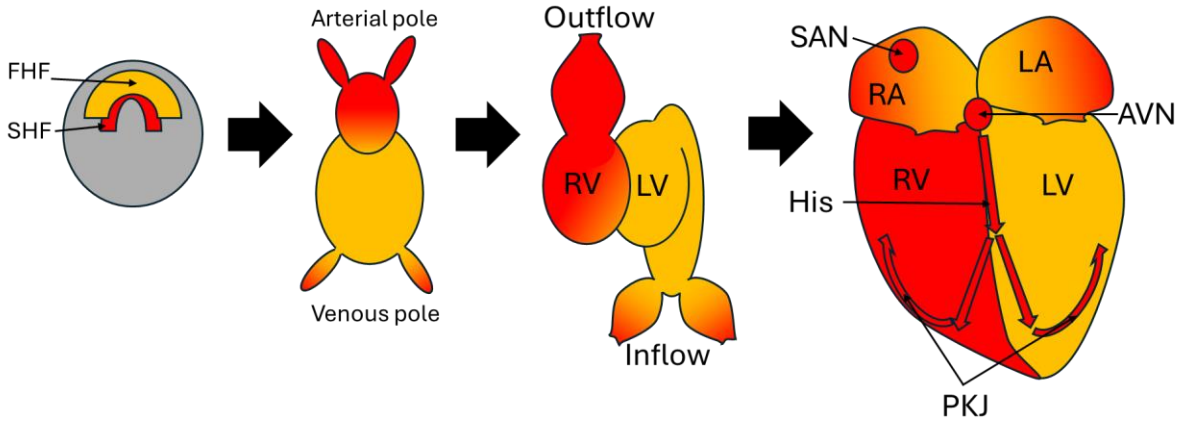

Figure 1-4. Two major populations give rise to distinct portions of the heart.

The distinct first and second heart field give rise to the different portions of the developing heart. FHF and its descendants are shown in red. The SHF and its descendants are shown in yellow.

Abbreviations: FHF: First Heart Field, SHF: Second Heart Field, RV: right ventricle, LV: Left ventricle, SAN: sinoatrial node, AVN: atrioventricular node, RA: right atrium, LA: left atrium, His: His bundle, PKJ: Purkinje Fibres.

These progenitors are most usually distinguished by their temporal contribution to the heart, with a first heart field (FHF) contributing primarily to the left ventricle and the atria, with a second delayed contribution from the second heart field (SHF) to right ventricle, the atria, and the cardiac inflow and outflow[243-249]. The development of the CCS remains more controversial, but primarily, the atrial CCS arises from the caudal posterior secondary heart field (pSHF)[250,251], and the ventricular CCS arises in situ from both the FHF- and SHF-derived left and right heart respectively[252,253]. The atrioventricular CCS has been proposed to arise from FHF-derived cells[252,254,255]. However, the SHF has been demonstrated to contribute to the developing atrioventricular canal[250], and the precise origin of the atrioventricular CCS remains unproven. The differentiations of these distinct cell types arises through the progressive expression of distinct transcription factor networks, which are associated with a number of marker genes specific for each transcription program (Figure 1-3)[135,244,256-279].

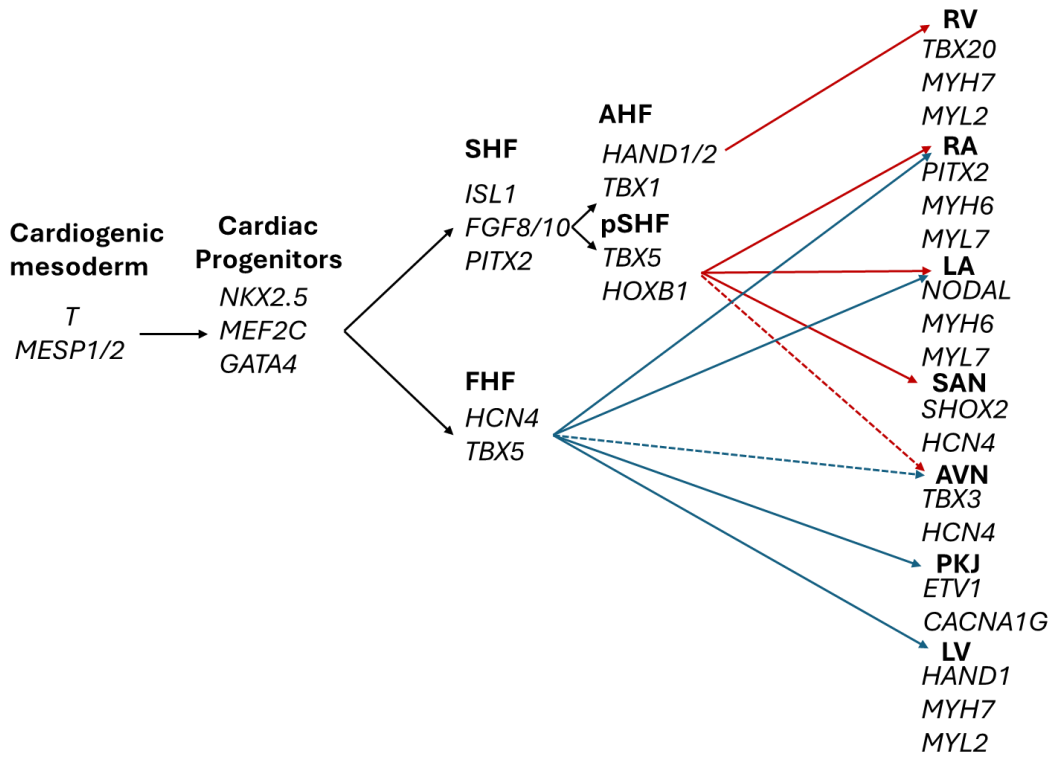

Figure 1-5. Each terminally differentiated cardiomyocyte population arises from specific progenitor populations.

From left to right, populations move from specification to differentiation into specific cardiomyocyte populations. Names of cell groups are in bold. Key marker genes are shown under each group name, in italics. Red and blue arrows respectively delineate the contributions from the SHF and FHF respectively. Dashed lines indicate mixed but uncertain contributions.

Abbreviations: SHF: second heart field, FHF: first heart field, AHF: anterior heart field, pSHF: posterior secondary heart field, RV: right ventricle, RA: right atrium, LA: left atrium, SAN: sinoatrial node, AVN: atrioventricular node, PKJ: Purkinje Fibres, LV: left ventricle.

ii. How do the atria develop

The atria develop from both the FHF and SHF, as guided by a spatiotemporally restricted cassette of signalling molecules. Two signalling pathways have been particularly implicated in the specification and differentiation of the atria: retinoic acid (RA) & bone morphogenetic proteins (BMPs). RA contributes to controlling the proliferation of the SHF and its segregation into the AHF and pSHF[280]– with RA signalling inducing Tbx5 expression in the pSHF to inhibit AHF-like transcriptional programs[268] and promote an atrial fate[281,282]. Furthermore, in utero application of exogenous RA to early cardiogenic mesoderm at E7.25 in mice, suppressed ventricular development and increased atrial development putatively through effects on cardiac progenitor differentiation, rather than heart field specification[271]. However, this is controversial to the traditional model of RA signalling within the heart fields[283] and may be explained by RA's well-characterised concentration sensitivity[284]. Whether RA's precise mechanism is to act through modulating specification or differentiation remains to be determined, and some have proposed that RA might act through setting the developmental point at which cardiac progenitors begin their differentiation, with corollary effects on the divide between FHF and SHF descendant number and phenotype[285]. Similarly, BMPs contribute to wider cardiogenesis[242,286-293] and BMPs must be titrated spatiotemporally for normal cardiogenesis[294]. GREMLIN-2 is a BMP-specific

antagonist that contributes to this titration, and that this BMP titration by GREMLIN-2 is particularly important in atrial development and induces the upregulation of a number of atrial-associated marker genes such as *nppa*, *sln*[295]. GREMLIN-2 was first implicated in atrial development through identifying its association with atrial fibrillation, and its expression by mesoderm contiguous with migrating cardiac progenitors[295]. However, some results have suggested that GREMLIN-2 might be expressed by the cardiac progenitor cells themselves[296]. Understanding how the atria develop has been important in the production of protocols for chamber-specific in vitro differentiation of pluripotent cultured cells into atrial cardiomyocytes.

c. hiPSC-derived cardiomyocytes

iii. The origin of hiPSC-derived cardiomyocytes

Human induced pluripotent stem cell (hiPSC)-derived cardiomyoctes (hiPSC-CMs) have become a major player in both basic and translational science over the past two decades. As science came to understand how stem cells differentiated in vivo, scientists started to explore how well we could replicate that in vitro. However, access to the most potent human stem cells, in terms of potential cell fates, was limited to the extraction of human embryonic stem cells (hESCs), which was limited, laborious, ethically complex, and could not produce autologous samples from patients. The Nobel Prize-winning work of Yamanaka, built on Gurdon's earlier work, to demonstrate not only that mature somatic cells could reprogrammed to totipotency[297], but that this could be done through the transfection of only *Oct4*, *Klf4*, *Sox2*, and *c-Myc*[298]. hiPSCs were then successfully differentiated to cardiomyocytes using a number of different protocols of temporally distinct exposure to various signalling molecules[299-303], that demonstrated the feasibility of producing cardiomyocytes from healthy patients, and also to produce cardiomyocytes that reproduced pathogenic phenotypes when derived from patients with inherited genetic arrhythmias[304-306]. Eventually, a protocol was developed that produced hiPSC-CMs in a meaningful quantity and the similar characteristics as the previously available hESC-based protocols[307] using only small-molecules[308]. This protocol was based on the activation of WNT signalling through inhibition of GSK3β by CHIR99021, followed by inhibition of WNT signalling by IWR1[308-310], and has broadly been adapted and adopted by the majority of the hiPSC-CM community[311]. However, these protocols mostly produce ventricular cardiomyocytes, with a mixture of nodal and atrial cardiomyocytes, which limits the research questions they can be efficaciously used for[308].

iv. Atrial-specific iPSC-CMs

Atrial-specific hiPSC-CM protocols have developed rapidly over the past decade. Different groups have sought to mimic RA's in vivo embryological role to differentiate hiPSC-CMs into a more atrial-like phenotype (Table 1-1). These approaches have been largely very successful in producing not only an atrial transcriptomic and proteomic signature but an atrial-like action potential in terms of it being shorter and more triangular than the respective control ventricular-like action potential[312-318]. However, their approaches all appear to suffer from a lack of mature I_{KACh} current density, which contributes to the major atrial-specific cholinergic modulation by parasympathetic input, with native current density being around -20 pA/pF with 1 μM ACh[319,320], and similar 1 μM Ach inducing only between -2-2.5 pA/pF with 1 μM ACh[312,314]. Beyond this, many have failed to demonstrate the atrial-specific currents that are presumed to contribute to the shorter atrial-like action potential observed, and instead rely on the gene-wise expression of the relevant channel subunit-encoding genes. However, the relationship between transcriptomic

signal and action potential has been suggested to be tenuous in PSC-derived CMs[321]. Although, this should be interpreted with caution as it relies on population-level variances, rather than single-cell covariances. Nonetheless, despite attempts to produce native-like atrial hiPSC-CMs and mature hiPSC-CMs[322], no-one has yet developed a robust protocol for producing mature atrial-like hiPSC-CMs. We recently worked to integrate the leading pro-atrial morphogens, RA & GREMLIN-2, into a single atrial-like hiPSC-CM differentiation protocol[1]. Alongside producing a more mature-like atrial transcriptomic and proteomic signature, the main advance from our work was to produce a native-like I_{KACh} current density (-30 pA/pF with 1 μM ACh) (Figure 1-4). Furthermore, this was associated with a robust response to α- and β-adrenoceptor agonists[1].

Name	**Protocol**	**Cell Source**	**Structure**	**E.Phys.**	**Neuro. Pharm.**	**Molecular Markers**
Many [273,319,320,323-331]	Native embryological development	Native human atrial cardiomyocytes	Elongated rod- or spindle/cone-like morphology, and clearly striated and well-organised myofibrils. Typically mononucleate.	Triangular-like AP. APD_{90} c. 150-500 ms. APD_{50} c. 8-150 ms. APD_{30} c. 4-24 ms. APD shorter than ventricular, and more depolarised resting membrane potential also (-74 mV vs -81 mV).	Adrenergic stimuli induce positive chronotropic, dromotropic, inotropic, and lusiotropic response from even 1 nM. Cholinergic stimuli induce opposing negative responses. I_{KACh} activation by 1 μM Ach: -20 pA/pF at -90 mV.	NR2F2 acts as master regulator of atrial transcriptome to maintain difference from ventricles across many gene sets.
Devalla[3] [14]	RA	hESC	Spontaneously contracting embryoid bodies. Cell morphology mostly round and most without well-organised myofibrillar ultrastructure.	Pronounced phase 1 'notch' and shorter APD vs control. Plateau and max amplitude height reduced vs control. APD_{20}: 20.8 ± 3.7 ms. APD_{50}: 44 ± 10 ms. APD90: 145 ± 21 ms. RMP c. -72 mV and no difference from control.	I_{KACh} activation by 10 μM CCh induced -2 pA/pF current at -120 mV.	Ventricular marker genes downregulated (IRX4, MYL2, HEY2) and atrial markers (NPPA, SLN, PITX2, NR2F2, KCNA5) up-regulated in a COUP-TFII (NR2F2) dependent manner. Atrial-specific potassium channel subunit-encoding genes also upregulated.

Li[317]	RA	hiPSC	Engineered heart tissue (EHT) and monolayers with well-organised sarcomeric structure.	Triangular-like AP shorter than ventricular control, but indistinguishable from nodal control. Faster maximal upstroke velocity than nodal control.	Positive chronotropic response to noradrenaline (100 nM) in single cells, with the opposite response to 1 μM CCh. Positive chronotropic response in dose-dependent manner to noradrenaline in EHT, with opposite effect from CCh.	Upregulation of atrial markers (*NPPA, NR2F2, KCNJ3*) vs ventricular control, but only *NPPA* significantly upregulated compared to nodal control.
Cyganek [313]	RA	hiPSC	Monolayers. Myofibrillar alignment good in some areas.	Triangular-like APs. APD_{50} 167 ± 5 ms.	Positive inotropy with 1 μM ISO, oppositve with 10 μM CCh.	Atrial markers (*NPPA, NR2F2, KCNJ3, HOXA3, KCNA5*) upregulated and ventricular markers downregulated (*MYL2, IRX4, MYH7, LPL, HEY2*). Also confirmed at protein level for atrial markers.
Argenziano[312]	RA	hiPSC	Monolayers produce fibre-like structures.	Triangular-like APs. Very depolarised RMP: -45.2 ± 2.7 mV. APD_{50} 57.5 ± 2.7 ms. APD_{90}: 89 ± 4.5 ms.	I_{KACh} activation by 10 μM CCh: -2.5 pA/pF at -120 mV. 100 μM adenosine activated I_{KACh} current: -1 pA/pF at -120 mV.	Atrial markers (*KCNJ3, KCNA5, NR2F2, GJA5*) upregulated and ventricular markers (*MYH7, MYL2*) downregulated. Confirmed upregulation at protein level for KCNA5, COUP-TFII, and $Ca_{V3.1,}$ alongside downregulation of MLC2v.
Laksman [316]	RA	hiPSC	Elongated cells in monolayers. Well-organised myofibrils	APs with pronounced phase 1 and phase 2 ('spike-and-dome').	Not shown.	Upregulated atrial markers (*NPPA, KCNJ3, GJA5*) and downregulated

			along long axis of cell.	Very depolarised RMP: -56 ± 2 mV. APD_{30}: 37 ± 11 ms. APD_{90}: 247 ± 37 ms. Monolayers can elicit organised rotor waves.		ventricular markers (*MYL2, IRX4*).
Pei[318]	RA	hiPSC	Beating monolayers with striated sarcomeres.	Triangular APs. APD_{90}: c. 75 ms, from RMP of c. -55 mV.	Not shown.	Upregulated *NR2F2* and downregulated *IRX4*. Monolayers did not display MLC2v at the protein level.
Goldfracht[315]	RA	hiPSC	Ring-shaped EHT.	Triangular APs. APD_{90}: 205 ± 9 ms. APD_{50}: 147 ±10 ms. APD_{30}: 115 ± 9 ms. RMP: 63 ± 2 mV.	Positive inotropic response (c. 70% increase) from 10 μM ISO. Dose-dependent decrease in APD_{90} in response to CCh from 297 ± 16 ms at baseline, to 233 ± 17 ms at 10 μM CCh (22% decrease).	Atrial markers (*KCNA5, KCNJ3, NPPA, MYL7, NR2F2*) upregulated and ventricular markers (*MYL2, MYH7, HEY2*) downregulated. At protein level, MLC2v downregulated and SLN and GJA5 upregulated.
Tanwar[332]	GREMLIN-2	CGR8 mESC	Not shown.	Triangular APs vs control with pronounced 'spike-and-dome'. APD_{90}: c. 40 ms vs control c. 70 ms.	Not shown.	Upregulated atrial markers (*Myh6, Gata4, Myl7, Gja5, Kcnj5, Hey1*) and downregulated ventricular markers (*Myl2, Gja1, Kcnq1*).
Bylund[333]	GREMLIN-2	mESC	Increased contracting cells.	Not shown.	Not shown.	Upregulated atrial markers *Myh6* and *Myl7*.
Ahmad[1]	GREMLIN-2 & RA	hiPSC	Elongated rod- or spindle/cone-like morphology, with well-organised myofibrils.	Triangular APs, but with some phase II plateau. RMP: -67 ± 6 mV. APD_{90}: 215 ± 30 ms. APD_{50}: 130 ± 30 ms.	α-adrenergic stimuli (10 μM PE) and β-adrenergic stimuli (100 nM ISO) separately increased	Atrial markers upregulated (*NR2F2, GATA4, HEY1, SFRP5, NPPA, MYL7, KCNA5, KCNJ3*). At protein level COUP-TFII, NPPA upregulated.

			Beating monolayers.		calcium transient amplitude. I_{KACh} activation by 1 μM ACh: c. -30 pA/pF at -110 mV.	

Table 1-1. A summary of the major advances in generating atrial-like PSC-CMs.

Each column represents a particular aspect, with headers in the first row. Each row represents a different differentiation protocol. Data are presented with as much quantiative accuracy as possible. Where numerical values are not given in the original paper, approximations based on presented graphs and figures are used.

Table in part adapted from Ahmad, Jin, Grassam-Rowe et al.[1].

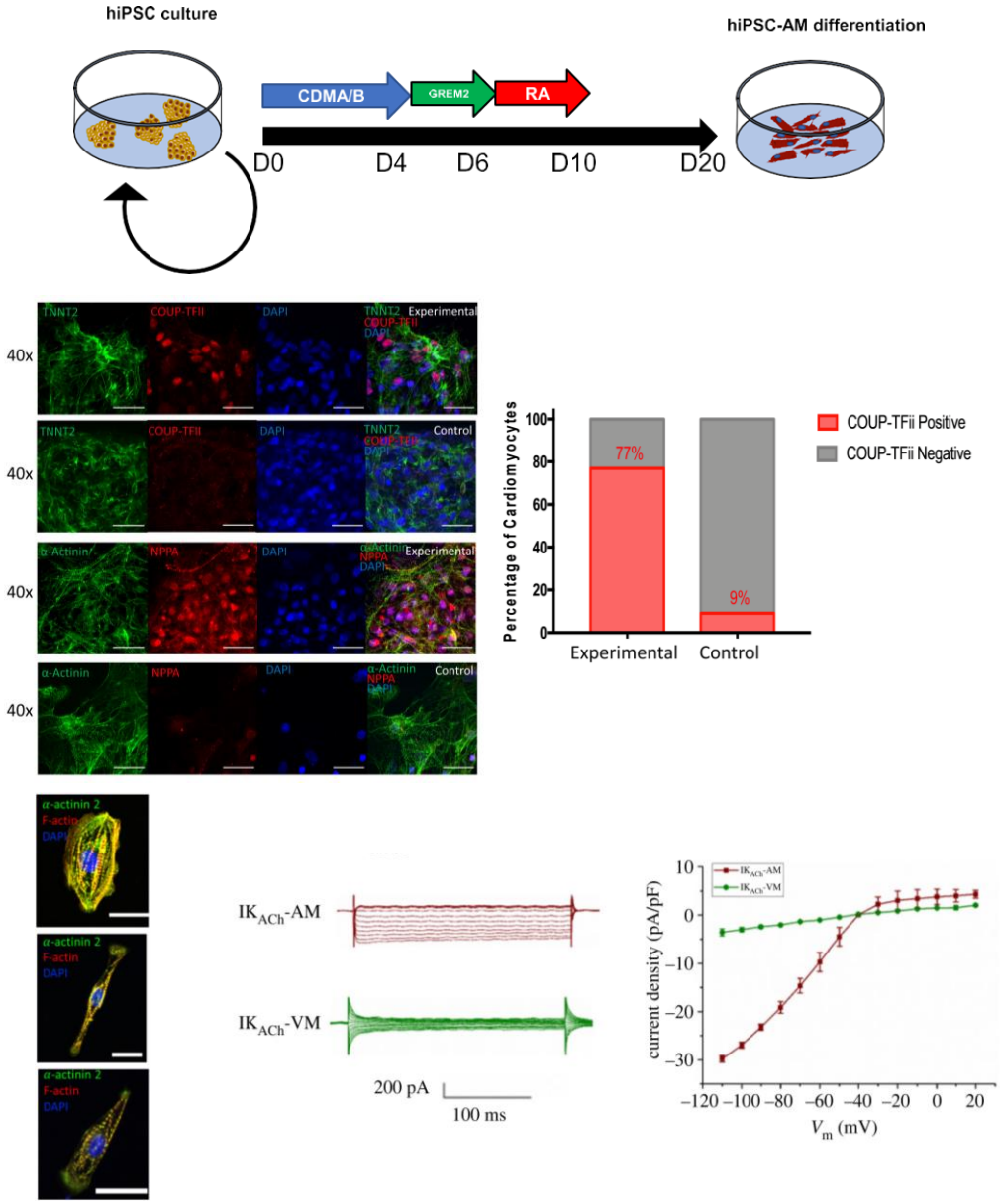

Figure 1-4. GREMLIN-2 and retinoic acid influences hiPSC differentiation into atrial-like cardiomyocytes.

A) Schematic diagram of the differentiation protocol. c. 70% confluency hiPSC colony differentiation was initiated at Day 0 by the addition of CDMA, followed by CDMB at Day 2. Then, our G2RA protocol began with GREMLIN-2 (1 μg/ml) in CMM from Day 4 to Day 6. Retinoic acid (1.0 μM) was then included in the CMM feeds between Day 6 and Day 10. After Day 10, CMM only was used. Cells were had fresh solution changes every 2 days with respective solution for that stage. Cells were ready for experimentation after Day 20. The control group here used CMM only from Day 4 onwards.

B) hiPSC-derived cardiomyocytes at Day 20 express cardiomyocyte-specific α-actinin and cTnT in the G2RA and CMM groups. However, only the G2RA group expressed atrial cardiomyocyte-specific COUP-TFII and NPPA.

C) COUP-TFII$^+$ cardiomyocytes compose 77% of the G2RA group, compared to 9% in the CMM control. 94 DAPI$^+$ cell nuclei, and their overlap with COUP-TFII expression was used to calculate the percentage of COUP-TFII positive cells.

D) G2RA-treated hiPSC-derived cardiomyocytes demonstrated a range of cell morphologies and sarcomeric organisation consistent with a more mature phenotype.

E) Whole-cell voltage clamp recordings of acetylcholine-induced (1 μM) currents. Left) Representative currents from the G2RA (IK_{ACh}-AM) and CMM (IK_{ACh}-VM) groups in response to voltage steps in the range −110 to +20 mV. Right) I–V plot of current density against membrane potential. IK_{ACh} current density was much greater in the G2RA-treated group, and very weak within the CMM-treated group. The I-V relationship of the G2RA-treated group demonstrates the associated inward rectification expected from IK_{ACh} currents.

Abbreviations: CDM – Cardiac Differentiation Medium, CMM – Cardiac Maintenance Medium.

N.B. The data collected and analysed in this Figure was from Dr. F. Ahmad, Dr. J. Yin, or Dr. Y Zhou. I contributed to the final interpretation of the data.

Figure in part adapted from Ahmad, Jin, Grassam-Rowe et al.[1]

d. Hypothesis and Aims

Hypothesis 1: Examining the heart from the perspective of its heterogeneity may reveal previously unconsidered aspects of its biology – both at the level of cardiomyocyte and non-cardiomyocyte heterogeneity. In particular, recent discoveries have implicated that cardiomyocytes might produce the major parasympathetic neurotransmitter (ACh)[334-336] and that a subset of cardiomyocytes possess some of the biosynthetic machinery conducive to producing adrenaline[337-339] – if cardiomyocytes also possess the biosynthetic enzyme that creates the substrate for Pnmt, this would be supportive of a potential wider role of cardiomyocytes within the signalling milieu of the heart.

Aim 1 – What is the cardiac expression of catecholaminergic biosynthetic genes and does it have any importance?

Hypothesis 2: hiPSC-CMs remain an intriguing potential source of human cardiomyocytes for both pre-clinical and clinical contributions to the discovery of novel therapies. However, they remain limited by their immaturity[322]. Recent attempts to overcome this have included identifying pro-maturity factors that may be included during the differentiation process of hiPSC-CMs[322,340]. Comparing and contrasting the differentiation and maintenance of cardiac phenotypes in native tissue may be illustrative for hiPSC-CMs and single-cell RNA sequencing may provide the appropriate dataset for this. Whilst original single-cell RNA sequencing focused on embryology[341,342], neurology[343,344], and immunology[345-347] it has increasingly been applied to the cardiac field[266,270,273,348]. These interrogations of cardiac single-cell biology have progressed from work describing the molecular heterogeneity of the developing heart[266,270,273,348], through to more computationally complex descriptions of transcriptional networks driving cardiac development, physiology, and pathophysiology[265,267,269,272,330,349]. However, despite many intriguing discussions around the importance of cardiac heterogeneity, there has only been extremely limited clinical translation from cardiac single-cell RNA sequencing work[350]. The most impactful work in terms of meaningful and actionable changes to scientific practice and understanding from cardiac single-cell RNA sequencing has been in identifying pro-maturation targets in hiPSC-CM differentiation[349]. Ultimately, the use of single-cell RNA sequencing has an assumption that sampling the transcriptome is informative about the phenotype of the cell. However, in the cardiac space this remains controversial[321,351,352] and work is required to understand which questions this tool is suited to answer in the cardiac space.

Aim 2 – Can we use scRNA-seq to produce actionable insights into atrial development and maturation, and how do these relate to hiPSC-AM differentiation?

Hypothesis 3: There have been attempts to relate the transcriptome through to the assumed emergent electrophysiological activity of the underlying proteins encoded by the respective genes[128,353,354]. However, no-one has yet robustly determined whether co-variance is a more informative metric for describing these transcriptional networks rather than metrics derived from population-level transcript abundance. This information, coupled with the appropriate experimental validation data, I believe is likely to be informative. Furthermore, using hiPSC-CMs, which have less well-regulated calcium handling[355], may provide a secondary exemplar case to determine whether the use of covariance-derived networks are of physiological interest.

Aim 3: What is the relationship between calcium handling components at the level of the transcriptome?

Hypothesis 4: Recent attempts to produce hiPSC-AMs have relied on the use of pro-atrial morphogens[271,281,283,285,312,315]. However, our model appears to produce a phenotype notably closer to that of native human atria[1]. However, a more comprehensive assessment of their channel and neuropharmacology is necessary to determine whether this phenotype is holistic, reliable, and accurate across the many axes of variation that define the native human atrial phenotype.

Aim 4: Can we characterise our hiPSC-AMs further, with a particular focus on their wider pharmacology?

Chapter 2. Methods

a. Single-cell RNA Sequencing

i. Mouse model generation

All mouse model generation was performed by collaborators in Sun, Grassam-Rowe et al[2]. Alexander Grassam-Rowe contributed to conceive and interpret experiments, alongside data collection, analysis, and presentation across certain different models.

Dbh^{Cre} mouse model: As described in Sun, Grassam-Rowe et al[2]. CRISPR/Cas9 was used to insert the 2A-iCre-WPRE-polyA construct into the stop codon site of *Dbh*. This process involved first the in vitro production of Cas9 mRNA and gRNA with the construct vector produced by homolgous recombination through in-fusion cloning of a 3.0 kb 5' homology arm, the 2A-iCre-WPRE-polyA segment, and a 3.0 kb 3' homology arm. Subsequently, Cas9 mRNA, gRNA, and the vector construct were microinjected into fertilized C57BL/6J mouse eggs. PCR amplification and sequencing was used to identify F0 mice that were successfully expressing the vector, and were then crossed with C57BL/6J mice to obtain the F1 generation *Dbh*^{Cre} mouse line.

Dbh^{Cre}/Rosa26-tdTomato mouse model: As described in Sun, Grassam-Rowe et al[2], the *Dbh*^{Cre} mice were then crossed with a commercially available B6.CgGt(ROSA)26Sortm9(CAG-tdTomato)Hze/J strain (#007909 Jackson Labs) to produce the *Dbh*^{Cre}/Rosa26-tdTomato used for lineage tracing.

Dbh^{Cre}/ChR2-tdTomato mouse model: As described in Sun, Grassam-Rowe et al[2], the *Dbh*^{Cre} mice were then crossed with a commercially available B6.Cg-Gt(ROSA)26Sortm27.1(CAG-COP4*H134R/tdTomato) Hze/J strain (#012567 Jackson Labs). The resulting gene product then produces a hChR2-tdTomato fusion protein.

Dbh^{CreERT}mouse model: As described in Sun, Grassam-Rowe et al[2], the *Dbh*^{CreERT} mice were produced using CRISPR/Cas9-guided insertion of a 2A-iCre-WPRE-polyA. The *Dbh*^{CreERT} mice were then crossed with a C57BL/6JSmoc-Gt(ROSA)26Sorem(CAG-LSL-tdTomato)1Smoc line (Shanghai Model Organisms Centre), to produce a *Dbh*$^{CreER/Rosa\text{-}26\text{-}tdTomato}$ mouse line. Adult 8-week old mice were induced with Tamoxifen (Sigma) at 150 mg/kg gavage for 5 days consecutively. Mice were only used for downstream experiments after a recovery period of a week.

Dbh^{CFP} mouse model: As described in Sun, Grassam-Rowe et al[2], was produced with CRISPR/Cas9-guided insertion of an IRES-CFP-5xFlag-WPRE-polyA construct into the stop codon of *Dbh*.

Dbh$^{Cre/ChR2\text{-}tdTomato/Cx40\text{-}eGFP}$ mouse model: As described in Sun, Grassam-Rowe et al[2], these mice were the result of crossing *Dbh*$^{Cre/ChR2\text{-}tdTomato}$ mice with a *Gja5*^{eGFP} mouse line kindly provided by Prof. Lucile Miquerol (Institut de Biologie du Développement de Marseille-Luminy)[133]

Dbh$^{flox/flox}$ and *Dbh*^{CKO} mouse model: As described in Sun, Grassam-Rowe et al[2], CRISPR/Cas9 was used by to insert two *LoxP* sites flanking exons 3-5 of *Dbh*. Then *Dbh*$^{flox/flox}$ mice were crossed with a *Myh6*^{Cre} mouse line to produce a cardiomyocyte-specific homozygous knockout of *Dbh* expression. *Myh6*^{Cre} mice were kindly provided by Prof. Gillian Douglas (Radcliffe Department of Medicine, University of Oxford). Genotypes for both lines were confirmed with PCR and knockout efficacy was confirmed with rt-PCR. Primers: sense: 5'-GCTGGGGTCCTGTTTGGAAT-3'; Anti-sense: 5'-CTCCAGGCATCCGCAAAGT-3'.

Myh6$^{Cre/ChR2\text{-}tdTomato}$ mouse model: As described in Sun, Grassam-Rowe et al[2], C57B6J B6.FVB-Tg(Myh6-cre)2182Mds/J (#011038 Jackson Labs), with *Myh6*^{Cre} expression were crossed with a B6.Cg-Gt(ROSA) 26Sortm27.1(CAG-COP4*H134R/tdTomato) Hze/J strain (#012567, Jackson Labs) to drive cardiomyocyte-specific ChR2-tdTomato fusion protein expression.

Gja5$^{CreERT/ChR2\text{-}tdTomato}$ mouse model: As described in Sun, Grassam-Rowe et al 2023[2], C57B6J mice with *Gja5*^{Cre} expression were crossed with a B6.Cg-Gt(ROSA) 26Sortm27.1(CAG-COP4*H134R/tdTomato) Hze/J strain (#012567, Jackson Labs) to drive cardiomyocyte-specific ChR2-tdTomato fusion protein expression. *Cx40*^{CreERT} mice were kindly provided by Prof. Lucile Miquerol (Institut de Biologie du Développement de Marseille-Luminy)[133]. Adult mice (8 week old) were induced with Tamoxifen (Sigma) (150 mg/kg, gavage) for 5 consecutive days. One week after induction mice were used for subsequent experiments.

ii. Single-cell RNA sequencing data collection

All sample collection was performed by collaborators in Sun, Grassam-Rowe et al 2023[2] and sequencing and preliminary quality control was performed by Novogene (a sequencing company).

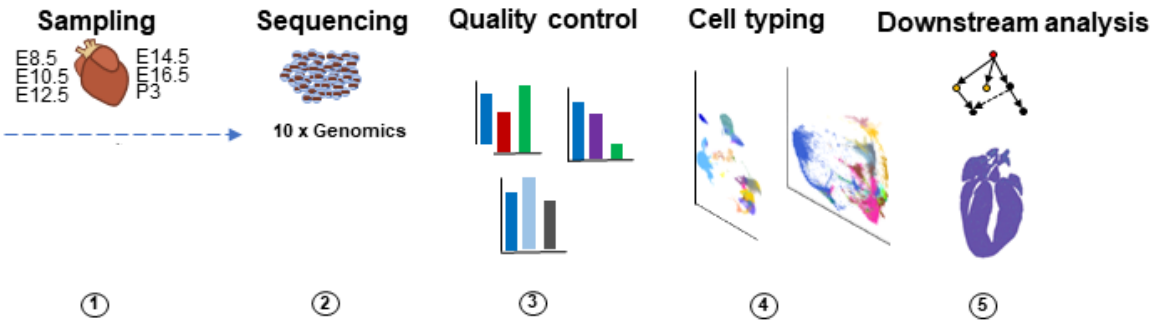

Figure 2-1. A summary of the pipeline of our scRNA-seq data flow.

1) Samples were collected from mouse hearts across development.
2) Cells were processed and sequenced using a 10X Genomics droplet-based sequencing technique.
3) The dataset underwent quality control at the gene and cell level.
4) Cells were then grouped and classified into cell types.
5) Further downstream analysis was performed.

This Figure was adapted from Sun, Grassam-Rowe et al.[2]

Single-cell library construction: As described in Sun, Grassam-Rowe et al[2], mouse embryos were collected from stages E8.5 and E10.5. Hearts were dissected from embyros, fetuses, or pups at stages E12.5, E14.5, E16.5, and P3 and single cardiomyocytes were dissociated as described previously using standard enzymatic dissociation techniques[356]. Samples were collected in two batches per stage, containing multiple animals per batch. Single cell suspensions were subjected to quality control to ensure cell concentrations of 700-1200 cells/μL and cell diameter 5-40 μm. Single cell preparation followed the device manufacturer's advice as per the 10X Genomics protocol. Chromium microfluidic chips were loaded with the cell suspension with 30 (v3) chemistry. Cells were then barcoded via a 10X Chromium controller. The barcoded cells' mRNA pool was then incubated with reverse-transcriptase to form the cDNA library, which was then amplified with reagents from, and in line with protocols from, the manufacturer's instructions and Chromium Single cell 30 v3 reagent kit (10X Genomics). Illumina HiSeq was used to sequence the libraries as per the manufacturer's instructions. Raw reads underwent basic QC via FastQC and were then mapped to the reference mouse genome via CellRanger using default parameters. Unique molecular identifiers (UMIs) were included in the library construction phase, and were used to construct count expression matrices with gene expression matched to respective barcodes that represent single-cells.

iii. Single-cell RNA sequencing analysis

All single-cell RNA sequencing analysis was performed by Alexander Grassam-Rowe. Data collected by Murphy et al[357], was downloaded and analysed additionally, as detailed below.

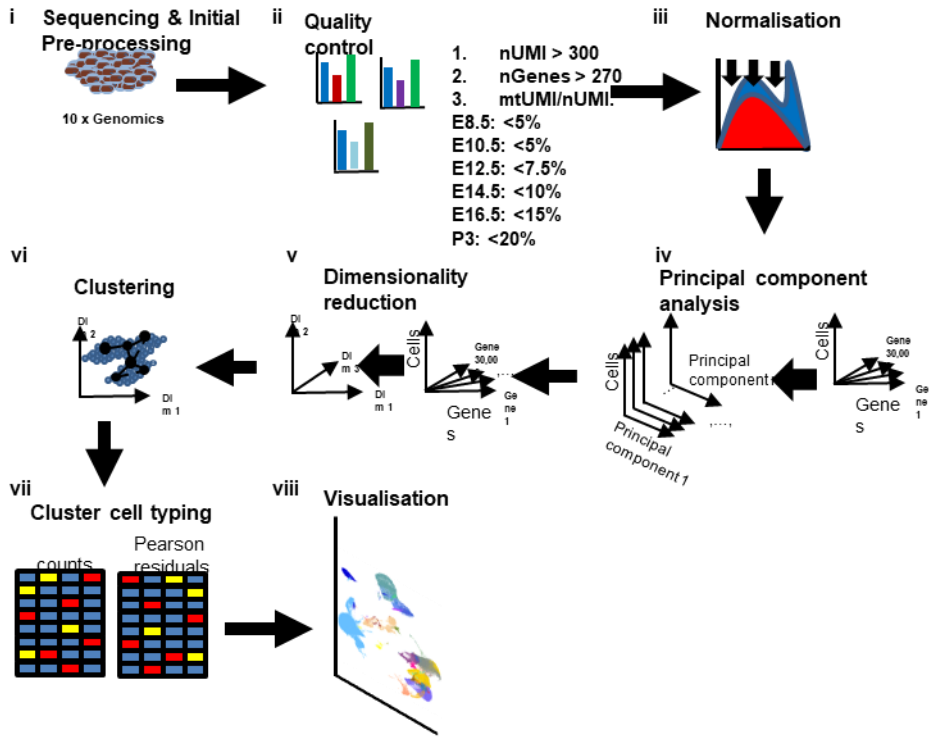

Figure 2-2. I curated a new cardiac-focused pipeline for transcriptomic analyses.

i) Cells were sequenced. Cell libraries were subjected to read-wise quality control and UMI barcode matrix construction.
ii) Single-cell libraries were then subjected to cell-wise quality control, with cells kept only if they met all of the following characteristics described to the right.
iii) SCTransform was used to normalise raw RNA counts to mitigate variance from single-cell library size.
iv) I performed principal component analysis to identify and select only those components contributing the major elements of computational and biological variation for downstream analyses.
v) Initial dimensionality reduction using UMAP, reduced the dimensionality of the dataset around 10,000x. Dimensionality reduction techniques enable more intuitive low dimensional interaction with datasets.
vi) Louvain clustering identified transcriptomically similar clusters of cells. I labelled clusters with biological identities based on their gene expression, using both normalised count data and their Pearson's residuals from respective average gene expression.
vii) I visualised the data and performed further analysis.

This Figure was adapted from Sun, Grassam-Rowe et al[2].

Initial cell typing: As described in Sun, Grassam-Rowe et al[2], I sought to balance robust and reliable transcriptomic signal-to-noise ratios whilst retaining sensitivity to small signals in the data. Figure 1 illustrates my workflow. Thus, our initial quality control filtered out all cells with unique RNA counts (nUMI) < 300, or distinct genes (nFeatures) < 270, to remove under-sampled cells and simple cells such as erythrocytes. Figure 2 demonstrates the post-quality control distributions of various quality control metrics. The ratio of mitochondrial-genome derived transcripts to nuclear genome-derived transcripts is often used as a metric of cell stress in single-cell RNA sequencing, with 5% as a commonly used arbitrary ceiling. However, there is a growing body of literature that supports that this arbitrary cut-off might be pertinent in certain cell types, but fails to allow for normal biological variance in this number across different cell types. In particular, cardiomyocytes can reach ~30% mitochondrial transcripts[358] and this varies across cardiomyocyte populations[359]. During normal cardiac development, there is a temporally dynamic change in mitochondrial biogenesis[309]. Therefore, I used a dynamically changing filter for quality control of mitochondrial transcript ratios: E8.5: 5%, E10.5: 5%, E12.5: 7.5%, E14.5: 10%, E16.5: 15%, P3: 20%. I normalised cell libraries using SCTransform, an approach that preserves differential variation between highly variant and lowly variant genes [360]. I utilised uniform manifold approximation and projection (UMAP), following principal component analysis (PCA) and PCA dimension selection, to enable more readily human-interpretable low dimension visualisation of the high dimension (~27,000 dimension) transcriptomic space through dimensionality reduction. I then inspected the data for any batch effect during data collection between stages. Only P3 displayed any significant batch differences. There are a number of suggestions for the mathematical 'correction' of batch differences[361]. However, these methods have been shown both a priori and empirically to produce aberrant downstream statistical results[362], and thus I elected not to use them here. I visualised our UMAP dimensions in 3D, using Plotly (https://plotly.com/) and used Louvain clustering, with clusters labelled based on expression profiles. Further sub-clustering was performed as necessary, and a small number of cells were manually assigned where appropriate. All the above was done using Seurat[363] functions in R (v3.6/4.0) unless specified. Following pre-processing and library quality control, our data had mean UMI and gene counts of 6417 and 1482 respectively across 175237 cells in our scRNA-Seq.

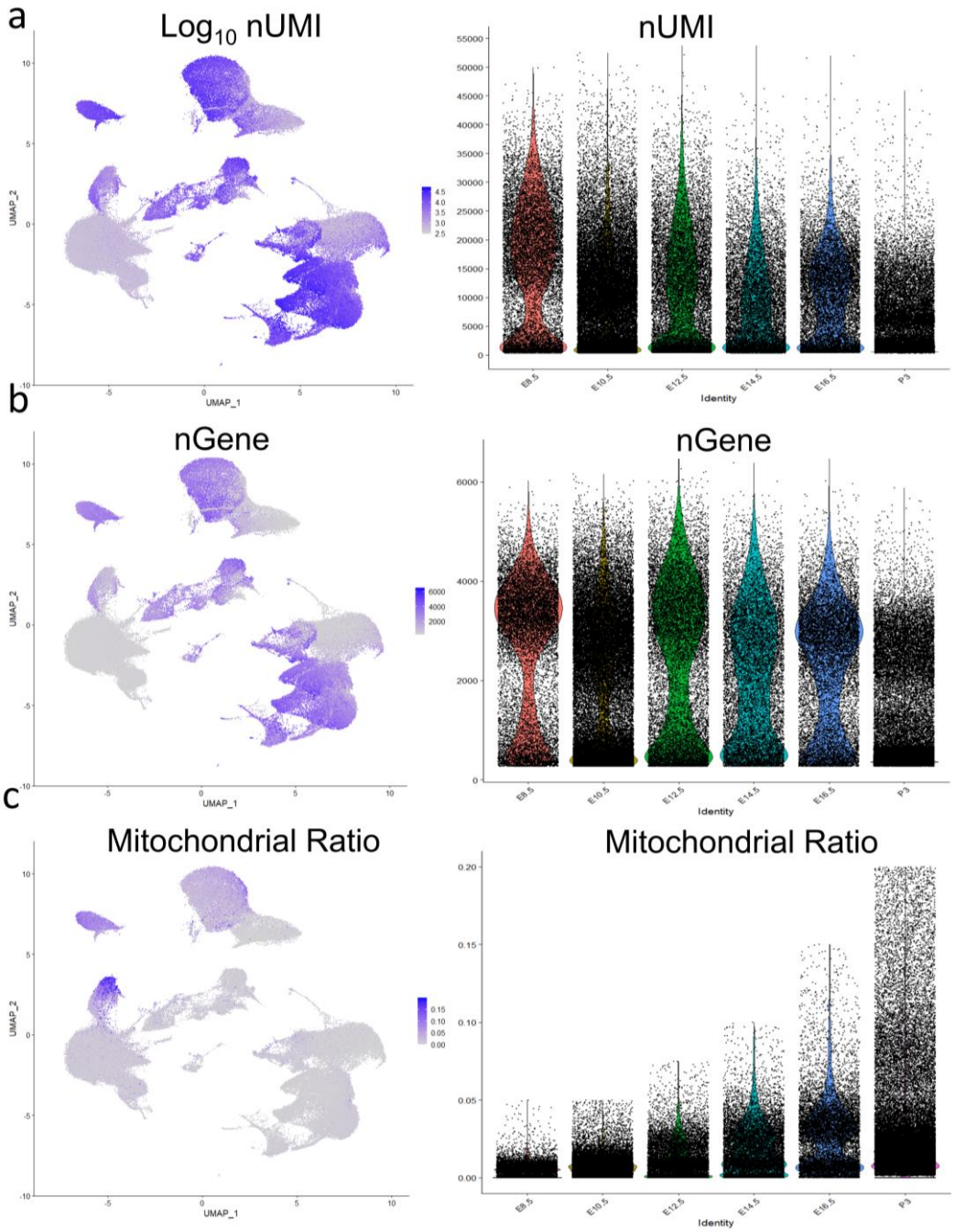

Figure 2-3. Single-cell quality control measurements across sequencing.

a) Left) All initial cells post-quality control, coloured by Log_{10}(nUMI) and plotted in 2D UMAP. Right) a violin plot plotting Log_{10}(nUMI) separated by stage.
b) Left) All initial cells post-quality control, coloured by nGene and plotted in 2D UMAP. Right) a violin plot plotting nGene separated by stage.
c) Left) All initial cells post-quality control, coloured by the ratio of mitochondrial nUMI to total nUMI and plotted in 2D UMAP. Right) a violin plot plotting the ratio of mitochondrial nUMI to total nUMI separated by stage.

This Figure was adapted from Sun, Grassam-Rowe et al[2].

Cardiomyocyte-specific cell typing: As described in Sun, Grassam-Rowe et al[2], I sought to isolate the cardiomyocyte lineage from our single-cell RNA sequencing dataset, to improve the

discrimination of specific cell types within this lineage. Thus, I isolated the cardiomyocyte-lineage cell types I had identified: "Cardiac Progenitors, Early Cardiomyocytes, Immature Atrial Cardiomyocytes, Immature Ventricular Cardiomyocytes, Cardiac Conduction System, ECM Atrial Cardiomyocytes, ECM Ventricular Cardiomyocytes, Atrial Cardiomyocytes, Ventricular Cardiomyocytes, and *Myh6*$^{+}$ Ventricular Cardiomyocytes". I subsequently normalised nUMI counts using SCTransform[360], and used potential of heat-diffusion for affinity-based transition embedding (PHATE) for dimensionality reduction[364]. PHATE preserves global and local distances between points in transcriptomic space, whereas other dimensionality reduction techniques fail to maintain both global and local distances[364]. The preservation of global and local distances respectively facilitates reliable and robust interpretation of between cell-type and within cell-type variation across the transcriptome. I also used PHATE's spectral-like clustering and cell types were assigned by comparison with literature expression profiles. I identified 15 cardiomyocyte lineage cell types over n=107705 cells. I used the parallel implementation of Seurat's FindMarkers [https://github.com/vertesy/Seurat.multicore], implemented with min.pct=0.2,logfc.threshold=0.5, and test.use="bimod" to compare differential gene expression between cell types. The 'bimod' model uses a hypothesis test that models both the discrete and continuous distributions of gene expression as a likelihood ratio test[365]. Post-hoc Bonferroni corrections were used to adjust for multiple comparisons.

Dbh^{+}-cardiomyocyte identification: I isolated all cells with raw nUMI > 0 for *Dbh* from the cardiomyocyte lineage. These cells were then re-normalised with SCTransform and subjected to PHATE dimensionality reduction. I transferred cell classifications based on the classifications assigned from within the cardiomyocyte lineage. I used a two-tailed Chi Squared test for independence to determine if Dbh expression (as binary >0 or =0), was independent of cell type. Only cardiomyocyte lineage cell types composed primarily of cells beyond E10.5 were included, as before this *Dbh* expression was extremely limited. Therefore, I excluded the following cell types: Primary heart tube, Misc., Heart Fields, Endocardial-gene rich cardiomyocytes, and Developing cardiomyocytes.

Identification of atrial lineage within single-cell RNA sequencing: I further filtered the dataset to include only the working myocardium lineages (Figure 3a) and nUMI > 1000. I then repeated normalisation, PCA, and PHATE. I then identified lineage-specific pseudotimes using Slingshot [Slingshot] and isolated the atrial lineage from beyond E12.5 with 3000 < nUMI < 15,000. In brief, Slingshot uses a low (2-/3-D) reduced dimension transcriptomic space, and projects one or more principal curves that describe the overall trajectory along pseudotime. Cells are then scored by their relative positions along the curve and given a calculated pseudotime. I then performed PHATE followed by MAGIC imputation[366] on this dataset to recover gene dropout.

Maturation GRN analysis: I performed differential expression analysis between each stage of the imputed atrial lineage from E12.5, E14.5, E16.5, and P3 using Seurat's FindMarkers with logfc.threshold=0.25, min.pct=0.25, assuming a negative binomial error model. I then filtered the atrial dataset's genes to those genes differentially expressed with an adjusted p-value <1x10-5 and added 202 additional genes of interest. This highly filtered atrial dataset was then used for SCENIC[367] analysis, selecting only those transcription factors (TFs) identified in >70/100 runs of SCENIC. For each of these TFs, I identified the top 75 percentile of genes regulated by each TF and exported these modules to Cytoscape[368]. I used MCODE with default settings to identify

submodules within the wider TF network. I then performed gene ontology (GO) using the TopGO implementation within the ViSEAGO package[369].

Calcium network analysis: I utilised GEOquery[370], to download the dataset (GSE165917) from Murphy et al[357]. In brief, Murphy et al expertly used large-particle flow-assisted cell sorting (LP-FACS) to isolate murine cardiomyocytes which were than sequencing using SCRB-seq for library construction and Illumina NextSeq500 for sequencing, and then reads aligned onto Mm10 reference genome. I then excluded all except wild type P0 cardiomyocytes and normalised them using SCTransform[360]. We then excluded all genes apart from those that we had assigned as matching to Hinch model[67] parameters as in Table 2-1. Following this, I examined expression levels, Pearson's correlations, and correlations of combinations of these parameter groupings as described in results.

Hinch Model Parameter	Brief description	Genes included
B_CMDN	Total cytosolic calmodulin concentration	*Calm1, Calm2, Calm3*
B_TRPN	Total cytosolic troponin concentration	*Tnnc1, Tnnc2, Tnnc3*
gSERCA	Maximum pump rate of SERCA	*Atp2a2, Atp2a1, Atp2a3, Pln, Sln*
rSR_l	Rate of leak of Ca^{2+} from SR to cytosol	*Ryr2, Ryr3, Itp1r, Itp2r, Itp3r, Casq1, Casq2, Jph1, Jph2, Trdn, Calr, Tpcn1, Tpcn2, Fkbp1a, Fkbp1b, Fkbp1c, Fkbp4, Fkbp5*
gNCX	Pump rate of NCX	*Slc8a1, Slc8a2, Slc8a3*
gpCa	Maximum pump rate of sarcolemmal Ca^{2+} pump	*Atp2b1, Atp2b2, Atp2b3, Atp2b4*
gCa_B	Conductance of background Ca^{2+} currents	*Cacna1c, Cacnb2, Cacna2d1, Cacna1s*
$[Na_i]$	Cytosolic Na^+ concentration	*Scn5a, Slc4a4, Slc4a7, Gja1, Kcnj2, Kcnj12, Atp1a1, Atp1a2, Atp1a3, Atp1a4, Atp1b1, Atp1b2, Atp1b3, Atp1b4*

Table 2-1. Parameters modelled from the Hinch model (2004) and the genes included

iv. Spatial transcriptomics data collection

All sample collection was performed by collaborators in Sun, Grassam-Rowe et al[2]. Alexander Grassam-Rowe contributed to troubleshooting and optimising discussions during data collection.

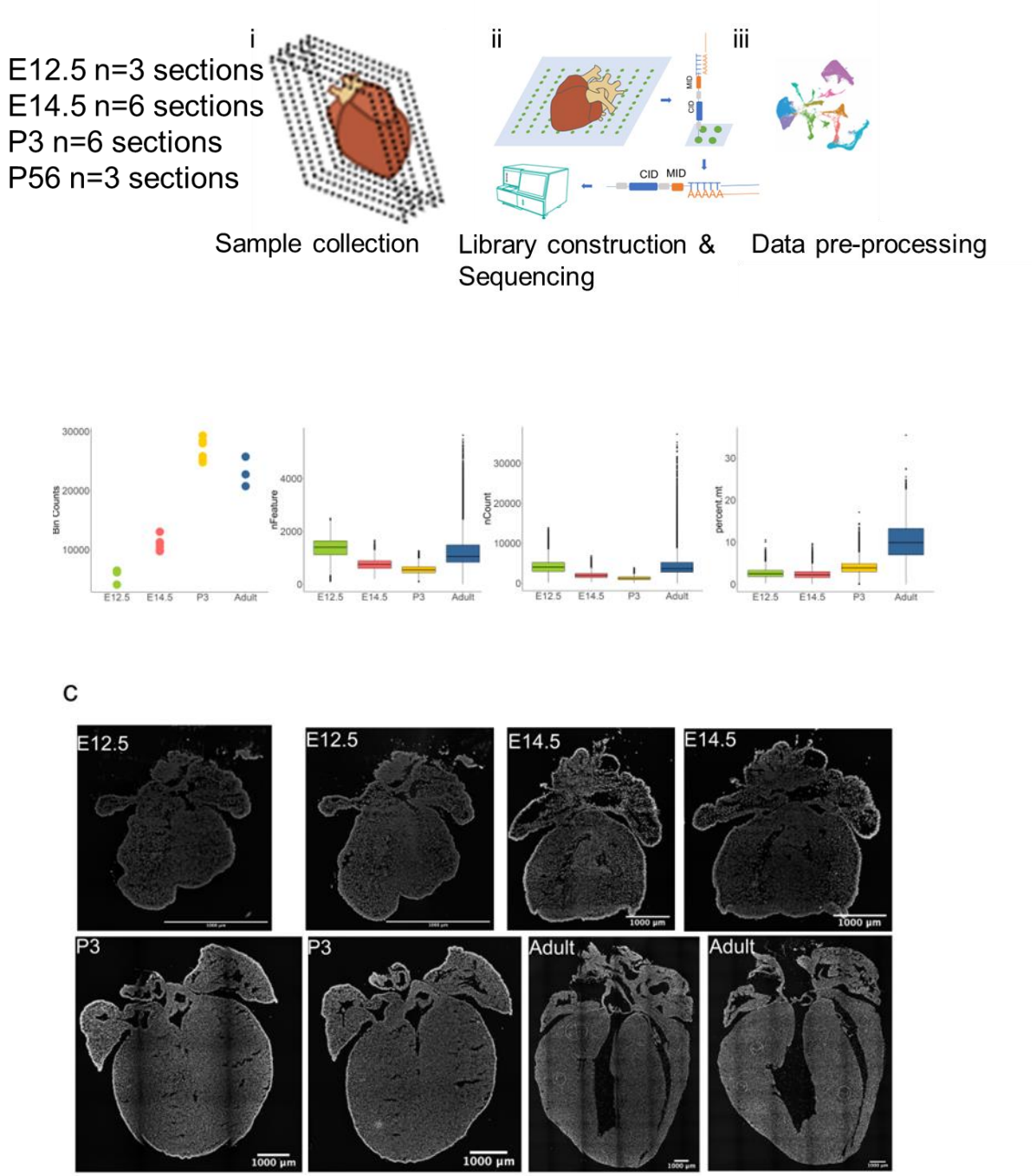

Figure 2-4. Stereo-Seq data collection and pre-processing.

a) Schematic diagram of Stereo-Seq data collection from: i) data collection; ii) library construction and sequencing; iii) Data pre-processing.
b) Final bin number per stage and section. nFeature, nCount, and percentage of UMIs that are mitochondrial across each stage.
c) Images of heart sections stained with ssDNA to identify nuclei. 1000 µm scale bar.

This figure is adapted in part from Sun, Grassam-Rowe et al[2]. The data in this figure was collected by collaborators in the paper from Beijing Genomics Institute (BGI).

Embryo and heart dissection: As described in Sun, Grassam-Rowe et al[2] hearts were dissected from embyros, fetuses, or pups/mice at stages E12.5, E14.5, P3, P56. Mice used were either wild type or *Dbh*$^{Cre/Rosa26\text{-}tdTomato}$ mice. All samples were dissected and washed in PBS to remove any

blood. For adult (P56) samples, the heart was cannulated and washed with retrograde aortic PBS perfusion to aid in washing. Samples where embedded in Tissue-Teck OCT (Sakura, 4583) and then frozen on isopentane dry-ice slurry and stored at -80°C. A Leica CM1950 cryosection was then used to cut 10 μm sections of samples, which were then rapidly transferred to Stereo-Seq sequencing chips for downstream experiments. Adjacent sections to the ones used for sequencing were examined for tdTomato fluorescence under fluorescence light microscopy.

Stereo-Seq sequencing: As described in Sun, Grassam-Rowe et al[2] and adapted from previous work[371,372]. Stereo-Seq chips with sections were dried at 37°C for 3 minutes followed by immersion in chilled methanol for 30 minutes. Tissues sections were then stained with a ssDNA-binding reagent (Invitrogen Q10212) for 5 minutes, and then washed using a 1:10 diluted SSC buffer (Ambion AM9770), supplemented with a 0.05 U/μL RNAse inhibitor. ssDNA images were then recorded with a Ti-7 Nikon Eclipse microscope with standard FITC excitation and emission filters. 0.1% pepsin (Sigma P7000) in 10 mM HCl (pH 2) was then used to permeabilise the tissue at 37° for the optimised times for each stage (E12.5, E14.5, P3: 6 minutes; P56: 18 minutes). Subsequently, sections were washed with the SSC buffer and RNAse inhibitor, and then cDNA library construction was initiated by the addition of SuperScript II (Invitrogen 18064014, 10 U/μL reverse transcriptase, 1 mM dNTPs, 1 M betaine solution (PCR reagent), 7.5 mM $MgCl_2$, 5 mM DTT, 2 U/μL RNAse inhibitor, 2.5 μM Stero-TSO and 1X First-Strand buffer) at 42°C overnight. Tissues were then washed twice with SCC buffer, and then were digested with Tissue Removal Buffer (10 mM Tris-HCl, 25 mM EDTA, 100 mM NaCl, 0.5% SDS) at 37°C for 30 minutes. Subsequently, the chips are washed twice with SCC buffer, and treated with Exonuclease I (NED, M0293L) at 37°C for 1 hour. Following a single wash in SCC, cDNA amplification was performed using KAPA HiFI HotStart Ready Mix (Roche, KK2602) with 0.8 μM cDNA-PCR primer. Following cDNA amplification, cDNA products were fragmented through an in-house (BGI) Tn5 transposase amplified with KAPA HiFi HotStart Ready Mix, and purified using AMPure XP beads (Beckman Coulter, A63882). The PCR products, purified, were converted into DNA nanoballs (DNBs) prior to sequencing via a MGI DNBSEQ-Tx sequencer.

v. Spatial transcriptomics analysis

Preliminary raw sequencing analysis, gene expression matrix construction, and unsupervised clustering was performed by collaborators in Sun, Grassam-Rowe et al[2]. Alexander Grassam-Rowe performed all subsequent downstream analysis and was the lead for assigning cell cluster identity from unsupervised clustering results and in designing the unsupervised clustering workflow. Alexander Grassam-Rowe conceived the use of RCTD, and the pipeline for it, with collaborators performing the final execution of the single RCTD calculation as detailed below, under his direction.

Preliminary raw Stereo-Seq sequencing analysis: As described in Sun, Grassam-Rowe et al[2], and as adapted from prior work[373], cDNA sequences output from FASTQ files from the MGI DNBSEQ-Tx sequencer were aligned using STAR against a reference mouse genome (mm10), supplemented with WPRE sequences matching the transgenic construct in our mouse models. Each spatial region was marked with a unique identifier (CID) and a similar process as with UMIs was used as well (MID). Thus, for each gene with each CID, reads with the same MID were counted as 1, to eliminate PCR amplification bias in our sequencing results. After alignment

and counting, gene expression matrices corresponding to each CID were produced. Gene-expression matrices were divided into bins with 20 x 20 DNBs for E12.5, E14.5, and P3, and 50 x 50 DNBs for adult hearts. Density plots were used to exclude bins with low gene counts. Genes expressed in fewer than 5 bins were also discarded. In total there were three E12.5 slices, six E14.5 slices, and six P3 slices that were clustered using Seurat. SCTransform was used for normalisation and variable gene identification. Then PCA was computed, and the first 30 PCA dimensions were then used to produce a 2D UMAP. Louvain clustering was then used to identify clusters, and FindAllMarkers was used to identify differentially expressed genes for each group, with the parameters: min.pct=0.1, logfc.threshold=0.25. Each cluster was annotated in correspondence to the literature and spatial location of bins within clusters.

Integration of single-cell and spatially resolved sequencing data: As described in Sun, Grassam-Rowe et al[2], I sought to identify if our single-cell RNA sequencing cell classifications could be mapped onto our spatially resolved transcriptomics (SrT) maps. I used a composite library of distinct cell types from our whole dataset and our cardiomyocyte lineage, to build a representative library of potential cell types in the developing murine heart from E12.5 to P3. This reference library consisted of: "Atrial Cardiomyocytes, Ventricular Cardiomyocytes, Immature Atrial Cardiomyocytes, Immature Ventricular Cardiomyocytes, Immature Trabecular Ventricular Cardiomyocytes, Trabecular Ventricular Cardiomyocytes, Sinoatrial Node, Atrioventricular Node, Purkinje Fibres, Fibroblast-like, Smooth Muscle-like, Endothelium, Epicardium, Endocardium, Neural Crest, Haematopoetic Precursors, Immune Cells, and Platelets". This subpopulation library was then re-normalised using SCTransform. To identify marker genes in an unbiased manner for specificity and robustness for each cell type in the reference library, I used SMASH[358]. Genes were ranked by their contribution to cell type classification, using gene-wise Gini importance based off a trained ensemble supervised machine learning classifier. The top 50 genes were then kept and used to predict the cell type classification of the spatially resolved bins, via RCTD – performed by collaborators under my direction. RCTD decomposes spatial bin cell composition via a probabilistic classifier[374].

vi. Structural imaging

All structural imaging of murine hearts was performed by collaborators in Sun, Grassam-Rowe et al[2]. Alexander Grassam-Rowe contributed to the conception, planning, discussion, interpretation, and presentation of imaging results.

Immunohistochemistry: As described in Sun, Grassam-Rowe et al[2], frozen tissue sections were fixed in 4% PFA for 15 minutes at room temperature. Sections were then washed thrice in PBS for 5-minute duration washes. Sections were then permeabilised in 0.1% TritonX-100 in PBS for 30 minutes, washed thrice in PBS, 5-minute duration washes, and then blocked in 0.1% Tween-20 in 10% normal (goat or donkey as appropriate) serum for 1 hour at room temperature. Sections were then incubated overnight with primary antibodies at 4°C. Sections were then allowed to recover at room temperature for an hour and washed thrice in PBS before being incubated with secondary antibodies for 2 hours protected from light. To finish, protective mounting medium containing DAPI was used to cover the sections and nail polish was used to seal coverslips over sections on slides.

Fluorescent multiplexed in situ nucleic acid hybridization (RNAscope): As described in Sun, Grassam-Rowe et al[2], fixed frozen tissue slides were thawed at room temperature for 15 minutes. Samples were then baked for 30 minutes at 60°C. Subsequently, slides were fixed with 4°C-chilled 4% PFA for 15 minutes and then subjected to serial dehydration through submersion for 5 minutes each in 50%, 70%, 100% and 100% ethanol. Slides were then allowed to dry for 5 minutes and left in hydrogen peroxide for 10 minutes. Next, target retrieval reagent was applied and slides were left at 95°C for 5 minutes, with 2 subsequent washes in distilled water. Protease digestion (ACD Protease III) was used for 20 minutes to permeabilise tissue. Probes were labelled in channels C1 and C3 respectively using Opal 520 and 690 fluorophores (Akoya Biosciences, 1:200). Channel 4 probes were developed using TSA biotin (TSA Plus Biotin Kit, Perkin Elmer, 1:500). DAPI was used to stain nucleic acids within the nuclei. A Zeiss confocal LSM780 microscope was used to capture images with either 10X/20X non-immersion objectives, or a 63X water-immersion objective. Zeiss Black software was used for image capture and storage, with excitation and emission laser and filter settings at: DAPI (375 nm excitation, 435-480 nm emission); Opal 520 (488 nm excitation, 500-550 nm); and Opal 690 (676 nm excitation, 690-700 nm). These experiments were performed at least twice to ensure representative results.

Transmission electron microscopy and energy dispersive x-ray spectrometry: As described in Sun, Grassam-Rowe et al[2], $Dbh^{Cre/ChR2\text{-}tdTomato}$ 8-week old mouse hearts and adrenal tissue were isolated and tdTomato positive regions identified under fluorescence microscopy. Tissues were then fixed with 5% potassium chromate/dichromate solution at pH 5.6, with 4% formaldehyde, for 48 hours at 4°C. Deionized running water was then used to wash, with storage in 4% formaldehyde prior to serial dehydration with 15 minutes in each solution of 50%, 70%, 90%, 100%, and 100% again of propan-2-ol. Samples were then submerged in 50% LR white acrylic resin in propan-2-ol, followed by 4X LR white acrylic resin for 30 minutes each. Samples were then polymerised by 24 hours at 50°C. Light microscopy of slices used 0.1% toluidine blue in borax buffer to stain 0.35 μm thick sections. These sections were then imaged using an Olympus BX51 microscope (Olympus, UK) and a Zeiss Axiocam digital camera and Axiovision software (Carl Zeiss, Germany). 100 nm thick sections were used for transmission electron microscopy (TEM), collected onto 150 mesh formvar/carbon-coated copper grids which were stained by 2% uranyl acetate, prior to charge elimination by carbon coating evaporation of several nanometres. Imaging used the JEM2000 electron microscope (JEOL, UK), with STEM and EDAX Genesis 4000 energy dispersive X-ray spectrometry (EDAX, UK) using electron beams at 100 kV. An in-line Getan Orius camera (Gantan, UK) was used to record images.

vii. Functional interrogation of mouse hearts

Functional experiments were performed in collaboration with Southwest Medical University China, and with Dr Tianyi Sun and Asst. Professor Ming Lei, and other collaborators in Sun, Grassam-Rowe et al[2]. In particular, Alexander Grassam-Rowe assisted with the conception, design, implementation, execution, and optimisation of the ex vivo Langendorff perfused heart optogenetics which were performed in part in Oxford and in part in Southwest Medical University China. Alexander Grassam-Rowe contributed to the conception, discussion, design, analysis, interpretation, and presentation of the functional experiments included.

Optogenetic stimulation of ex vivo Langendorff perfused hearts: As described in Sun, Grassam-Rowe et al[2], blue (470 nm) light pulses of 5-10 ms duration each were delivered to the epicardial surfaces of the heart via LEDs (OptoFlash Cairn Research). Pulses were controlled by Spike2 software communicating via a 1401 digitiser (CED). Adult mice received an i.p injection of a terminal dose of 0.2 ml/10 g of 1.2% 2,2,2 – Tribromoethanol (Avertin) and then c. 0.5 ml of >1800 U/ mL heparin dissolved in distilled water. Following deep induction of terminal anaesthesia, confirmed by paw squeeze or eye touch, mice were sacrificed by Schedule 1 cervical dislocation. The heart was accessed by clamshell thoracotomy, and rapidly excised with the great vessels and placed into ice-cold Krebs-Henselt buffer without Ca^{2+} and containing c. 0.2 ml of >1800 U/ mL heparin solution per 10 ml of Krebs-Henselt buffer. The heart was then cannulated using a dissection microscope, within 10 minutes, typically using either a modified 20G or 18G cannula depending on the operator. The heart was then perfused with normal heated Krebs-Henselt buffer at 37°C around 3.5 ml/minute, oxygenated and pH-calibrated to pH 7.4 with 95% O_2 / 5% CO_2. Hearts were given a 15-minute equilibration period once perfused before any subsequent experimentation. A single lead (Lead II-like) electrode set-up was used on hearts and ECG parameters were collected and analysed. Two major protocols were carried out: continuous pacing with S1S1 pacing at a frequency between 8-10 Hz; S1S2 pacing with eight S1 stimuli at a cycle length of 100 ms followed by a premature S2 stimulus at progressively decreasing shorter intervals from the final S1 stimulus. The use of the S1S2 protocol enables the identification of the effective refractory period (ERP) of the stimulated region and was used to deliver blue light pulses to determine the ventricular ERP of *Dbh*$^{Cre/ChR2\text{-}tdTomato}$, *Myh6*$^{Cre/ChR2\text{-}tdTomato}$, *Gja5*$^{Cre/ChR2\text{-}tdTomato}$ mouse lines. Krebs-Henselt buffer was constituted at (mM): NaCl 128, KCl 4.8, $NaHCO_3$ 21.98, Glucose 11.0, $MgCl_2$ 1.0, $CaCl_2$ 1.8.

Chemical ablation of Purkinje Fibres: As described in Sun, Grassam-Rowe et al[2], we carefully injected 0.5 – 1 ml of Lugol's solution (5% (wt/v) iodine and 10% (wt/v) potassium iodide in distilled water) directly into the RV lumen through a 34G cannula carefully inserted into the RV through a transmural puncture.

b. hiPSC models

i. hiPSC generation and characterisation from patient samples.

hiPSCs lines were purchased from Gibco (USA, or were the CPVT cell line kindly provided by Prof. David Paterson's group, with original creation from the University of Nottingham Biodiscovery institute. No patient identifying information was provided. The Gibco hiPSC line was derived from cord blood-derived $CD34^+$ progenitor cells that were subjected to three plasmids and seven factors in an episomal system (OCT4, SOX2, MYC, KLF4, NANOG, SV40LT, and Lin antigen) to reprogram into hiPSCs. hiPSC readiness for use was determined by Gibco prior to sale, or by the University of Nottingham Biodiscovery Institute. hiPSC colonies were continuously monitored for signs of spontaneous differentiation.

ii. hiPSC culture and passage

All hiPSC culture presented here was performed by Alexander Grassam-Rowe apart from the work published in Ahmad, Jin, Grassam-Rowe et al[1], where Dr Faizzan Ahmad, and Dr Yongcheng Jin previously cultured hiPSCs. All hiPSC culture for new electrophysiology and pharmacology work presented in this thesis was performed by Alexander Grassam-Rowe.

As described in part in Ahmad, Jin, Grassam-Rowe et al[1], hiPSCs were cultured in 6 well culture plates coated with Corning® Matrigel®. hiPSCs were fed daily with mTeSR™ Plus (STEMCELL Technologies) to maintain an undifferentiated state as per the manufacturer's instructions. mTeSR™ Plus is rich in growth factors such as FGF2 that maintain hiPSCs in an undifferentiated state. mTeSR™ Plus was otherwise stored separately with its supplement aliquoted and stored at -20°C or -80°C. Whereas, mTeSR™ Plus base medium was stored at 4°C. Supplement aliquots were defrosted overnight at 4°C, and then complete medium was stored at 4°C for a maximum of 2 weeks. All mTeSR™ Plus media and components were stored protected from light as much as possibe. hiPSCs were passaged once reaching c.70% confluency, which typically occurred around day 3±1. To passage cells, their old media was aspirated, and then they were washed with room temperature Dulbecco's Phosphate-Buffered Saline (DPBS). Each well was then left at room temperature with 1 ml of ReLeSR™ for 40±5 seconds before the aspirating the ReLeSR™ media, leaving only a thin film as per the manufacturer's instructions, and incubating the plate for 5 minutes at 37°C 5% CO_2 before addition of pre-warmed mTeSR™ Plus per well. The plate was then tapped on the side by hand for up to 40 seconds to encourage detachment as per manufacturer's instructions. ReLeSR™ is designed to selectively cause detachment of only undifferentiated hiPSCs without manual selection and in an enzyme-free proprietary mechanism – similar to the use of EDTA-containing solutions. However, in certain cases with the ps-hiPSCs manual selection was necessary to purify specific passages and was done through marker pen application to the base of respective wells to highlight appropriate colonies under light microscopy, which were then manually aspirated with a 100 μL micropipette under sterile conditions in a laminar flow hood. hiPSC colonies were then collected and carefully agitated within a 10 mL pipette to facilitate colony disaggregation to the optimal size, prior to transferral onto new Matrigel-coated wells. For passages immediately after resuscitation from freezing, the split ratio was 1:2, but for other passages was typically 1:3. Colonies were seeded on new wells in a drop-wise fashion followed by several rapid side-to-side movements to distribute colonies equally across the wells. No lines were used past 30 passages.

Matrigel coating of wells: Corning® Matrigel® was defrosted overnight at 4°C on ice, and aliquoted on ice rapidly. Corning® Matrigel® was stored at -20°C. However, Corning® Matrigel® aliquots were diluted in 4°C mTeSR™ Plus or RPMI 1640 (Thermo Fisher) and then stored at 4°C for no longer than 2 weeks. For coating of 6-well dishes for culture of undifferentiated hiPSCs, Corning® Matrigel® was diluted 1:60 and 1 ml was used to coat each well. For differentiation of hiPSC-cardiomyocytes, Corning® Matrigel® was diluted 1:30 and 0.5 ml was used to coat each well of a 4-well plate. Plates were primed for use by Corning® Matrigel® solidification at 37°C for at least 1 hour prior to use, at which point media was carefully aspirated.

iii. hiPSC cryopreservation and resuscitation

All hiPSC stock expansion, cryopreservation, resuscitation, and management performed by Alexander Grassam-Rowe apart from the work presented in Ahmad, Jin, Grassam-Rowe et al [1], where Dr Faizzan Ahmad, and Dr Yongcheng Jin previously maintained the stock, and apart from the prior work of Ms. Ni Li to initially provide the cryopreserved ps-hiPSCs.

As described in part in Ahmad, Jin, Grassam-Rowe et al[1], undifferentiated hiPSCs were stored using cryopreservation. hiPSC cultures ready for passaging (c.70% confluency) in 6-well plates were washed once with room temperature DPBS and then treated with ReLeSR™ for 40 seconds, before ReLeSR™ was aspirated and plates were incubated at 37°C for 5 minutes. Wells then had 1 ml of cryo-medium added and the plates were tapped by hand on the side for up to 40 seconds to promote cell detachment. Cryo-medium comprised by volume: 50% mTeSR™ Plus, 40% KnockOut™ Serum Replacement (Gibco®), and 10% DMSO. Colonies were then gently agitated in a 10 ml pipette and transferred into cryovials at 1:1 well:cryovial. Cryovials were then placed in a Mr Frosty™ (Nalgene®), and stored overnight at -80°C. Mr Frosty™ (Nalgene®) provides an internal cooling rate of c. -1°C/minute, which minimises cell lose during cryopreservation. Once frozen, cryovials were then transferred to liquid nitrogen in a cell-line specific container (without primary tissue). The hiPSC stock expansion and management was performed as needed to maintain sufficient low-passage number undifferentiated hiPSC stocks.

hiPSC-containing cryovials were removed from liquid nitrogen and transported on dry ice to a 37°C water bath. Cryovials were gently agitated in the bath until only a small amount of ice remained. In sterile conditions cells were then transferred to a 15 ml Falcon tube and 6 ml pre-warmed mTeSR™ Plus or RPMI 1640 was added in a drop-wise fashion to minimise osmotic shock. Tubes were then centrifuged at 800 rpm for 3 minutes and the supernatant was aspirated and cells were resuspended in pre-warmed mTeSR™ Plus with 10 μM Y-27632 (STEMCELL Technologies or Tocris or Cambridge Biosciences). Y-27632 is an anti-apoptotic small molecule commonly used to minimise iPSC cell death. Cells were then plated in a drop-wise fashion 1:2 cryovial:well on Matrigel-coated 6-well plates. Colonies were maintained with mTeSR™ Plus and 10 μM Y-27632 for up to 3 days before normal feeding with only mTeSR™ Plus.

iv. hiPSC atrial-specific cardiomyocyte differentiation

All hiPSC differentiation was performed by Alexander Grassam-Rowe who also designed the new control group differentiations, apart from the work presented in Ahmad, Jin, Grassam-Rowe et al [1], where Dr Faizzan Ahmad, and Dr Yongcheng Jin previously differentiated hiPSCs to CMs.

As described in part in Ahmad, Jin, Grassam-Rowe et al[1], undifferentiated hiPSCs at c. 70% confluency were dissociated into single cells using 1 ml Accutase™ (STEMCELL Technologies) per well. Plates were incubated for 5 minutes at 37°C with Accutase™, before addition of 3 ml of pre-warmed mTeSR™ Plus medium containing 10 μM Y-27632 to quench the Accutase™ reaction. Cells were then gently agitated in a 10 ml pipette to encourage complete dissociation before being seeded in a drop-wise fashion into 4-well plates (Nunc™) with side-side and forward-backward movements to encourage equal distribution of hiPSCs. mTeSR™ Plus medium containing 10 μM Y-27632 was used for up to 3 days after seeding.

As described in part in Ahmad, Jin, Grassam-Rowe et al[1], once hiPSCs in 4-well plates reached c. 70%±10 confluency, pre-warmed Cardiac Differentiation Medium A (CDMA) (PSC Cardiac Differentiation kit - Gibco Life Technologies) was added to wells and this initiated Day 0 (D0) of the differentiation protocol. On day 2, approximately 48 hours later, CMDA was replaced by pre-warmed Cardiac Differentiation Medium B (CDMB) with 10 μM Y-27632. Then on day 4, approximately 48 hours later, pre-warmed Cardiomyocyte Maintenance Medium (CMM) was

used to replace media and this media was then changed every two days unless indicated otherwise. The control group used for Ahmad, Jin, Grassam-Rowe et al [1] was then the continual use of CMM as per the manufacturer's instructions. However, the experimental group was subjected to a regime of day 4 CMM containing 1 μg/mL GREMLIN-2 (R&D Systems) followed by day 6 and day 8 containing no GREMLIN-2 but instead containing 1 μM retinoic acid. Additionally, our RA^6 control group presented in this thesis was without GREMLIN-2 treatment, but included the day 6-10 treatment with retinoic acid (Figure 1-4). All groups were grown out from day 10 with CMM feeding every 2 days until day 20.

v. hiPSC-derived cardiomyocyte immunostaining

hiPSC-derived cardiomyocyte immunostaining was performed by Alexander Grassam-Rowe, apart from the work presented in Ahmad, Jin, Grassam-Rowe et al [1] – which was performed by collaborators and the methods are not presented here.

hiPSC-CM colonies were dissociated with Accutase™ for 8-10 minutes as above. Cells were then replated on Ibidi© polymer chambered coverslips with pre-warmed CMM and 5 μM Y-27368. After two days, these cells were washed with room temperature DPBS. All subsequent steps took place on a rocker. Cells were then fixed with chilled 4% paraformaldehyde for 20 minutes. Cells were then washed 3 times, 5 minutes each, with room temperature DPBS. Cells were then permeabilised with 0.1% Triton X-100 (in DPBS) for 20 minutes. Cells were then washed 3 times, 5 minutes each, with room temperature DPBS. Cells were then blocked with 0.1% Tween-20 (in DPBS) containing 10% normal donkey serum for 60 minutes. Cells were then washed 3 times, 5 minutes each, with room temperature DPBS. Cells were then transferred to a 4°C rocker, and incubated overnight with mouse anti-TNNT2 (1X: Life Technologies A25969) in 0.1% Tween-20 with 1% normal donkey serum. Cells were then washed 3 times, 5 minutes each, with room temperature DPBS. Subsequent steps were performed in the dark at room temperature. Cells were then incubated for 2 hours with Alexa Fluor® 488 donkey anti-mouse (1X: Life Technologies A25972) in 0.1% Tween-20 (in DPBS) and 1% normal donkey serum. Cells were then washed 3 times, 5 minutes each, with room temperature DPBS. Finally, the solution covering the cells was aspirated, and cells were covered with Prolong Gold Anti-Fade Mounting Medium containing DAPI (Life Technologies). Cells were sealed within their Ibidi chambers and the chamber was covered with Parafilm. The parafilm-wrapped chamber was then surrounded by moistening tissue paper and wrapped in tin foil. This was then kept at 4°C in the dark until imaging within 4 days. A Zeiss confocal LSM780 microscope was used for image collection using either air-immersion 10 or 20X objectives or a water-immersion 63X objective. Image analysis was done using Fiji ImageJ.

vi. hiPSC-derived cardiomyocyte single-cell RNA sequencing

Single-cell RNA sequencing data collection was performed by Dr Yongcheng Jin and an external contractor Single Cell Discoveries B.V.

As described in part in Ahmad, Jin, Grassam-Rowe et al[1], at day 20 hiPSC-derived cardiomyocytes (hiPSC-CMs) were washed with DPBS and then incubated with pre-warmed 100 U/mL Collagenase I (Gibco) dissolved in RPMI 1640 for 40 minutes at 37°C. Cells were then gently agitated using a 1 mL micropipette before a further 10 minutes at 37°C. Cells were collected and transferred into a 1.5 mL centrifuge tube with 1 mL of pre-warmed CMM. Cells

were spun at 300 rcf for 3 minutes before aspiration of the supernatant and resuspending the cell pellet in 0.3 mL Accutase followed by incubation at 37°C for a final 10 minutes. Afterwards, chilled DPBS was added and the suspension passed through a 70 μm cell strainer. The single cell suspension was then once again spun at 300 rcf for 3 minutes to remove debris. The final pellet was resuspended in chilled 90% methanol in DPBS, and stored on ice prior to storage at -80°C after 15 minutes. Fixed cells were then spun at 3000 rcf for 10 minutes at 4°C, with the supernatant aspirated and the cell pellet resuspended in chilled rehydration buffer. The suspension was gently agitated 10 times in a micropipette before further centrifugation and resuspension to achieve a final concentration of 700 – 1200 thousand cells per millilitre. Rehydrated cells were then sorted using either FACS Aria II or FACSJazz (BD biosciences). Forward/side scatter and DAPI exclusion were used to sort single cells into single wells of 384-well plates (BioRad). 5 μL Vapour-lock (QIAGEN) was added to each well, with 100-200 nL of reverse transcriptase (RT) primers, dNTPS, and synthetic mRNA (ERCC) Spike-ins, with subsequent freezing to -80°C. hiPSC-CMs were sequenced as follows. Cardiomyocytes were lysed by incubation at 65°C for 5 minutes, with RT and second strand mixes dispersed using a Nanodrop II liquid handling platform (GC Biotech). CEL-Seq2 was then used for library preparation, with primers comprising 4 bp random molecular barcodes, 24 bp polyT strands, T7 promoters, a well-specific 8 bp barcode, and a 5' Illumina TruSeq RNA kit adaptor. Following in vitro transcription, Illumina NextSeq was used for 75 bp sequencing of reads and reads were then aligned to a reference genome.

vii. hiPSC-derived cardiomyocyte single-cell RNA analysis

Single-cell RNA sequencing data pre-processing and preliminary analysis was performed by Dr Yongcheng Jin. Downstream analysis such as gene ontology analysis, and heatmap-based comparison and visualisation were designed, and performed by Alexander Grassam-Rowe.

As described in Ahmad, Jin, Grassam-Rowe et al[1], single-cell expression data was analysed in R. Initial quality control excluded any cells with fewer than 12000 unique reads, and any genes expressed in fewer than 5 cells. Differential gene expression analysis was performed by RaceID[375], with visualisation using ggplot2[376]. Heatmaps and gene ontology analysis were performed using ComplexHeatmap[377] and ClusterProfiler[378] respectively.

viii. Dataset acquisition and processing for calcium handling

Single-cell RNA sequencing analysis for calcium handling was performed by Alexander Grassam-Rowe using the single-cell RNA sequencing dataset collected by Dr Jin and in collaboration with Dr Marina Riabiz who performed mathematical analysis on previously collected calcium transient data. Prof. Pawel Swietach & Prof. Steven Niederer contributed to study conception, discussion, and interpretation.

I used the single-cell RNA expression dataset and for both the experimental GREMLIN2/Retinoic acid group and the control CMM group normalised them using SCTransform[360]. We then selected all genes apart from those that we had assigned as matching to Hinch model[67] parameters as in Table 1. Following this, we examined expression levels, Pearson's correlations, and correlations of combinations of these parameter groupings as described in results.

ix. Lactate purification of hiPSC-derived cardiomyocytes

Purification media, adapted from other groups,[322,379-381] was made as Dulbecco's Modified Eagle Medium without glucose and without pyruvate (Gibco #11966025) was used with sodium lactate added to a final concentration of 5 mM lactate, with pH balanced with HEPES to pH 7.4 and sterile filtered using a .22 μm sterile filter and stored at 4°C for no more than 2 weeks. At day 20, where specified, instead of normal CMM feeds, purification media was pre-warmed and used for feeds on day 20 and day 22. On day 24, cells were then dissociated as above, and hiPSC-CMs seeded onto fresh 4-well Matrigel-coated plates with pre-warmed CMM and 5 μM Y-27632, with the day 26 and subsequent feeds returning to simply pre-warmed CMM.

x. Dissociation of hiPSC-derived cardiomyocytes

Dissociation of hiPSC-derived cardiomyocytes was performed by Alexander Grassam-Rowe apart from the work presented in Ahmad, Jin, Grassam-Rowe et al[1], where Dr Faizzan Ahmad, and Dr Yongcheng Jin previously dissociated cells.

Cells were washed with room temperature DPBS and dissociated using Collagenase Type 1 (Cambridge Bioscience) dissolved in pre-warmed RPMI 1640 at 2 mg/ml with incubation for 35-40 minutes at 37°C 5% CO_2. Collagenase Type 1 in RPMI 1640 was first made at 10 X concentration, sterile filtered through a .22 μm filter and aliquoted and stored at -20°C and defrosted at 4°C for several hours. After 35-40 minutes, once cells had detached from the culture surface, room temperature DPBS was added and cells were gently agitated with a 1000 μL micropipette to disperse structures before transferral into a 15 ml Falcon tube and centrifugation at 1000 rpm for 3 minutes. The supernatant was discarded and the pellet resuspended in 500 μL of room temperature Accutase™ with gentle agitation of cells for 2 minutes to further disperse single cells. 2 ml of room temperature DPBS is then added and the cells are spun again at 1000 rpm for 3 minutes. With the supernatant discarded, the pellet is once again resuspended, but now in pre-warmed CMM with 5 μM Y-27632 until the next feed in 2 days time.

xi. Laminar flow hood and incubator management

All laminar flow hood and incubator management was performed by Alexander Grassam-Rowe apart from the work presented in Ahmad, Jin, Grassam-Rowe et al[1], where Dr Ahmad, and Dr Jin managed these. 80-100% EtOL was used for cleaning and aseptic technique was used where possible. No antibiotics were present in media at any stage. Only a single contaminated well was observed across the entire project.

c. Electrophysiology studies of hiPSC-derived cardiomyocytes

i. Establishing imaging set-up

The imaging set-up utilised an electrically heated metal pad, which was covered in black paper to reduce glare, and an in-line perfusion heater, which were optimised to produce a stable 37±0.5 temperature in wells even with changing perfusion. An electrically controlled flow actuator was used to control flow from gravity-fed perfusion between different solutions. An LED emitting blue 420 nm light was used to stimulate optical dyes. Transmitted light was recorded by a 128 x 128 EMCCD camera (Photometrics, USA) and c. 10s recordings at 125 Hz were recorded using MetaMorph software (Molecular Devices, UK). Cells were stimulated with two custom-designed

carbon electrodes controlled via a digitizer (1401 CED, UK) controlled by Spike2 custom-written script, adapted from original code by Dr Yuanlong Song.

ii. Pipette preparation and solutions

'Sharp' 35-50 MΩ glass micropipette electrodes were prepared using a horizontal micropipette puller (Sutter P-97, Sutter, UK) with a box filament. I calibrated the most stable setting for reliably producing such high resistance as pull=35, heat=559, velocity=120, time =250 when using borosilicate glass capillaries with outer diameter 1.5 mm and inner diameter 1.17 mm (GC150-TF-7.5 Clark Electromedical Instruments, UK). ~3-5 MΩ glass micropipette electrodes were prepared using a vertical micropipette puller (Narashige PP-830, Narashige, Japan) with borosilicate glass capillaries of outer diameter 1.5 mm and internal diameter 0.84 mm (1B150-3, World Precision Instruments).

Internal solution was prepared with the following final concentrations: K-Aspartate 110 mM, KCl 10 mM, NaCl 5 mM, $MgCl_2$ 5.2 mM, HEPES 5 mM, K_2ATP 5 mM, and P_iCr 5 mM. pH was adjusted to 7.2 with KOH and osmolarity was measured at c. 225 mOsm. This internal solution was then aliquoted and stored at -20°C.

External solution was the same as used for all other hiPSC-CM electrophysiology in this thesis, and was made fresh every day for experimentation at the following concentrations: NaCl 140 mM, KCl 5.4 mM, $CaCl_2$ 1.8 mM, $MgCl_2$ 1.0 mM, Glucose 10 mM, HEPES 20 mM, and pH 7.4 with NaOH.

iii. Patch clamp data acquisition

For both 35 – 50 MΩ and 3-5 MΩ pipettes whole-cell ruptured patch current clamp was attempted. All recordings were made used an Axon 200B Amplifier (Molecular Devices, USA) and were grounded through an Ag-AgCl reference electrode inserted in the external solution of the bath. Experiments were conducted at 37°C, with constant perfusion of heated external solution into the bath.

iv. FluoVolt optical analysis data acquisition

Cells were incubated in external solution containing 1X FluoVolt and 1X PowerLoad Concentrate as per the manufacturer's instructions. Cells were then incubated at 37°C 5% CO_2 in the dark for 35 minutes prior to being washed twice with external solution and perfused for downstream experiments in a dark room.

v. Image stack conversion and region of interest selection

Building on the previous work of COSMAS[382], using Python (v3.6), we use the COSMAS framework to build upon and add new features. I used the COSMAS[382] framework to load in .tif video stacks using the tifffile module and then use the binning option to bin pixels into 8x8 bins to improve signal fidelity. I then continued to use the COSMAS framework to automatically

detect the top 97th percentile of signal intensity and extract the signal from these pixels. Preliminary testing identified that any number below this led to the inclusion of excessive low-quality traces.

vi. Trace filtering

The program then extracts each pixel's trace across the ~10 seconds and applies a 3rd order Savitzky-Golay filter with a window length of 11 to the entire trace to produce a filtered first derivative and second derivative of the entire trace. The workflow then uses the filtered trace to identify peaks using a fixed-duration (e.g. 1000 ms for 1 Hz pacing) 'comb' global maxima search as detailed in the original COSMAS work[382], with inverting of voltage signal where necessary. Again, as detailed in COSMAS[382], it then segments the trace into bins such that each bin encapsulates a single action potential through to just before the beginning of the next. However, each bin does not explicitly start at the beginning of the action potential in question. My addition now improves on this to use the first derivative signal to identify the local maximum within the given bin. The local maximum first derivative corresponds to the maximum upstroke rate, which is typically around the midpoint of the action potential upstroke. The bin trace between the beginning of the bin and this first derivative peak is then used to find the second derivative local maximum in an area constrained to be the beginning of the upstroke of the action potential – as it comes before the maximum upstroke rate. This second derivative local maximum is taken to represent the beginning of the action potential upstroke. The use of these first and second derivative measures as correlates for the described action potential behaviour is common in the action potential literature and other analysis options[383] (OptiQ, Cairn Research), and now implemented here. The program then retrieves the raw trace for this bin, without any Savitzky-Golay filtering, and segments it into 3 segments: 1. The values leading up to the previously identified start of the action potential upstroke; 2. The upstroke; 3. The values from the peak leading through to the end of the bin. The program then implements a split repolarisation and pre-depolarisation filter inspired by similar optionality in OptiQ (Cairn Research). I utilised the scipy signal module to implement a digital Butterworth 5 Hz low-pass 2nd order filter of the repolarisation (3) part of the signal and used signal.filtfilt() to apply the filter forwards and backwards to maintain the temporal fidelity of the filtered signal to give a final 4th order filtered output. Then the program applies a similar digital Butterworth 1 Hz low-pass 2nd order filter of the pre-depolarisation portion of the signal (1), and similarly used signal.filtfilt() to maintain the temporal fidelity of the filtered output. The upstroke element of the trace (2) is not used and the original Savitzky-Golay filtered upstroke is used through combining the newly filtered portions of the trace into replace their respective portions of the original Savitzky-Golay filtered trace.

vii. Parameter measurement

I used the standard COSMAS framework to measure action potential parameters APD20, APD30, APD50, APD70, and APD90 with linear interpolation between frames of traces to produce output traces and values in milliseconds. To identify the baseline of the action potentials, we use the average of up to the first 5 frames prior to the beginning of the upstroke. I also use the distance between the upstroke beginning and the depolarisation peak to determine the 'time-to-peak'.

viii. Quality control and data exclusion

I added additional output to the standard output of COSMAS[382], such that I now store each action potential indexed relative to the pixel it came from and the bin it came from within that

trace. This enables me to have greater control over the statistical output and data quality for downstream calculations. I automatically exclude any action potential with a time-to-peak greater than 120 ms, or for calcium transients with a time-to-peak greater than 300 ms. Any trace with these values greater than this typically represents noise and not a faithful trace. I then use an excel sheet, with indexing to the relative files for each trace, and can manually select which files, pixels, or bins to exclude from further analysis if of poor quality or arrhythmic etc. This excel sheet can then be loaded into the Python script to automatically approve, exclude, or invert data as necessary.

ix. Computational action potential data generation

I used LongQT[384] to generate data for error measurement and quantification. I used the 3 human atrial models included: Courtemanche 1998[385], Grandi 2011[386], and Onal 2017[387]. For each model we performed 100 trials where we simulated 1 Hz pacing for 100 seconds, and recorded the final 10 seconds in current clamp mode. Pacing was achieved with a simulated -12.50 μA/μF depolarising pulse of 4.00 ms duration. I then loaded in each model and treated each trial as if it were a separate pixel. To simulate the addition of white Gaussian noise, I identified the average peak height of traces at baseline, and then generated Gaussian distributions with means around the respective values corresponding to 1%, 2%, 2.5%, 5%, 10%, 15%, and 20% of peak height values. Then, for each level of noise, I added that level of noise to each pixel's trace. Thus, a given pixel would have a trace generated for each level of noise, in an independent and non-additive fashion.

x. Data visualisation and statistical analysis

I used matplotlib for visualisation in Python unless explicitly stated otherwise. Statistical tests were performed in Python using either the pingouin module, or statsmodels module. All statistical tests are 'two-way' unless stated otherwise. All variables were entered into ANOVAs with the appropriate data category e.g. integers for integers. Adjustments for multiple hypothesis testing, where appropriate, were made using the Benjamini-Hochberg method for controlling the false discovery rate. The following demonstrates the relationship between graphical displays of p-values, and the values they represent: $p <= 0.05$: *, $p <= 0.005$: **, $p <= 0.0005$: ***, and $p <= 0.00005$: ****.

xi. Drug preparation and perfusion

All reagents and drugs were stored as per manufacturer's instructions. Drugs were dissolved in aqueous buffers where possible, unless explicitly stated as DMSO. Drug solutions were made fresh on the day of experimentation unless stated otherwise.

xii. Fluo4-AM optical analysis data acquisition

Fluo-4-AM (Life Technologies, UK) was stored at -20°C in the dark as per manufacturer's instructions. Aliquots of 5 mM in DMSO with Pluronic F-127 Acid (Life Technologies, UK) were made in the dark and stored. Cells were washed once with external solution, and then incubated for 20 minutes at 37°C 5% CO_2 in the dark in external solution containing final concentrations of 10 μM Fluo-4-AM and 0.01% Pluronic F-127 acid to aid with loading of dye. Cells were then washed with pre-warmed external solution and used for downstream experiments. Dye-containing media were made fresh on the day of use.

xiii. Micro-pipette culture dish production

Mr Matthew Read manufactured the pipette-based constructs in sawing and sanding. However, I then sterilised, assembled, coated, and seeded the following constructs. Dr Andreas Koschinski advised on the use of these.

As per prior work[388] standard 2 ml serological pipettes were sawn into small (~1 cm) pieces, and edges were sanded to a fine finish. Then under sterile conditions I placed all pieces into 100% ethanol in a 50 mL Falcon tube which was then agitated, and then carefully extracted them, allowed them to dry with at least an hour of UV exposure, before they were then returned to 100% ethanol and then allowed to dry a final time. Then pieces were balanced on the centre of a 30 mm specialised culture dish with high optical clarity (Ibidi), and 50 μL of 1:30 Matrigel was carefully pipetted into the piece to coat the culture surface. Matrigel was then allowed to solidify at 37°C for at least 1 hour prior to be aspirated just before use and cell seeding.

xiv. FRET transfection and imaging

All FRET work and LAMP2 immunostaining was performed by Ms Emily Akerman using hiPSC-AMs that I cultured, differentiated, dissociated, and seeded in 30 mm Ibidi dishes and the following two paragraphs are her methods.

"FRET: FRET imaging experiments were performed 24 h after infection of the NRAMs with adenovirus carrying EPAC-SH187 cytosolic biosensor, at a multiplicity of infection (MOI) of 1000 virus particles per cell (vp/cell). During experiments, cells were maintained at RT in a modified Ringer solution (in mM:). Dynamic measurements were done using an inverted microscope attached to a cool SNAP HQ2 camera and an optical beam splitter (Photometrics) for simultaneous recording of YFP and CFP emissions. FRET changes were measured as changes in the background-subtracted 480 nm/545 nm fluorescence emission intensity on excitation at 430 nm. For recording, cells were left to settle for 4 min and Ned-19 (1 uM) or control (1 μL of DMSO) were then added. 1 nM of IS0 was then added after 6 mins f drug and left for 5 mins. After the 5 mins, 10 μM of forskolin that activates ACs and increases intracellular levels of cAMP and 100 μM of IBMX (3-isobutyl-1-methylxanthine) a competitive non-selective phosphodiesterase inhibitor which raises intracellular cAMP, activates PKA was added for maximum response.

Immunostaining: cells were fixed with 2% paraformaldehyde for 12 minutes. The cells were washed 3 times with PBS. Cells were then blocked with 10% Donkey serum, 0.3% BSA and 0.1% triton X100 in PBS for 1 hour. Following the removal of the blocking buffer, cells were incubated overnight in 4°C with primary antibody (1:100, LAMP2 (PA1-655)). Cells were then washed 3 times with PBS and incubated in the dark at room temperature with the secondary antibodies (1:400) goat anti-rabbit IgG conjugated to Alexa Fluor 488 (Molecular probes, Eugene, Ore). Cells were washed 3 times in PBS and coverslips were mounted on slides with vectashield with DAPI to stain the nuclei. The dishes were viewed using a Leica DMIRB inverted microscope modified for confocal laser-scanning microscopy (x63 oil objective) and Leica TCSNT software or using Zeiss LSM 510 (x40 oil objective). For detection of AlexaFluor 488, fluorescence excitation was at 488 nm with emission collected >515 nm."

Ethical statement
As described in Sun, Grassam-Rowe et al: animal experiments on mice were performed in line with the United Kingdom Animals (Scientific Procedures) Act 1986 as approved by the

University of Oxford Department of Pharmacology ethical committee (PPL: PP8557407) or when performed by colleagues in Southwest Medical University Sichuan (China) under the Animal Care and Use Committee (#20160930) in line with the institute's national guidelines. All mice used, both wild-type and mutant, were maintained in pathogen-free facilities with ad libitum food and water access at the University of Oxford or Southwest Medical University. As described in part in Ahmad, Jin, Grassam-Rowe et al.: hiPSC lines used were either purchased from Gibco® Life Technology, Carslbad USA, or kindly provided by Prof. David Paterson's group, with original creation from the University of Nottingham Biodiscovery institute. No patient identifying information was provided. Patient fibroblast isolation and use was approved by the Nottingham Research Ethics Committee (License 09/H0408/74), and sample collections are registered with the UK Clinical Research Network under project 8164; "Modelling Long QT Syndrome".

Chapter 3. RNA sequencing reveals catecholaminergic cardiomyocytes within the atrioventricular junctions of mice.

a. Introduction

This section in introduced in Chapter 1A & B.

Recent discoveries have implicated cardiomyocytes as expressing some of the biosynthetic enzymes to produce autonomic signalling molecules that are normally associated with neuronal expression – both catecholamines and cholinergic[3,334-336,338]. If cardiomyocytes were capable of producing functionally important amounts of these signalling molecules, it would represent a new axis in our understanding of cardiac regulation and the neurocardiac axis that could potentially open new avenues to explain both physiology and pathophysiology. This Chapter builds primarily upon our earlier work in the Lei Group, alongside that of our collaborators who identified other non-neuronal sources of catecholamines in the heart[179,180,338,339,389].

b. Methods

The methods used to produce this data are described in Chapter 2A:

c. Results

i. Establishing a single-cell RNA sequencing transcriptomic landscape of the developing mouse heart.

This chapter is in part adapted from Sun, Grassam-Rowe et al[2].

I used scRNA-seq to establish a transcriptomic library of the mouse heart from embryonic (E8.5, E10.5, E12.5, E14.5, E16.5) stages through to postnatum (P3). After preliminary data processing and quality control, the data had mean UMI and gene counts of 6417 and 1482 across 175237 cells respectively in our scRNA-seq library from an original ~400k cells before quality control.

My scRNA-seq analysis recapitulated the known major populations of cells in the developing murine heart. I identified 4 major populations: E8.5 and E10.5 early embryonic tissue (endoderm *Afp*^{hi}, mesodermal *Prxx1*^{hi}, or neural *Sox2*^{hi}), various non-cardiomyocyte populations such as epicardial and endocardial cells and fibroblasts (e.g. *Col1a1*^{hi}, *Fbln2*^{hi}, *Emcn*^{hi}, *Up3kb*^{hi}, *Lmod1*^{hi}), ventricular (*Myl2*^{hi}, *Myl7*^{lo}, *Myh7*^{hi}, *Kcne1*^{hi}), and atrial (*Myl7*^{hi}, *Myh6*^{hi}, *Nppa*^{hi}, *Sln*^{hi}). These major populations were composed of 26 distinct cell types across the developing mouse heart (Figure 3-1, Figure 3-2, Figure 3-3, Figure 3-4). I observed the expected finding that a greater percentage of the earlier (E8.5 and E10.5) cells were in the more proliferative phases (S & G1-M) of the cell cycle. Whereas, the later stages, particular P3, were predominantly in the growth phases of the cell cycle. I also observed a number of cell types with interesting mixed transcriptomic signals, such as ECM Atrial Cardiomyocytes with a mixed atrial and fibroblastic transcriptomic signature. Whether these cells represent true biology, or perhaps a 'doublet' of the two underlying cells sequenced at once, remains to be investigated.

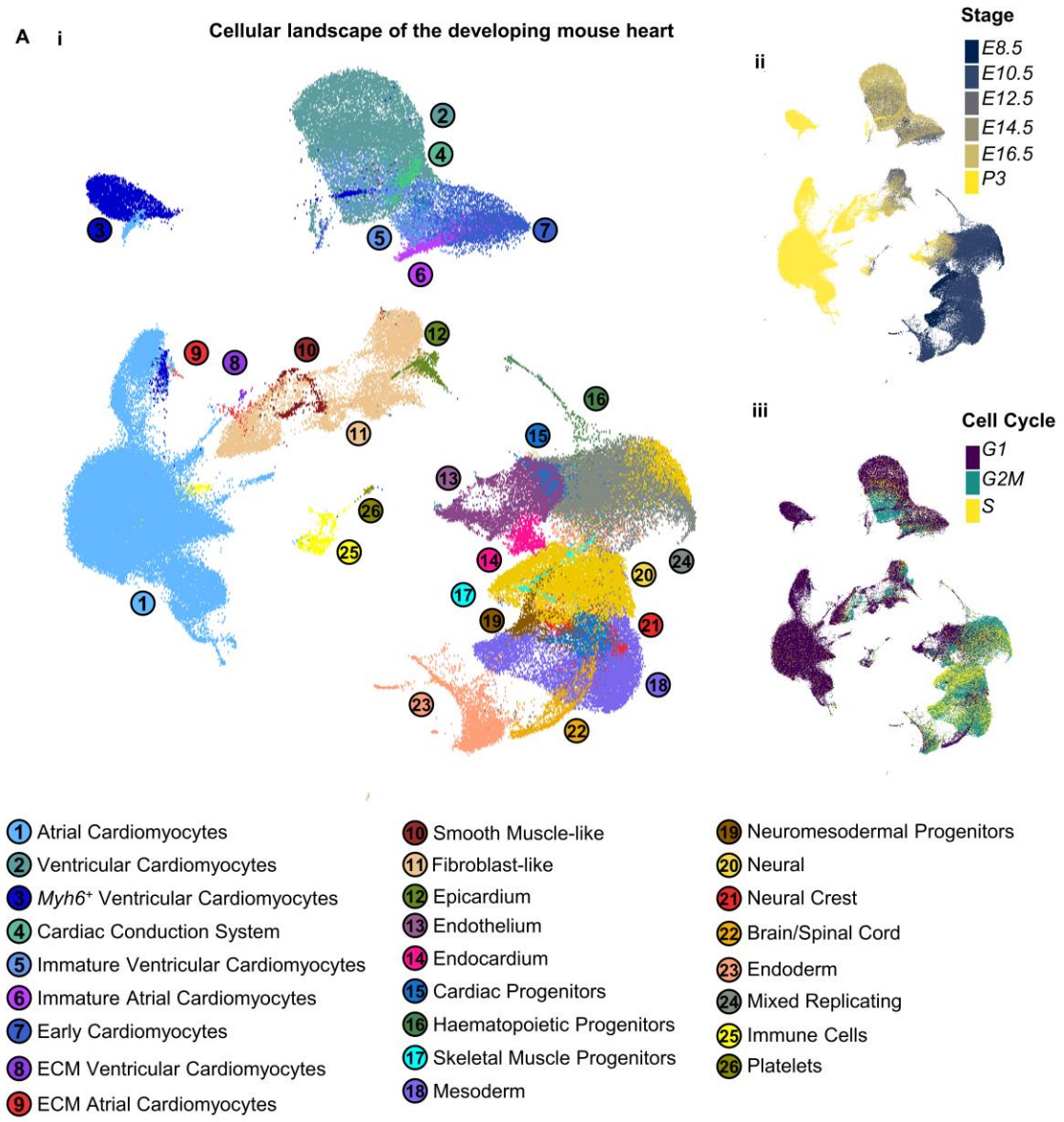

Figure 3-1. scRNA-Seq described 4 major populations of cells in our dataset, including the developing and postnatal mouse heart.

i) All initial cells post-quality control plotted in 2D UMAP. Cells are coloured as distinct cell type identified with unsupervised clustering. This dataset includes E8.5 and E10.5 whole embryos, and whole isolated hearts from E12.5, E14.5, E16.5, and P3 mice. Corresponding cell types are labelled below.

ii) All initial cells post-quality control plotted in 2D UMAP. Coloured by stage of tissue isolation.

iii) All initial cells post-quality control plotted in 2D UMAP. Coloured by predicted Cell Cycle stage identified using Seurat.

This figure is adapted from Sun, Grassam-Rowe et al[2].

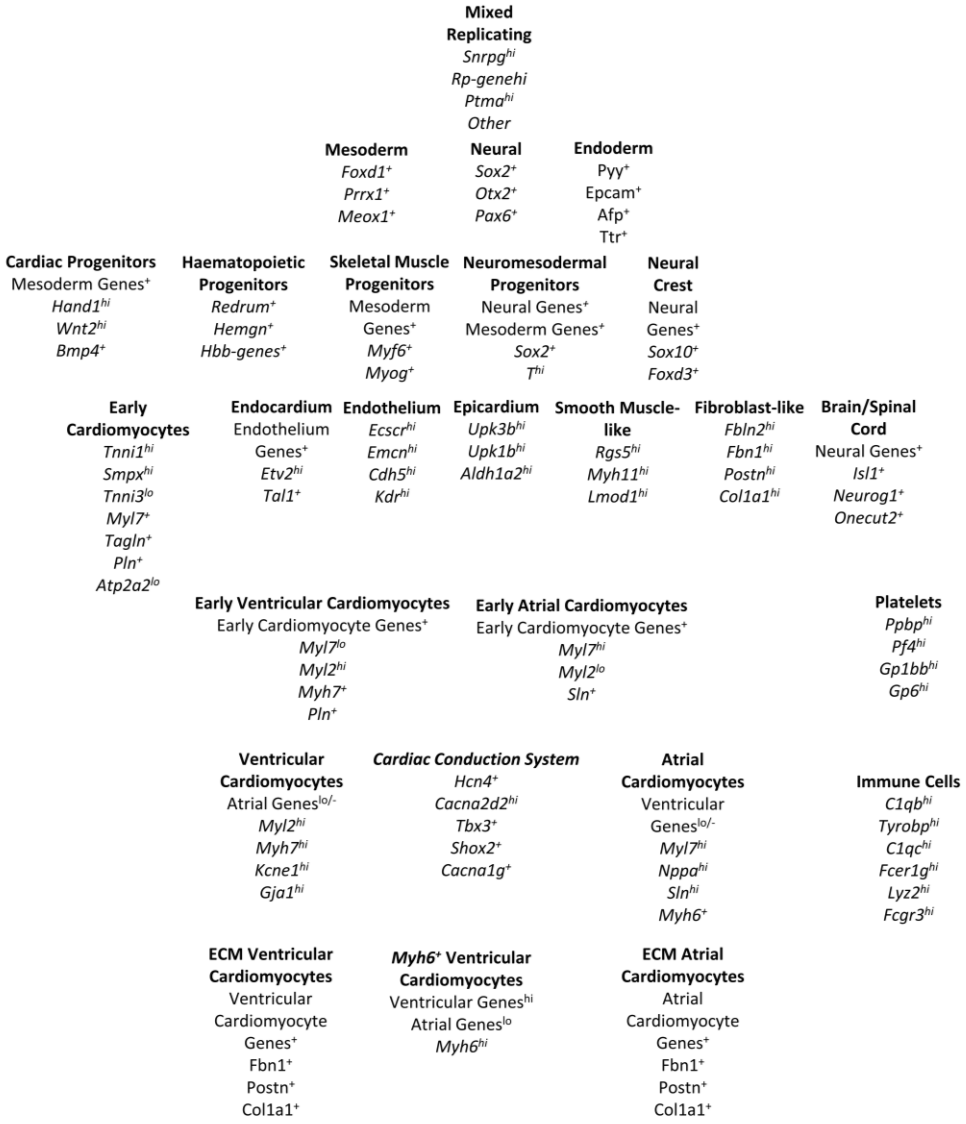

Figure 3-2. Key marker genes for cell types identified within our whole scRNA-Seq dataset.

Each cell type corresponding is identified in bold, with key marker genes underneath. Gene^{+} denotes a gene expressed above the level of other cell types. Gene^{hi} denotes a gene highly expressed above the level of other cell types. Gene^{lo} denotes a gene expressed below the level expected if it were of a particular other cell type – this is typically with regards to comparing against another cell type rather than against the whole dataset.

This figure is adapted from Sun, Grassam-Rowe et al[2].

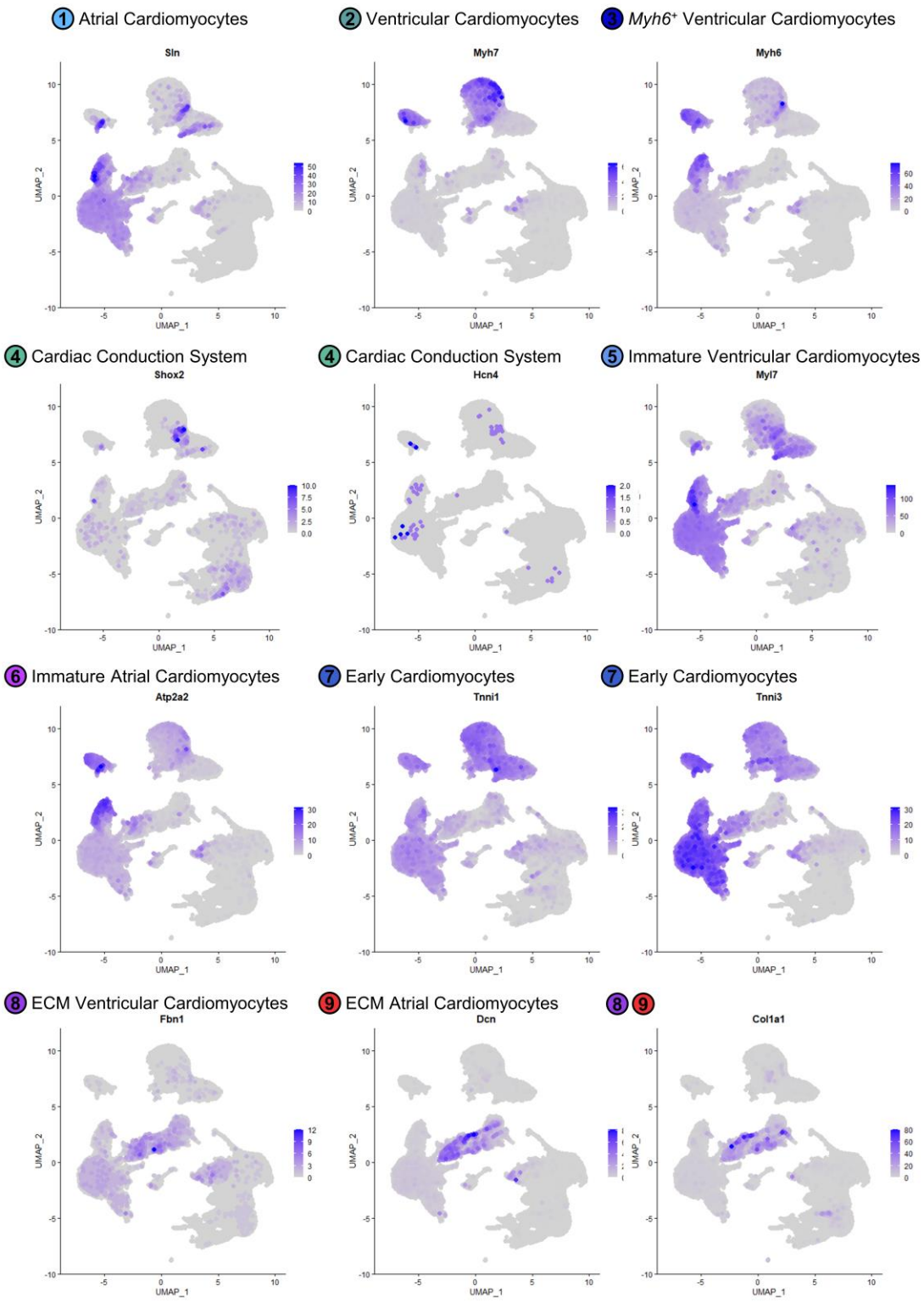
1 Atrial Cardiomyocytes
Sln
2 Ventricular Cardiomyocytes
Myh7
3 Myh6+ Ventricular Cardiomyocytes
Myh6
4 Cardiac Conduction System
Shox2
4 Cardiac Conduction System
Hcn4
5 Immature Ventricular Cardiomyocytes
Myl7
6 Immature Atrial Cardiomyocytes
Atp2a2
7 Early Cardiomyocytes
Tnni1
7 Early Cardiomyocytes
Tnni3
8 ECM Ventricular Cardiomyocytes
Fbn1
9 ECM Atrial Cardiomyocytes
Dcn
8 9
Col1a1
UMAP_1
UMAP_2

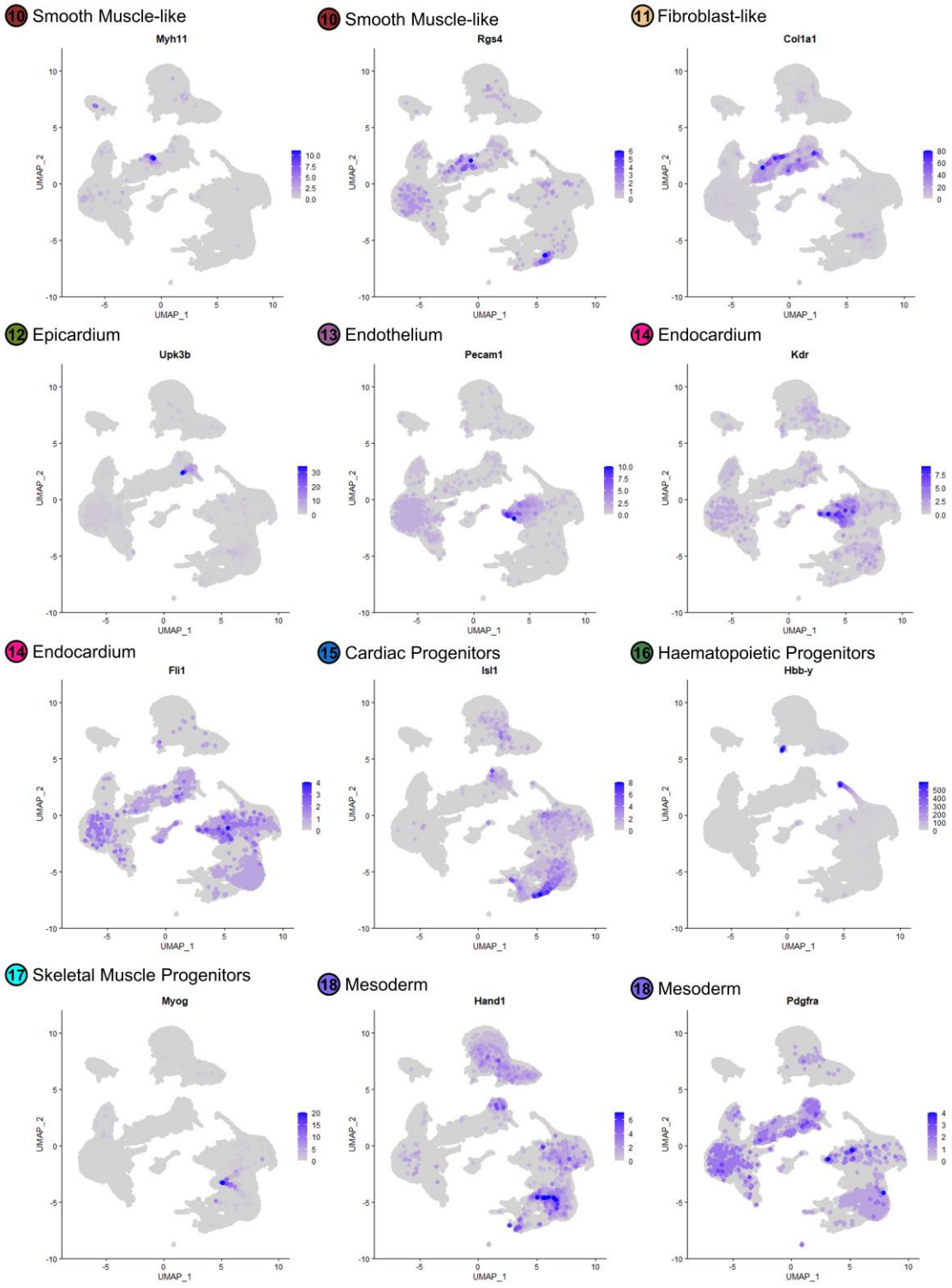
10 Smooth Muscle-like
Myh11
10 Smooth Muscle-like
Rgs4
11 Fibroblast-like
Col1a1
12 Epicardium
Upk3b
13 Endothelium
Pecam1
14 Endocardium
Kdr
14 Endocardium
Fli1
15 Cardiac Progenitors
Isl1
16 Haematopoietic Progenitors
Hbb-y
17 Skeletal Muscle Progenitors
Myog
18 Mesoderm
Hand1
18 Mesoderm
Pdgfra
UMAP_1
UMAP_2

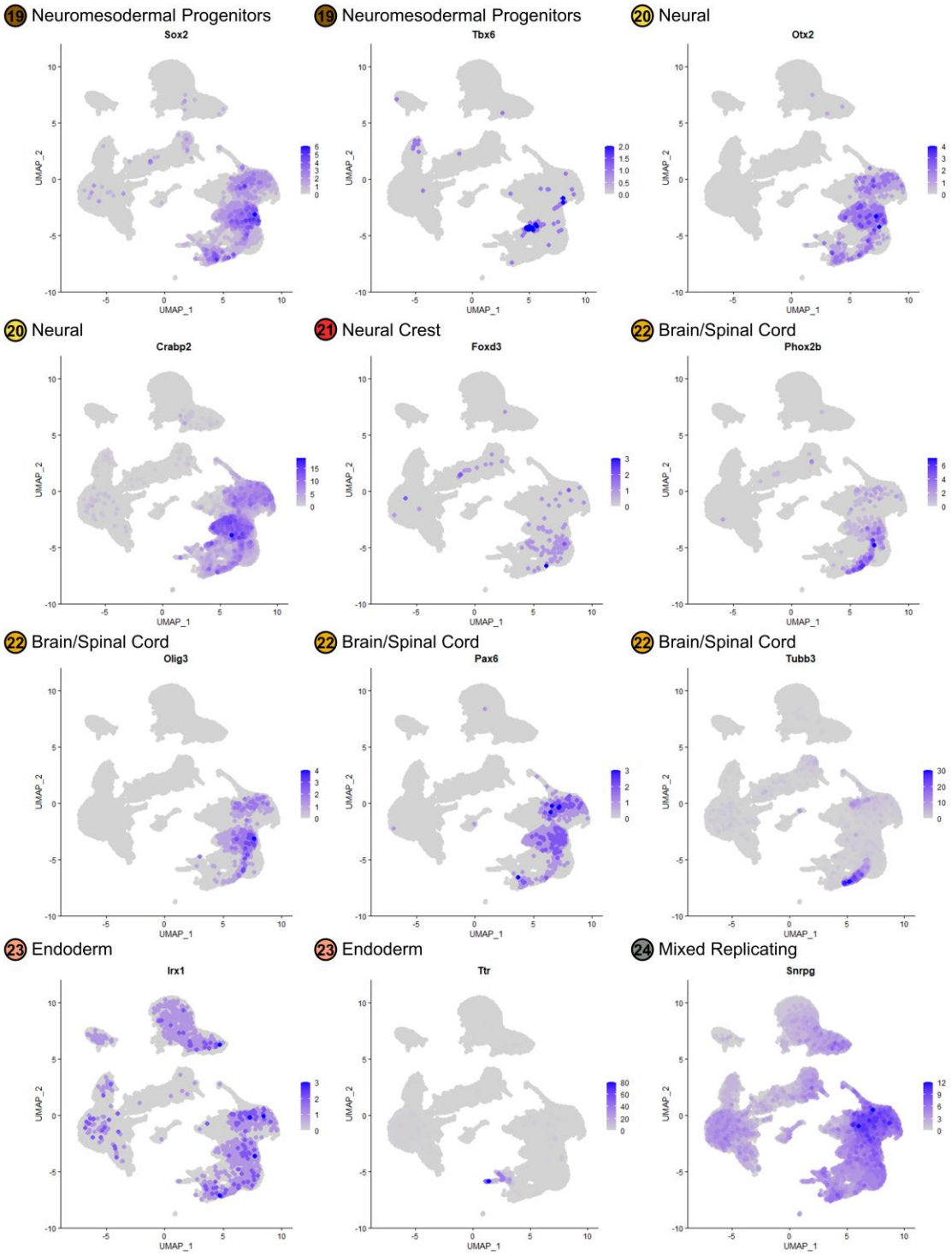
19 Neuromesodermal Progenitors
Sox2
19 Neuromesodermal Progenitors
Tbx6
20 Neural
Otx2
20 Neural
Crabp2
21 Neural Crest
Foxd3
22 Brain/Spinal Cord
Phox2b
22 Brain/Spinal Cord
Olig3
22 Brain/Spinal Cord
Pax6
22 Brain/Spinal Cord
Tubb3
23 Endoderm
Irx1
23 Endoderm
Ttr
24 Mixed Replicating
Snrpg
UMAP_1
UMAP_2

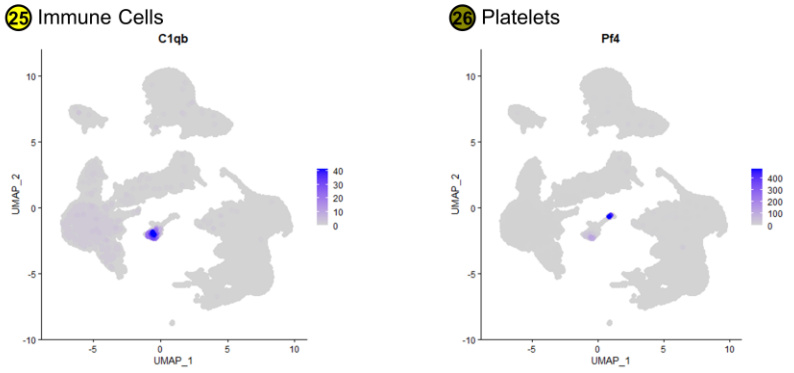

Figure 3-3. Expression of key marker genes across different cell types identified in whole scRNA-Seq dataset.

2D UMAP plots of the whole dataset with cells coloured by the expression of the specific gene identified at the top of the plot. Corresponding cell types for each plot are indicated above, with the same colours and numbers as Figure 3-1.

This figure is adapted from Sun, Grassam-Rowe et al[2].

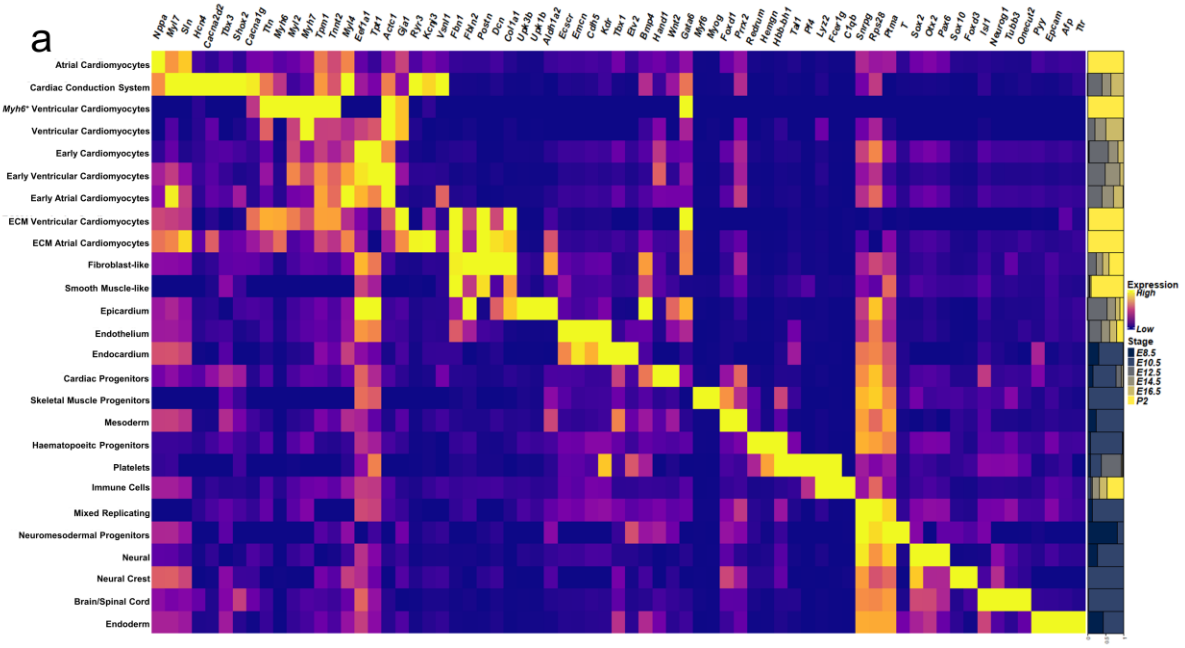

Figure 3-4. Cell types express the expected selective and specific marker genes of each group.

A heatmap describes the expression of specific genes on the y-axis, by cell types on the x-axis. The annotation on the right describes the relative proportions of each cluster in terms of developmental stage. Values for expression are normalised by row and then by column for visualization purposes. Yellow indicates a high level of relative expression, purple indicates a low level of expression.

This figure is adapted from Sun, Grassam-Rowe et al[2].

ii. Establishing a single-cell RNA sequencing library of the murine cardiomyocyte lineage and the cardiac conduction system

I undertook more detailed analysis to discriminate between working and non-working cardiomyocyte populations within our dataset. I selected cell types expected to contribute to the developmental cardiomyocyte lineage from mesodermal cardiac progenitors through to postnatal cardiomyocytes. I used a recently established dimensionality reduction technique (PHATE)[364], that transforms the high-dimensional gene space (c. 27k) down to a 2- or 3-dimension PHATE space that is more intuitive to interpret both by humans and data science techniques that rely on distance-based measures in the gene space or reduced dimension space, such as the spectral-like clusterting technique we used[364]. PHATE does this through the preservation of both global and local distance in this reduced dimension space, whereas similar techniques such as UMAP and t-SNE do not[364]. I identified 15 distinct cell types over n=107705 cells (Figure 3-5). PHATE's preservation of the latent manifold structure of the high-dimensional gene space approximates pseudotime[364]. I observed a lineage-like progression along this manifold from the meosdermal cardiogenic heart fields (*Hand1*^{hi}, *Wnt2*^{hi}, *Osr1*^{hi}) through to (*Acta2*^{hi}, *Tagln*^{hi}, *Pmp22*^{hi}) formation, to immature ventricular (*Myl2*$^{+}$, *Myl7*^{lo}, *Actc1*$^{+}$, *Tnni1*^{hi}, *Tnni3*^{lo}) and atrial (*Actc1*$^{+}$, *Sln*$^{+}$, *Myl7*^{hi}) cardiomyocytes, and then through into more mature atrial (*Myl7*^{hi}, *Sln*^{hi}, *Nppa*^{hi}, *Tnni3*^{hi}) and ventricular (*Myh7*^{hi}, *Myh6*^{lo}, *Myl2*^{hi}, *Kcne1*^{hi}, *Tnni3*^{hi}) cardiomyocytes (Figure 3-6, Figure 3-7, Figure 3-8). Sun, Grassam-Rowe et al includes supplementary interactive figures that enable the interactive 3-D exploration of the transcriptomic space[2]. Unlike many prior scRNA-seq studies[273,390-392], we were readily able to distinguish distinct CCS cell types within our dataset without the use of selective microdissection or other enrichment techniques[348,373] (Figure 3-9).

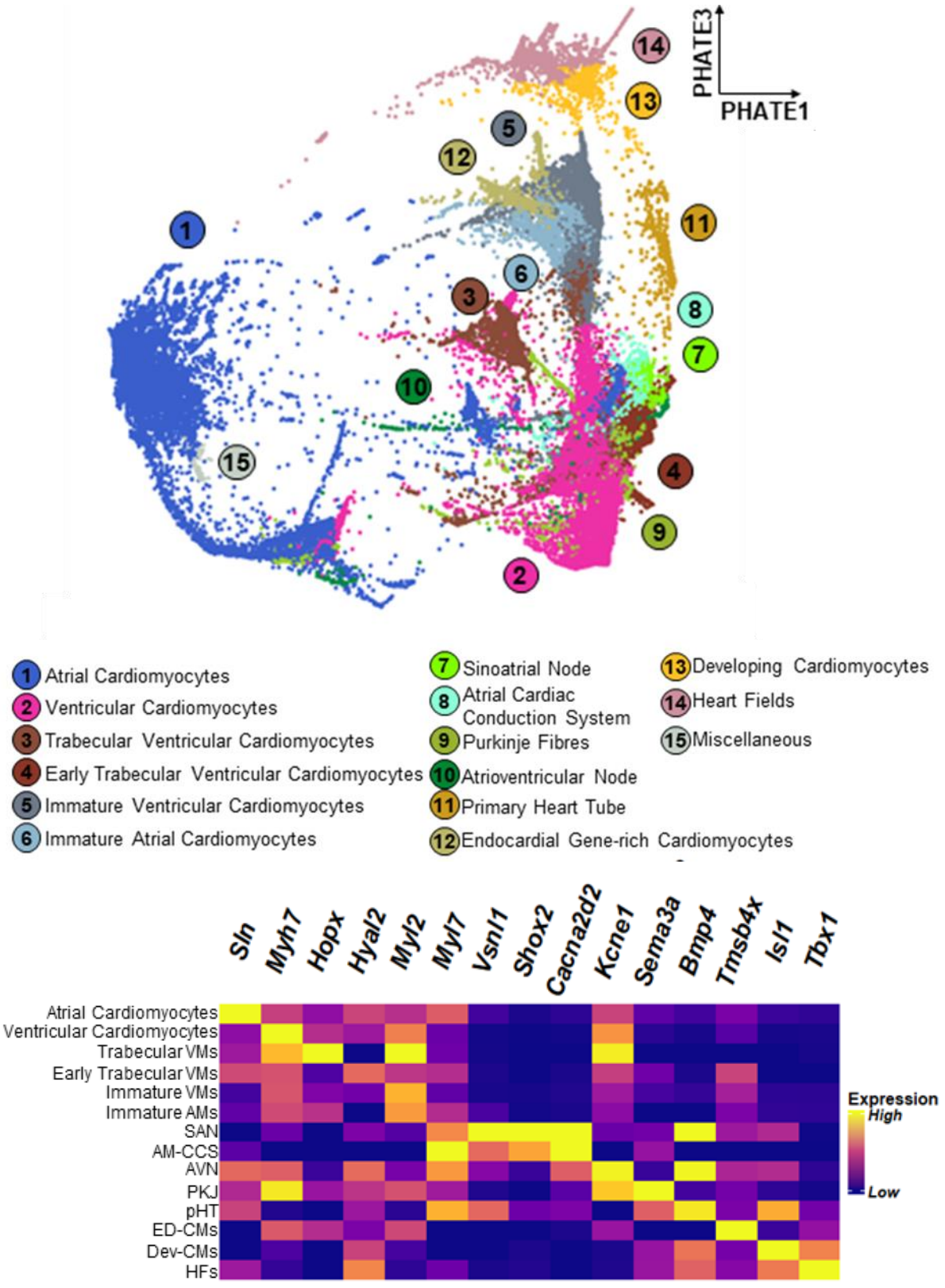

Figure 3-5. Single-cell RNA sequencing characterised the cellular landscape of the murine cardiomyocyte lineage.

Top) The transcriptomic cellular landscape of the cardiomyocyte lineage as a 2D PHATE plot. Numbered labels are placed near their corresponding cell type with the corresponding colour on the PHATE plot, with full names described below with the same number.

Bottom) A heatmap of the most pertinent marker genes for cell types identified in the plot above. Gene expression values were normalised across heatmap rows, and then across columns. Yellow denotes high relative expression. Purple denotes low relative expression.

Abbreviations: VMs – ventricular cardiomyocytes; AMs – atrial cardiomyocytes; SAN – sinoatrial node; AM-CCS – atrial cardiac conduction system; AVN – atrioventricular node; PKJ – Purkinje fibres; pHT – primary heart tube; ED-CMs – endocardial gene-rich cardiomyocytes; Dev-CMs – developing cardiomyocytes; HFs – heart fields.

This figure is adapted from Sun, Grassam-Rowe et al[2].

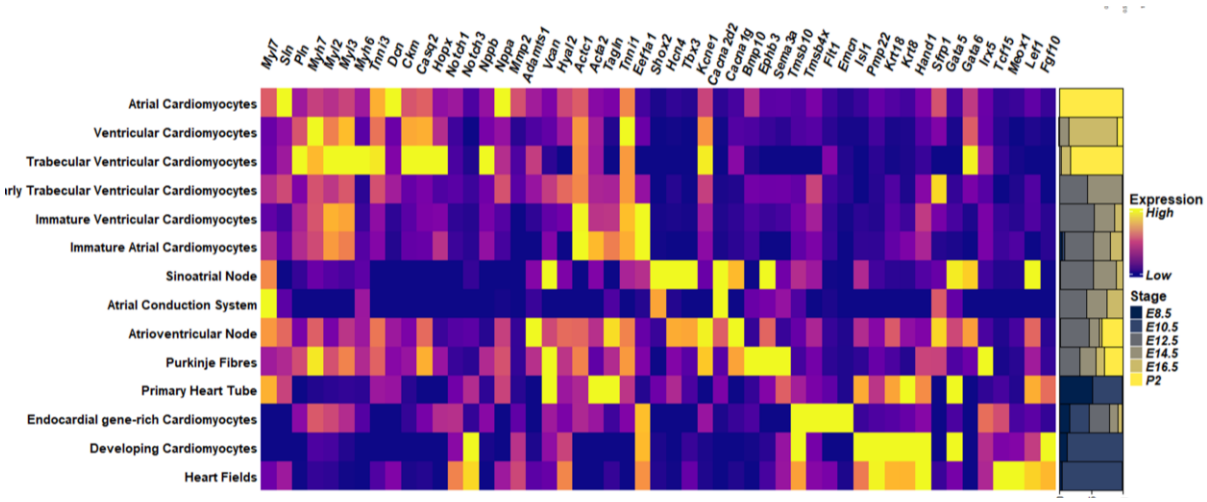

Figure 3-6. Cardiomyocyte lineage cell types display their specific cassettes of marker genes.

A heatmap shows the expression of genes on the y-axis by each cell type on the x-axis. The annotation on the right describes the relative proportions of each cluster in terms of developmental stage. Values for expression are normalised by row and then by column for visualisation purposes. Yellow denotes high relative expression, and purple denotes low relative expression.

This figure is adapted from Sun, Grassam-Rowe et al[2].

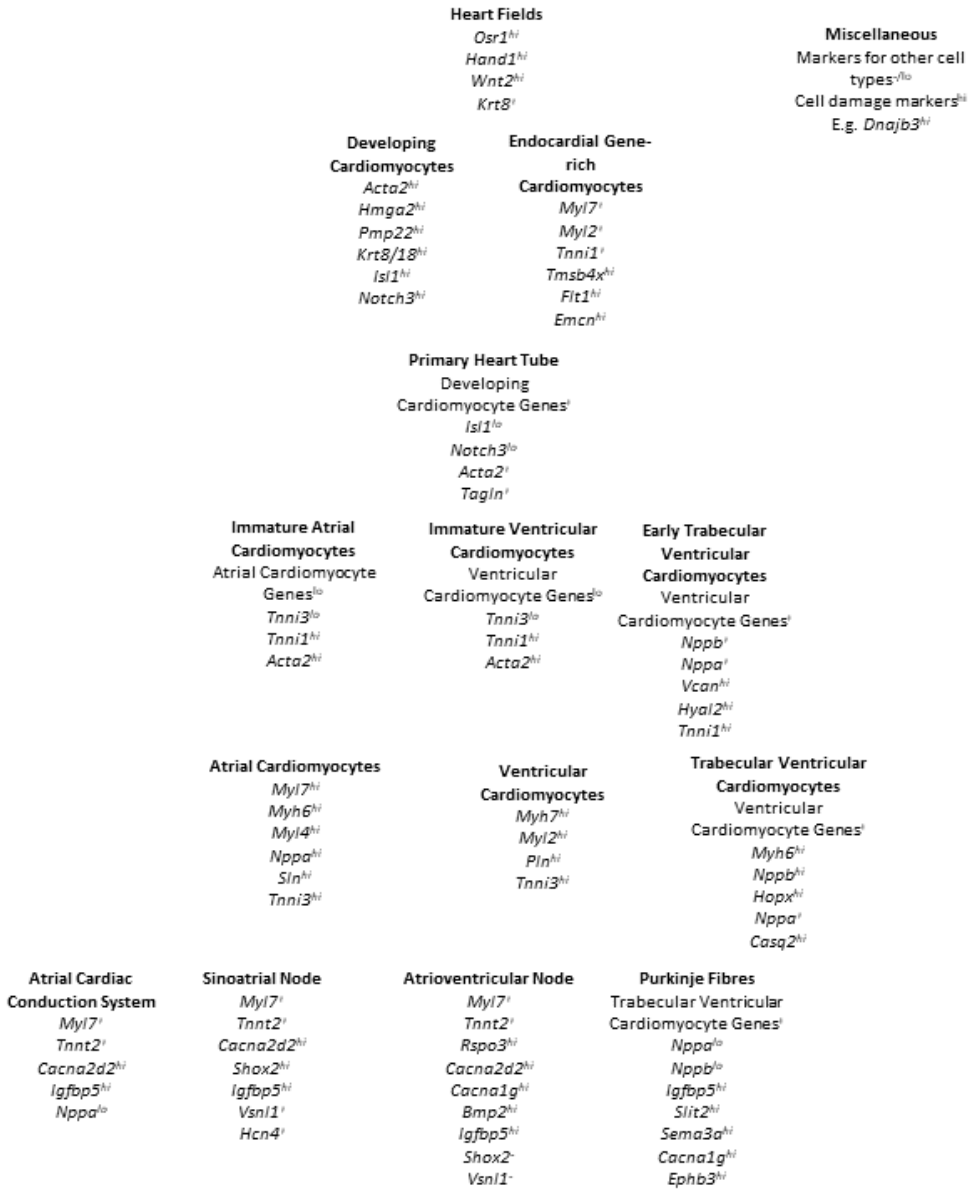

Figure 3-7. Key marker genes for cell types identified within our cardiomyocyte lineage.

Each cell type corresponding is identified in bold, with key marker genes underneath. Gene^{+} denotes a gene expressed above the level of other cell types. Gene^{hi} denotes a gene highly expressed above the level of other cell types. Gene^{lo} denotes a gene expressed below the level expected if it were of a particular other cell type – this is typically with regards to comparing against another cell type rather than against the whole dataset.

This figure is adapted from Sun, Grassam-Rowe et al[2].

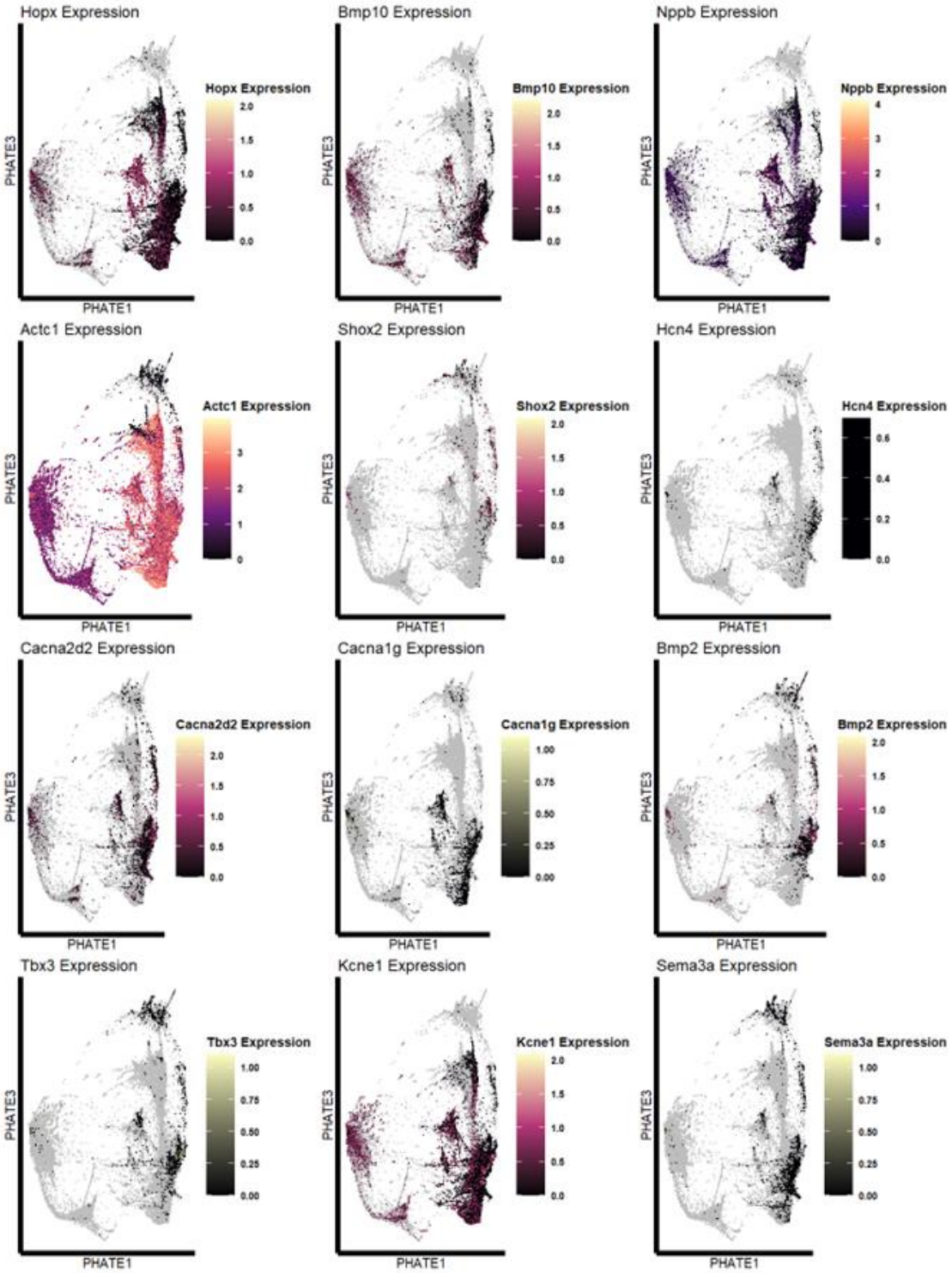
Hopx Expression
Hopx Expression
Bmp10 Expression
Bmp10 Expression
Nppb Expression
Nppb Expression
Actc1 Expression
Actc1 Expression
Shox2 Expression
Shox2 Expression
Hcn4 Expression
Hcn4 Expression
Cacna2d2 Expression
Cacna2d2 Expression
Cacna1g Expression
Cacna1g Expression
Bmp2 Expression
Bmp2 Expression
Tbx3 Expression
Tbx3 Expression
Kcne1 Expression
Kcne1 Expression
Sema3a Expression
Sema3a Expression
PHATE1
PHATE3

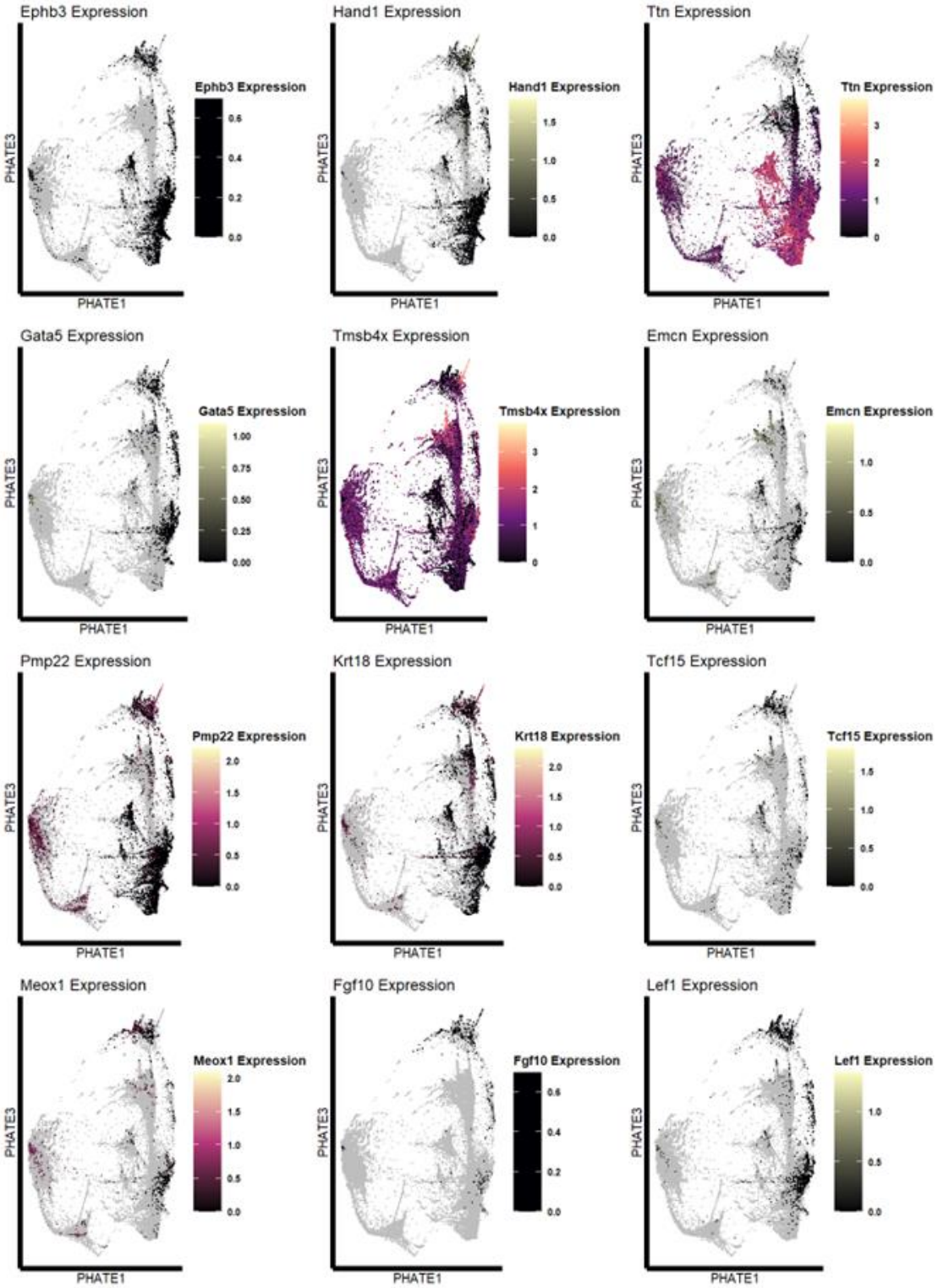
Ephb3 Expression
Hand1 Expression
Ttn Expression
Gata5 Expression
Tmsb4x Expression
Emcn Expression
Pmp22 Expression
Krt18 Expression
Tcf15 Expression
Meox1 Expression
Fgf10 Expression
Lef1 Expression
PHATE1
PHATE3

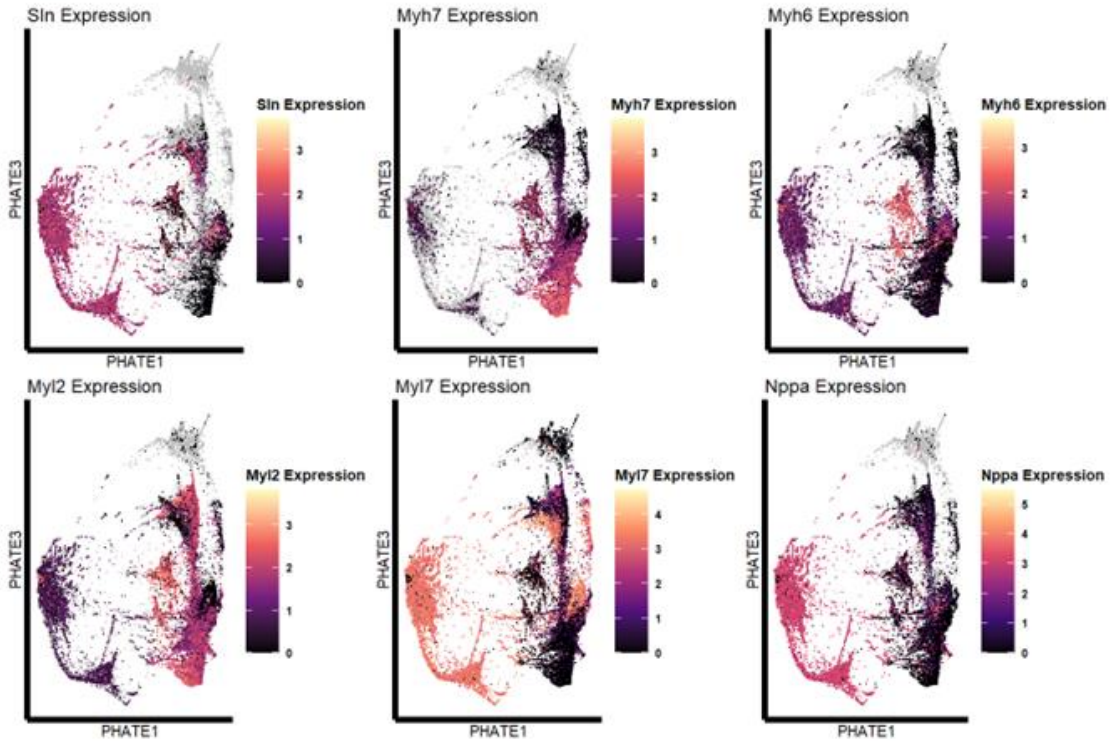

Figure 3-8. Marker genes expressed across cell types identified within the cardiomyocyte lineage.

Cardiomyocyte lineage cells plotted in 2D PHATE with cells coloured by the expression of the specific gene identified at the top of the plot. The expression is given in log counts on the legend to the right of each plot.

This figure is adapted from Sun, Grassam-Rowe et al[2].

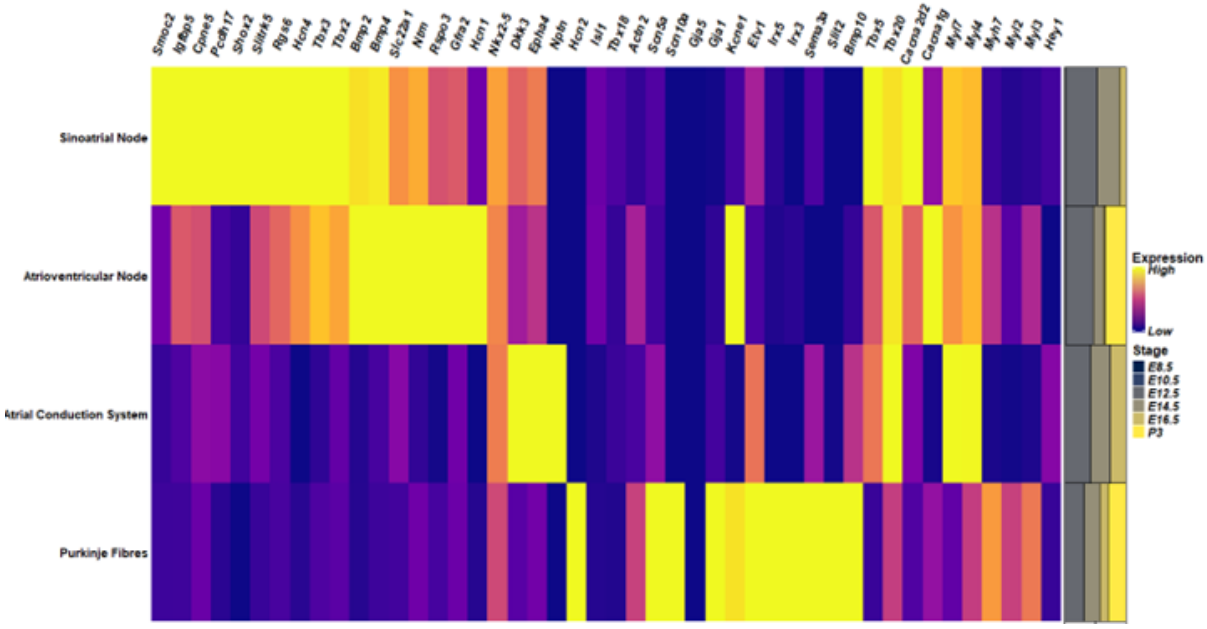

Figure 3-9. Distinct CCS populations are resolvable within our cardiomyocyte lineage.

A heatmap indicating the expression of genes on the x-axis by specific cell types on the y-axis. The annotation on the right describes the relative proportions of each cluster in terms of developmental stage. Values for expression

are normalised by row and then by column for visualisation purposes. Yellow denotes high relative expression and purple denotes low relative expression.

This figure is adapted from Sun, Grassam-Rowe et al[2].

iii. Certain populations of cardiomyocytes express *Dbh* in the developing mouse heart.

After having now established a single-cell landscape of the developing mouse heart, with resolution of functionally distinct and important cell types, I sought to use the dataset to investigate specific biological questions. I identified a subpopulation of cardiomyocytes expressing dopamine β-hydroxylase (*Dbh*$^+$-CMs). I observed *Dbh* expression across a range of more canonically *Dbh*$^+$ cell types, including expected sources such as the developing brain stem in our initial whole data but also across both working and non-working cardiomyocytes (Figure 3-10). In total, the cardiomyocyte lineage had n=2951 *Dbh*$^+$-CMs, which represented 2.43% of all cardiomyocyte lineage cells from E8.5 to P3. However, there was little expression of *Dbh* before E12.5.

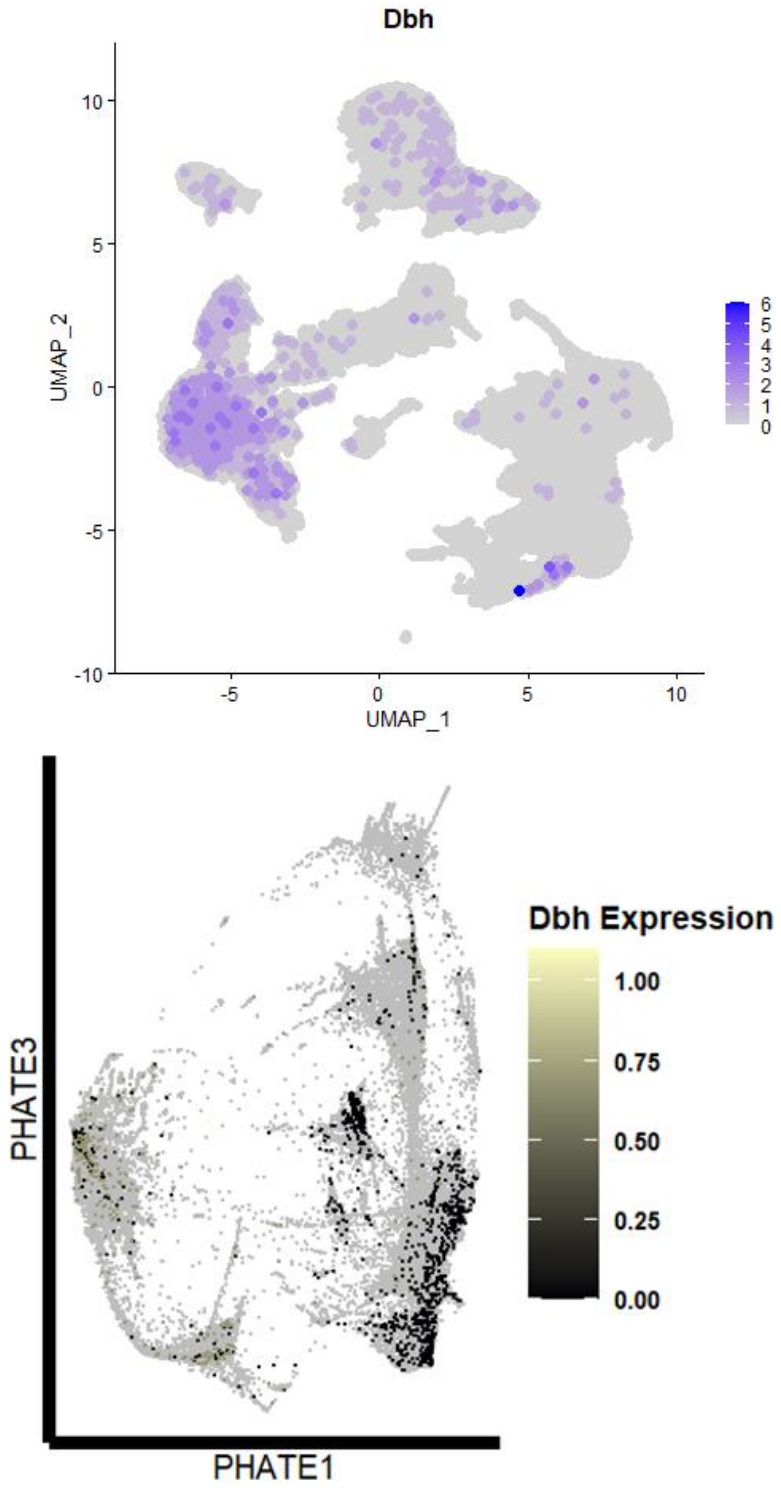

Figure 3-10. Dbh is expressed across developing and postnatal cardiomyocytes.

Top) 2D UMAP of Dbh expression across whole dataset. Dbh expression can be observed primarily across cardiomyocytes and the developing brainstem/brain. Cells are coloured by normalised counts as denoted by legend on right.

Bottom) 2D PHATE of Dbh expression across the cardiomyocyte lineage. Dbh expression is particularly prevalent in the CCS cell types. Cells are coloured by $\log_{10}$ counts as denoted by legend on right.

This figure is adapted from Sun, Grassam-Rowe et al[2].

These *Dbh*$^{+}$-CMs expressed both the expected pan-cardiomyocyte markers and respective CCS cell-type specific markers (Figure 3-11, Figure 3-12). *Dbh*$^{+}$-CMs comprised relatively small numbers of the general working cardiomyocyte subpopulations (AM: 2.13%, VM: 3.90%, VM-trab: 4.18%, and eVM-trab: 2.26%) (Figure 3-11, Figure 3-13). However, CCS cell-types were over-represented in *Dbh*$^{+}$ cardiomyocytes as percentages of their respective total cardiomyocyte lineage numbers (PKJ: 12.76%, AVN: 12.14%, SAN: 8.39%, and AM CCS: 3.82%) (Figure 3-11, Figure 3-13). I used a Pearson's Chi-Squared test for independence, which suggested that cell type, within cardiomyocytes beyond E10.5, and *Dbh* expression (positive or negative) are not independent (X^2 = 1155.2, df = 9, p= 5.8e-243, n=103008). Thus, I concluded that these *Dbh*$^{+}$-CMs represented a real population of CMs, that were particularly populous in the CCS.

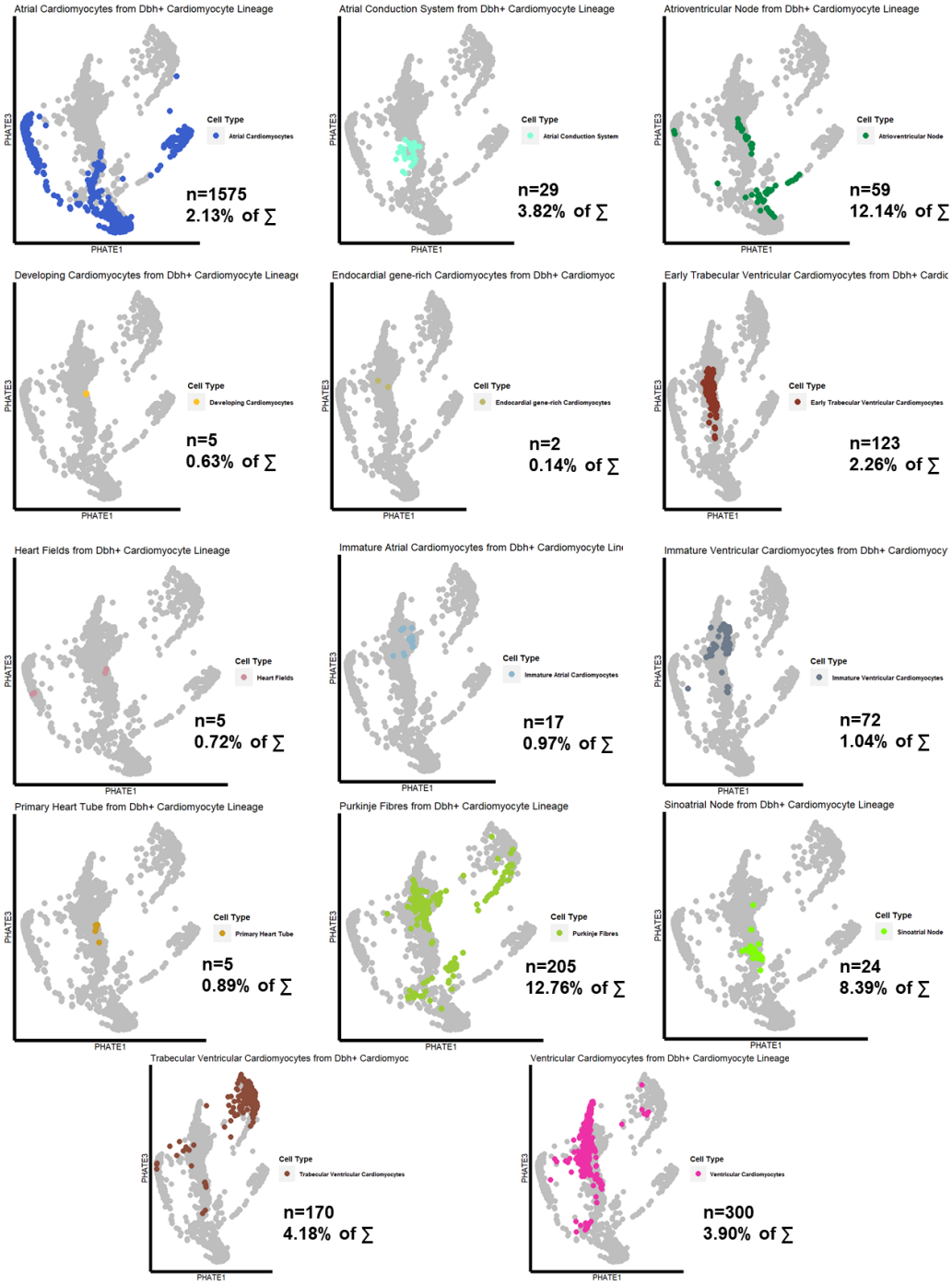

Figure 3-11. Dbh+ cardiomyocytes were particularly populous within the CCS.

2D PHATE plots of Dbh^{+}-CMs. Each plot demonstrates a particular cell type, as described at the top of the respective plot. Cells are coloured by the respective colour of their cell type on the cardiomyocyte lineage. Each plot also includes the total number and percentage of Dbh^{+}-CMs within the particular cell type. ∑ defines the total number of cells of a given type.

This figure is adapted from Sun, Grassam-Rowe et al[2].

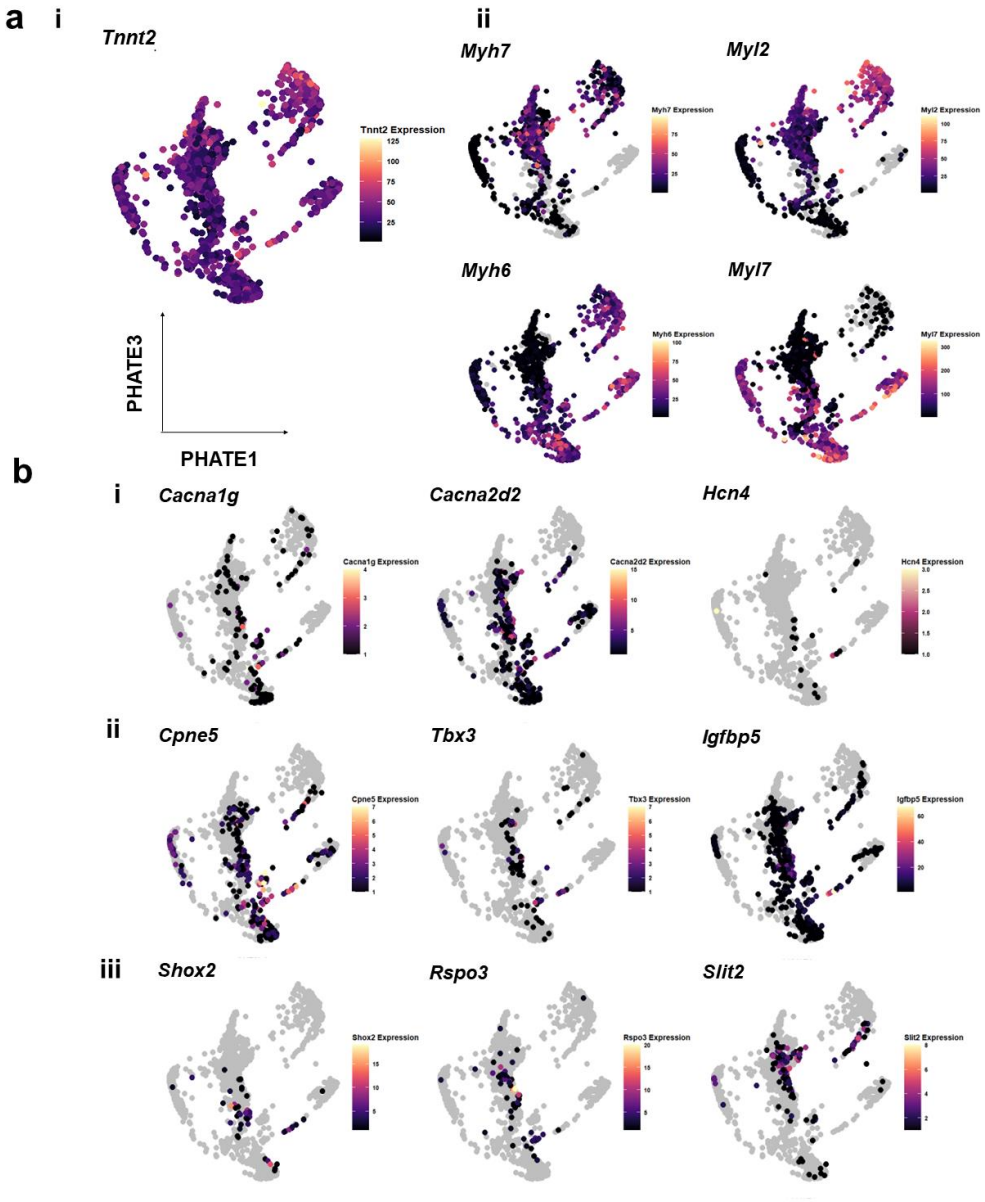

Figure 3-12. Dbh⁺ cardiomyocytes express the transcriptomic signature of their respective CCS cardiomyocyte cell types.

2D PHATE plots of Dbh⁺-CMs, coloured by the normalised expression of their respective gene denoted above each plot and on the legend on the right.

a) i) A pan-cardiomyocyte marker ii) atrial and ventricular chamber-specific genes.
b) i) CCS-associated ion channel-encoding genes ii & iii) CCS-associated developmental genes and transcription factors.

This figure is adapted from Sun, Grassam-Rowe et al[2].

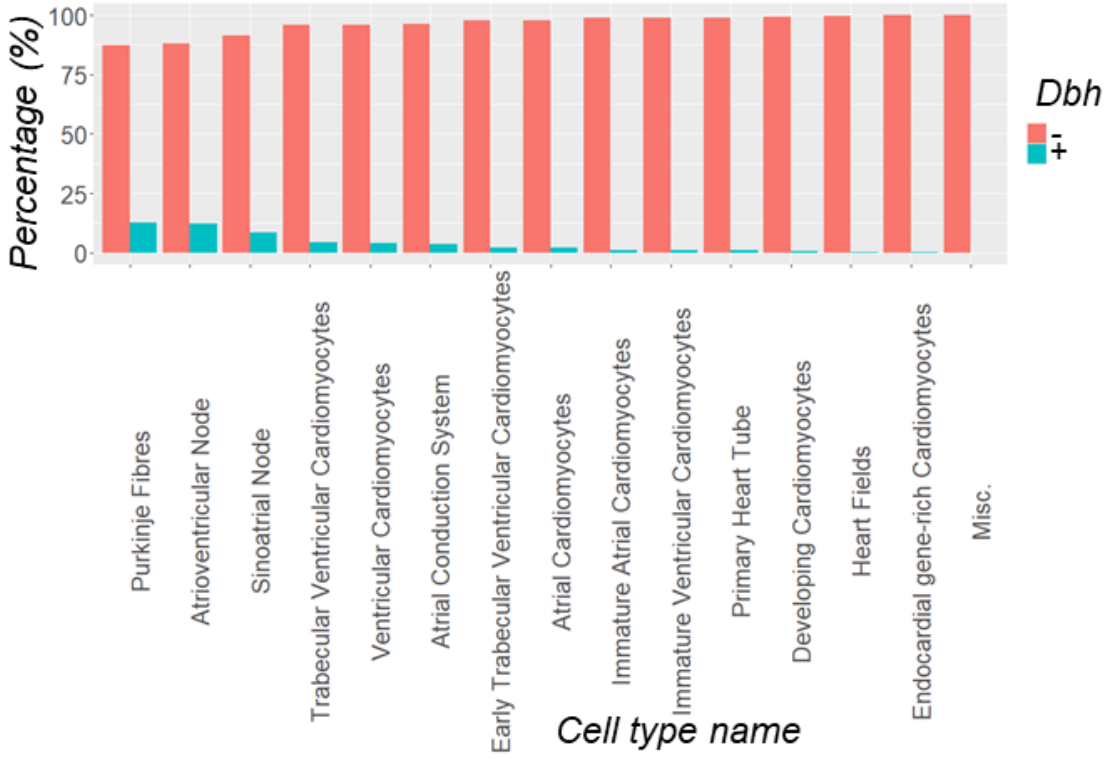

Cell type	Total number of cells in type (N)	Number of cells *Dbh+* (N)	Number of cells *Dbh-* (N)	Percentage *Dbh+* (%)
Atrial Cardiomyocytes	74021	1575	72446	2.1
Early Trabecular Ventricular Cardiomyocytes	5439	123	5316	2.3
Heart Fields	1783	5	1778	0.3
Ventricular Cardiomyocytes	7692	300	7392	3.9
Immature Ventricular Cardiomyocytes	6897	72	6825	1.0
Atrioventricular Node	486	59	427	12.1
Purkinje Fibres	1606	205	1401	12.8
Primary Heart Tube	561	5	556	0.9
Trabecular Ventricular Cardiomyocytes	4069	170	3899	4.2
Immature Atrial Cardiomyocytes	1752	17	1735	1.0
Endocardial gene-rich Cardiomyocytes	1407	2	1405	0.1
Developing Cardiomyocytes	793	5	788	0.6
Sinoatrial Node	286	24	262	8.4
Atrial Conduction System	760	29	731	3.8
Misc.	153	0	153	0.0

Figure 3-13. The highest percentage of Dbh+ cardiomyocytes are within the CCS.

Top) The percentage of each cell type which is Dbh^+ (blue) or Dbh^- (red).

Bottom) Absolute numbers of total, Dbh^+, and Dbh^- CMs for each cell type. Dbh positive expression was defined as >0 counts in the raw data.

This figure is adapted from Sun, Grassam-Rowe et al[2].

iv. Spatial transcriptomics as a model for studying cardiac development and lineages

Following my scRNA-seq characterisation of these *Dbh*$^{+}$-CMs, we sought to validate their transcriptomic signature with the additional benefit of their anatomical ground-truth within the heart. We utilised a new spatially-resolved transcriptomics technique (Stereo-Seq)[371] to investigate this. To track this specific population of *Dbh*$^{+}$-CMs, we developed a *Dbh*$^{+}$ cell lineage reporter mouse line (*Dbh*^{Cre}/*Rosa26-tdTomato*). We had at least n=3 sections from these mouse hearts at E12.5, E14.5, P3, and P56, following quality control. Following binning of DNBs at each stage, as described in the methods, E12.5, E14.5, and P3 had individual spot diameters of ~14 um, and P56 had a spot diameter of ~35 um.

I first sought to confirm whether Stereo-Seq could faithfully recapitulate the known biological expression of different anatomically- and developmentally-restricted transcriptional profiles. The data faithfully described the anatomically- and developmentally-restricted expression of not just broad chamber-specific markers, such as *Myh6*, *Myl2*, and *Nppa*, but also more cell-type restricted markers such as *Hcn4* (Figure 3-14).

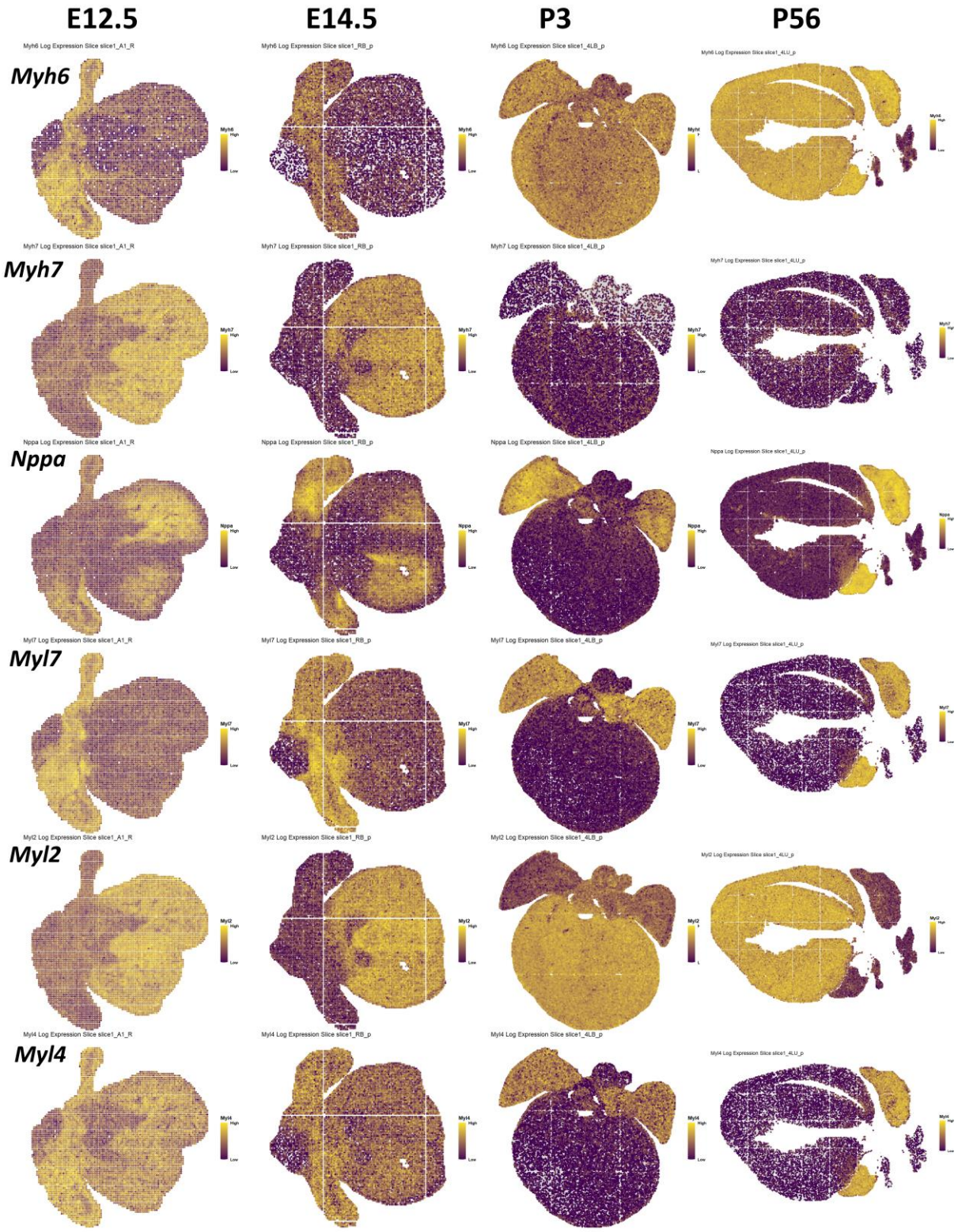
E12.5
E14.5
P3
P56
Myh6
Myh7
Nppa
Myl7
Myl2
Myl4

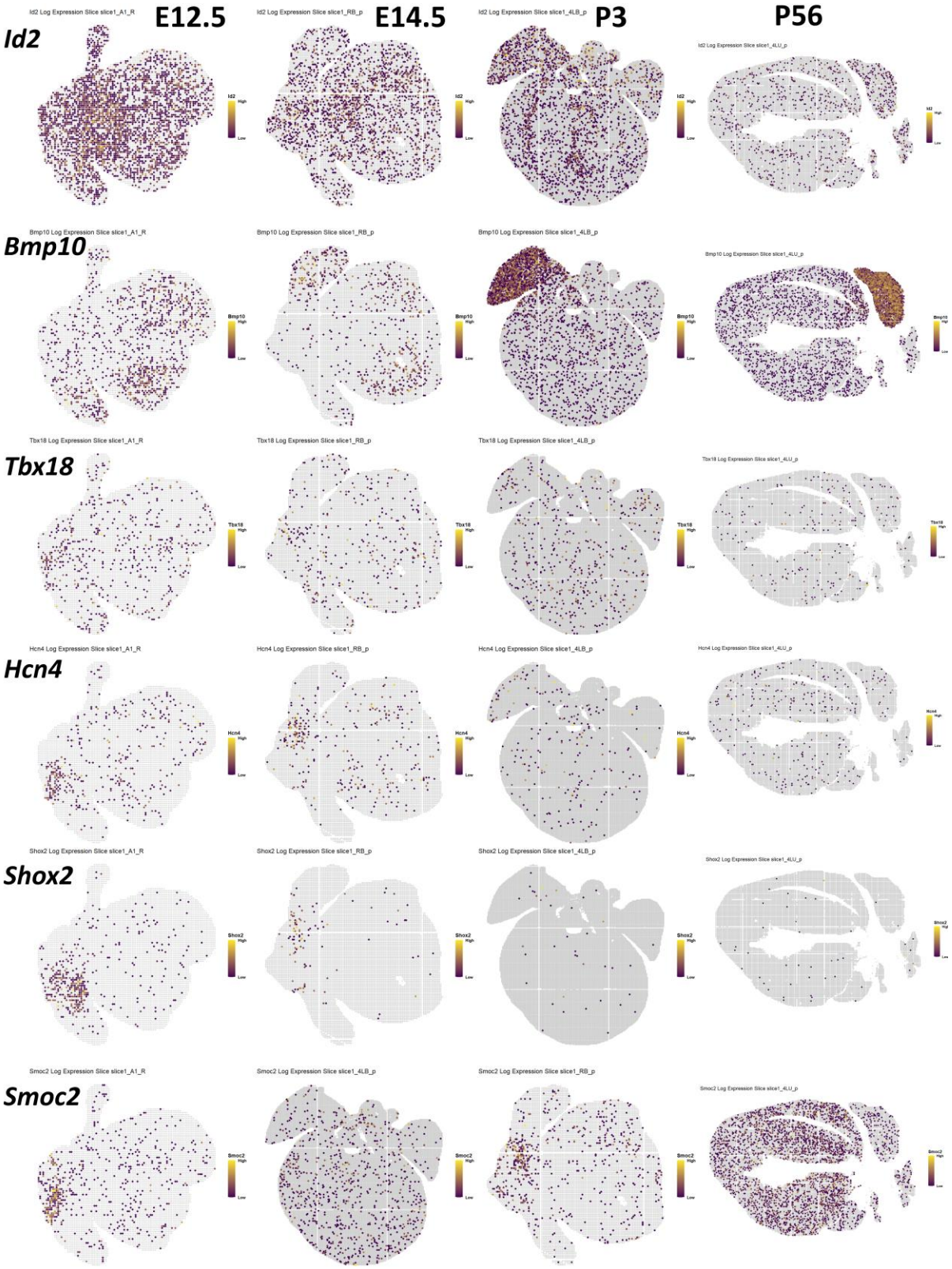
E12.5
E14.5
P3
P56
Id2
Bmp10
Tbx18
Hcn4
Shox2
Smoc2

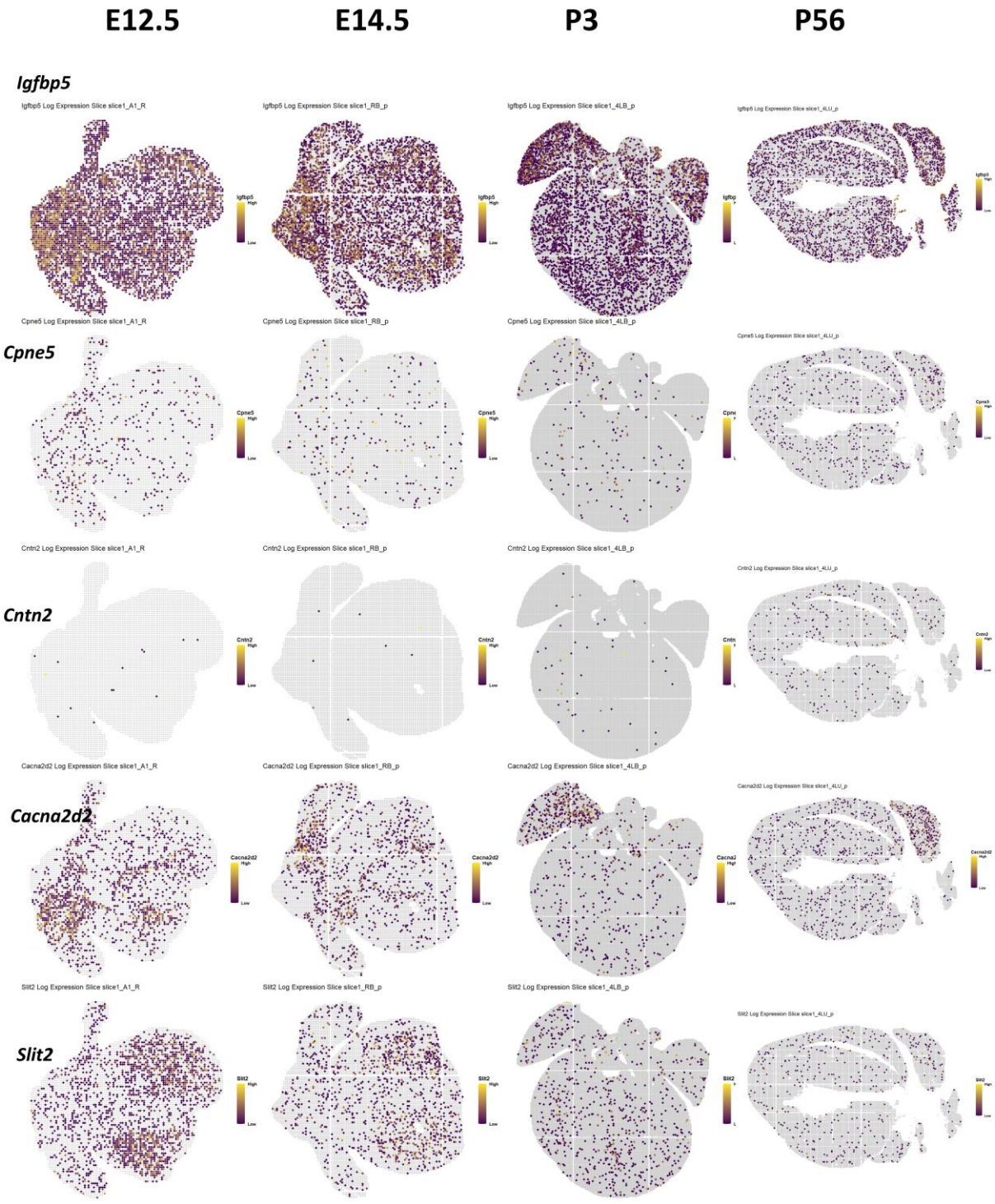

Figure 3-14. Stereo-Seq faithfully reproduces well-characterised changes in gene expression across the developing, perinatal, and mature murine heart and anatomically within those stages.

Each row contains a plot for each of the stages listed at the top of the columns. Each row corresponds to the same gene and each column corresponds to the same stage, which increases in chronological age from left to right. Each plot is coloured by the relative expression of that gene at that stage. High gene expression is indicated by yellow and low gene expression is indicated by purple. Expression has been normalised on a per stage basis for visualisation purposes.

This Figure is adapted from Sun, Grassam-Rowe et al[2].

Now I had confirmed that Stereo-Seq could describe the global gene expression patterns across the heart; I wanted to confirm that these transcriptomic signals were internally consistent at the level of individual spots such that they could capture individual transcriptomic profiles matching expected cellular transcriptomic profiles. I omitted P56 from this process to ensure comparability with our scRNA-seq data. First, using unsupervised clustering, I identified a range of working and non-working cardiomyocyte populations across E12.5, E14.5, and P3, that matched their respective anatomical distributions (Figure 3-15) and their transcriptomic profiles (Figure 3-16, Figure 3-17).

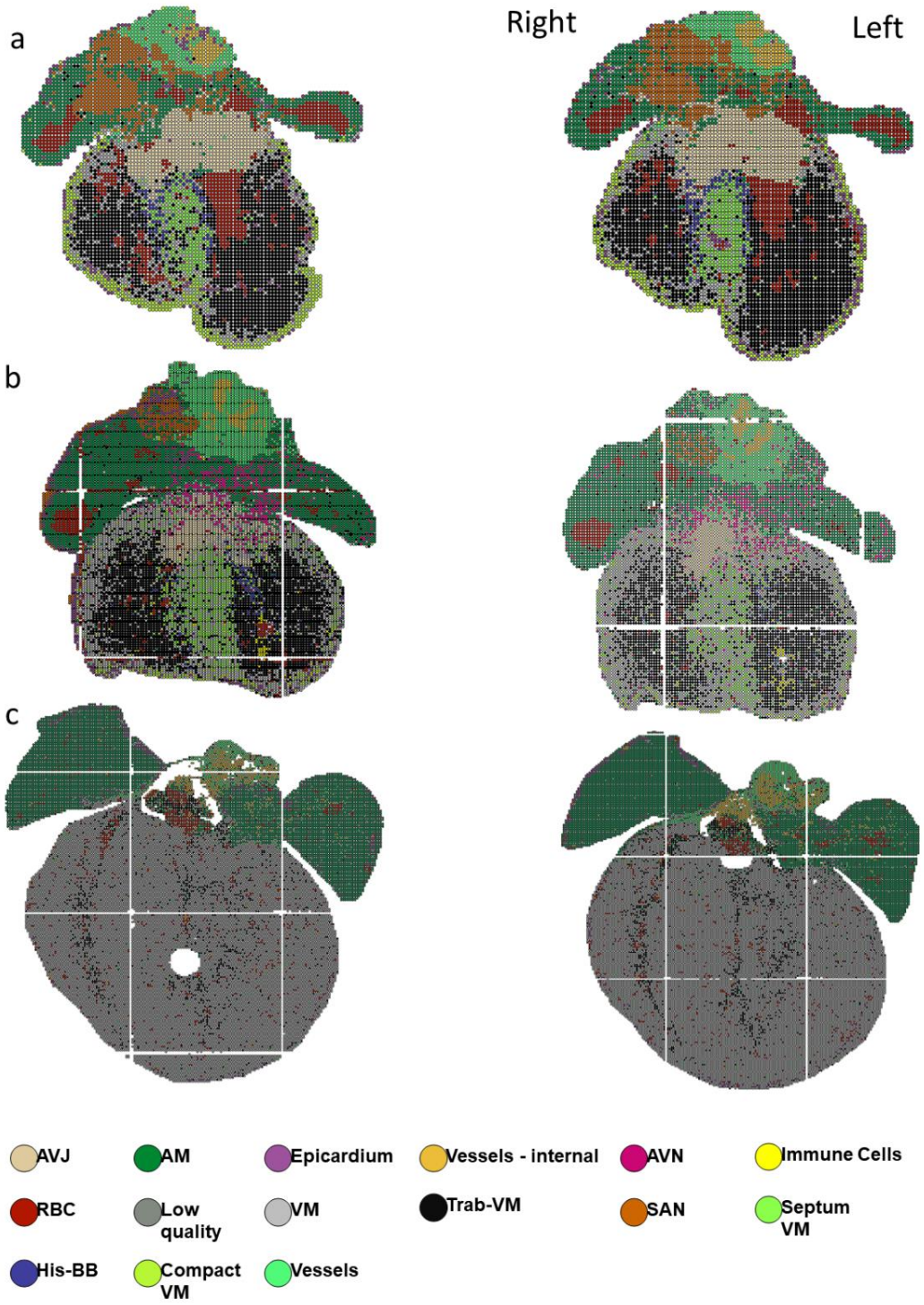

Figure 3-15. Cell types could be identified using unsupervised clustering in our Stereo-Seq data.

Bins are coloured by respective cell type as per the coloured labels at the base of the figure. All slices are presented in same orientation right to left anatomically.

Top) Representative slices from E12.5.

Middle) Representative slices from E14.5.

Bottom) Representative slices from P3.

This Figure is adapted from Sun, Grassam-Rowe et al[2].

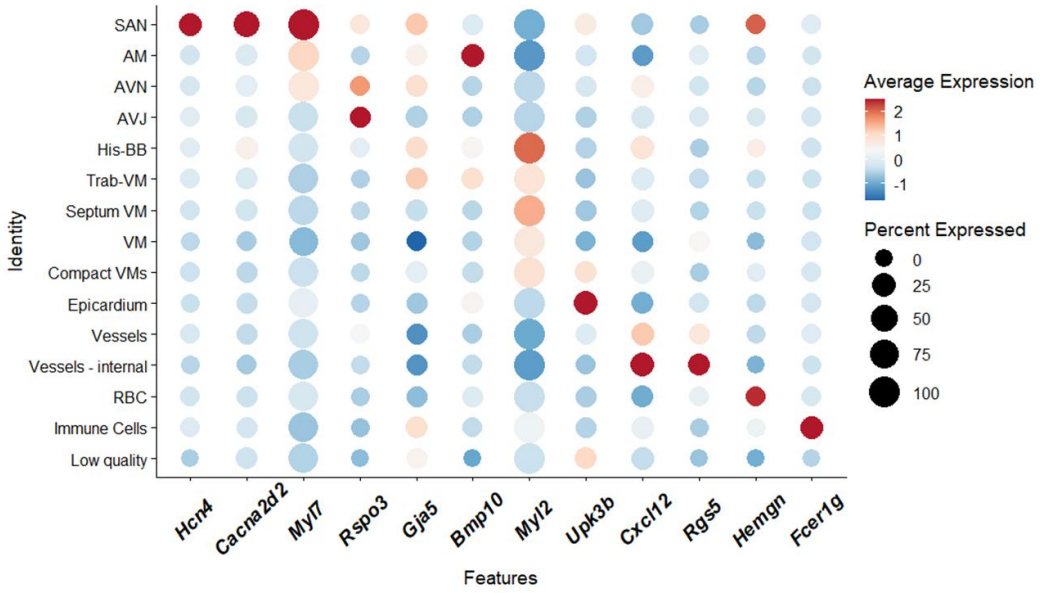

Figure 3-16. Our Stereo-Seq could be used to identify underlying cell types and anatomy through unsupervised clustering.

A dot plot describes the z-scored expression of key marker genes on the x-axis, by their expression by different populations on the y-axis. The size of dots corresponds to the percentage of cells in that cluster that express the given gene. Populations are from across E12.5, E14.5, and P3.

This Figure is adapted from Sun, Grassam-Rowe et al[2].

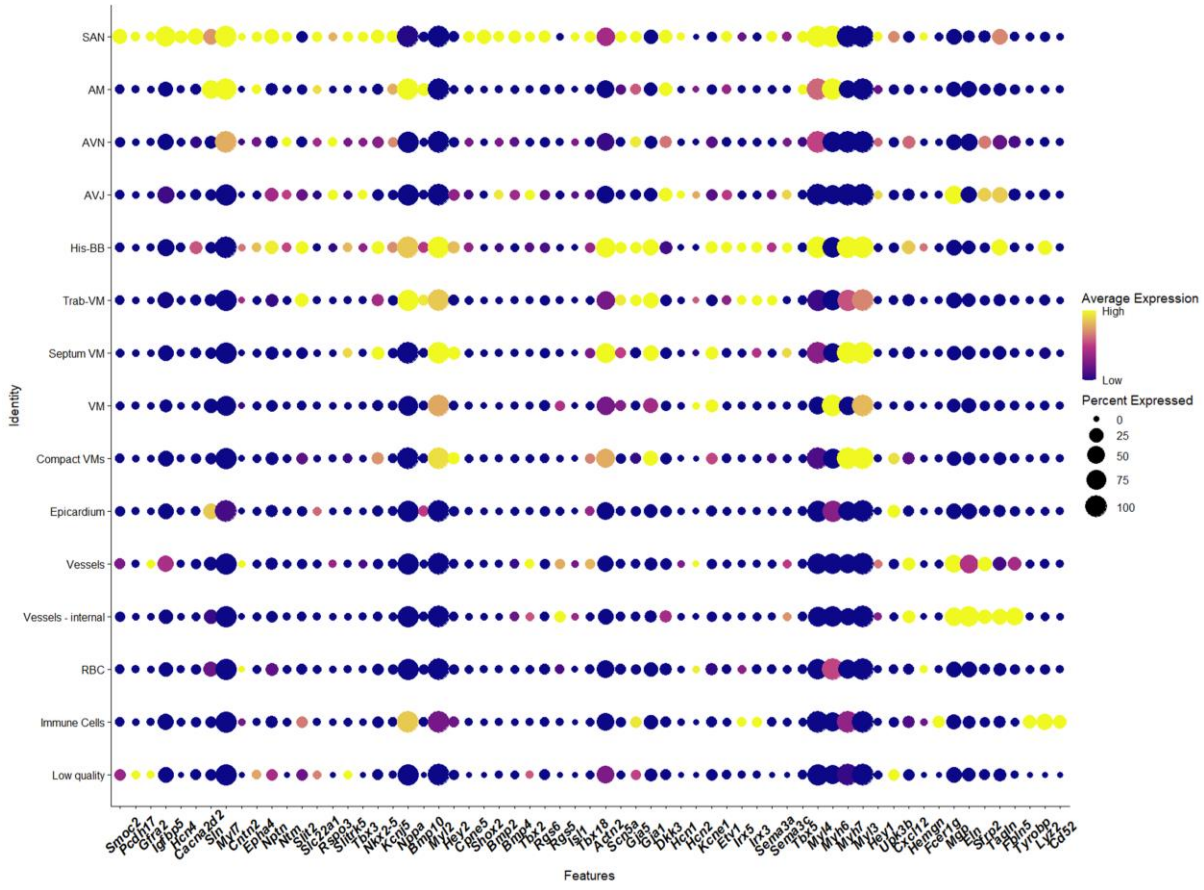

Figure 3-17. Cell types identified through unsupervised clustering demonstrated robust expression of marker genes across the developing and postnatal mouse heart.

A dot plot describes the z-scored expression of key marker genes on the x-axis, by their expression by different populations on the y-axis. The size of dots corresponds to the percentage of cells in that cluster that express the given gene. Populations are from across E12.5, E14.5, and P3. Expression has been scaled for visualisation purposes.

This Figure is adapted from Sun, Grassam-Rowe et al[2].

To minimize the impact of potential bias through the manual classification of unsupervised clusters I also used novel supervised learning classification workstreams to cross-validate our manual classification of the Stereo-Seq data. To minimise the bias from manually selecting marker genes from my scRNA-seq reference, I used a novel unsupervised marker gene selection workflow, which could accurately classify the scRNA-seq library based on learning key marker genes for each cell type (Figure 3-18)[358]. We then used the top 50 most important genes for each cell type identified through this process restrict the gene universe of the supervised learning approach (RCTD[374]) used to decompose the cellular composition of the spatially-resolved Stereo-Seq bins.

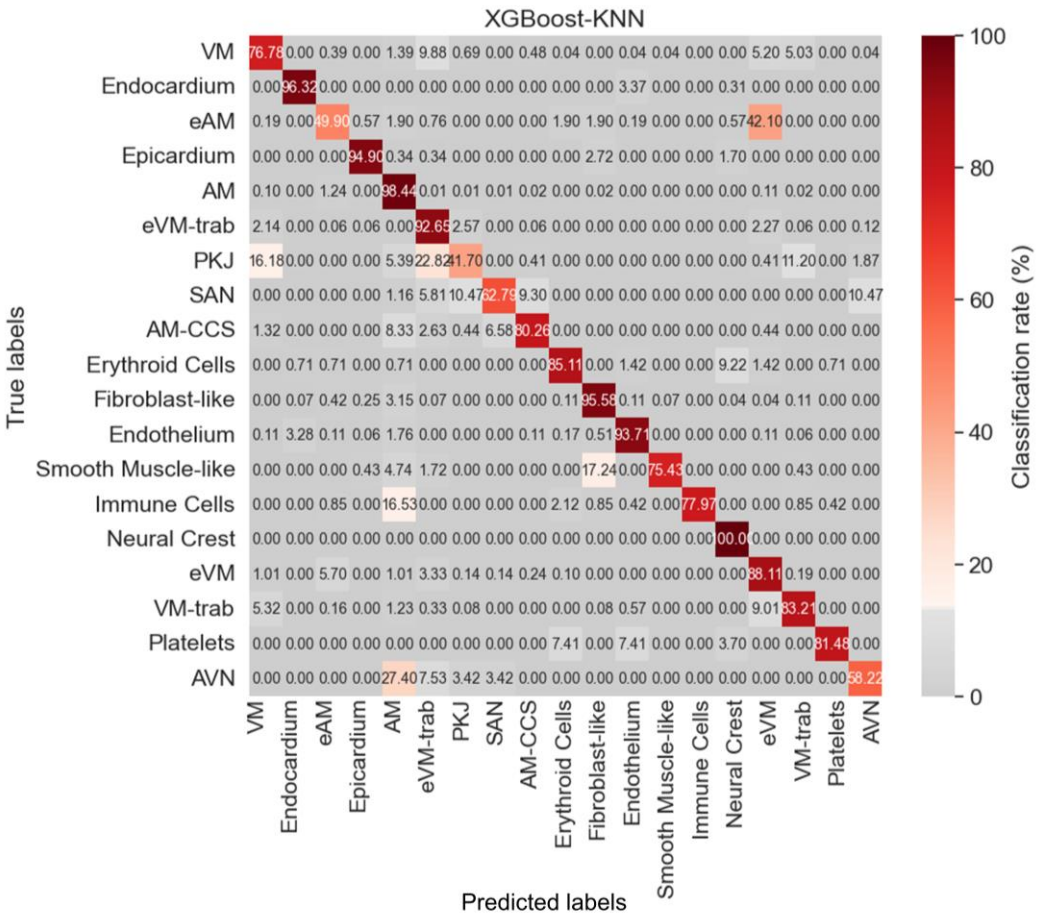

Figure 3-18. Machine learning approaches could accurately learn how to classify cells into cell type by their gene expression.

This matrix demonstrates the highly accurate classification of cell types by a trained classifier, on withheld test data, for subsequent identification of cell type marker genes in single-cell RNA sequencing data by SMASH .

The classifier classifies all the cells in the previously unseen training data, and then identifies how well these predicted labels (on the x-axis) match to the true labels (y-axis). Each cell within the heatmap corresponds to how many of the cells with a specific true label (y-axis) were predicted to have a specific label by the classifier (x-axis). Dark red indicates a higher classification rate. Each row sums to 100%.

Abbreviations: VM - ventricular cardiomyocytes; eAM –immature atrial cardiomyocytes; AM – atrial cardiomyocytes; eVM-trab – early trabecular ventricular cardiomyocytes; PKJ – Purkinje fibres; SAN – sinoatrial node; AM-CCS – atrial cardiac conduction system; eVM – immature ventricular cardiomyocytes; VM-trab – trabecular ventricular cardiomyocytes; AVN – atrioventricular node.

This Figure is adapted from Sun, Grassam-Rowe et al[2].

Overall, the supervised learning classification method mostly agreed anatomically with my manual classification of unsupervised clustering (Figure 3-19). Of particular interest, this integrated mapping was sufficiently robust to plausibly identify even certain rarer and more transcriptomically complex cell types such as the Purkinje Fibres. However, certain cell populations appeared to map unexpectedly. For example, 'AM-CCS' did map in a somewhat non-specific manner across the atrial myocardium (Figure 3-19). This likely reflected the weaker expression of CCS markers in AM-CCS, compared to the SAN/AVN, but with stronger expression of less cell-type specific atrial markers (Figure 3-9). I believe that the AM-CCS likely represents either some transitional sinus node population during development, or perhaps the

inter-atrial conduction pathways. However, further work is required to investigate this and delineate its unique transcriptional signature.

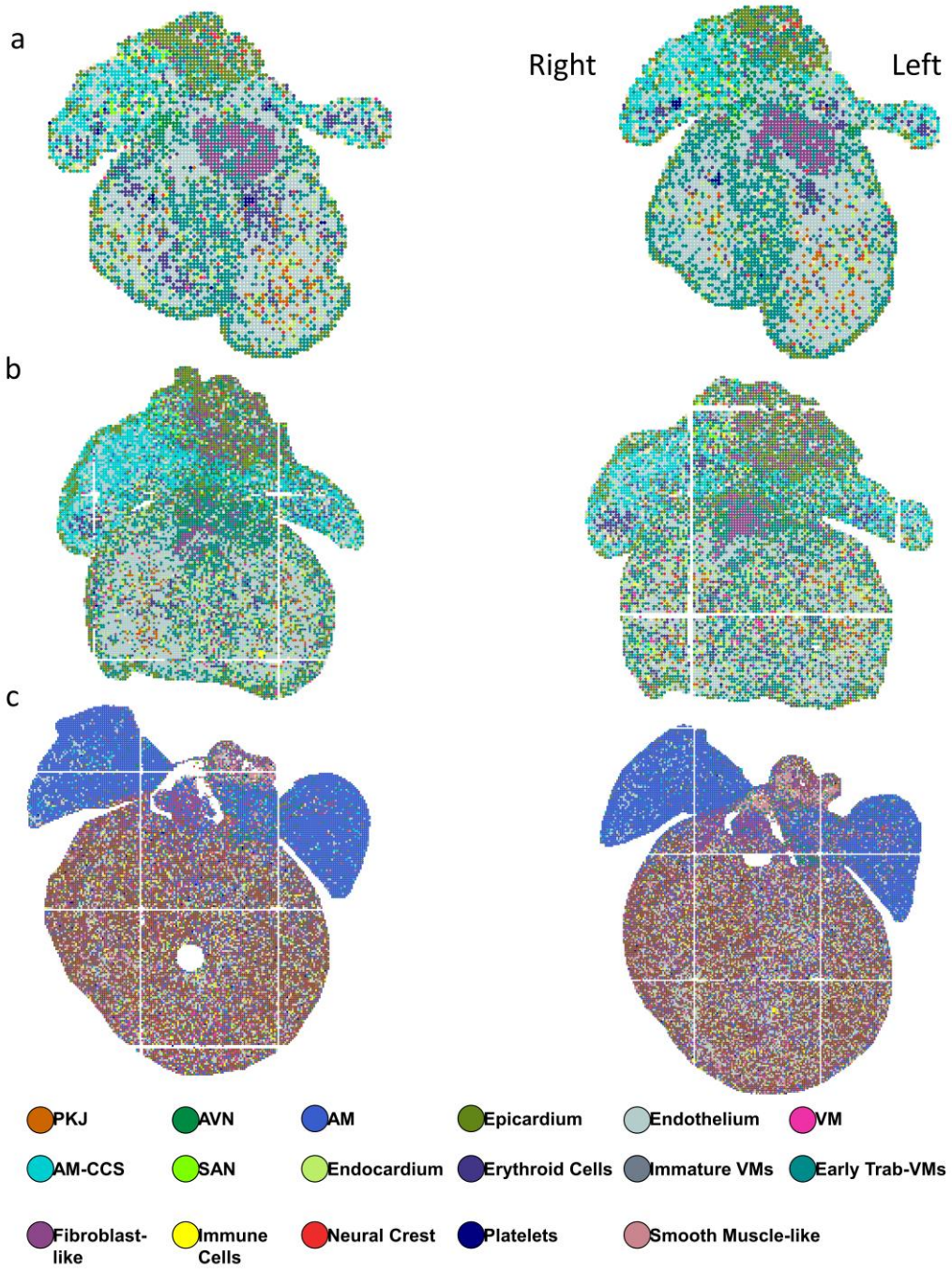

Figure 3-19. Stereo-Seq with spatial decomposition of cell types could identify a range of cell types across the heart.

Bins are coloured by respective cell type suggested as top by RCTD as per the coloured labels at the base of the figure. All slices are presented in same orientation right to left anatomically.

Top) Representative slices from E12.5.

Middle) Representative slices from E14.5.

Bottom) Representative slices from P3.

This Figure is adapted from Sun, Grassam-Rowe et al[2].

Those cell types that mapped imperfectly were typically cell types that mapped to very transcriptomically similar cell types with often only a few key defining genes separating them. When I analysed the prediction error, we saw that many of the incorrectly mapped cell types were in fact strongly identified by the scoring system. However, the use of a final single highest score and classification likely obscured the complexity of these highly transcriptomically similar, or anatomically overlapping, cells captured in each bin (Figure 3-20). Of particular interest is the mapping of the CCS, which has a nuanced transcriptional signature that can be difficult to distinguish from working cardiomyocytes of the same region. However, RCTD was able to clearly label these CCS cell types and suggest reasonable anatomical distributions. Unfortunately, however, the use of a single-best score for each bin resulted in many of these appropriate signals being lost. In general, I found the suggested classifications of cell types and distributions by this more complex pipeline to be overall inferior to those produced by our earlier unsupervised clustering-based classification of cell types in terms of feasibility of suggested anatomical distributions and clarity with regards to underlying assumptions and interpretability. Thus, I continued downstream analyses using the unsupervised clustering-based classification of cells.

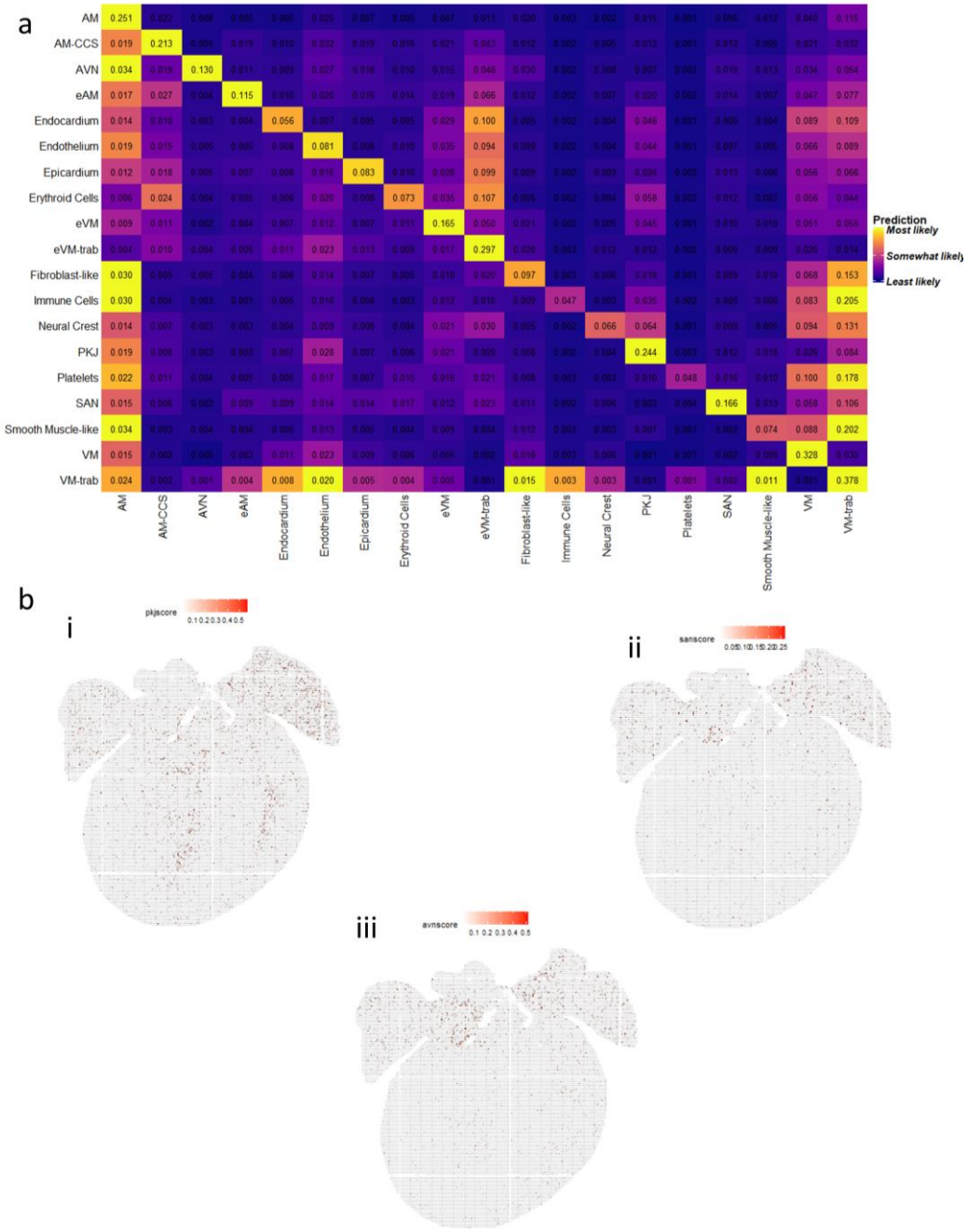

Figure 3-20. RCTD could identify rare cell types, even if they were not considered the primary cell type within a bin.

A) A heatmap plotting the RCTD prediction likelihoods of different cell types across all 3 developmental stages. Bins were clustered by their highest scoring RCTD label as the most likely primary label. Mean prediction scores were then calculating for the other predicted labels for each bin. Rows represent the primary cell type labels, and the columns represent additional predicted labels, such that a whole row describes for a given primary label, how likely were the other labels in the respective columns. Yellow indicates more likely. The prediction score is displayed in black text in each cell.

B) P3 heart sections coloured by RCTD predicted score for respective cell type: i) Purkinje fibres ii) SAN iii) AVN. Red indicates a stronger likelihood.

Abbreviations: VM - ventricular cardiomyocytes; eAM –immature atrial cardiomyocytes; AM – atrial cardiomyocytes; eVM-trab – early trabecular ventricular cardiomyocytes; PKJ – Purkinje fibres; SAN – sinoatrial

node; AM-CCS – atrial cardiac conduction system; eVM – immature ventricular cardioyocytes; VM-trab – trabecular ventricular cardiomyocytes; AVN – atrioventricular node.

This Figure was adapted from Sun, Grassam-Rowe et al[2]. Dr. Tianyi Sun produced the images in Bi,ii,iii under my direction after I conceived the idea.

v. Stereo-Seq supports *Dbh*$^{+}$ cardiomyocytes in the developing and adult mouse heart.

Having established that Stereo-Seq, with the use of expert manual classification of clusters, could discriminate broad whole-organ gene expression through to single or oligo-cell transcription profiles, I then sought to now proceed to investigate *Dbh* expression. I recapitulated my earlier scRNA-seq findings and demonstrated that *Dbh* was indeed expressed across the developing and perinatal myocardium (Figure 3-21). However, now I also demonstrated that *Dbh* was indeed expressed in the mature P56 mouse heart and thus was not simply some transient developmental expression (Figure 3-21). Furthermore, using our *Dbh*^{Cre}/*Rosa26-tdTomato* reporter line, with *Wpre* acting as a proxy mRNA transcript for the reporter construct, I identified that the *Wpre* signal was present across a large proportion of the myocardium, albeit in an anatomically restricted fashion. *Wpre* was used as 3'-end 100 base pair RNA sequencing did not readily detect the tdTomato portion of the construct, but did detect *Wpre* (expressed at 3'-end of the tdTomato reporter cassette construct). Thus, indicating that certain anatomically-restricted cardiac populations are particularly enriched in cells that either currently express *Dbh*, or are the progeny of cells that at some point expressed *Dbh*.

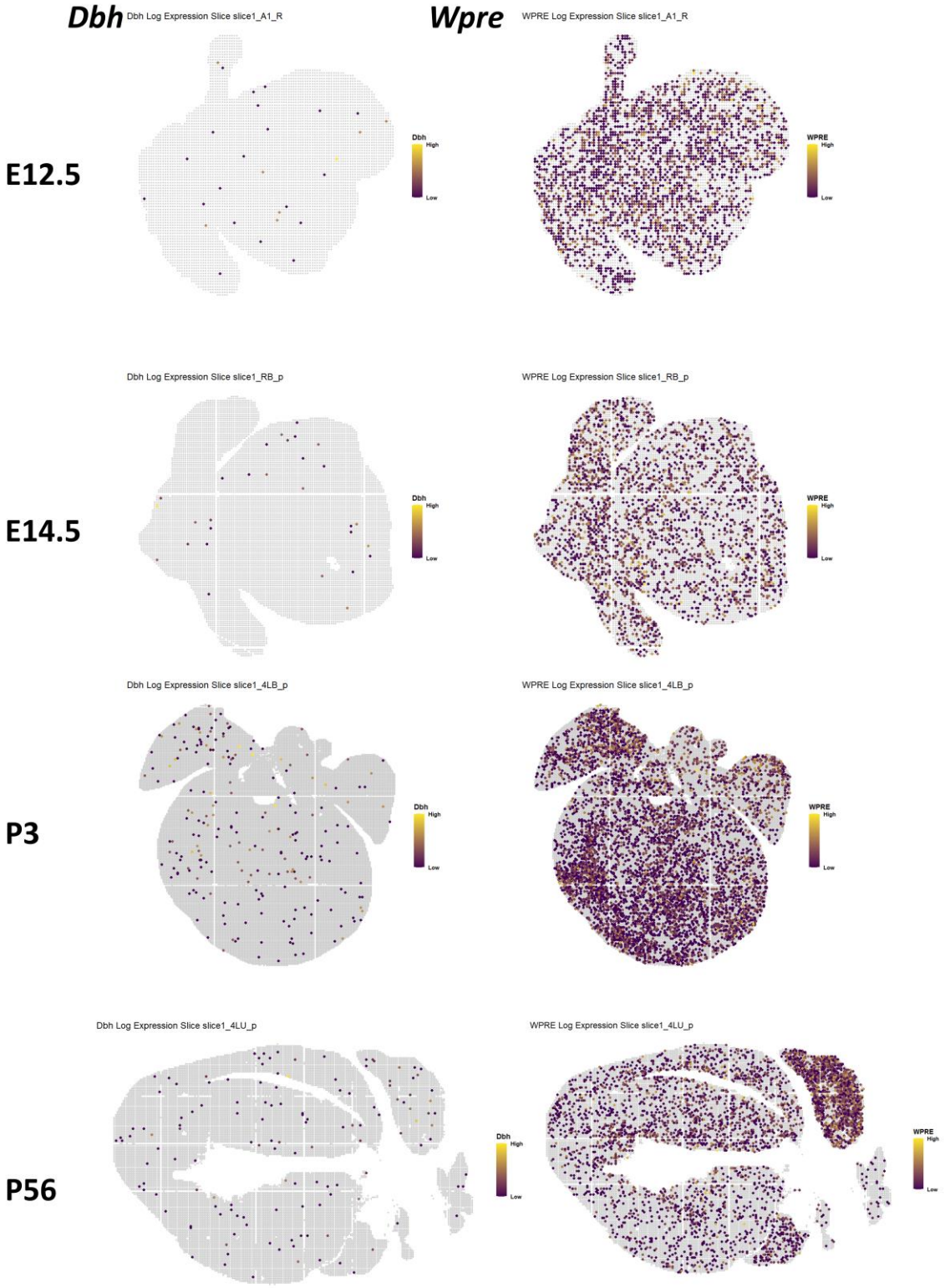

Figure 3-21. Stereo-Seq further supported that Dbh expression was enriched in anatomically-restricted regions of the developing, perinatal, and mature murine heart.

Representatives slices are shown from each stage (E12.5, E14.5, P3, and P56) across rows from top to bottom. Each slice has bins coloured by their expression of either *Dbh* (left column) or *Wpre* (right column).

High gene expression is indicated by yellow and low gene expression is indicated by purple. Expression has been normalised on a per stage basis.

This Figure has been adapted from Sun, Grassam-Rowe et al[2].

Beyond examining the anatomical distribution of these two genes in isolation, we investigated their co-expression with key cardiomyocyte subpopulation markers (Figure 3-22). Broadly, I saw that across the developing and perinatal heart, the Stereo-Seq data agreed with my earlier work to show the co-expression of *Dbh* across both working (AM, VM, Trab-VM) and non-working cardiomyocyte (His-BB) groups (Figure 3-22a). Of note, is that *Wpre* expression was most strong in the SAN and the atrioventricular conduction system and junction (His-BB, AVJ), but was expressed by a higher percentage of all cell types (Figure 3-22a). We also see the same expression pattern anatomically across a representative slice of P3 heart, where *Dbh* has overlapping anatomical expression with certain CCS markers, such as *Cntn2* , *Cacna2d2*, and *Id2* (Figure 3-22b). However, *Wpre* has overlapping expression with these CCS markers and other non-CCS markers (Figure 3-22b). Interestingly, *Wpre* was expressed more strongly in the SAN than the ventricular CCS. This is in contrast to the Dbh expression pattern seen both here and in my earlier scRNA-seq results. This discrepancy may reflect temporal expression differences between *Dbh* and the reporter construct, such that SAN expression might reflect cells that express *Wpre* as a result of once having expressed *Dbh*, but do not express it anymore. Alternatively, it might suggest that ranking on the basis of expression 'strength' is not necessarily an informative process especially when considering different sequencing platforms and techniques.

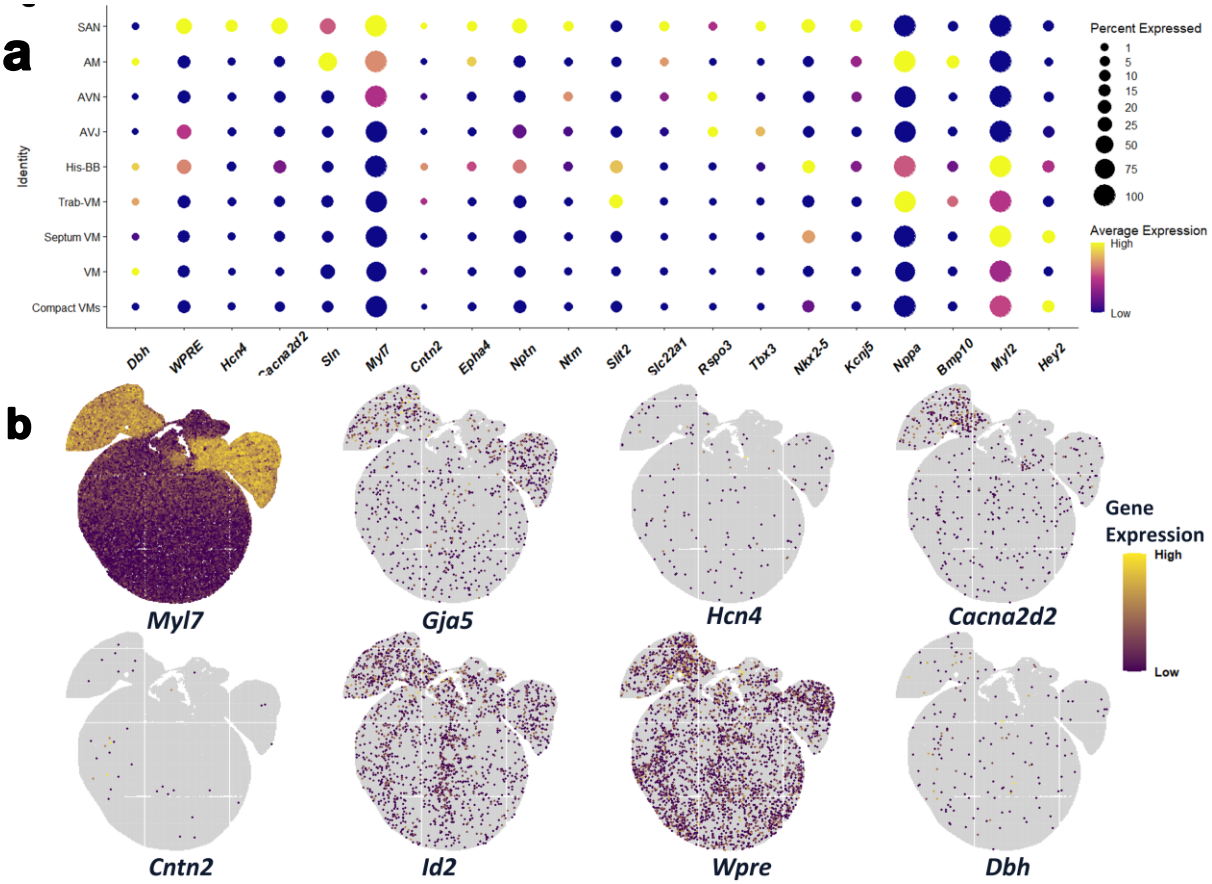

Figure 3-22. Dbh is co-expressed with markers of working and non-working cardiomyocytes within the developing mouse heart, as revealed by Stereo-Seq.

A) A dot plot demonstrates Dbh and Wpre expression and co-expression with cell type marker genes from cardiomyocyte populations clustered from E12.5, E14.5, and P3 Stereo-Seq data. Dots are coloured by average expression of the respective gene in the respective cell type. Dots are sized by percentage of cells expressing each respective gene in each respective cell type. Yellow denotes higher expression, and purple lower expression.

b) Plots of a representative slice from P3 mouse heart describing gene expressions of the respective gene named below each plot. Yellow indicates higher expression and purple lower expression.

Abbreviations: VM – ventricular myocardium; Trab-VM – trabecular ventricular myocardium; SAN – sinoatrial node; AVN –atrioventricular node; AVJ – atrioventricular junction; AM – atrial myocardium; His-BB – His-bundle branch; AM-CCS – atrial cardiac conduction system; PKJ – purkinje fibres; VM-CCS – ventricular cardiac conduction system.

This Figure was adapted from Sun, Grassam-Rowe et al[2].

vi. Wet-lab validation of transcriptomic work

After having now identified and characterised these *Dbh*$^{+}$ and *Dbh*$^{+}$-derived cardiomyocytes at the transcriptomic level, with supporting multi-platform and spatial localisation of the transcriptomic signal, we sought to investigate and validate this signal across more traditional techniques. Using the same *Dbh*^{Cre}/*Rosa26-tdTomato* mouse line, we investigated how *Dbh* was expressed across the developing mouse. As expected, the major signals across the entire embryo were primarily located in the presumedly catecholaminergic neurons of the developing spinal cord and brain stem (Figure 3-23a). However, we also observed tdTomato fluorescence move from the area of the pharyngeal arches ventrally through to heart from E10.5 to E12.5 (Figure 3-23a). We observed the expected tdTomato signal in the developing sympathetic ganglia, yet also identified signal within the sinus venosus: the primordial SAN (Figure 3-23b).

We then sought to confirm whether fluorescence in situ RNA hybridisation (RNAscope) was in agreement with our earlier scRNA-Seq and Stereo-Seq, suggesting overlap of *Dbh* and key CCS markers in terms of current expression rather than the lineage tracing reporter. Not only was *Dbh* expressed across all the anatomical regions of the CCS (sinus venosus, atrioventricular junction, and the innermost ventricular trabeculum), but *Dbh* expression overlapped with key CCS markers *Id2* and *Cacna2d2* as suggested by my earlier work with Stereo-Seq (Figure 3-23d).

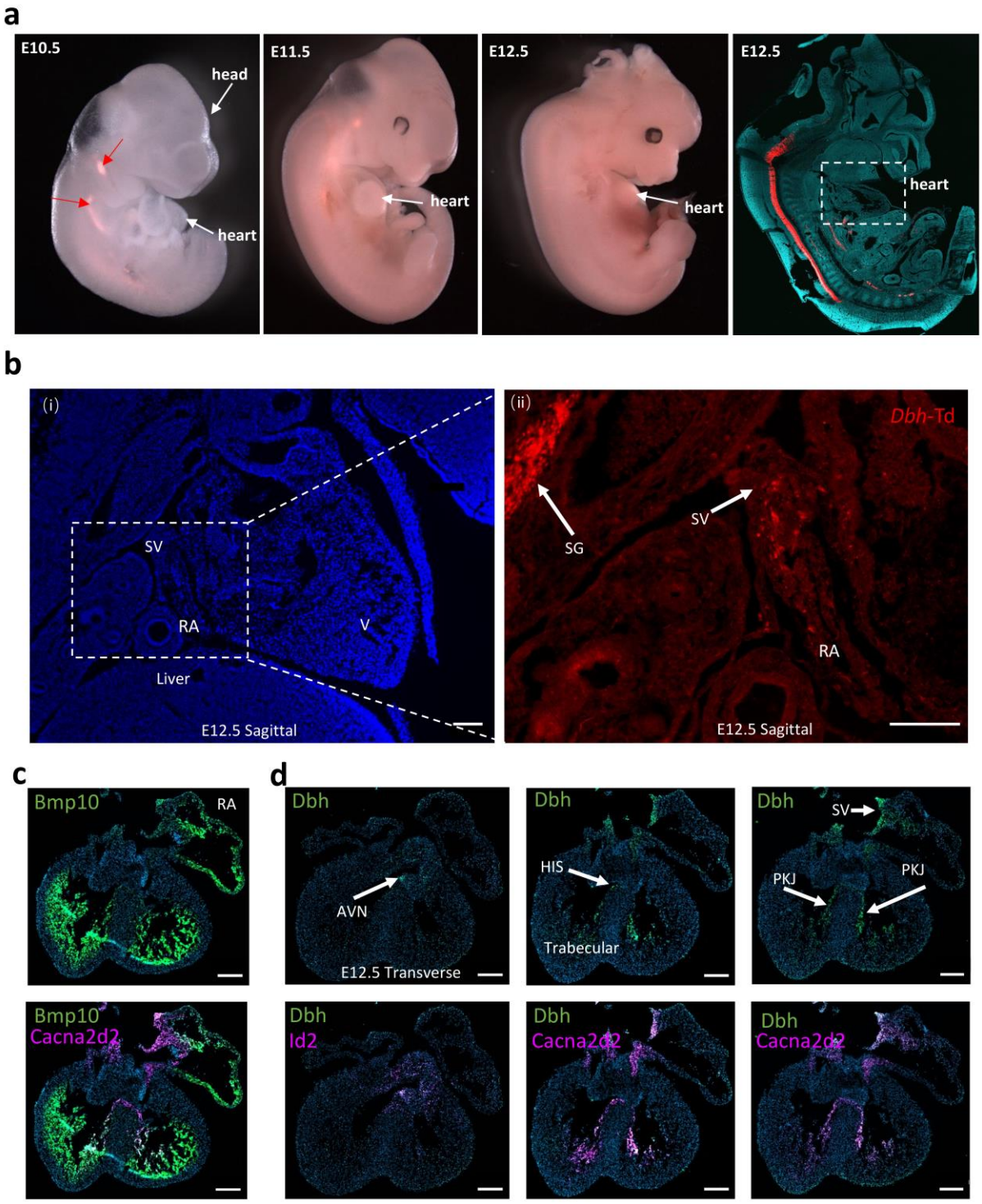

Figure 3-23. Dbh expression was confirmed in the E12.5 mouse heart.

A) Representative images of E10.5, E11.5 and E12.5 whole mouse embryos and sagittal sections demonstrating tdTomato^{+} fluorescence.

B) Representative images demonstrating tdTomato^{+} fluorescence entering the E12.5 heart (i), with strong fluorescence in the developing atria and primordial CCS (ii).

C) Representative RNAscope images supporting our scRNA-Seq and Stereo-Seq predicted expression of known markers (*Bmp10* & *Cacna2d2*).

D) Representative RNAscope images demonstrating the co-expression of Dbh with markers of the CCS (*Id2, Cacna2d2*) within the anatomical regions of the CCS.

200 µm scale bar across all images in this Figure.

Abbreviations: SG - Sympathetic Ganglia, SV - Sinus Venosus, RA - Right Atrium, V - Ventricles, AVN - Atrioventricular node, HIS - His bundle/bundle branch, PKJ - Purkinje fibres.

N.B. The images in this figure were collected by Dr. Sun. However, myself, Dr. Sun, and Prof. Ming Lei, Prof. Nicola Smart, and Prof. Weinan Shou collaborated to plan the experiments and interpret and present the results.

This Figure is adapted from Sun, Grassam-Rowe et al[2].

vii. Postnatal and adult expression and localisation of Dbh-derived cells

Our work had now confirmed that a population of *Dbh*$^{+}$-derived cells entered the heart between E10.5 and E12.5. We now sought to confirm whether these cells were in fact cardiomyocytes and whether this signal persisted beyond the transcriptomic level and beyond the perinatal period.

We first used a new model crossing our *Dbh*^{Cre}/*Rosa26*-tdTomato line with a Cx40-eGFP line. We observed that in the perinatal ventricular trabeculum tdTomato signal was present across both the Cx40^{+} and Cx40^{-} cells (Figure 27a). Cx40 expression in the ventricular trabeculum indicates the Purkinje Fibre network[393]. Thus, supporting that our *Dbh*-derived cells were in fact cardiomyocytes within the CCS.

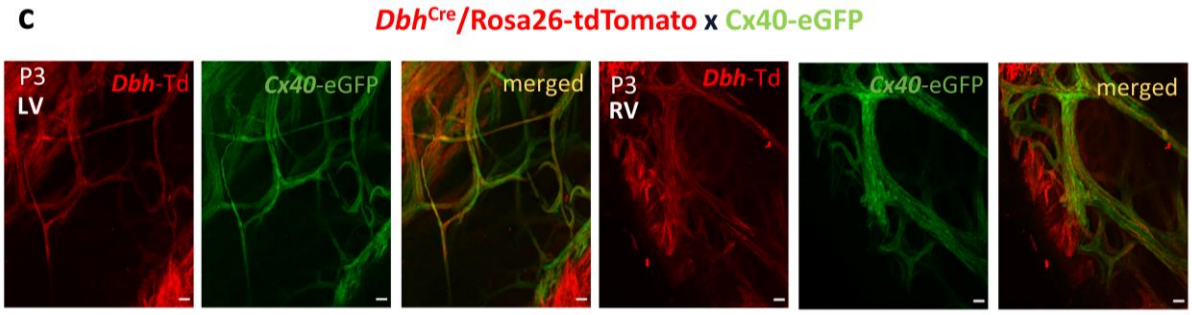

Figure 3-24. Dbh+-derived CMs constitute part of the ventricular CCS.

Representative images of the right and left Purkinje Fibre network with co-expression of tdTomato (*Dbh*$^{+}$-derived CMs) and eGFP (PKJs) in P3 mouse hearts.

N.B. The images in this figure were collected by Dr. Sun. However, myself, Dr. Sun, and Prof. Ming Lei, and Prof. Nicola Smart and Prof. Weinan Shou collaborated to plan the experiments and interpret and present the results.

This Figure was adapted from Sun, Grassam-Rowe et al[2].

We had now identified that *Dbh*$^{+}$-CMs and *Dbh*$^{+}$-derived CMs were present in the adult mouse heart and appeared to be closely associated with the CCS. However, we next sought to confirm that they formed an electrically functional part of the myocardium. We used our Dbh^{Cre}/Rosa26-tdTomato-ChR2 hearts in ex vivo Langendorff perfusion with regional optogenetic stimulation to reveal that *Dbh*$^{+}$-derived CMs did form excitable cardiomyocytes electrically connected to the rest of the myocardium (Figure 3-25a).

Furthermore, we sought to identify whether these *Dbh*$^{+}$-derived CMs were electrophysiologically consistent with being functional components of the CCS, with a particular focus on the

ventricular CCS where we had just established the supporting molecular basis. We assayed ECG reponses to regionally-specific epicardial photostimulation using fibre optic pulses of 470 nm LED-generated blue light on Langendorff-perfused mouse hearts. We sought to identify a positive 'CCS-like' control and a negative 'pan-cardiomyocyte' control and thus compared our *Dbh*^{Cre}/*Rosa26*-tdTomato-ChR2 line against Cx40^{CreERT}/Rosa26-tdTomato-ChR2 and MHC^{Cre}/Rosa26-tdTomato-ChR2 mouse lines building on previous work similarly assaying the ventricular CCS[394,395].

MHC^{Cre}/Rosa26-tdTomato-ChR2 mice displayed reliable responses to photostimulation across all 4 major chambers of the heart (LA, RA, LV, and RV) (Figure 3-25b). However, Cx40^{CreERT}/Rosa26-tdTomato-ChR2 hearts did not respond to epicardial left ventricle pacing, but did respond to all other chambers, as previously described[394,395]. *Dbh*^{Cre}/*Rosa26*-tdTomato-ChR2 hearts responded in a similar manner as Cx40^{CreERT}/Rosa26-tdTomato-ChR2 hearts, yet with a much more variable response in the left atrium (Figure 3-25b). These results match with the expected expression profiles of each gene[393,396], with the endocardial location of the Cx40^{+} or *Dbh*$^{+}$-derived cardiomyocytes being unreachable only through the thick ventricular wall of the left ventricle, which can however still be epicardially activated in the MHC^{Cre}/Rosa26-tdTomato-ChR2 lines, as previously described for the Cx40 line[395].

That the *Dbh*$^{+}$-derived CMs are more similar electrophysiologically to the ventricular CCS than the working myocardium is supported by the significantly longer effective refractory period (ERP) elucidated from epicardial photo stimulation using an S1S2 protocol (Figure 3-25c). This is in line with prior work highlighting the longer action potential duration of the cells of the ventricular CCS compared to ventricular working cardiomyocytes[395,397].

We then sought to use ascertain whether the chemical ablation of the ventricular CCS could alter the response to photostimulation. Using ex vivo Langendorff-perfused mouse hearts we performed right ventricular intracavital injection of a potassium iodide and iodine solution to chemically ablate the ventricular CCS over 5 minutes, as previously described[395,398]. In optimising the technique, I examined the different cavities of the right and left ventricles, through serial cardiac slices and under a dissection microscope, for staining consistent with the exposure to the iodine-containing solution to confirm specific and selective injection into only the right ventricle (data not shown). The selective chemical ablation of the ventricular CCS within the right ventricle ablated the cardiac response to photostimulation in the *Dbh*$^{+}$-derived CMs, and the Cx40^{CreERT}/Rosa26-tdTomato-ChR2 hearts (Figure 3-25d). However, the MHC^{Cre}/Rosa26-tdTomato-ChR2 hearts retained a response to photostimulation (Figure 3-25d). This was expected for the MHC^{Cre} hearts given their unaffected epicardial expression of ChR2. Thus, we provided further evidence that the *Dbh*$^{+}$-derived CMs were more functionally similar to the ventricular CCS than the working ventricular myocardium.

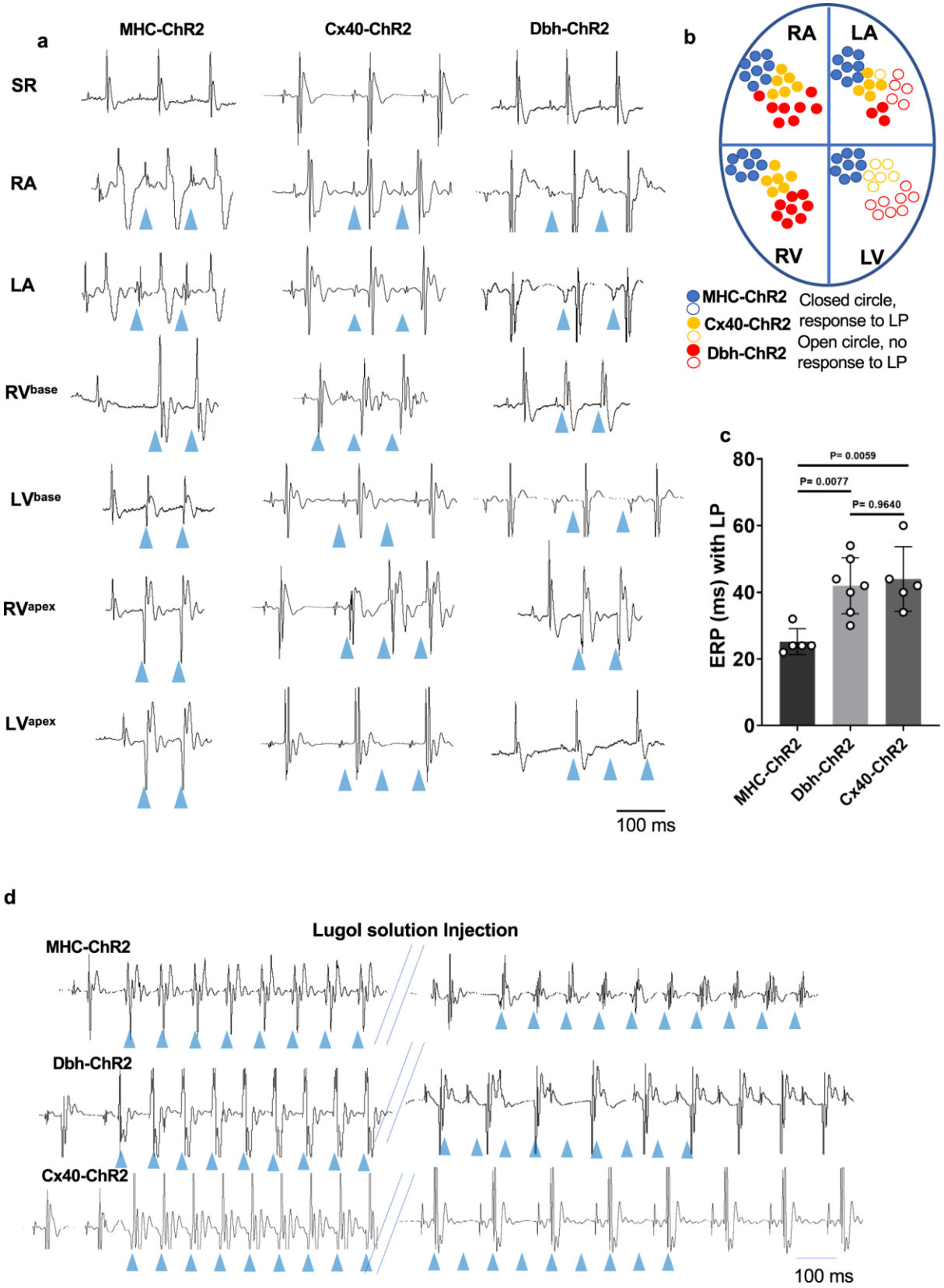

Figure 3-25. Regional optogenetic stimulation supports the electrical connectivity of Dbh-derived CMs with the ventricular CCS.

Representative ECG traces from ex vivo Langendorff-perfused hearts subjected to localized light pacing in 6 different anatomical subregions with blue light. 3 different transgenic mouse models were used with expression of a tdTomato-ChR2 fusion protein under different promoters: MHC (MHC-ChR2), Dbh (Dbh-ChR2) and Cx40 (Cx40- ChR2). Blue light pacing was applied as indicated by blue arrows beneath.

A) Representative ECG recordings demonstrating the response to epicardial blue light stimulation (denoted by small blue arrows) in the respective area of the heart as named for each row, and for each genotype as named in each column.
B) A diagram denotes the different heart chamber responses to regional photostimulation across the different transgenic mouse models.
C) A bar chart of effective refractory periods (ERP) between the transgenic mouse models as elucidated through RV epicardial photostimulation. (n=5-8 per group, * $p<0.05$, ** $p< 0.01$, + $p>0.05$.)
D) Representative ECG traces demonstrating light-induced beats from RV epicardial photostimulation before and 5 minutes after injection of Lugol's solution into the RV lumen (n = 5-6 mice per mouse model). Light pulses are indicated by blue arrows.

Abbreviations: SR - sinus rhythm, LA - left atrium, RA - right atrium, RVbase - right ventricle base, LVbase - left ventricle base, RVapex - right ventricle apex, LVapex - left ventricle apex.

N.B. I constructed this figure in collaboration with Prof. Ming Lei. The underlying data was collected by myself, Dr. Sun, Prof. Ming Lei, and collaborators after myself, Dr. Sun, and Prof. Ming Lei optimised the experimental technique.

This Figure was adapted from Sun, Grassam-Rowe et al[2].

viii. Validation of functional adult significance of Dbh

However, thus far our 'wet lab' investigations had only confirmed details about CMs that either were currently expressing *Dbh* or their progenitors had expressed *Dbh* even transiently. We then used a new Dbh-CFP-FLAG knock-in model to identify real-time expression of *Dbh*. Unfortunately, the CFP signal itself was very weak. However, we used immunostaining against FLAG and CFP instead. We confirmed that both anti-FLAG and anti-CFP signal was present within cardiomyocytes (α-actinin$^+$) at both E14.5 and P56 (Figure 3-26a). However, in the adult P56 hearts, this expression of the CFP-Flag reporter was mostly restricted to the AVN/His bundle region of the atrioventricular junction and was co-expressed with α-actinin indicating that these were cardiomyocytes with active transcription of *Dbh* (Figure 3-26b). To further cross-validate this, we utilised an inducible *Dbh^{CreERT}/Rosa26-tdTomato* mouse line, which after induction at 8 weeks displayed tdTomato signal primarily within the AVN/His bundle region of the atrioventricular junction, with co-expression across α-actinin$^+$ cardiomyocytes (Figure 3-26b). Thus, we had evidence supporting that Dbh expression continued in the adult mouse heart in a manner primarily restricted to the atrioventricular CCS.

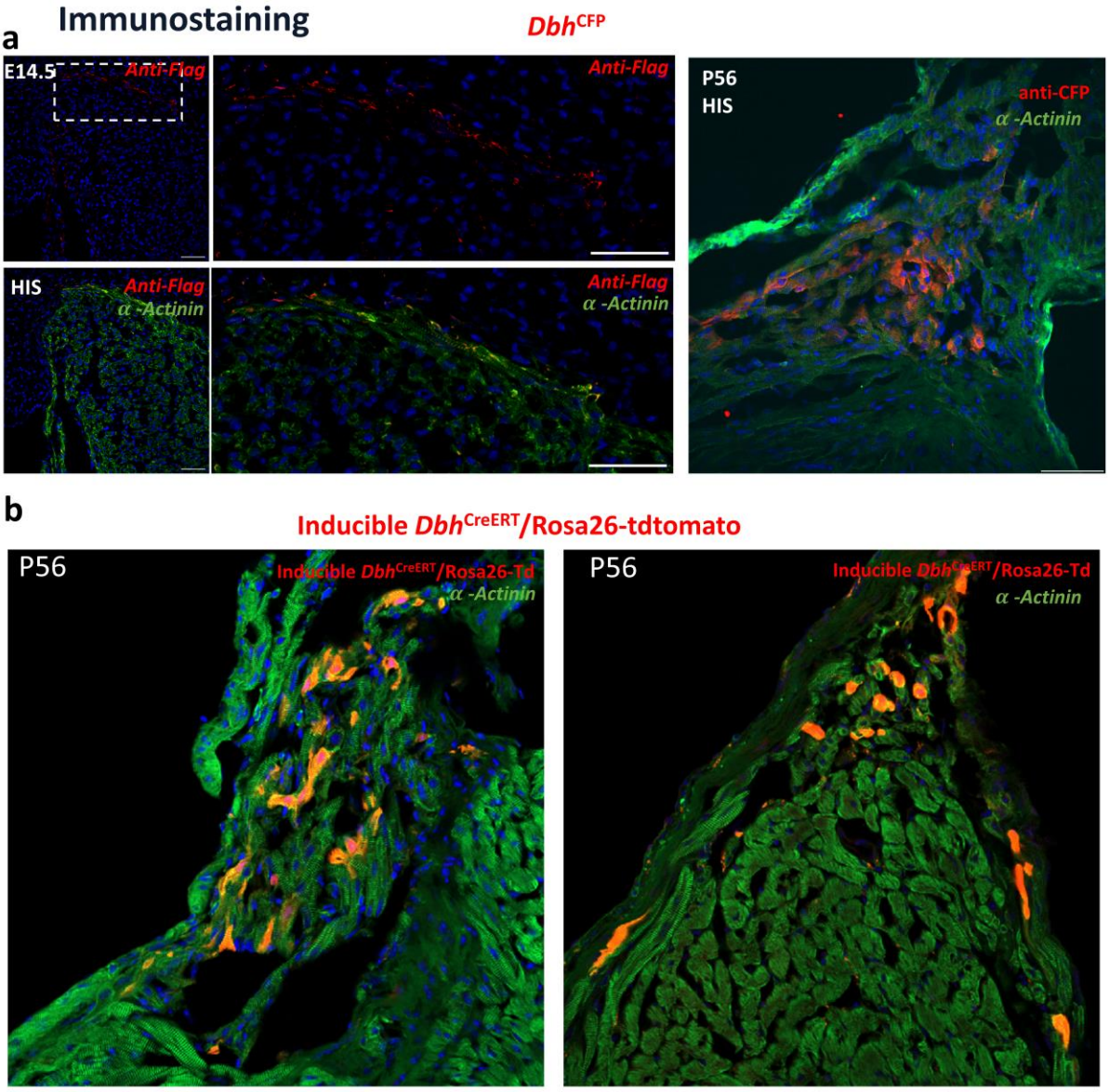

Figure 3-26. Dbh is expressed in the cardiomyocytes of the adult mouse CCS.

a) Representative immunostaining images denote FLAG or CFP co-expression with α-actinin in the AVN/His Bundle in E14.5 and P56 $Dbh^{CFP\text{-}FLAG}$ transgenic mice.

b) Representative immunostaining images denote $tdTomato^{+}$ fluorescence co-expression with α-actinin in the AVN/His Bundle in P56 Dbh^{CreERT}/Rosa26-tdTomato inducible transgenic mice.

N.B. The images in this figure were collected by Dr. Sun (Oxford) or Dr. Pu (Southwest Medical University. China). However, myself, Dr. Sun, and Prof. Ming Lei, Prof. Nicola Smart, Prof. Weinan Shou, and those at Southwest Medical University collaborated to plan the experiments and interpret and present the results.

This Figure is adapted from Sun, Grassam-Rowe et al[2].

After having established the real-time expression of *Dbh* most robustly within cardiomyocytes in the AVN/His Bundle: we sought to understand whether this was associated with catecholamine biosynthetic capabilities. We then utilised traditional chromium salt staining techniques and transmission electron microscopy (TEM) imaging alongside energy dispersive X-ray spectroscopy (EDS) to investigate whether these Dbh^{+}-CMs contained catecholamines. We used microdissection of $tdTomato^{+}$ fluorescing mouse hearts to isolate samples from the AVN/His-

Bundle region rich in Dbh^+-CMs. We confirmed that a small number of cardiomyocytes within these regions contained high-electron density vesicles that were similar in size and content density as those present in the catecholamine-producing chromaffin cells of the adrenal medulla, yet with fewer vesicles per cell (Figure 3-27a-c). EDS confirmed that these vesicles were associated with a chromium signal also similar to that observed in the chromaffin cells, yet with a weaker signal amplitude (Figure 3-27d). Thus, we now had evidence that not only were these regions rich in Dbh^+-CMs, but they also included CMs containing catecholaminergic vesicles.

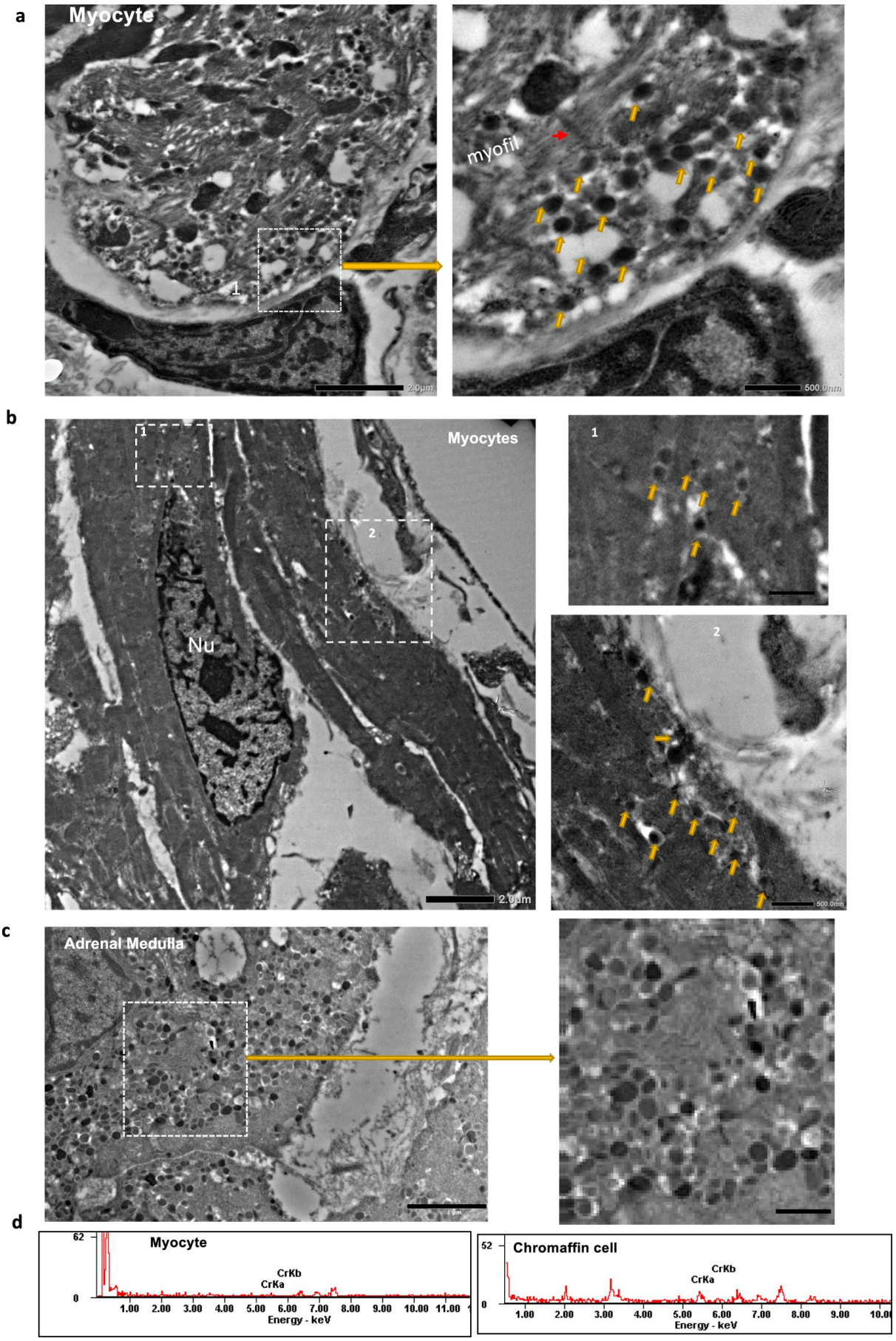
a
Myocyte
1
myofil
2.0µm
500.0nm
b
Myocytes
1
2
Nu
2.0µm
1
2
500.0nm
c
Adrenal Medulla
d
Myocyte
62
0
CrKb
CrKa
1.00 2.00 3.00 4.00 5.00 6.00 7.00 8.00 9.00 10.00 11.00
Energy - keV
Chromaffin cell
52
0
CrKb
CrKa
1.00 2.00 3.00 4.00 5.00 6.00 7.00 8.00 9.00 10.00
Energy - keV

Figure 3-27. CMs in the AVN/His Bundle contain catecholaminergic vesicles, as identified by transmission electron microscopy.

A) Transmission electron microscopy (TEM) imaging of cardiomyocytes identified vesicles with a high-electron density luminal contents. Scale bars: left - 2 μm, right - 500 nm.
B) Transmission electron microscopy (TEM) imaging of cardiomyocytes identified vesicles with a high-electron density luminal contents. Scale bars: left - 2 μm, right - 500 nm.
C) Transmission electron microscopy (TEM) imaging of adrenal medulla chromaffin cells identified vesicles with a high-electron density luminal contents. Scale bars: left - 1 μm, right - 500 nm.
D) Energy dispersive X-ray spectroscopy detected chromium within the contents of the cardiomyocytes albeit at lower levels than that identified in chromaffin cells.

Abbreviations: Nu – nucleus.

N.B. This figure was prepared and data collected by Dr. Sun. However, myself, Dr. Sun, Prof. Lei, and Prof. Xia (Swansea) collaborated to conceive, plan, and interpret the experiments and results.

This Figure was adapted from Sun, Grassam-Rowe et al[2].

Alongside establishing the presence of catecholamines within cardiomyocytes in the AVN/ His Bundle region: we sought to understand whether cardiomyocyte-specific *Dbh* expression had any functional importance within the CCS. We produced $Dbh^{f/f}$ and Dbh^{CKO} mice, with the latter being a conditional knock out of *Dbh* within cardiomyocytes. In vivo ECG revealed no difference (data not shown). However, using ex vivo Langendorff-perfused mouse hearts, we first identified that Dbh^{CKO} hearts have significantly prolonged P-R intervals and thus delayed atrioventricular conduction (Figure 3-28). However, we also used two different electrical stimulation programs to identify that these Dbh^{CKO} hearts were less able to conduct higher frequencies from the atria to the ventricles, as determined by the prolonged atrioventricular effective refractory periods (S1S2) and Wenkebach cycle lengths (S1S1) compared to $Dbh^{f/f}$ hearts (Figure 3-28). Thus, our electrophysiological interrogation revealed that cardiomyocyte-specific *Dbh* expression is redundant for rhythmogenesis, but contributes to normal atrioventricular conduction.

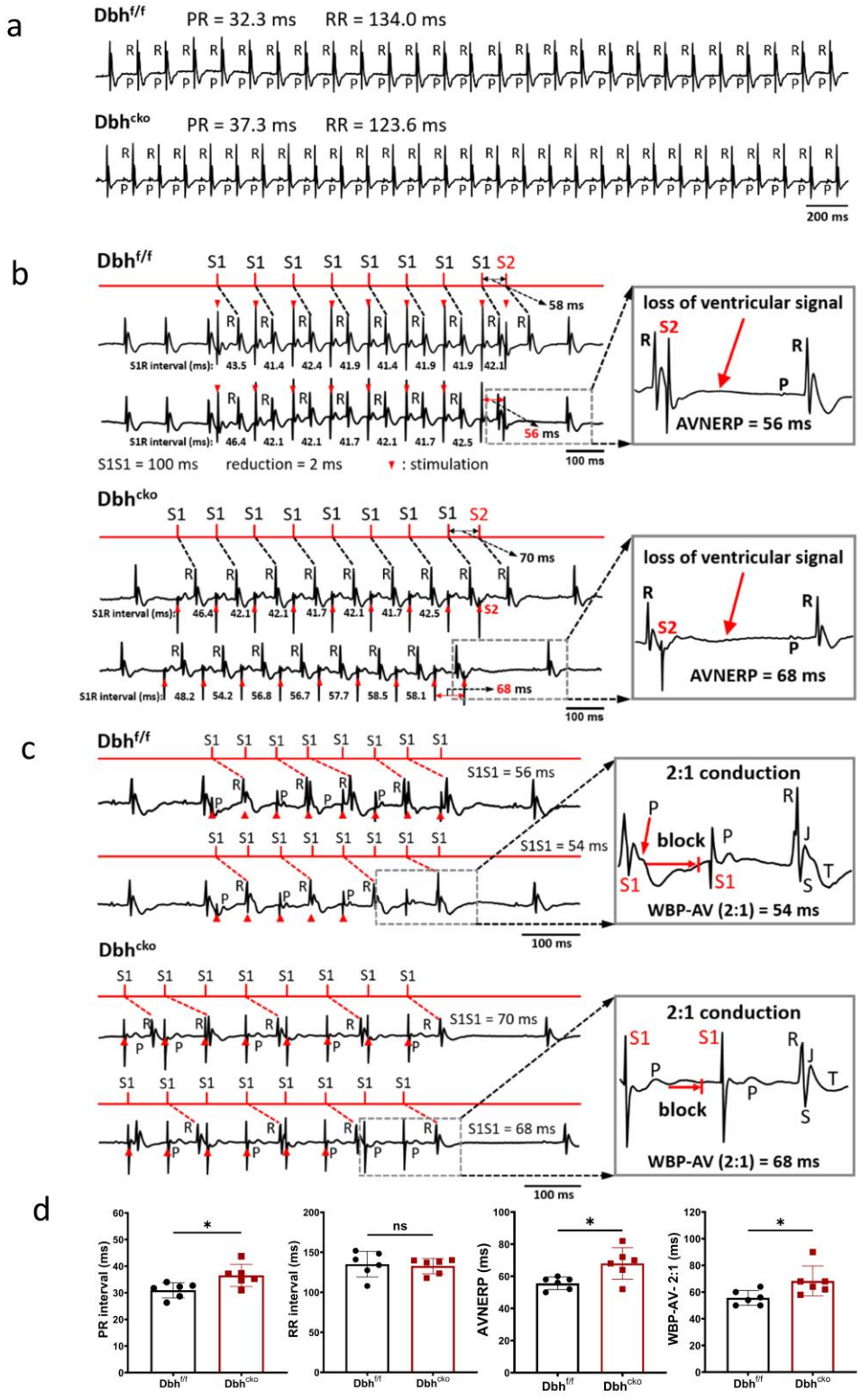

Figure 3-28. Cardiomyocyte-specific expression of Dbh is redundant for cardiac rhythmogenesis but necessary for normal intracardiac conduction ex vivo.

A) Representative ECG recordings from ex vivo Langendorff-perfused Dbh^{cko} and Dbh$^{f/f}$ mouse hearts.

B) Representative ECG traces from S1S2 electrical stimulation of the atria to determine the AVNERP as the ventricular response to S2 is lost at the AVNERP.

C) Representative ECG traces from S1S1 electrical stimulation of the atria to determine the Wenckebach cycle length at which 1:1 coupling of ventricular response to atrial stimulation is lost.

D) Plots demonstrating the comparison of P-R, RR intervals, AVNERP and Wenckebach cycle length between Dbh^{cko} and $Dbh^{f/f}$ hearts. n=6 per group, * $p<0.05$, ** $p< 0.01$, + $p>0.05$ – Student's t-test.

The data in this Figure was collected, analysed, and presented by collaborators from Southwest Medical University China. However, I collaborated to conceive and interpret the experiments and results.

This Figure was adapted from Sun, Grassam-Rowe et al[2].

d. Discussion:

I integrated a range of computational transcriptomic techniques, with the collaborative conception, planning, execution, analysis, and interpretation of a range of supporting structural and functional interrogations to identify and characterise the cardiomyocyte-specific expression of *Dbh* within the cardiac conduction system.

I built upon existing best practice to produce a scRNA-Seq analytical workflow that enabled me to discriminate transcriptomically similar cell types, such as discerning non-working cardiomyocytes from their anatomically proximate working counterparts. Many others have produced similar transcriptomic landscapes of the developing mouse heart, but our work here has the advantage of unbiased cell sampling across a broad developmental time point, and is coupled with, to our knowledge, the highest-resolution and largest field-of-view spatial transcriptomics technique – Stereo-Seq, which enabled us to use the anatomical ground truth to support our scRNA-Seq findings. Our droplet-based scRNA-seq protocol, in comparison to well-based sequencing approaches used by others to investigate the developing CCS, provided a large dataset, albeit with some compromise on sequencing depth which is typical for droplet-based scRNA-Seq. My cardiac-focused analytical pipeline enabled me to identify rare cell types discretely, whereas others have relied typically on biased sampling techniques such as microdissection. However, certain populations I identified, such as the AM-CCS, did not have a clear mapping to known populations. AM-CCS, for example, had expression of a mixture of atrial (*Myl7* and *Myl4*) and CCS molecular markers. AM-CCS might represent either interatrial conduction pathways, or perhaps part of the transition zone of the SAN, where the pacemaker cells meet the surrounding working atrial CMs, given its low expression levels of canonical and novel SAN markers (*Shox2*, *Smoc2*, *Hcn4*, and *Pcdh17*) but high expression of transition zone-associated markers (*Dkk3* and *Scn5a*)[350]. Another cell group of interest is the 'Endocardial gene-rich cardiomyocytes'. This group expresses a range of markers indicative of a cardiomyocyte transcriptional program, but with other markers such as *Tmsb4x7* and *Flt1* that are more associated with signalling to and from endocardial, endothelial and other vascular components in the heart[399,400]. This population of $Tmsb4x^{hi}$ cells has been identified and noted as 'heterogenous' by others in cardiac scRNA-Seq[274]. However, their analyses suggests that this expression was highest in the non-cardiomyocyte vascular populations of the developing chick heart[274]. Whether this reflects a species-specific difference, or perhaps a different in sequencing technology and analysis, remains to determined. This population remains of interest given the importance of the gene product of *Tmsb4x* (thymosin β4) as a putative regulator of cardiac regeneration in the adult heart[274,401,402]. Thus, while I have investigated a particular aspect of this dataset: future work should further characterise the other signals present in the data.

Through our integrated scRNA-Seq and Stereo-Seq investigations, I contributed to the evidence base surrounding current analytical techniques integrating the two. To reduce the impact of bias, I used both unsupervised and supervised machine learning techniques to try and map from our scRNA-Seq data to our Stereo-Seq data. This integration of the two different but related data types is a nascent field, and this was reflected in the promising but imperfect results achieved through using supervised machine learning techniques to map from scRNA-seq data to Stereo-Seq. Ultimately, the next steps with our work could have included a comparison between the transcriptional feasibility of the cell types identified by the unsupervised and supervised approaches. I believe the most likely areas for improvement in this space will come from including a 'human feedback' or prior knowledge element to computational techniques attempting to integrate these two datasets, which has some promise in other machine learning applications[403]. Until then, perhaps the use of combinatorial scoring based on the top most likely cell-type predictions for a spot could produce simple-to-implement improvements. This is a rapidly expanding space from both the perspective of both sequencing and analytical techniques, and will likely see effective solutions as the community reaches consensus on what are acceptable compromises between accuracy and complexity of the solution. Overall, our use of these unbiased transcriptomic approaches empowered us to creatively but systematically explore and 'prune' hypotheses before committing to resource-intensive generation of transgenic mice and traditional 'wet-lab' experimentation.

We originally speculated whether the tdTomato^{+} E10.5 – E12.5 pharyngeal arch population might be a neural crest population as the progenitors of our *Dbh*$^{+}$-derived CMs. However, after attempts led by myself and Mr. A. Lipov, to perform RNA velocity-based assessments of origin for our *Dbh*$^{+}$-CMs (data not shown), we were unable to conclude any difference in origin between *Dbh*$^{+}$-CMs and other CMs. However, this is most likely the result of a lack of information captured in the scRNA-Seq dataset, rather than evidence either supporting or disproving this suggestion. On balance, others who have previously suggested neural crest differentiation into cardiomyocytes, particularly those in the CCS, have since been disproved and thus it is unlikely that this is the origin of these cells. However, future work remains to determine their origin, and what transcriptional programs are associated with this expression of *Dbh*.

We then specifically examined whether cardiomyocyte-specific expression of *Dbh* was of any importance to the heart. We produced an *Dbh* conditional knock-out model specific to cardiomyocytes. In vivo ECG suggested no difference between the *Dbh*^{CKO} and the control *Dbh*$^{f/f}$ mice. However, our ex vivo ECG with selected pacing protocols did reveal a difference between the two hearts, with impaired atrioventricular conduction in the *Dbh*^{CKO} model. It is possible that this disparity reflects the interaction of the sympathetic nervous system and the heart to maintain appropriate conduction in the intact heart, but with the sympathetic nervous system unable to do so in the Langendorff-perfused ex vivo preparation . This might reflect a role of local catecholaminergic cardiomyocyte signalling interacting with the neuro-cardiac axis to maintain appropriate cardiac conduction. Of note is that despite the enrichment of the SAN with *Dbh*$^{+}$-derived CMs and *Dbh*$^{+}$-CMs, cardiomyocyte-specific *Dbh* expression was redundant for rhythmogenesis in both in vivo and ex vivo preparations. However, our Dbh^{CKO} results might also reflect some defect arising during development from the lack of cardiomyocyte-specific *Dbh* expression, and future work should determine whether inducible CreERT models replicate these findings with post-natal or adult induction.

In support of the hypothesis that the effects of our *Dbh*^{CKO} model are being mediated through impaired cardiomyocyte catecholamine production, we identified that the atrioventricular

junction of the P56 adult mouse heart did contain cardiomyocytes with vesicles similar in content and morphology as the catecholaminergic vesicles of the adrenal medulla. However, we do not yet know whether these cardiomyocytes are able to secrete these vesicles, or their specific contents in terms of catecholamines. We are not the first group to imply that cardiomyocytes might play a role in local signalling mediation for the autonomic nervous system. However, previous suggestions have focused on acetylcholine, which is the canonical transmitter of the parasympathetic nervous system, and requires a much less complicated biosynthesis and storage solution than catecholamines[404]. Certainly, given the primarily antagonistic interactions between the parasympathetic and sympathetic innervations of the heart, that there might be additional signalling modulation independent of higher neural control is a stimulating suggestion. There has been a rapidly growing body of work highlighting the role of local sympathetic signal modulation in adipose tissue, and it is tempting to speculate that our modern tools with increasing resolution may lead us to discover a wide range of similar more fine-grained local regulatory systems than previously known. However, this work remains to be done.

The putative importance of cardiomyocyte catecholamine production opens a number of questions across physiology and pathophysiology. Cardiac noradrenaline release locally from sympathetic neurons, and with endocrine adrenaline from Chromaffin cells, contributes to regulating cardiac output across changing physiological states. Yet, a number of acute and chronic cardiovascular diseases have inappropriate cardiac catecholamine release implicated in their pathophysiology, such as myocardial infarctions, heart failure, and arrhythmias and sudden cardiac death[197,405,406]. In particular, Dbh appears to be important for a range of physiology and pathophysiology. $Dbh^{-/-}$ mice are bradycardic, hypotensive, and do not appropriately mount a cardiovascular response to exercise[407]. There have also been a limited number of DBH deficient humans reported in the case literature, who have displayed orthostatic hypotension and rarely sudden cardiac death with a fibrotic CCS[408]. However, our work is the first to examine cardiomyocyte-specific Dbh deficiency, which might explain the discrepancy as to why globally Dbh-deficient mice displayed bradycardia and ours did not, as the persistent neuronal production of catecholamines provided redundant catecholaminergic tone in our mice. Our Dbh^{+}-CMs have potential ramifications in a number of pathologies and interventions, such as catecholaminergic polymorphic ventricular tachycardia, heart failure, atrial fibrillation, and post-orthotopic heart transplants. For example, there is a great degree of heterogeneity across individuals with atrial fibrillation and their propensity for developing a ventricular response to rapid atrial fibrillatory waves. Perhaps heterogeneity in Dbh^{+}-CMs distributions in the atrioventricular junction contribute to this. Finally, given the noted reversion of many transcriptional programs to a more fetal-like program in heart failure, and the wide expression of *Dbh* across the heart in our embryonic and fetal samples, it is tempting to speculate whether there might be any wider cardiac reactivation of the *Dbh* transcriptional program in heart failure. There is much work to be done to follow-up this discovery, replicate with orthogonal techniques, and ascertain the basic biology of this putative cell type, the *Dbh* cardiomyocyte transcriptional program and its clinical implications.

Chapter 4. Transcriptional signatures of murine and hiPSC atrial development and differentiation.

a. Introduction

This section is introduced in Chapter 1B & C.

Key transcriptional regulators have been identified in the developing atria, and their pro-atrial effects characterised – primarily through looking at several key genes of interest[267,268,271,325,409,410]. However, little work has focused on applying larger transcriptional efforts to understanding the transcriptional networks of cardiac development in the atrial-specific context. Beyond the putative importance of this in understanding atrial disease directly, there is great promise in leveraging insights from native atrial transcription networks to better identify pathways of interest for the directed specification and differentiation of hiPSC-AMs. Comparing and contrasting transcriptional networks between native atria and hiPSC-AMs may reveal such insights. This work builds primarily on our earlier work in the Lei Group to produce our hiPSC-AM differentiation method[1], and that of those who have developed the field of cardiac single-cell RNA sequencing with a goal of understanding both development and its applications to hiPSC-CMs in the ventricular context[266,267,269,270,274,277,349,357,371,373,390,411,412].

b. Methods

THE RELEVANT METHODS FOR THIS CHAPTER ARE DESCRIBED IN CHAPTER 2A AND B:

c. Results

i. The working myocardium forms transcriptomically distinct atrial and ventricular lineages.

To investigate atrial-specific transcriptional networks, I filtered our scRNA-Seq dataset to better discriminate the specific atrial and ventricular cardiomyocyte lineages (Figure 4-1a). Prior to E12.5, the atrial and ventricular lineages were mostly indistinguishable in transcriptomic space. However, from about E12.5, I could start to ascertain distinct atrial and ventricular populations (Figure 4-1). These populations could be separated into their distinct trajectories from origin to final atrial or ventricular fate using in silico techniques that map distinct curves onto the manifold structure of the populations in transcriptomic space (data not shown)[413].

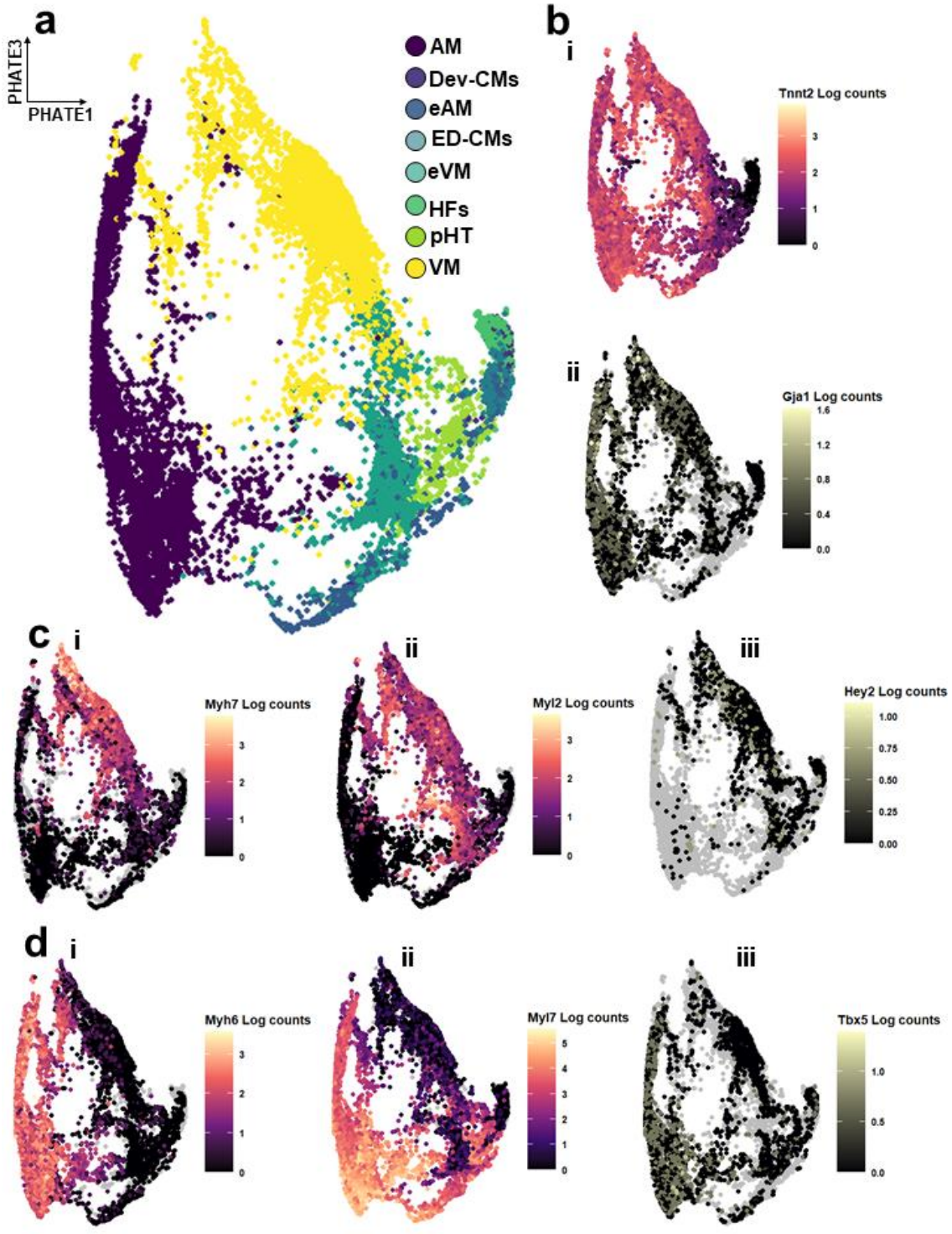

Figure 4-1. Working cardiomyocytes form distinct atrial and ventricular lineages.

A) A PHATE plot of the working cardiomyocyte populations forming atrial and ventricular lineages. Labels indicate the cell type with the corresponding colour on the PHATE plot, with full names below.

B) i) A PHATE plot coloured by log counts of Tnnt2 expression – a common cardiomyocyte marker. ii) A PHATE plot coloured by log counts of Gja1 expression – a common cardiomyocyte marker.

C) i) A PHATE plot coloured by log counts of Myh7 expression – a ventricular marker. ii) A PHATE plot coloured by log counts of Myl2 expression – a ventricular marker. iii) A PHATE plot coloured by log counts of Hey2 expression – a ventricular marker.

D) i) A PHATE plot coloured by log counts of Myh6 expression – an atrial marker. ii) A PHATE plot coloured by log counts of Myl7 expression – an atrial marker. iii) A PHATE plot coloured by log counts of Tbx5 expression – an atrial marker.

Abbreviations: VMs – ventricular cardiomyocytes; AMs – atrial cardiomyocytes; pHT – primary heart tube; ED-CMs – endocardial gene-rich cardiomyocytes; Dev-CMs – developing cardiomyocytes; HFs – heart fields; eAMs – early atrial cardiomyocytes; eVMs – early ventricular cardiomyocytes.

ii. The developing atria from E12.5 to P3 display maturation across a range of genes key to cardiomyocyte function.

After establishing an atrial lineage in our cardiomyocyte scRNA-Seq data: I used a filtered atrial-specific lineage to characterise 4 key components of mature cardiomyocytes: calcium handling, action potential morphology, metabolism, and chamber-specific markers. To overcome gene dropout, a common artefact of RNA sequencing methods, I utilised a biologically rational imputation method[366] to recover expression. Our data reveal that the period between E14.5 and E16.5 appears to be the major inflection point for maturation-associated transcriptional changes (Figure 4-2). I observed perinatal upregulation of genes across calcium handling, membrane currents, metabolism, and key atrial marker genes (Figure 4-2). Figure 4a shows upregulation of *Ryr2*, *Atp2a2*, and *Casq2* – suggesting maturation of sarcoplasmic reticulum calcium uptake and release. Potassium channels are a key contributor to the unique atrial action potential[414-416] and I observed upregulation of key atrial specific I_{KACh}-encoding *Kcnj3* and *Kcnj5* as the atria mature perinatally (Figure 4-2bii,iii). However, even with imputation, certain more weakly expressed genes could not be well recovered in the expected fashion – such as *Kcna5*. Given the importance of metabolic maturation in the heart – of particular interest is the upregulation of fatty acid-handling genes in the atria *Fabp3* and *Fabp4* (Figure 4-2ci,ii) and the perinatal switch from *Cox8a* to *Cox8b* (Figure 4-2cv,vi). Counterintuitively, some atrial development-associated transcription factors, such as *Tbx5* and *Gata4* appeared to be most strongly expressed in the E16.5 – P3 range, rather than earlier in the atrial lineage.

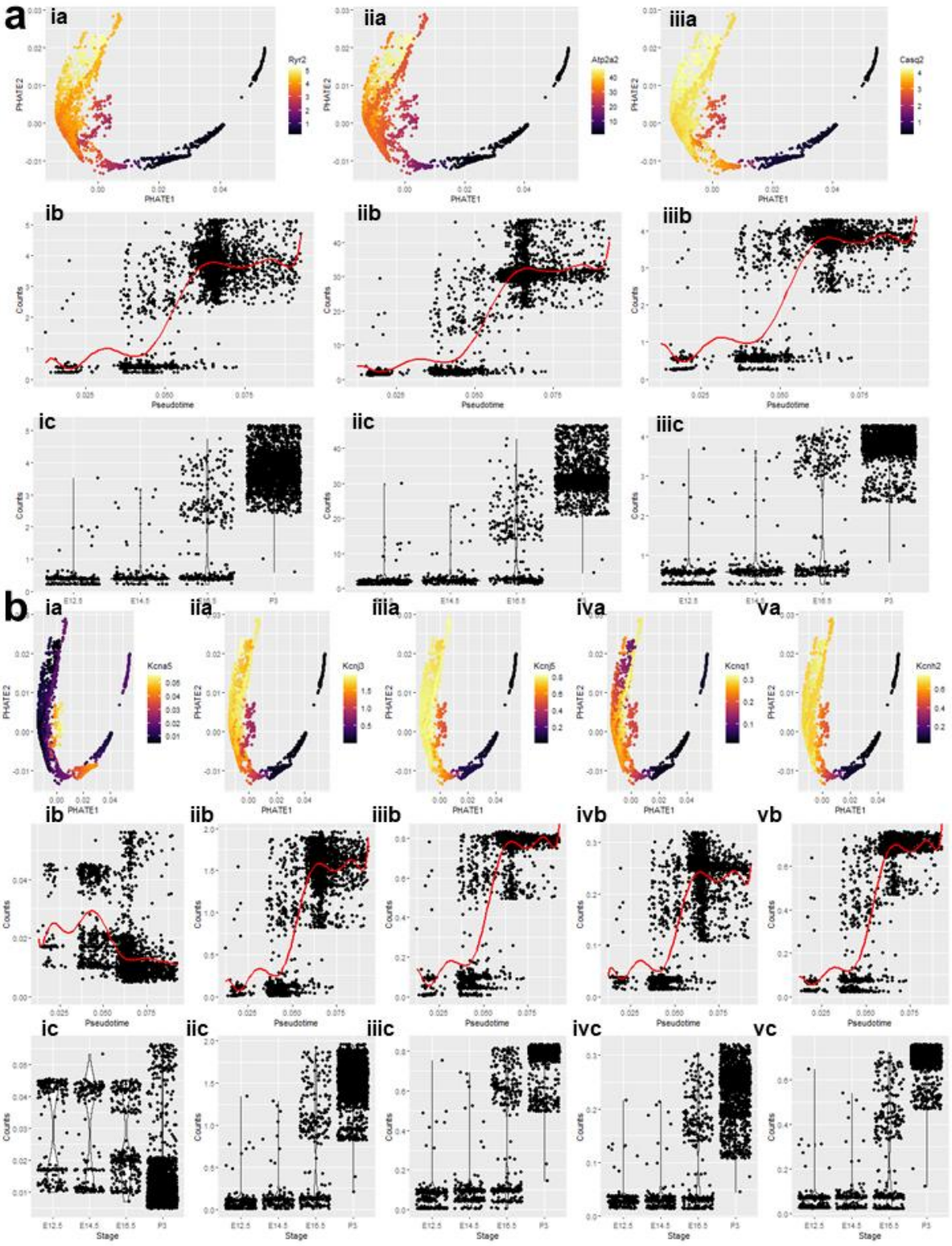
a
ia
iia
iiia
ib
iib
iiib
ic
iic
iiic
b
ia
iia
iiia
iva
va
ib
iib
iiib
ivb
vb
ic
iic
iiic
ivc
vc
PHATE1
PHATE2
Pseudotime
Counts
Stage
Ryr2
Atp2a2
Casq2
Kcna5
Kcnj3
Kcnj5
Kcnq1
Kcnh2
E12.5
E14.5
E16.5
P3

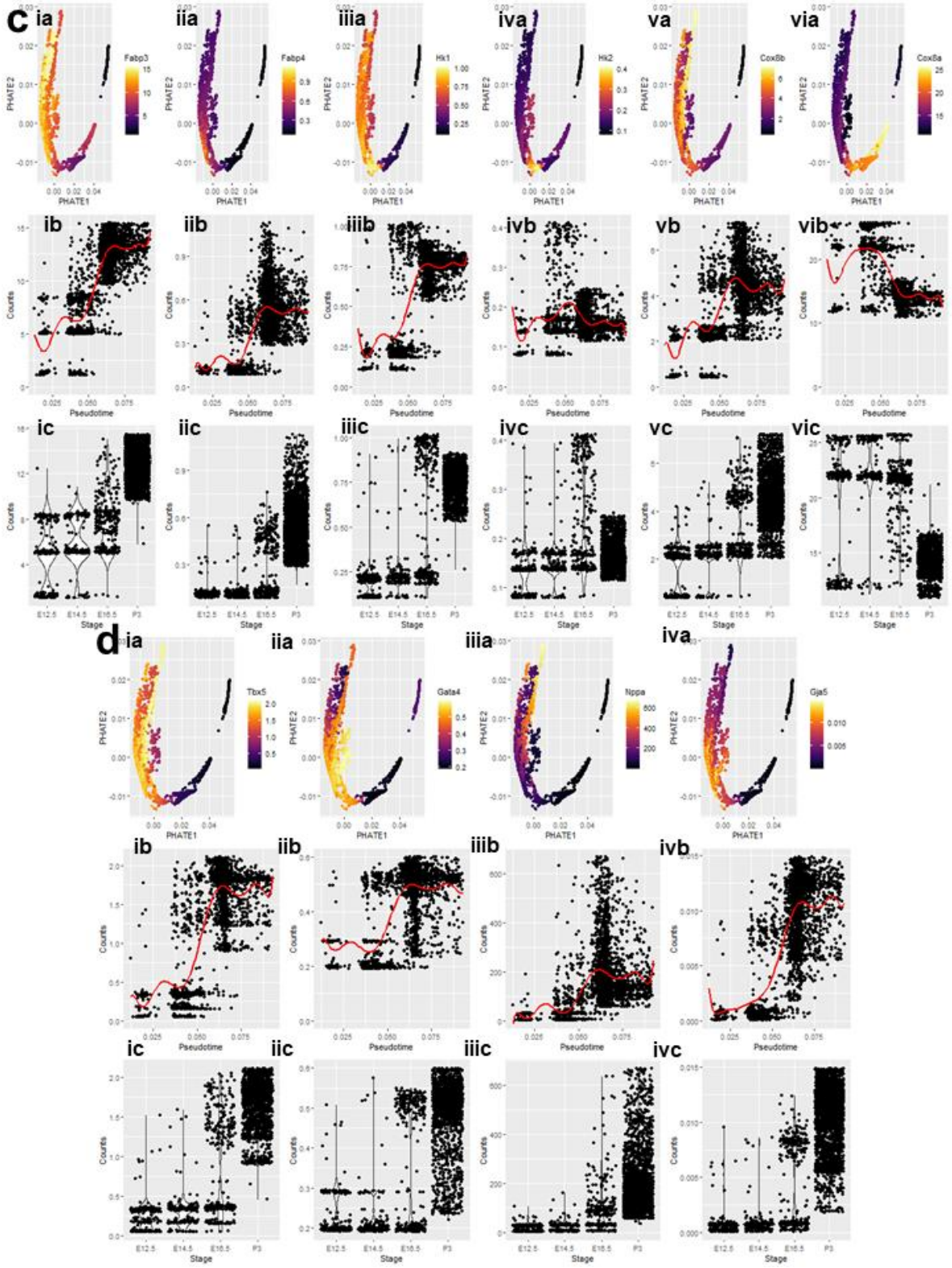

Figure 4-2. The developing atria from E12.5 to P3 display maturation across a range of genes key to cardiomyocyte function.

A) The top row are PHATE plots of the atrial lineage from E12.5 to P3, coloured by the recovered expression of specific calcium-handling genes denoted for each column by the colour bar legend – the x and y axes represent 2D PHATE space. The middle row contains scatter plots demonstrating the same gene expression against pseudotime with average expression approximated by a polynomial shown in red.

The bottom row plots the same gene expression as a violin plot across developmental stages (E12.5, E14.5, E16.5, P3). i) *Ryr2* ii) *Atp2a2* iii) *Casq2*

B) Same plots as in A, but for potassium channel-encoding genes: i) *Kcna5* ii) *Kcnj3* iii) *Kcnj5* iv) *Kcnq1* v) *Kcnh2*.
C) Same plots as in A, but for metabolic genes: i) *Fabp3* ii) *Fabp4* iii) *Hk1* iv) *Hk2* v) *Cox8b* vi) *Cox8a*.
D) Same plots as in A, but for atrial marker genes: i) *Tbx5* ii) *Gata4* iii) *Nppa* iv) *Gja5*.

iii. Distinct gene modules regulate general proliferation and 'atrialization' in the developing murine atria.

Cellular processes are rarely defined by changes in expression of a single gene, particularly in development. To best understand the maturation of the atria, I identified the differentially expressed genes across maturation and used a range of in silico techniques to reveal that they formed 4 major modules of interacting transcription factors (TFs) and the genes they regulate (Figure 4-3a, Table 4-1). Modules 1 and 2 regulate a range of processes associated with cell growth and differentiation, such as transcription and proliferation (Figure 4-3b). Modules 3 and 4 regulate specific cardiomyocyte differentiation and specialisation (Figure 4-3b). However, there is some overlap between these two distinct 'meta-modules' around more general processes (Figure 4-3b). The TFs within these modules include well-established regulators of atrial development, such as the master regulator of the atrial transcription program – *Nr2f2*. However, it also reveals new potential relationships between such well-characterised TFs in cardiac development and TFs such as *Ppargc1a* – which has only recently been implicated in its role driving cardiomyocyte development and maturation[417,418]. There are a number of potential relationships here that mandate further in silico validation, followed by establishing their interactions in vitro and in vivo. However, this work provides a sufficient basis for further study of these networks in atrial development.

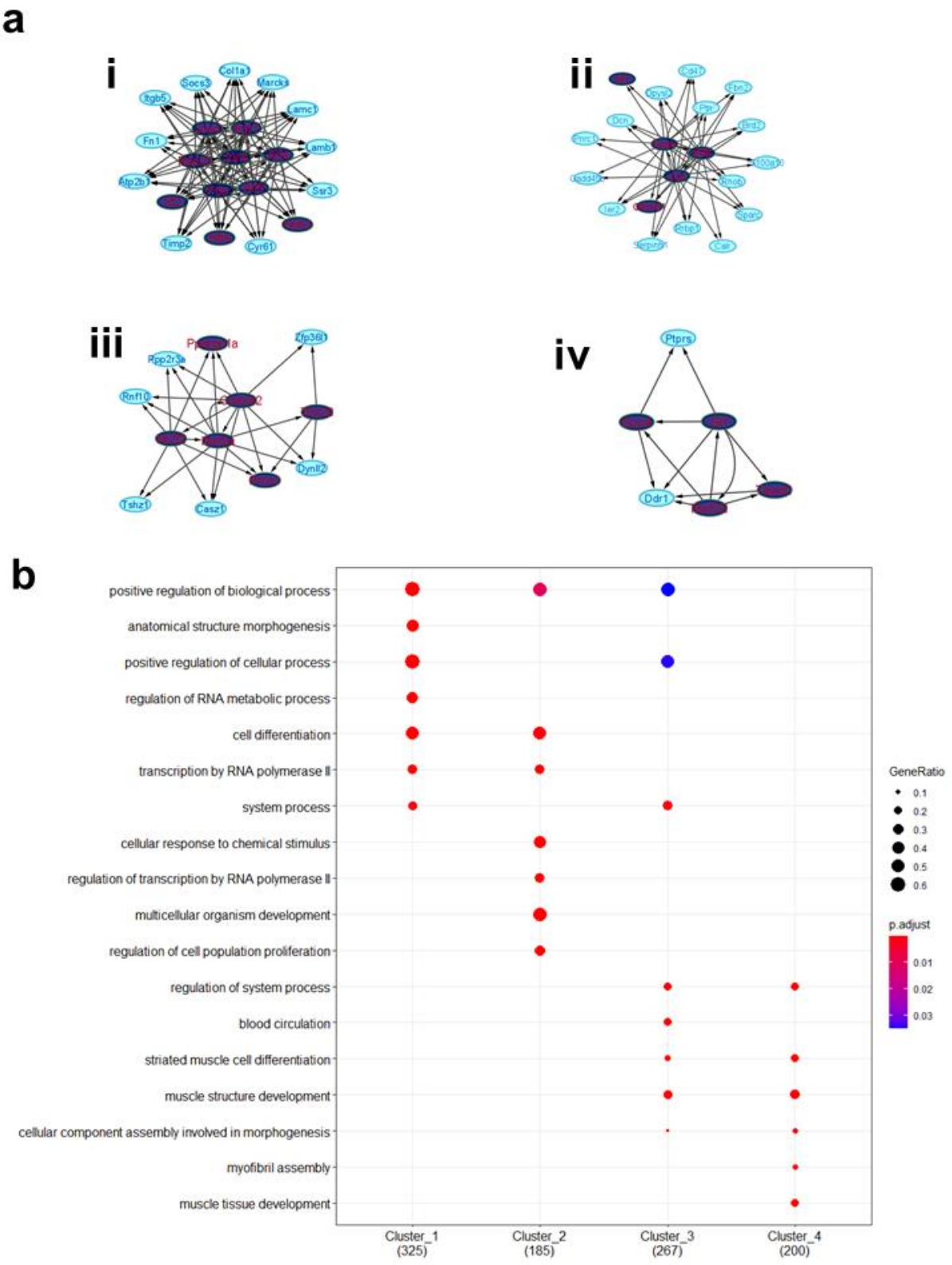

Figure 4-3. Distinct gene modules regulate growth and 'atrialization' in the developing murine atria.

A) Modules of interacting genes identified as distinct sub-modules from network analysis of gene co-expression. Arrows indicate downstream regulation along the direction of the arrow. Transcription factors are coloured in dark blue with red text. Non-transcription factors are coloured in light blue with blue text. i) Cluster 1. ii) Cluster 2. iii) Cluster 3. iv) Cluster 4. Genes are listed in Table 2.

B) Gene ontology (GO) analysis showing commonly enriched GO terms for between modules in each column. GeneRatio refers to the ratio of genes present in the respective GO term per respective total genes in a module. p.adjust is the adjusted p-value for enrichment, following post-hoc Benjamini-Hochberg adjustment. The number under each cluster name represents the number of genes in each cluster.

Module/Cluster	TFs	Downstream
1	*Jund, Egr1, Klf4, Junb, Rad21, Fos, Id2, Atf3, Nfia, Hes1*	*Itgb5, Col1a1, Socs3, Marcks, Lamc1, Lamb1, Ssr3, Cyr61, Timp2, Atp2b1, Fn1*
2	*Id1, Fosb, Klf6, Jun, Ctnnb1*	*S100a10, Rhob, Sparc, Calr, Rrbp1, Serpinh1, Ier2, Gadd456, Pnrc1, Dcn, Dpysl, Cd17, Ptn, Fbn2, Brd2*
3	*Ppargc1a, Creb3l2, Tbx20, Mef2a, Prox1, Nr2f2*	*Zfp36l1, Ppp2r3a, Dynll2, Casz1, Tshz1, Rnf10*
4	*Srf, Sox4, Mef2d, Tead1*	*Ptprs, Ddr1*

Table 4-1. The genes within the clusters identified in Figure 3-4.

Column 1 represents the row-wise cluster identifier. Column 2 represents the transcription factors in each cluster. Column 3 represents the genes identified as most closely downstream of the transcription factors.

iv. Transcriptional characterization identifies a more robust atrial transcriptional program in GREMLIN-2/retinoic acid-treated cells

We then sought to characterise the transcriptomic signature of the hiPSC-AMs in greater detail compared to the control mixed hiPSC-CM control. We utilised scRNA-Seq on >300 cells from each group. We used a different cassette of atrial-specific genes to cross-validate our previous use of NR2F2 as a marker of the broad efficacy of atrial specification, which was largely in agreement at 71% of the experimental group having high expression of *HEY1*, *MYL7*, *HOXA3*, and *SLN*[419-422], compared to only 16% in the mixed hiPSC-CM control group. This broadly supported our prior findings that this differentiation protocol could reliably produce a primarily atrial-like population of hiPSC-CMs.

We then sought to identify broadly differentially expressed genes in the comparison between our hiPSC-AM and hiPSC-CM groups. We observed that our hiPSC-AMs indeed had upregulated expression of a cassette of atrial-specific genes, including those encoding components of excitation-contraction coupling (*MYL7, SLN, MYH6*), more general pro-atrial transcription factors (*HOXA11, GATA4*), and atrial-specific potassium channels (*KCNA5*). Thus, supporting that the atrial transcriptome induced had breadth across different atrial-associated genes.

I then sought to further characterise this atrial-associated transcriptomic signal. First, I used gene ontology analysis to identify if the differentially expressed genes had coherent differences at the level of broad gene sets, as defined by function, between our atrial-like group and the control group. I highlighted the 10 most highly enriched GO terms, which described broad differences in gene sets between the two groups. I observed several gene sets that were enriched within the differentially expressed genes. These broadly related to the organisation of the extracellular matrix, replication, protein translation, and cardiac muscle development. This analysis

demonstrated that not only were there difference in individual genes between the two groups, but that these differences were part of larger coherent transcriptional programs.

I then sought to examine specific genes encoding axes of cardiomyocyte function that are known to differ between atrial and ventricular cardiomyocytes and across cardiomyocyte maturation – a key dimension for evaluating hiPSC-CM differentiation protocols.

First, I examined a range of atrial-specific transcriptional markers. Specific markers of an atrial-like transcriptome were broadly more highly expressed in the GREMLIN2/RA-treated group, such as *SLN*, *HOXA3*, *HEY1*, *SFRP5*, and *NPPA*. Whereas, the control group had higher expression of pro-ventricular transcription factors such as *IRX5*. However, it is of note that both groups had largely similar expression levels of NR2F2 and other genes that contribute to chamber-specific differentiation[410].

I then examined genes encoding potassium channels, as the atrial-specific cassette of potassium currents gives rise to its particular action potential morphology and much of its electrophysiological differences compared to ventricular cardiomyocytes. I observed that our GREMLIN2/RA-treated group had increased expression of a range of potassium channel subunit-encoding genes, such as *KCNJ3* and *KCNA5*. These genes respectively encode subunits of channels that produce key atrial currents I_{KACh} and I_{Kur} [423-425]. Furthermore, this group also expressed higher levels of *KCNH2* and *KCNJ2,* which respectively encode channel subunits that give rise to I_{Kr} and I_{K1}, which are two currents associated with the resting membrane potential[426,427], with I_{K1} being associated with a more mature electrophysiological phenotype[428].

The contractile apparatus in native mature cardiomyocytes requires not only the appropriate expression of actomyosin myofibrils, but their organisation into sarcomeres connected molecularly to the exterior of the cell. I observed that our GREMLIN2/RA-treated group had higher expression of general sarcomeric genes, such as *TTN*, *TNNT2*, *MYOM1*, and *MYBPC3*. Additionally, this group had stronger expression of *DES* and *DMD*, which encode proteins that connect sarcomeric contraction to the cytoskeletal-sarcolemmal network[429,430]. Finally, our GREMLIN2/RA-treated group also had higher expression of atrial-specific actomyosin contractile genes, such as *MYH6*, *MYL7*, and *MYL4*. Thus, it appears our hiPSC-AMs had a greater expression depth and breadth of not only general sarcomeric components, but also of the atrial-specific contractile elements.

Appropriate calcium handling is a fundamental process for cardiomyocyte function and the basis of hiPSC-derived CMs as a useful model of cardiomyocytes. I identified that our experimental GREMLIN2/RA-treated group had higher gene expression across genes that encode calcium-handling proteins across both the sarcoplasmic reticulum and the sarcolemma. For example, GREMLIN2/RA-induced hiPSC-CMs have higher expression of *RYR2*, *TRDN*, and *FKBP1B*, which all encode key SR calcium release proteins[431,432]. Whereas, the control group has higher expression of *RYR3*, which encodes a ryanodine receptor isoform more associated with fetal cardiomyocytes[433]. More broadly, our GREMLIN2/RA-treated group had stronger expression of most calcium channel-encoding genes, with *CACNA1H* and *CACNA1G* being of most interest as they respectively encode T-type calcium channels $Ca_{V3.2}$ and $Ca_{V3.1}$ which both contribute to the specific electrophysiology of atrial cardiomyocytes, and $Ca_{V3.2}$ is particularly implicated in this postnatally[434-436]. Whilst both groups had somewhat similar levels of *ATP2A2* expression, our GREMLIN2/RA-treated group had much stronger expression of *SLC8A1*. These genes encode the major transporters that remove calcium ions from the sarcoplasm, respectively encoding the major cardiac isoforms of SERCA and NCX. These data support that at the transcriptional level,

our hiPSC-AMs have stronger expression of calcium handling genes related to both the influx and efflux of calcium.

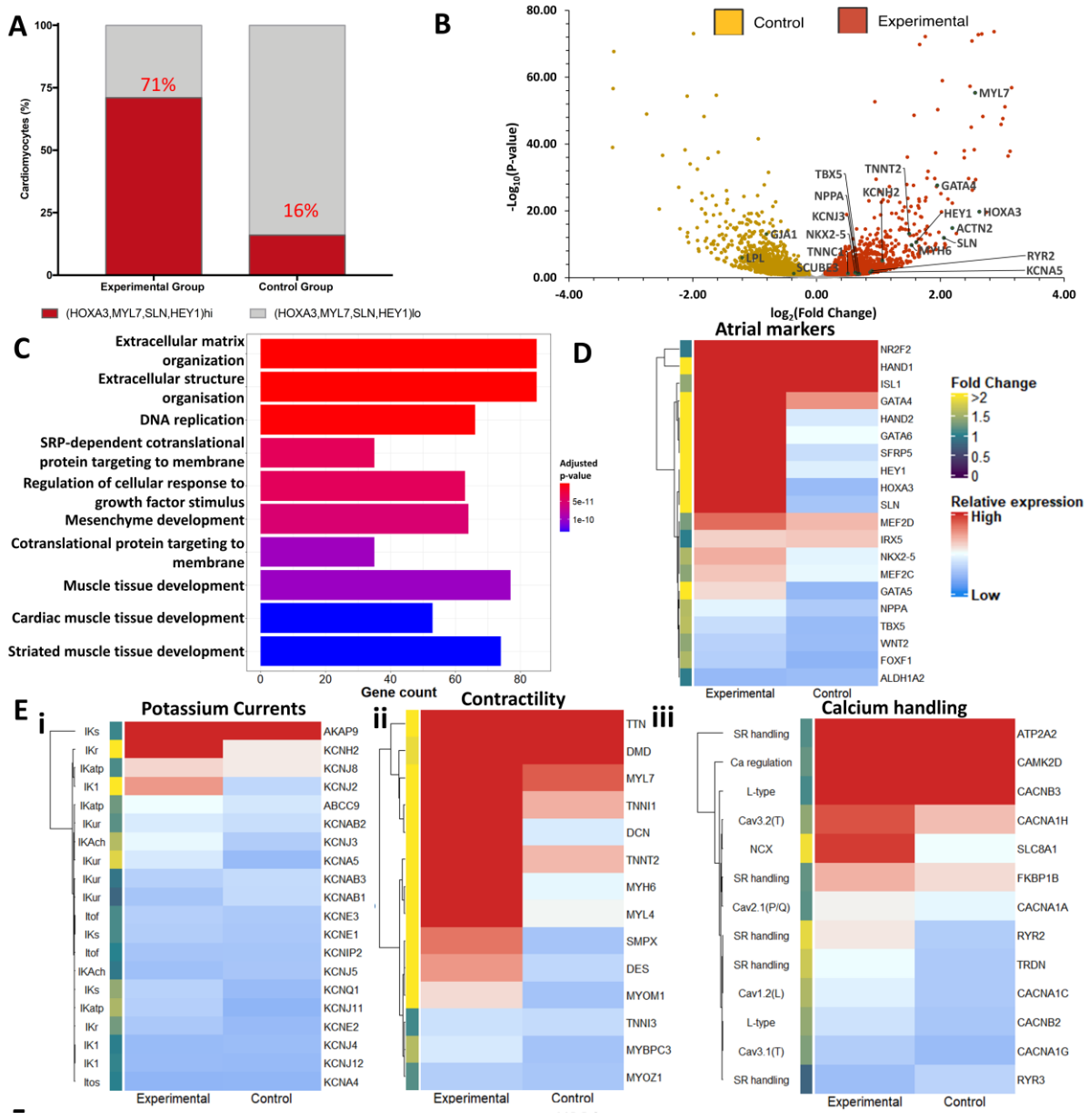

Figure 4-4. GREMLIN-2/RA-treatment induced a more atrial-like and mature transcriptome.

A) Plot showing the percentage of cardiomyocytes expressing atrial specific markers HEY1, MYL7, HOXA3 and SLN in the GREMLIN-2/RA and Control (CMM) groups.

B) Differential gene expression analysis showed many up-regulated atrial-specific gene in the GREMLIN-2/RA group with selected markers indicated.

C) Gene Ontology (GO) plot showing the top 10 most enriched GO terms in the genes differentially expressed between the GREMLIN-2/RA treated group and control (CMM). Coloured by Bonferroni-Hochberg-adjusted p-value. Gene count along the x-axis marks the number of genes enriched within each GO term.

D) Heatmap plot showing the expression of cardiogenic and chamber-specific markers. Cells are coloured by relative expression. The annotation on the left indicates the specific fold change in expression from the control group to the experimental group.

E) i) Heatmap plot showing the expression of potassium handling genes. The associated currents for each gene are annotated on the left. ii) Heatmap plot showing the expression of contractility-associated genes. iii) Heatmap plot showing the expression of calcium handling genes. The associated currents/roles for each gene are annotated on the left. In all heatmaps cells are coloured by relative expression. The annotation on the left indicates the specific fold change in expression from the control group to the experimental group.

This Figure is adapted from Ahmad, Jin, Grassam-Rowe et al[1]. Dr. Jin made panel A and B.

Metabolic maturity has been recognised as both an effector and driver of hiPSC-CM maturation[322]. I established that both groups of hiPSC-CMs had similar expression across a number of metabolic genes, such as adenosine phosphate transporters and fatty acid oxidation enzymes. However, the control hiPSC-CM group had higher expression of certain ventricular-associated metabolic genes such as *LPL*. However, our GREMLIN2/RA-treated group had higher expression of *PPARGC1A* – an important transcription factor that drives mitochondrial biogenesis and oxidative metabolism and is associated with more mature hiPSC-CMs[417,418].

The neurohormonal control of cardiomyocytes, and the effector and modulator second messenger cascades within them, define a vital aspect of native cardiomyocyte function. I identified that both groups had expression of both β- and α-adrenoceptor-encoding genes. However, it is noteworthy that the control hiPSC-CM group appeared to have a higher expression of *ADRB1*, which encodes the major cardiac β-adrenoceptor – β_1[437]. However, our GREMLIN2/RA-treated group had higher expression of *PDE3A* – which encodes a key cardiac phosphodiesterase[438]. Furthermore, our GREMLIN2/RA-treated group also had higher expression of *CHRM2*, which encodes the major cardiac muscarinic cholinergic receptor – M_2[439].

Sodium fluxes, both inwards and outwards, contribute to depolarisation and establishing the resting membrane potential respectively. I observed that our GREMLIN2/RA-treated group had higher expression of *SCN3B* and *SCN11A*, yet lower expression of *SCN5A*. *SCN3B* encodes a regulatory β subunit, and *SCN11A* encodes the α subunit of $Na_{V1.9}$[440,441]. However, *SCN5A* encodes the major cardiac α subunit[442]. Whilst this remains complex to interpret, a more simple observation was that our GREMLIN2/RA-treated hiPSC-CMs had lower expression of *GJA1*, but higher expression of *GJA5* – *GJA1* encodes CX43[443], and *GJA5* CX40[444]. Respectively, these connexins contribute primarily to the ventricular and atrial myocardium[445].

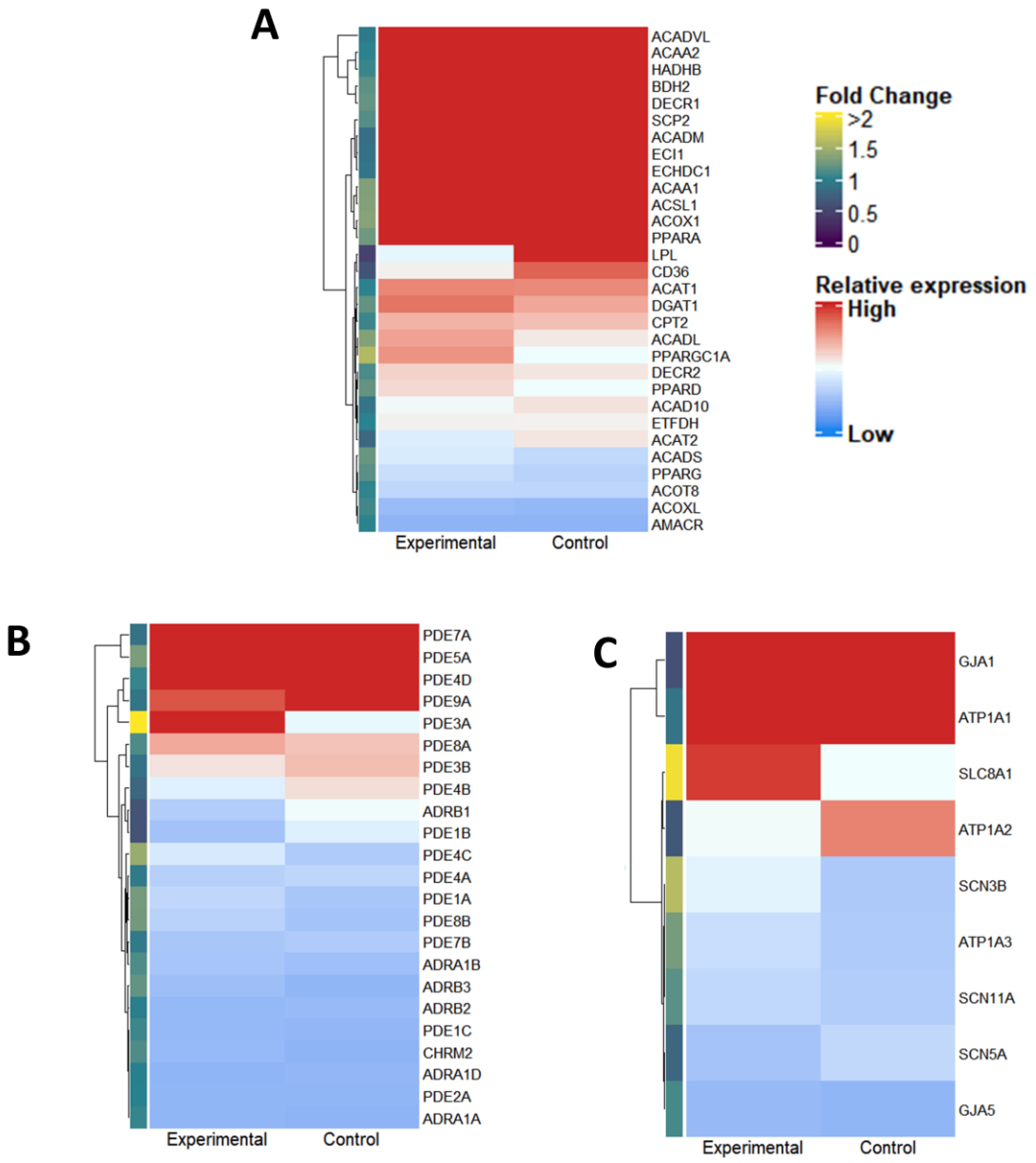

Figure 4-5. Our hiPSC-CMs have robust expression across metabolism, signalling, and sodium handling genes.

Heatmap plot showing the expression of metabolic genes.

a) Heatmap plot showing the expression of signalling genes.
b) Heatmap plot showing the expression of sodium handling genes.

Cells are coloured by relative expression. The annotation on the left indicates the specific fold change in expression from the control group to the experimental group.

This Figure is adapted from Ahmad, Jin, Grassam-Rowe et al[1].

v. Our atrial development networks are not clearly upregulated in our GREMLIN-2/RA-treated hiPSC-CMs.

Our GREMLIN2/RA protocol appeared to produce atrial-like hiPSC-CMs with a transcriptomic signature indicating some promising pro-maturity signals. I thus sought to clarify whether the maturation-associated networks I had identified in mouse atrial development were upregulated in our hiPSC-AM protocol. With regards to cluster 1, I observed that our hiPSC-AMs had higher expression of *TEAD1* and *MEF2D*, but similar or lower expression levels of *SOX4* and *SRF*. For cluster 2, I identified that our hiPSC-AMs had only higher expression of *PROX1* and *PPARGC1A*, and equal or lower expression of the other components of this module, including *NR2F2*. However, there was a much greater difference between the expression of cluster 3 and 4 genes, with our hiPSC-AMs demonstrating higher expression of certain genes, such as *ID2* and *FOS*, but lower expression of genes such as *HES1* and *KLF6*. Thus, whilst certain genes from our mouse maturation modules do appear to be upregulated in our hiPSC-AM compared to control, there are many which are less strongly expressed compared to control.

I then sought to determine whether there was any difference in expression of key downstream signalling genes related to the actions of GREMLIN2/RA. Our hiPSC-AMs express a higher level of a range of downstream markers of NOTCH/WNT signalling, such as JAG1 and DKK1[446,447]. Additionally, our hiSPC-AMs have higher expression of two key interacting markers of the first heart field – ISL1 and HAND1[244,264]. Our hiPSC-AMs do express TBX5 and WNT2 more strongly than the control, which are both implicated in atrial differentiation and patterning[258,267,268,448]. These results support that our hiPSC-AMs do have higher expression of genes associated with GREMLIN2/RA signalling, as well as other markers associated with a more atrial developmental pathway.

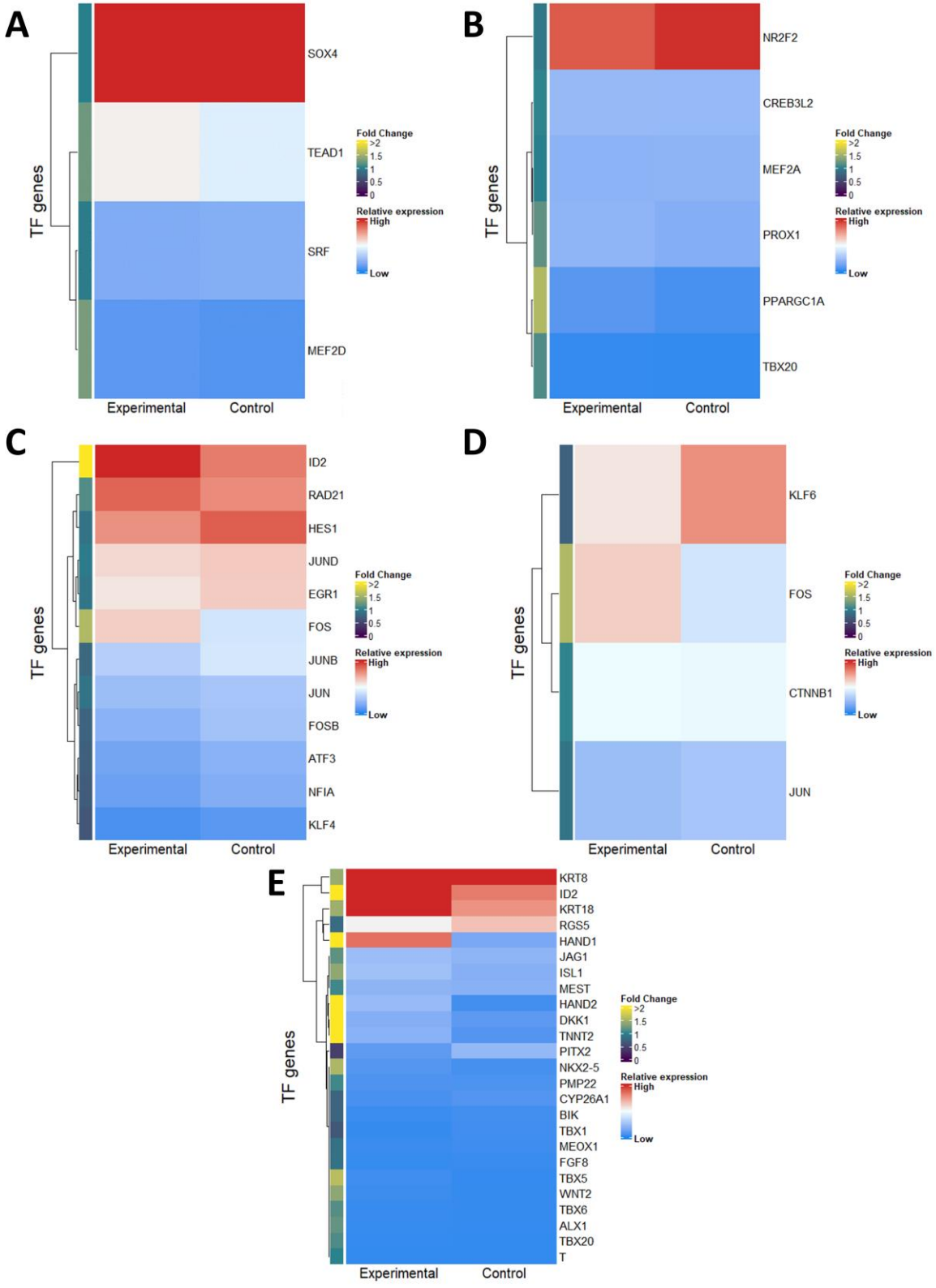

Figure 4-6. Our hiPSC-CMs both display similar expression of the maturation networks identified in mouse.

A) Heatmap plot showing the expression of Cluster 4.

B) Heatmap plot showing the expression of Cluster 3.

C) Heatmap plot showing the expression of Cluster 1.

D) Heatmap plot showing the expression of Cluster 2.

E) Heatmap plot showing the expression of various development-associated genes.

Cells are coloured by relative expression. The annotation on the left indicates the specific fold change in expression from the control group to the experimental group.

d. Discussion

i. I identified transcriptional changes associated with the maturation of the developing mouse atria

I built on my earlier work to establish a more selective transcriptomic dataset of the cardiomyocyte lineage excluding those cells with less than 1000 nUMI. This dataset reproduced the expected lineages of atrial and ventricular cardiomyocytes. This dataset provided me a dataset better suited for specific downstream analytical techniques, particularly those related to identifying gene changes across pseudotime. However, some of these more complex techniques such as wOT[449], failed to produce meaningful results (data not shown). However, I found that more easily-interpretable techniques that relied on the manifold structure of the data within the 3D transcriptomic space produced results that were readily explicable[413].

Furthermore, I relied on imputation techniques that also relied on the 3D manifold structure of the data in transcriptomic space[366]. These techniques provided again easily-interpretable results that demonstrated their efficacy, in the most part, in recovering gene 'droput' and provided a basis for understanding the transcriptional maturation of developing murine atrial cardiomyocytes. Whilst I recovered several previously known changes, such as the expression of many atrial-selective potassium currents: I also observed less well-characterised transcriptional changes in the atria, such as a range of metabolic genes. Metabolic maturation in the developing and postnatal ventricles have been well-studied. However, to my knowledge, this is not so well-studied in the developing and postnatal atria. In line with previous work by others, I identified that our postnatal atrial lineage had the expected perinatal expression of these noted metabolic markers (*Fabp3*, *Hk1*, and *Cox8b*)[276], but that the expression of the more adolescent/adult forms was beginning to appear (*Fabp4*, *Hk2*, and *Cox8a*). This work provides some evidence to support a similar metabolic transcriptional maturation occurring in the atria as in the ventricles. However, this should be validated with more extensive profiling using immunostaining and functional assays.

I then identified the co-ordinated changes of these genes in terms of the networks that characterise the overall transcription program associated with maturation. Broadly, I observed 4 modules of interacting TFs and downstream effector genes. These could best be grouped into 2 'meta-modules' that governed either general maturation, proliferation, and differentiation, or cardiomyocyte- and atrial-specific transcriptional programs. For example, Cluster 4 included the major regulator of atrial-specific transcriptional programs *Nr2f2*[410], alongside other markers such as *Ppargc1a*, a master regulator of cardiomyocyte metabolic maturation. Ultimately, further work is necessary to ascertain the completeness and accuracy of these networks – especially the functional importance, if any, of the non-TF downstream genes identified, which have a range of associated functions with less well-characterised associations to cardiac development – for example: Cluster 4's downstream genes consist of D*dr1*, and *Ptprs* – a tyrosine kinase receptor and protein tyrosine phosphatase respectively, but both without a clear function in cardiomyocytes[450,451]. Whereas, Cluster 4's TF *Tead1* and *Mef2d* have established functions in

postnatal cardiomyocyte proliferation and sarcomeric remodelling and hypertrophy respectively. I attempted to use in silico genetic knockouts to identify the sensitivity of these networks (data not shown). However, these techniques are intensely resource-demanding computationally and would likely be most productive using full-length isoform-sensitive and deep RNA sequencing techniques with datasets produced for this purpose.

ii. Our G2RA protocol produced an atrial-like transcriptomic signature

After having studied atrial development and maturation in mouse cardiomyocytes, I looked to describe the transcriptional changes associated with our novel atrial cardiomyocyte hiPSC differentiation protocol. We observed that compared to the mixed/ventricular transcriptome induced in the standard CMM protocol, our G2RA-based protocol did produce a more atrial-like transcriptome, and with an increased number of certain markers of maturity. Genes associated with an atrial transcriptomic signature showed enhanced expression in the G2RA group, such as *MYL7*, *HEY1*, *HOXA3*, *SLN*, *MYH6*, *KCNH2*, *GATA4* and *NPPA*. Our CMM control demonstrated greater expression of transcription factors associated with the ventricles, such as *IRX5* and *IRX4*. Furthermore, other genes more strongly expressed in our G2RA group are also associated with a more atrial and mature transcriptome, such as ion channels (e.g. *KCNA5*, *KCNJ2*, *KCNJ3* and *KCNH2*) and calcium-handling proteins (e.g. *RYR2*, *CACNA1H*, *CACNA1G* and *SLC8A1*) respectively. In our published work, we confirmed the relative upregulation of several atrial genes (MYL7, NPPA, KCNJ2, PITX2, & KCNA5) in our GREMLIN-2/RA treated group by qPCR, across 5 different batches of cells – thus providing supporting cross-validation of our observed results here[1]. In an unexpected manner, both the CMM and G2RA groups had robust expression of *NR2F2*. However, this does not appear to be coupled to an increase in the protein levels of its gene product COUP-TFII, nor to an atrial transcriptional programme. It is interesting to speculate about what post-transcriptional regulation might be involved, and highlights the use of in vitro differentiation to study cell signalling and epigenetics in normal development.

However, it was not clear that our G2RA protocol resulted in distinct changes across the atrial maturation-associated gene networks I identified earlier in mouse atrial cardiomyocytes. Whilst certain individual genes were upregulated in the same manner as in these native atrial cardiomyocytes, many had a conflicting pattern at the level of the TFs identified. These conflicting results could be the result of: differential sequencing biases between the two RNA sequencing techniques used; a species-dependent difference between human and mouse; differential relationships and ratios between TFs and downstream signalling in hiPSC-derived CMs vs native cardiomyocytes; or perhaps the networks identified in my earlier work are simply artefactual and not a true representation of the pertinent transcriptional changes; or finally the comparison of our day 20 hiPSC-AMs to our day 20 hiPSC-CMs is simply not a valid proxy to compare these embryonic to postnatal gene networks. Future work should repeat this with matched datasets prospectively gathered with these comparisons in mind. Understanding these gene networks associated with chamber-specific development and maturation of both native and PSC-derived cardiomyocytes may reveal new pathways to optimise hiPSC differentiation and maturation protocols, as others have already done in a chamber-agnostic fashion[357].

Chapter 5. Transcriptional calcium handling networks in cardiomyocytes.

a. Introduction

This section is introduced in Chapter 1A & C:

Calcium handling remains one of the defining tenets of cardiomyocyte biology. However, how cardiomyocytes balance the fluxes and buffers that give rise to calcium transients out of periods of stable quiescence, remains debated even now[452]. This work attempts to leverage the power of single-cell RNA sequencing, coupled with experimental validation work (not presented here) to ascertain the role of transcription covariance in balancing these networks. This work builds upon work in the Swietach Group (unpublished), and that in the Niederer Group to record the experimental electrophysiological data from cardiomyocytes, and to produce the mathematical approaches necessary to efficiently and yet effectively integrate a Bayesian approach to understanding these relationships[66].

a. Methods

The methods used for data presented in this chapter are in Chapter 2A and B:

b. Results

i. scRNA-Seq describes the expression of calcium handling genes in mouse and hiPSC-derived cardiomyocytes.

I sought to ascertain whether calcium handling correlation networks were present at the transcriptomic level. I used the genes that encode the different proteins primarily responsible for setting the different fluxes and ion concentrations that contribute to the Hinch model[67]. For closest comparison with the work of Riabiz et al (Unpublished), I first used neonatal mouse cardiomyocytes described previously[357]. However, I also sought to compare whether these calcium correlation networks were present or disrupted in our hiPSC-AM and -CM models.

I first sought to ascertain if these datasets had sufficient coverage of the different genes involved in calcium handling. As expected in the neonatal mouse cardiomyocytes, certain genes

dominated the mRNA fraction, such as *Atp2a2*, *Ryr2*, *Casq2*, *Slc8a1*, and *Cacna1c*. These respectively encode, or partially encode, key calcium handling proteins SERCA2A, RyR2, Calsequestrin2, NCX1, and an α_{1c}-subunit of $Ca_{v1.2}$. However, there was broadly coverage across the major cardiac isoforms of the genes that would be input into our model as agreed upon by myself and Prof. P. Swietach.

I next sought to examine the same gene coverage in our hiPSC-AMs and -CMs. However, the relative proportions of different calcium handling genes were notably different in our hiPSC-AM and -CM data compared to the neonatal mouse. Our hiPSC-AM and -CM mRNA fraction of these genes was predominated by buffer protein-encoding genes such as *Calm2* and *Calr*. There was much lower expression of the cardiac-associated calcium handling genes noted in the mouse cardiomyocytes – yet these genes were still mostly expressed. However, direct comparison of gene expression strength between the mouse cardiomyocytes and the hiPSC-derived groups is unlikely to be reasonable, given the many differences between the two in terms of data collection.

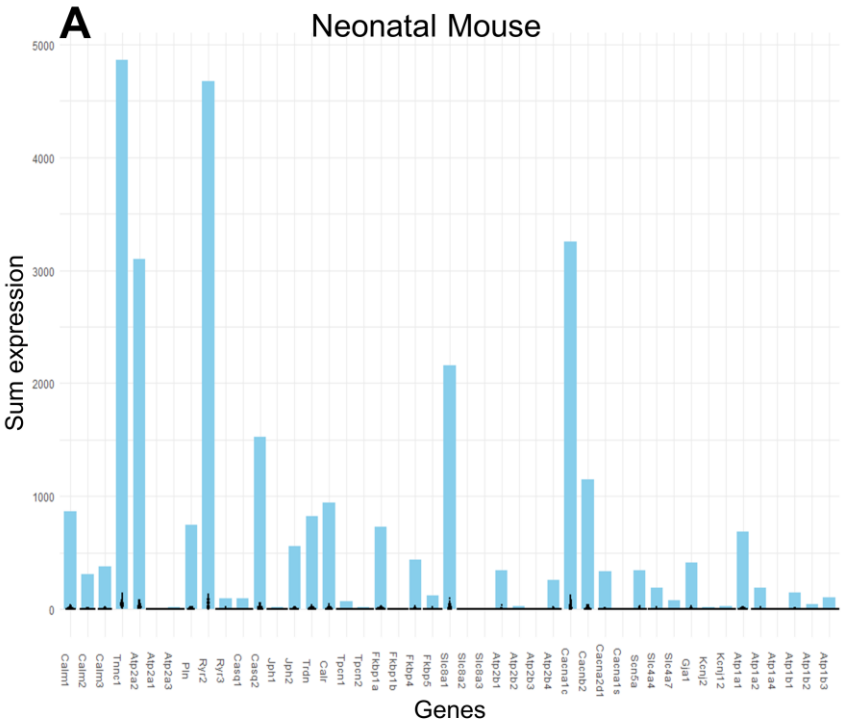

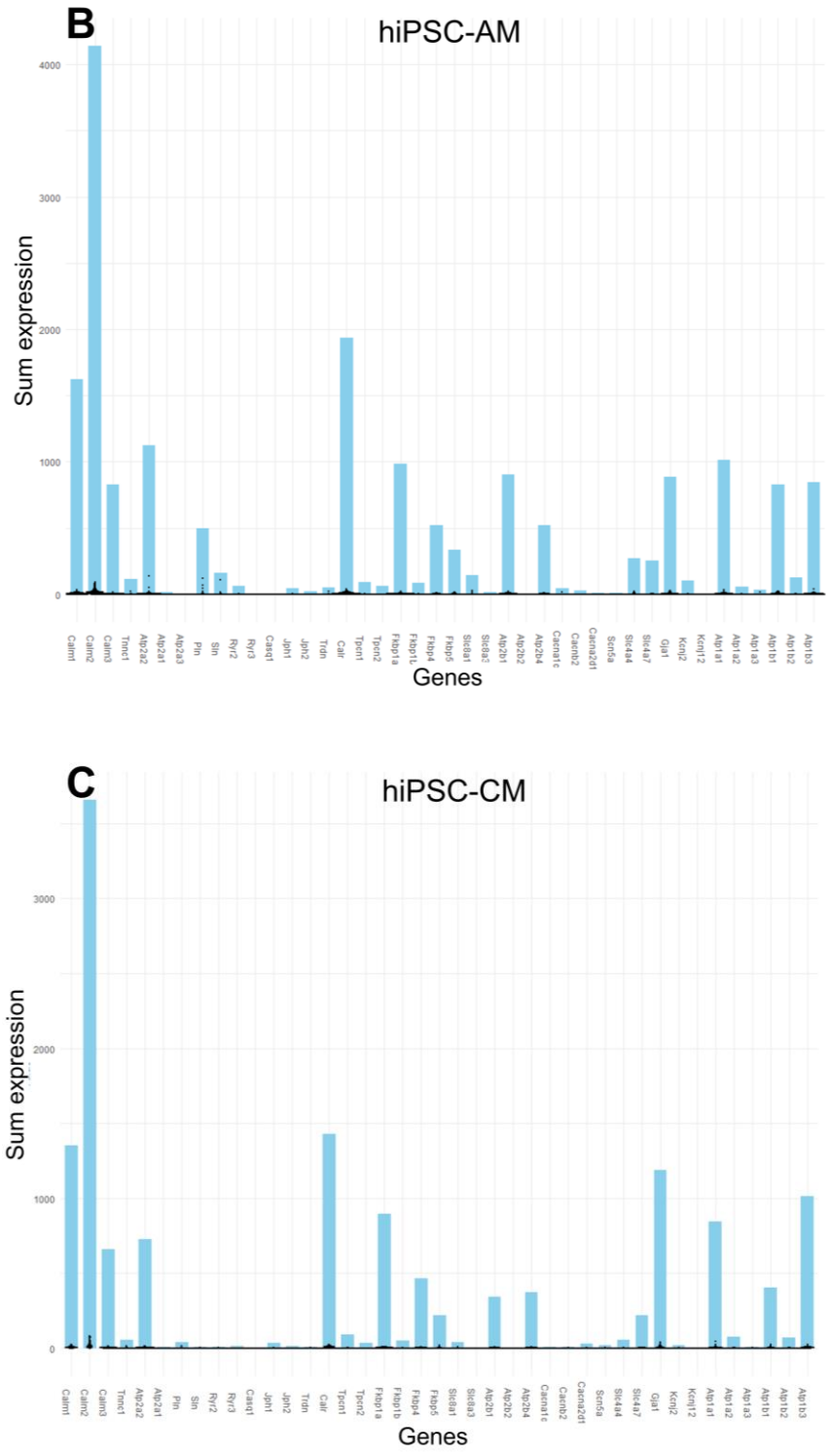

Figure 5-1. Calcium handling-associated genes have variable expression strength between mouse cardiomyocytes, and hiPSC-derived cardiomyocytes.

Individual genes are represented on the x-axis, and their respective sum expression is plotted on the y-axis.

A) Mouse cardiomyocytes.
B) hiPSC-AMs
C) hiPSC-CMs

ii. Calcium networks at the level of functionally-linked groups in population-level data

After establishing the expression levels of individual genes, which can be particularly noisy in scRNA-Seq data: I sought to establish whether grouping genes into their respective Hinch model parameters (Table 2-1) would provide further insight. We retain those parameters that we are most closely able to assume will correlate to the mRNA level of the given genes; primarily these parameters retained were the currents associated with different fluxes. This leaves our model with the retained components of calcium release, calcium re-uptake, and calicum efflux. However, of particular note, is that sarcolemmal calcium influx is now all mediated through a combined LTCC and background parameter g_{CaB}. Similarly, for SR calcium release, this is all mediated through a combined RyR and leak component – r_{SR_l}.

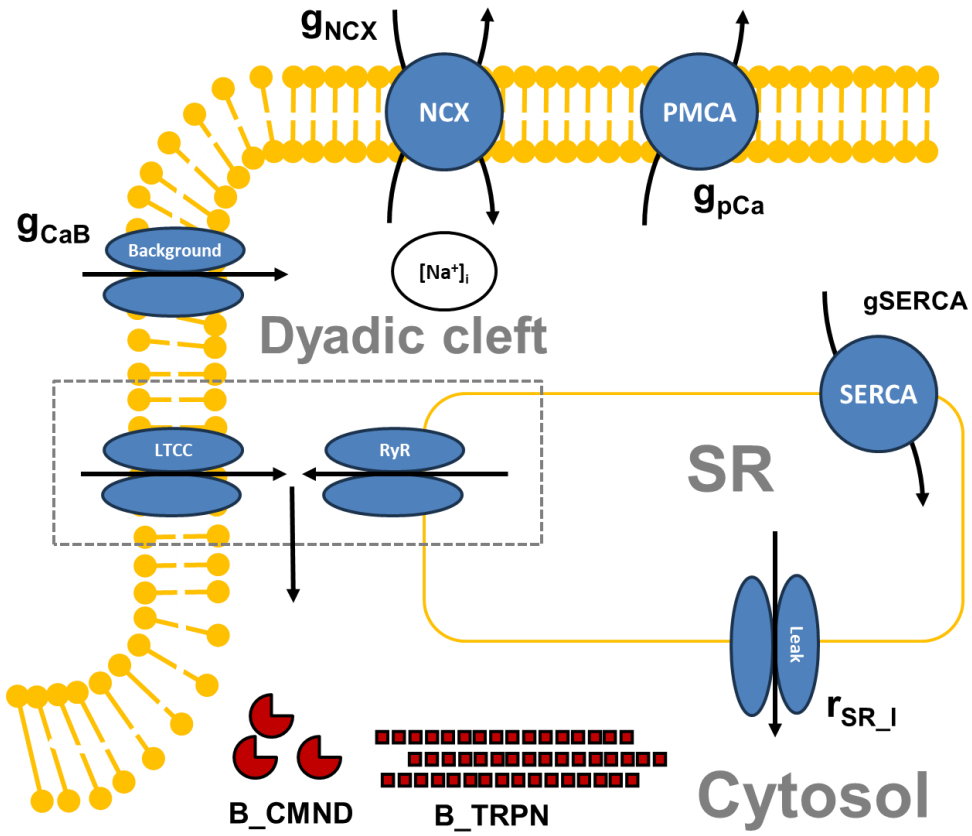

Figure 5-2. The Hinch model components we parameterise at the mRNA level.

Different compartments are described in grey. Calcium transport proteins are in blue, with spheres as exchangers or pumps, and channels as paired ovals – associated names in white. Black arrows show the direction of ionic fluxes. Ion concentrations are shown in small white spheres. The cytosolic buffers of calmodulin and troponin are represented in dark red. All parameters shown in black text.

Neonatal mouse cardiomyocytes revealed that even once grouped into different, presumably functionally-linked gene sets, there was a great deal of heterogeneity in the expression levels between different gene sets related to the different components of the Hinch model. The same was broadly true in the hiPSC-AMs and -CMs, albeit at the lower expression levels sampled in these cells. The comparison of each gene scaled within its own maximum expression revealed that the expression distribution of genes, regardless of their absolute value, did have some

similarities between the neonatal mouse and hiPSC-derived cells. In particular, the those genes grouped into B_CMDN and [Na_i] appeared most similar between all groups. However, the starkest differences were in those genes grouped into gNCX, and gCa_B – with the distribution of these genes sets at lower values and with less dispersion in the hiPSC-AMs and CMs. Therefore, at the population level, gene set expression levels remained highly dispersed between cells both within and between gene sets.

To account for the differences in aboslute expression level, and provide a universal unit of distribution to compare between the different datasets, I also described the distributions using entropy of the individual genes that comprise each gene set. Entropy provides a meaure of distribution that is irrespective of absolute values and makes no assumptions about the underlying distribution. This is to attempt to account for the unavoidable bias that genes sets with more genes in them are more likely to have a wide distribution of possible values. In sum, the hiPSC-CMs and -AMs were more similar to each other in terms of gene entropy, than they were to the mouse cardiomyocytes. In line with my other findings, this provides another method to examine the inter- and intra-group variability of calcium handling genes, demonstrating that even functionally-related groups of genes can have widely different expression level distributions.

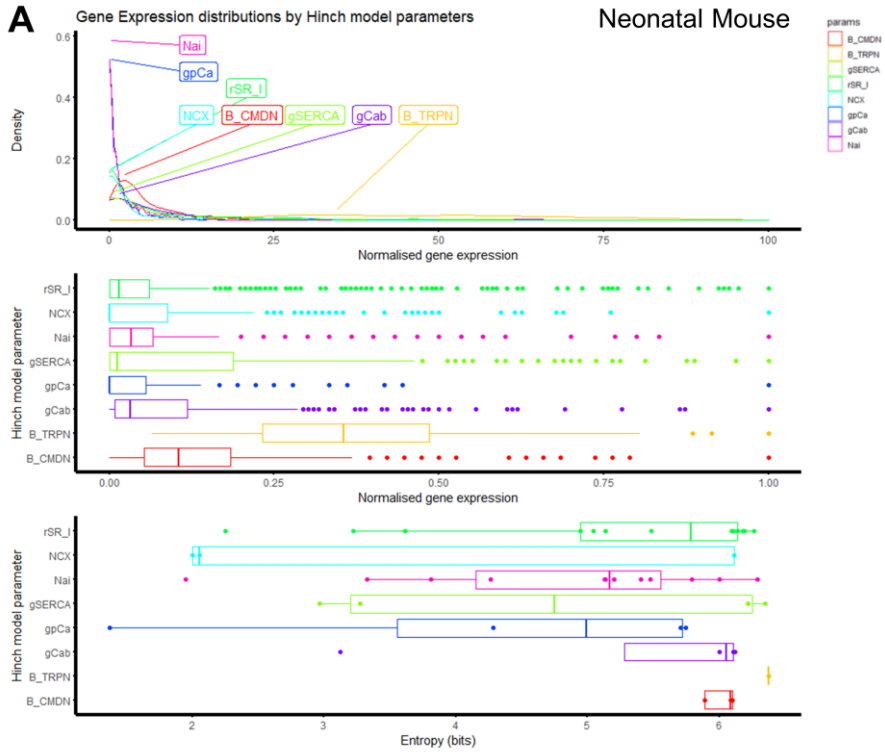

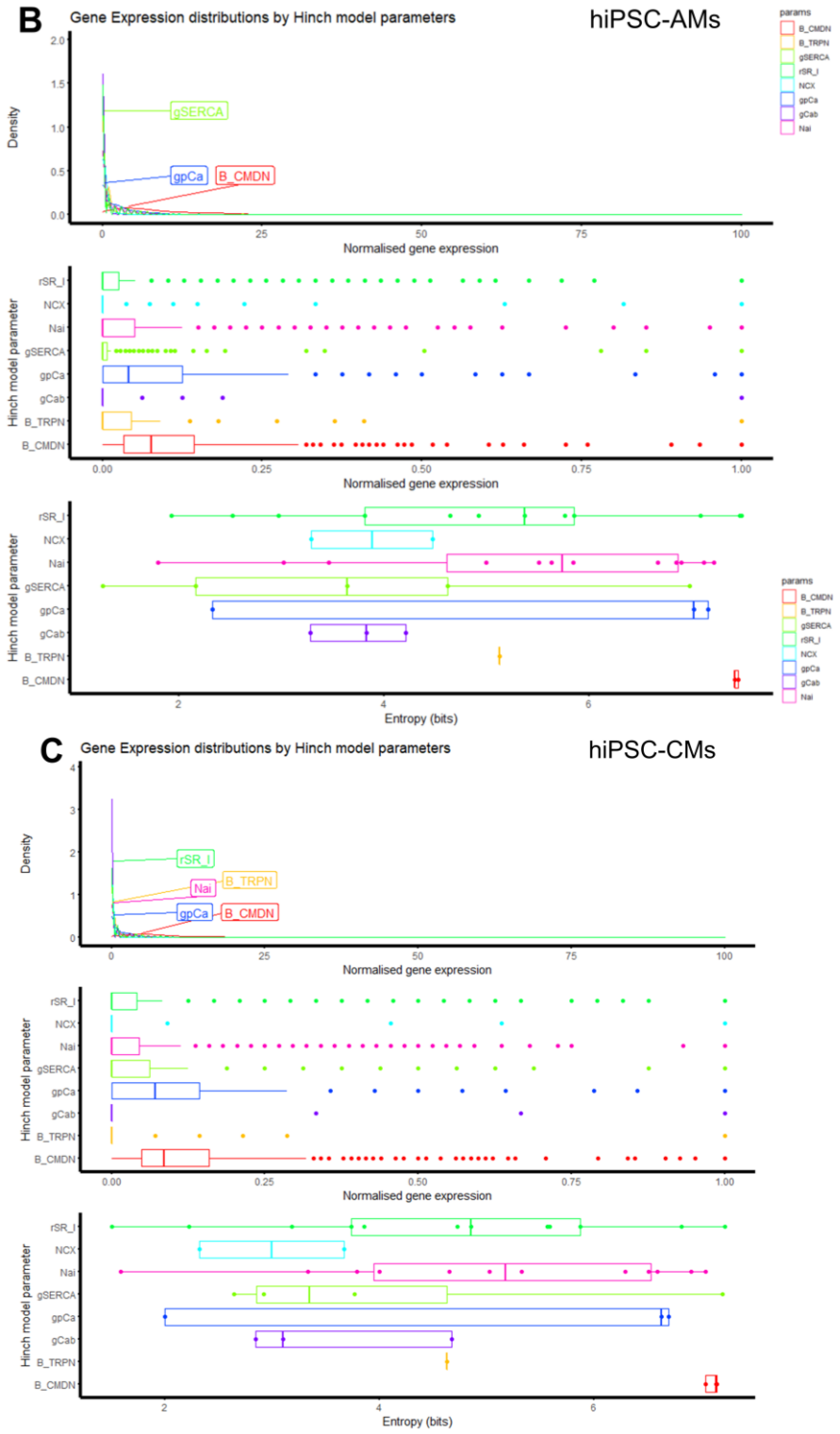

Figure 5-3. High population-level variability in calcium handling-associated genes persisted even when grouped into functionally related domains.

Neonatal mouse cardiomyocytes.

A) hiPSC-AMs
B) hiPSC-CMs

The top plot in each panel represents the expression level of the grouped genes by normalised counts on the x-axis, and the probability density for the different counts at each level. Individual groupings of genes into parameters are coloured as per the legend on the right, and labelled where overlap would allow.

The middle plot in each panel represents the respective groups of genes on the y-axis, normalised against their own respective maximum expression values, to display the distribution across their min-max expression.

The lower plot in each panel represents the distribution of the different entropies of the constituent genes within each group on the y-axis. This acts as a measure of gene dispersion independent of absolute amplitude, and without any assumptions made as to the underlying distribution's central tendency. A higher entropy indicates a more dispersed distribution. The boxplot is centred around the median represented by a vertical line in the box. The limits of the box describe the IQR. The extended error bars then describe Q1 or Q3 + 1.5IQR. Observations beyond this are plotted as individual dots.

iii. Calcium handling genes display correlative relationships across cardiomyocytes.

So far, I had revealed that at the population level, the calcium handling genes displayed a wide range of possible distributions, even when grouped as functional gene sets. I then sought to understand the nature of this relationship at a single-cell level. First, I observed that in neonatal mouse cardiomyocytes, the Hinch model gene sets primarily adopt strong pairwise correlations, both positive and negative depending on the specific model parameter. For example, there is a strong positive correlation between the expression of gSERCA-associated genes and rSR_l-associated genes, yet a strong negative correlation between B_CMDN-associated genes and B_TRPN-associated genes. These data support the idea that examining the covariance of calcium handling genes does reveal information beyond simply looking at population-level data.

However, the same relationship of primarily strong pairwise correlations between parameters was not present in our hiPSC-AM or -CM data. In both our hiPSC-AM and -CM data, I observed that the majority of pairwise correlations were indicative of no correlation, or a weak statistically insignificant correlation. Those correlations that did remain as strongly positive appeared either as a result of a limited number of cells with high co-expression, such as gSERCA and NCX, or were the inverse of the relationship observed in neonatal mouse, such as B_CMDN, and $[Na_i]$. This tentatively supports that differences in calcium handling between native and hiPSC-derived cells might be encoded at the transcriptomic level.

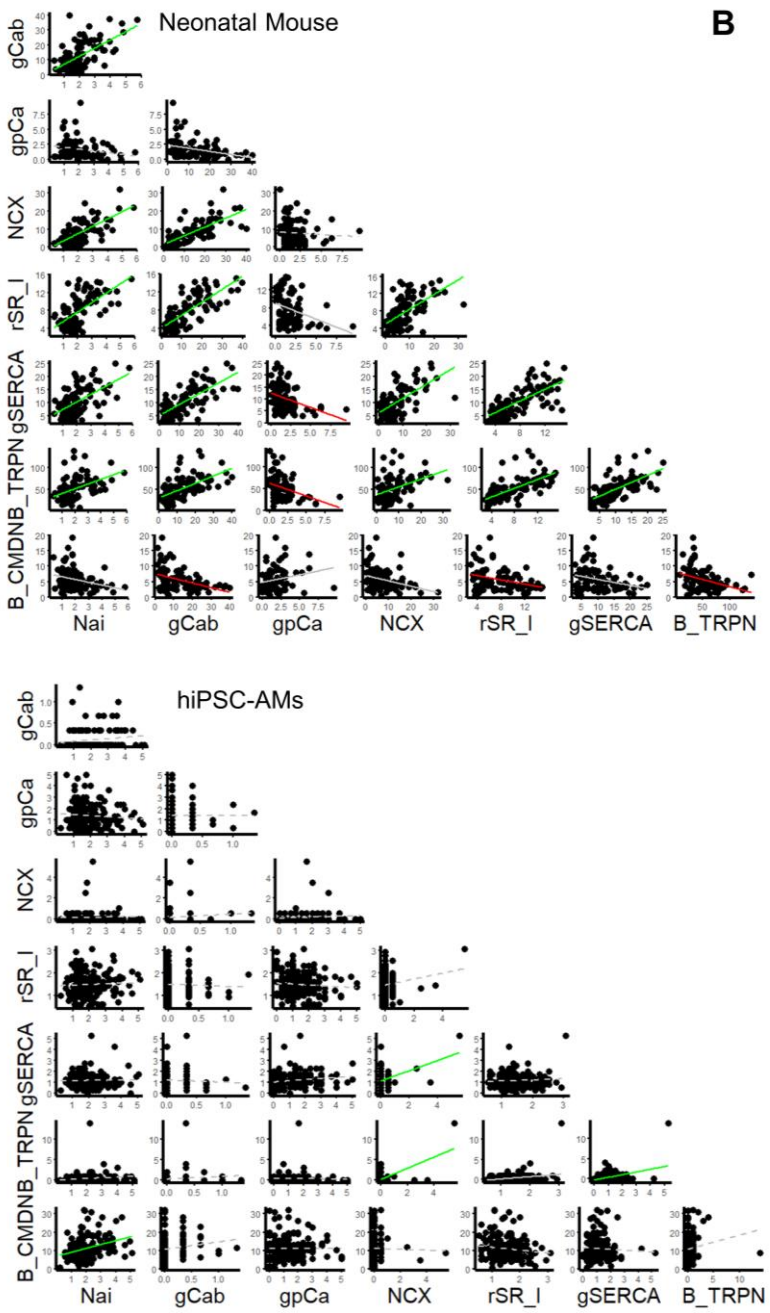
Neonatal Mouse
B
gCab
gpCa
NCX
rSR_I
gSERCA
B_CMDNB_TRPN
Nai
gCab
gpCa
NCX
rSR_I
gSERCA
B_TRPN
hiPSC-AMs
gCab
gpCa
NCX
rSR_I
gSERCA
B_CMDNB_TRPN
Nai
gCab
gpCa
NCX
rSR_I
gSERCA
B_TRPN

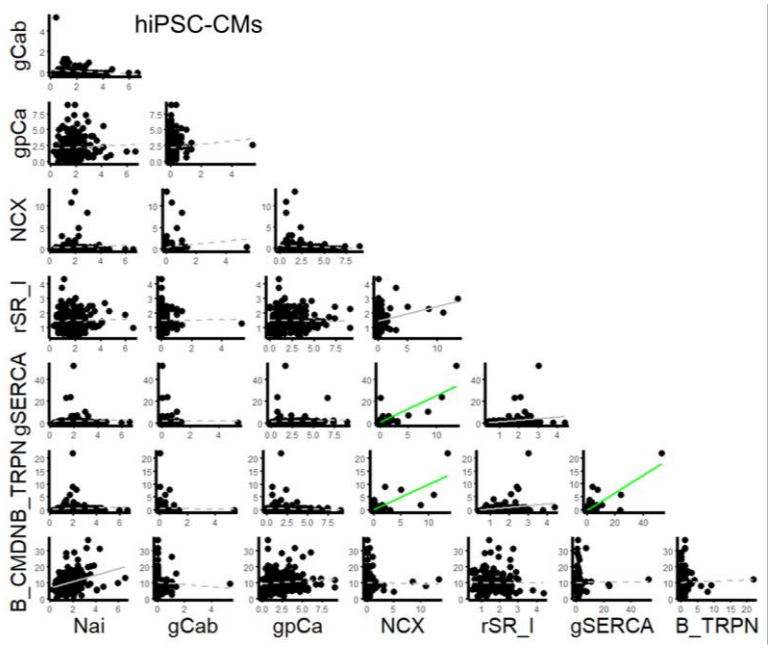

Figure 5-4. Gene-wise transcriptional correlation networks are robust between functionally-grouped calcium handling-associated genes in mouse cardiomyocytes but not hiPSC-derived cardiomyocytes.

Neonatal mouse cardiomyocytes

A) hiPSC-AMs
B) hiPSC-CMs

For each panel, each smaller plot displays a scatter plot of the respective parameter group in the y-axis row, against the respective parameter group in the x-axis columns. Each plot then has the respective linear line of best fit plotted. Each line is coloured by the respective Pearson's correlation coefficient (green > 0.333, 0.333 ≤ grey ≥ -0.333, red < -0.333). The line of best fit is solid if the respective correlation's adjusted p-value ≤ 0.05, and dashed if p-value > 0.05.

iv. The positive correlation between functionally linked modules of calcium handling genes may be conserved.

I then sought to investigate whether these parameters displayed any relationship when grouped into the respective 'blue' and 'purple' strongly correlated groups that had previously been observed by Riabiz et al (Unpublished). Our groups did not perfectly match, given the lack of certain physiological parameters that were unmeasurable in our mRNA-based data. However, parameters were grouped as described in Table 5-1.

Group	Parameters
'Blue'	gpCa, [Na_i], gSERCA
'Purple'	gCaB, gNCX, rSR_l, B_TRPN, B_CMDN

Table 5-1. The grouping of the model parameters into larger modules based on the modelling work by Riabiz et al.

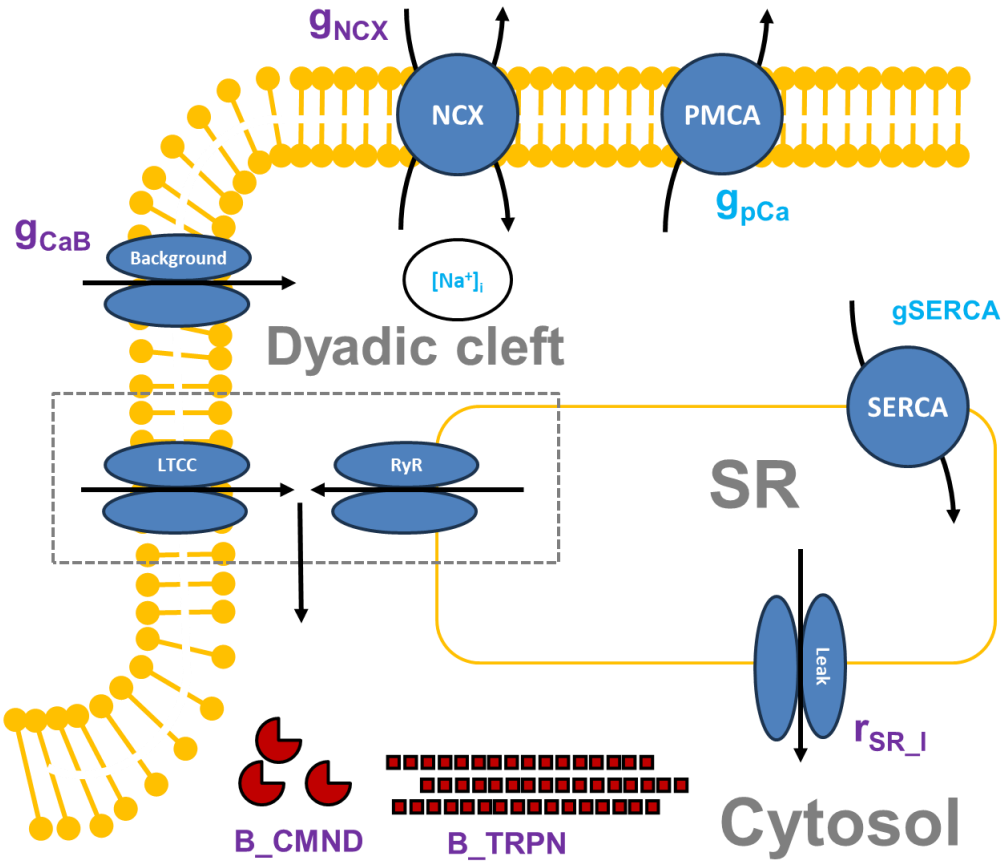

Figure 5-5. Further grouping of the Hinch model parameters into larger modules.

Different compartments are described in grey. Calcium transport proteins are in blue, with spheres as exchangers or pumps, and channels as paired ovals – associated names in white. Black arrows show the direction of ionic fluxes. Ion concentrations are shown in small white spheres. The cytosolic buffers of calmodulin and troponin are represented in dark red. All parameters shown in blue or purple are by respective grouping suggested by Riabiz et al. as highlighted in main text.

Abbreviations: gNCX.

In neonatal mouse, when grouped like this, our data suggested that instead of the negative intergroup correlation seen previously, there was a strongly positive correlation at the transcriptomic level (Spearman's r=0.741, p=2.15e-17). However, in our hiPSC-AM and -CM data, this positive correlation remained significant (p=2.58e-12 and p=1.86e-3 respectively), but was not as strong (Spearman's r=0.453 and 0.236 respectively). The 'blue' module contains parameters most closely related to removal of calcium from the sarcoplasm via PMCA, NCX, and SERCA (gpCa, [Na_i], gSERCA). Whereas, the 'purple' module's parameters are mostly more related to maintaining the total calcium content of the sarcoplasm. These parameters related to both calcium influxes into the sarcoplasm via the sarcolemma and sarcoplasmic reticulum (gCaB, rSR_l), and also buffers that act to sequester calcium ions within the sarcoplasm and delay calcium extrusion from the cell (B_TRPN, B_CMDN). However, it should be noted that gNCX

is also present in the 'purple' module.

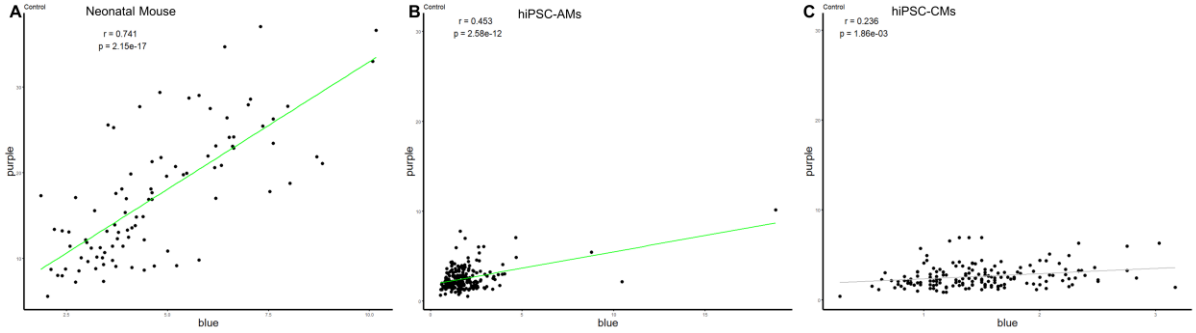

Figure 5-6. Further grouping of functionally-related calcium handling-associated genes reveals positive correlations across all cardiomyocyte groups.

A) Neonatal mouse cardiomyocytes
B) hiPSC-AMs
C) hiPSC-CMs

Each panel displays a scatter plot of the 'purple' module against the 'blue' module. Each plot then has the respective linear line of best fit plotted. Each line is coloured by the respective Pearson's correlation coefficient (green > 0.333, 0.333 ≤ grey ≥ -0.333, red < -0.333). The line of best fit is solid if the respective correlation's adjusted p-value ≤ 0.05, and dashed if p-value > 0.05.

c. Discussion.

i. Transcriptomic requirements of a dynamic system.

Firstly, my work builds on the work of Riabiz et al. to demonstrate that the inter-cell correlation network of calcium handling-related ion fluxes and concentrations is also present at the transcriptional level encoding the individual proteins that control these ion movements in mouse cardiomyocytes. Interestingly, I observed that whereas Riabiz et al. observed a negative correlation between the partially opposing groups of 'blue' and 'purple' parameters, I observed a strong positive correlation between these two groups. Intuitively, this is reasonable to expect, and in fact is arguably a necessary condition for the negative correlation observed by Riabiz et al. For a system with components that interact dynamically, such as opposing ion fluxes, the system requires that the relative ratios of these components would affect the ability of their dynamic behaviour to constrain the system. Thus, beyond post-transcriptional and post-translational regulation, some degree of positive correlation between the mRNA encoding interacting elements of this calcium handling system is likely a necessary condition to establish the relative ratios of the various proteins involved. This work may be important to help improve the accuracy of quantitative computational models of the calcium transient, through understanding the correlation networks that govern their dynamic interactions. Furthermore, my approach to describe the different Hinch model parameters at the level of their gene expression distributions, across both magnitude- and dispersion-dependent measures and only dispersion-dependent measures, might provide further information to help constraint the posterior estimates of the respective parameters in future work by Riabiz et al.

ii. Transcriptomic calcium handling network coordination in hiPSC-CMs

The second pertinence of my findings here is to understanding calcium handling in hiPSC-CMs. Whereas in the mouse cardiomyocytes, a network of strongly positive or negative relationships

became apparent at the level of inter-parameter correlation, there were only a few such strong correlations in the hiPSC-CMs and -AMs. Of note, it is interesting that in both the hiPSC-CMs and hiPSC-AMs the same parameters displayed the strongest correlations (gSERCA, gNCX, and B_TRPN). However, when these parameters are then themselves grouped into the 'blue' and 'purple' informed modules, the positive correlation is now more clearly similar to that observed in the native mouse cardiomyocytes, albeit a weaker positive correlation and much weaker in the CMM hiPSC-CMs. This might indicate that there is some conserved aspect to this positive correlation between the 'blue' and 'purple' modules in cardiomyocytes, as they all display discordant results otherwise but they become concordant when considered explicitly in this manner. It is well-described that hiPSC-CMs do not display the exact same calcium handling properties as native cardiomyocytes, and we observe this in our hiPSC-AMs and -CMs[1]. Perhaps these differences between native and PSC-derived cardiomyocyte calcium handling network coordination are present even at the transcriptomic level as I have described above.

However, our study has a key limitation, beyond those mentioned in X.i.a (discussion) that is likely relevant here; our 'blue' and 'purple' modules are limited in the number of parameters that we were able to include here, given our desire to maintain credible and reasonable mappings from genes to the parameters examined. Thus, our 'blue' and 'purple' modules consist only of gpCa, [Na_i], gSERCA, and then gCaB, gNCX, rSR_l, B_TRPN, B_CMDN respectively. Thus, whilst the positive correlation between these grouped parameters is interesting, it may simply reflect the 3 strongest relationships recognised between gSERCA, gNCX, and B_TRPN in the data. Future work should identify whether this work is reproducible with other datasets, with a particular focus on datasets collecting native cardiomyocyte sequencing using the same protocol as the hiPSC-derived cardiomyocytes.

Chapter 6. Electrophysiology data collection and analysis

a. Introduction

This section is introduced in Chapter 1A and C:

The use of calcium-sensitive and potentiometric dyes is commonplace in cardiac electrophysiology and enables the minimally invasive examination of calcium transients and action potentials. Similarly, patch clamp methods are a much lower throughput, and more invasive technique, but provide the highest spatiotemporal fidelity of electrical activity[453]. However, recently it has been observed that micropipette-based approaches to hiPSC-CM electrophysiology produce a number of unexpected pitfalls and uncertainties in interpretation[454]. Thus, as all-optical investigations become increasingly popular, our analysis pipelines must scale to match the data processing requirements of ever-more complex research questions. This work builds on work by the Lei Group[1], and others who have kindly provided their implementations of their work as open-source and well-documented code [382,383].

b. Methods

c. Results

i. Our iPSC differentiation protocol produces confluent sheets of cardiomyocytes with 2D tissue-like and cellular structure.

A key marker of cellular identity is the appropriate cellular structure and multi-cellular organisation. Our iPSC-AM differentiation protocol was previously established in our group to produce morphologically, structurally, transcriptionally, and functionally atrial-like iPSC-derived cardiomyocytes[1]. I confirmed the reliability of this protocol in producing the expected $TNNT2^{+}$ sheets of hiPSC-AMs, which organised into multi-cellular fibres, with clear subcellular sarcomeric organisation (Figure 6-1).

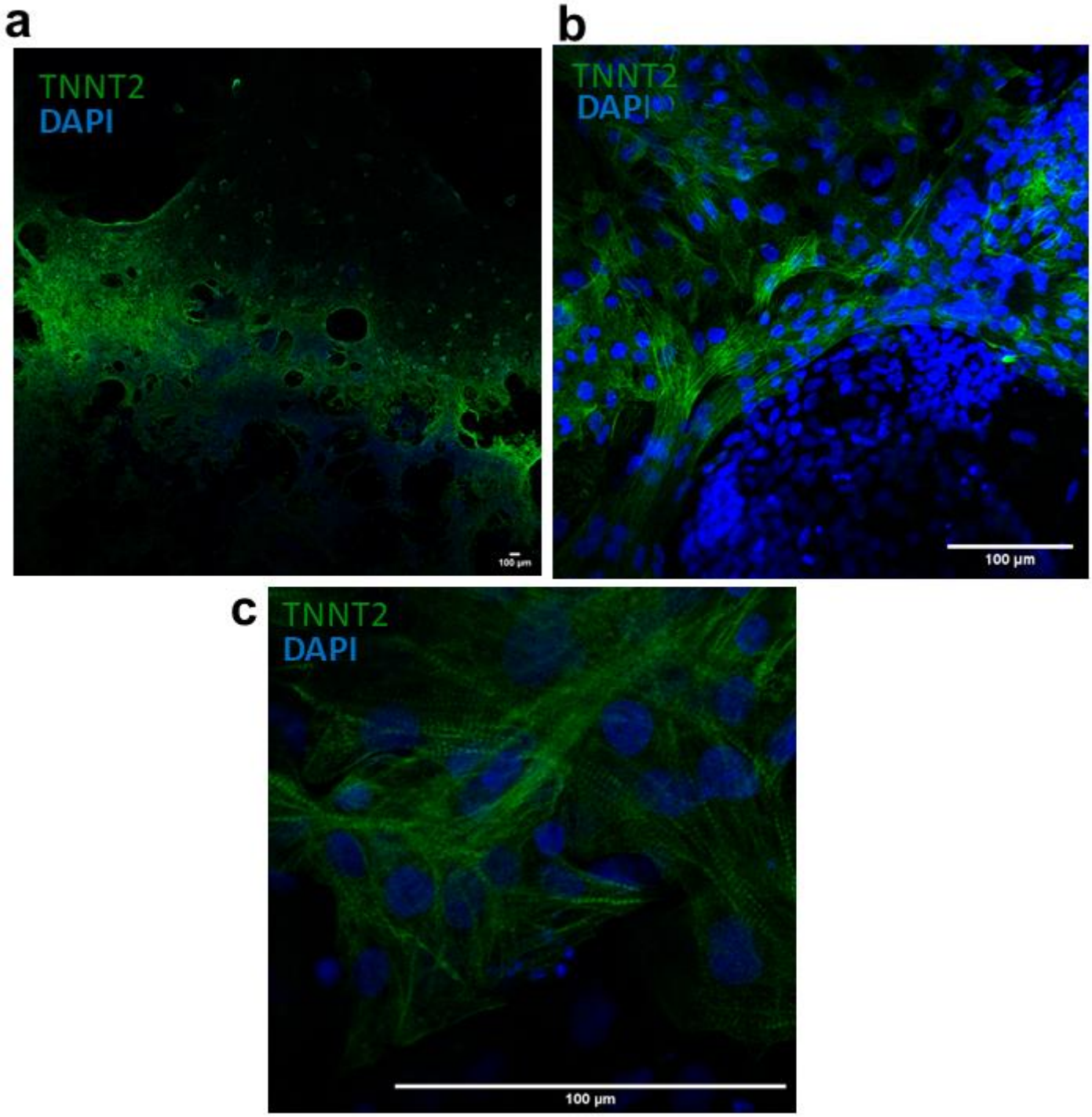

Figure 6-1. Our iPSC differentiation protocol produces confluent sheets of cardiomyocytes with 2D tissue-like and cellular structure.

A) Immunohistochemistry of iPSC-AM cell sheets showing large confluent sheets of TNNT2+ cells.
B) Immunohistochemistry of iPSC-AM cell sheets showing tissue-like organisation of cells into larger fibre-like structures.
C) Immunohistochemistry of iPSC-AM cell sheets showing sarcomeric banding and overall alignment of myofibrils along the long axis of hiPSC-AMs.

ii. Optical imaging set-up preparation

In order to reliably study the hiPSC-CMs I was producing, I sought to establish a robust and method of collecting data that integrating into my standard cell culture workstreams. I designed and specified a new pair of carbon electrodes that would fit in a standard Nunc 4-well plate to enable me to electrically pace the hiPSC-CMs within the dish. I then produced a micro-superfusion system based that enabled me to position all components of my pacing and superfusion rig into the well without disrupting access to the camera. These pacing electrodes could be controlled programmatically using custom Spike2 scripts that I adapted.

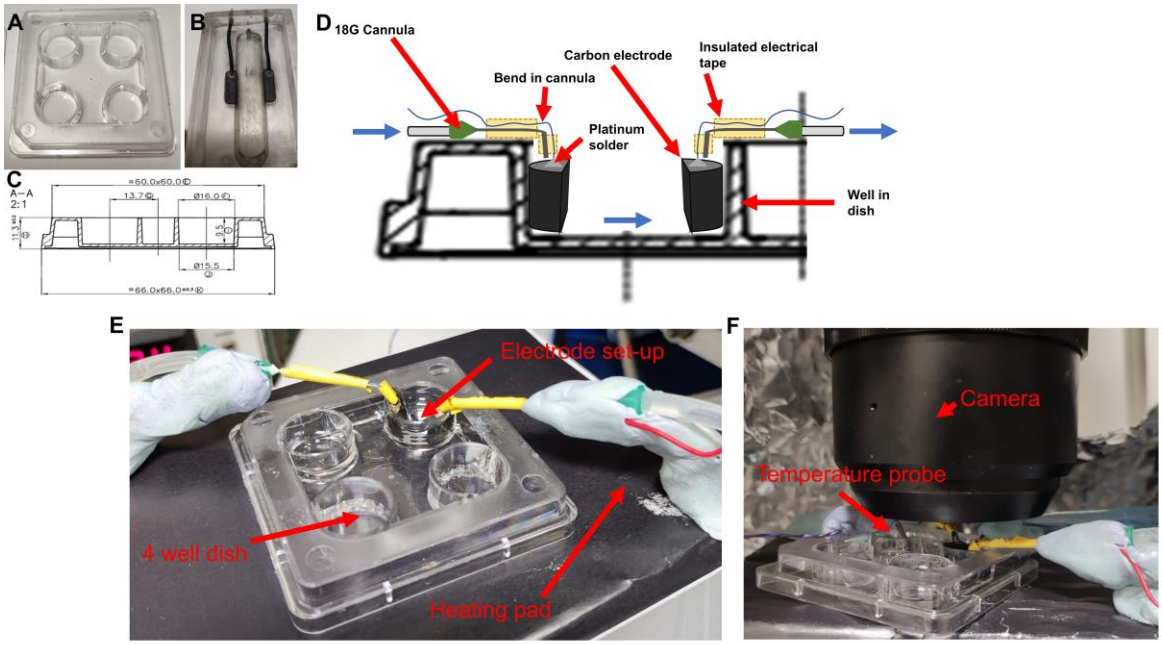

Figure 6-2. I designed and implemented a novel system for imaging hiPSC-CM monolayers in situ.

A) An example Nunc 4-well dish that was used for culturing hiPSC-CMs.
B) The original pacing platform that inspired the new set-up.
C) An extract of the Nunc 4-well dish from its technical drawing, which was used as a basis for designing the novel carbon electrode pacing set-up.
D) A labelled diagram showing how the carbon electrode pacing and perfusion rig sits within the wells during experiments.
E) A wider example showing how the electrodes and perfusion system could be placed into the wells.
F) An example demonstrating how the entire set-up was designed to enable multi-parameter monitoring with continuous thermal control, perfusion, pacing, and optical data collection.

Following preliminary experiments using calcium-sensitive and potentiometric dyes (data not shown), I established a complete imaging set-up optimised for the high throughput collection of optical dye-based electrophysiological data from hiPSC-CMs. I implemented a gravity-fed superfusion system, with controllable automatic switching between different solutions, and independent outflow control to remove solution from the well. The set-up was optimised to 37±0.5°C using a combination of a heating pad and a in-flow solution heater. This system enabled me to record robust electrophysiological signals from hiPSC-CMs – including both high

signal-to-noise calcium dyes and lower signal-to-noise potentiometric dyes.

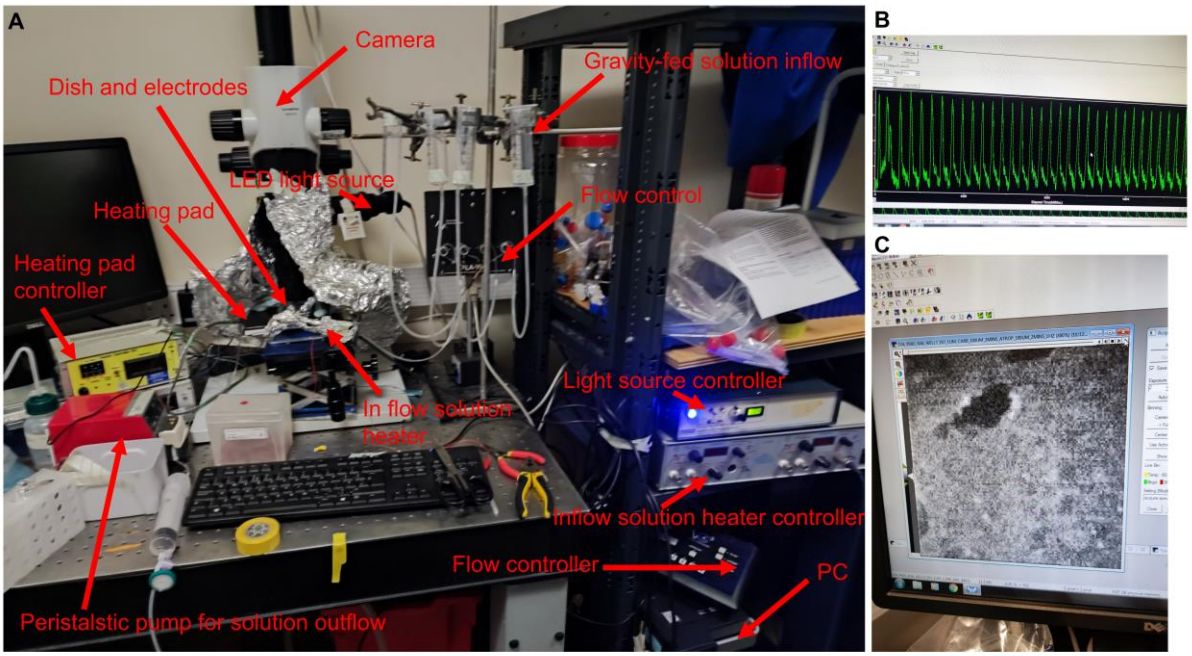

Figure 6-3. I implemented a novel imaging set-up to enable high-/mid-throughput imaging of hiPSC-CM monolayers locally.

A) An image demonstrating the set-up from the PC and Camera used to control the image capture, through to the rapid solution changing perfusion and heating system.
B) A representative trace recorded from a FluoVolt potentiometric recording from an hiPSC-AM monolayer captured using MetaMorph.
C) An example of an hiPSC-AM monolayer as recorded on MetaMorph.

iii. Patch-clamp single-cell electrophysiology

I also sought to establish a single-cell electrophysiology approach using patch clamp. I first had to optimise the production of glass microelectrodes, trying several pipette pullers. Initial attempts to patch clamp were unsuccessful whilst using 'sharp' microelectrodes around 35-50 MΩ. However, I then attempted to use more conventional 'patch' microelectrodes around 3-5 Ω and was able to establish successful whole-cell configurations on a limited number of hiPSC-CMs. I did observe individual cardiomyocytes with both quiescent and spontaneous activity under the single-cell rig. However, I was unable to record any action potentials arising from either internal current injection or external field stimulation despite several attempts across different batches of hiPSC-CMs.

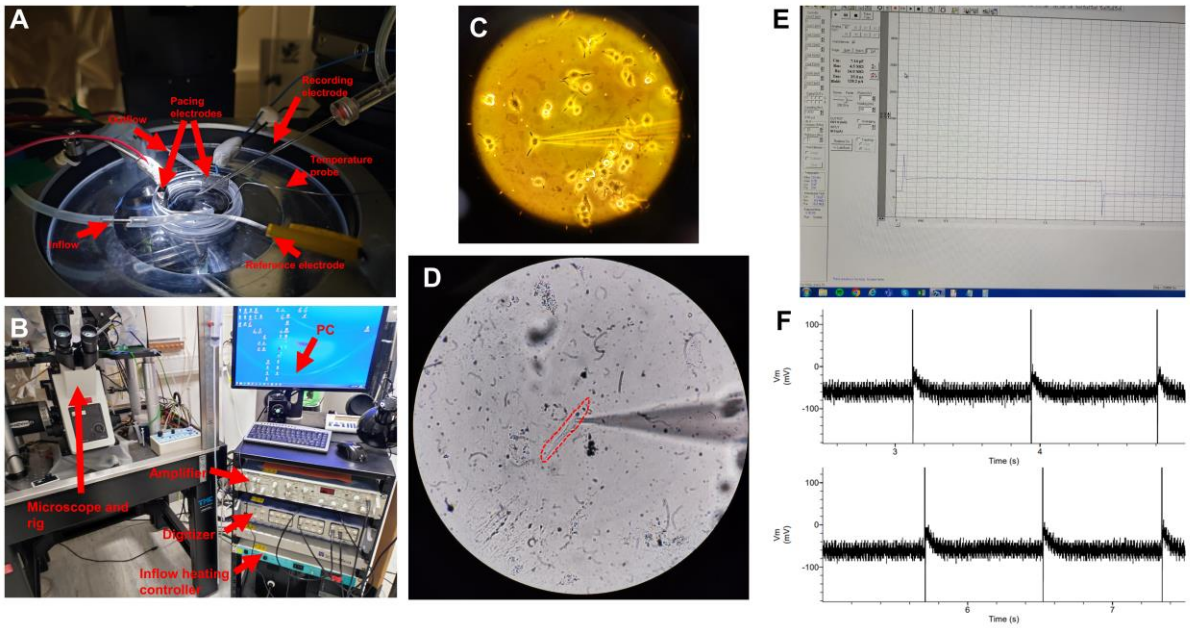

Figure 6-4. I established a workflow for single-cell electrophysiology of hiPSC-AMs.

A) A labelled image of the set-up used in the Swietach laboratory (DPAG, Oxford). I established the parameters to enable temperature-controlled perfusion of isolated single hiPSC-AMs.
B) A labelled image of the computer set-up used to record traces with pClamp v 10.
C) Exemplar HEK293 cells with successful whole-cell voltage clamp achieved in the Tammaro laboratory (Pharmacology, Oxford).
D) An example of an isolated hiPSC-AM highlighted within the red dashed line, with the micropipette attached.
E) Representative trace recorded upon entering whole-cell patch of hiPSC-AM.
F) Exemplar traces recorded upon field stimulation with an hiPSC-AM in whole-cell. However, this is believed to be most likely a capacitance current from the bath solution.

iv. Optical analysis method development

After having established and optimised a mid- to high-throughput method of optical imaging data collection from hiPSC-CMs, I sought to expand upon existing analytical pipelines and methods with statistical testing and comparison in mind. In particular, I built upon the work of Dr. Tomek's COSMAS as a framework skeleton[382]. First, I added the feature that beyond loading video files from specified folders, and import them with customisable settings, they would now be organised depending on specific experimental set-ups, such as by the day of the experiment. The pipeline automatically selects regions of interest (ROIs) depending on average signal amplitude across the video. However, I added the feature that now the user can retrospectively exclude erroneous pixels of noise that are included as ROIs.

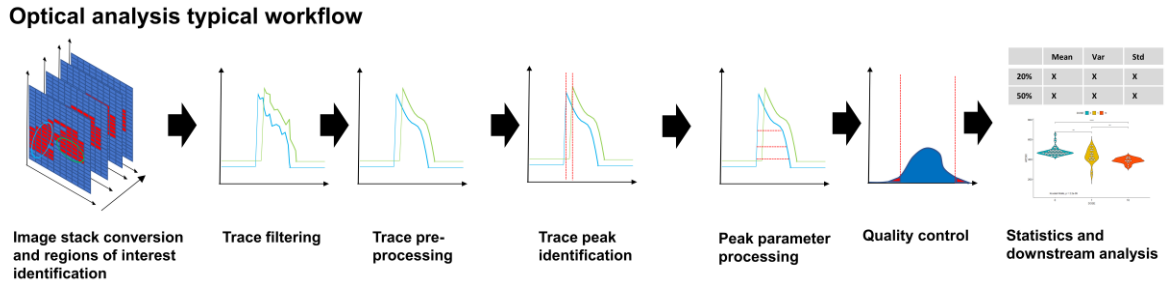

Figure 6-5. My optical data analysis pipeline builds on existing work to deepen the quality control and statistical output.

After having established more robust spatial quality control whilst leveraging the advantage of programmatic access to image files, I then sought expand the analytical tools with regards to the analysis of the underlying activation traces. Again, I used COSMAS as a framework, with its use of a comb-like peak detection process and parameter measurements. I first added additional parameters, such as the time-to-peak, a common metric that relates to upstroke phase 0 of the action potential. I also utilised the approach of OptiQ (Cairn Research) and implemented two separate forms of signal processing to account for the different typical noise profiles of the depolarisation and repolarisation periods of the action potential. I used an initial minimally restrictive Savitsky-Golay filter to filter and correct the baseline using a fitted polynomial, as implemented in COSMAS. This is then used to segment the traces into individual activations. Then, for each activation, I identify the initial moment of depolarisation of the trace precisely by first identifying the peak of the first derivative signal, which corresponds to the maximum upstroke velocity, and then I use this to search for the maximum second derivative signal only before the first derivative peak. This second derivative maximum before the maximum upstroke velocity corresponds to the beginning of the upstroke. I then use this to segment the baseline corrected but unfiltered signal into the phase 4 of the action potential (pre-depolarisation), and from the peak of the action potential onwards (repolarisation). The time between the end of the pre-depolarisation phase and the start of the repolarisation phase gives the time-to-peak, without the impacts of filtering. I then filter the repolarisation portion of the activation trace using a 2nd order Butterworth filter using zero-phase filtering to remove any effect on phase shift. The now filtered action potential is then analysed using the standard method from COSMAS, whilst using the initial portion of the upstroke as the beginning of the action potential. I then perform additional manual quality control to exclude specific pixels if appropriate. For example, if pixels fail to pace at 1:1 or display ectopics.

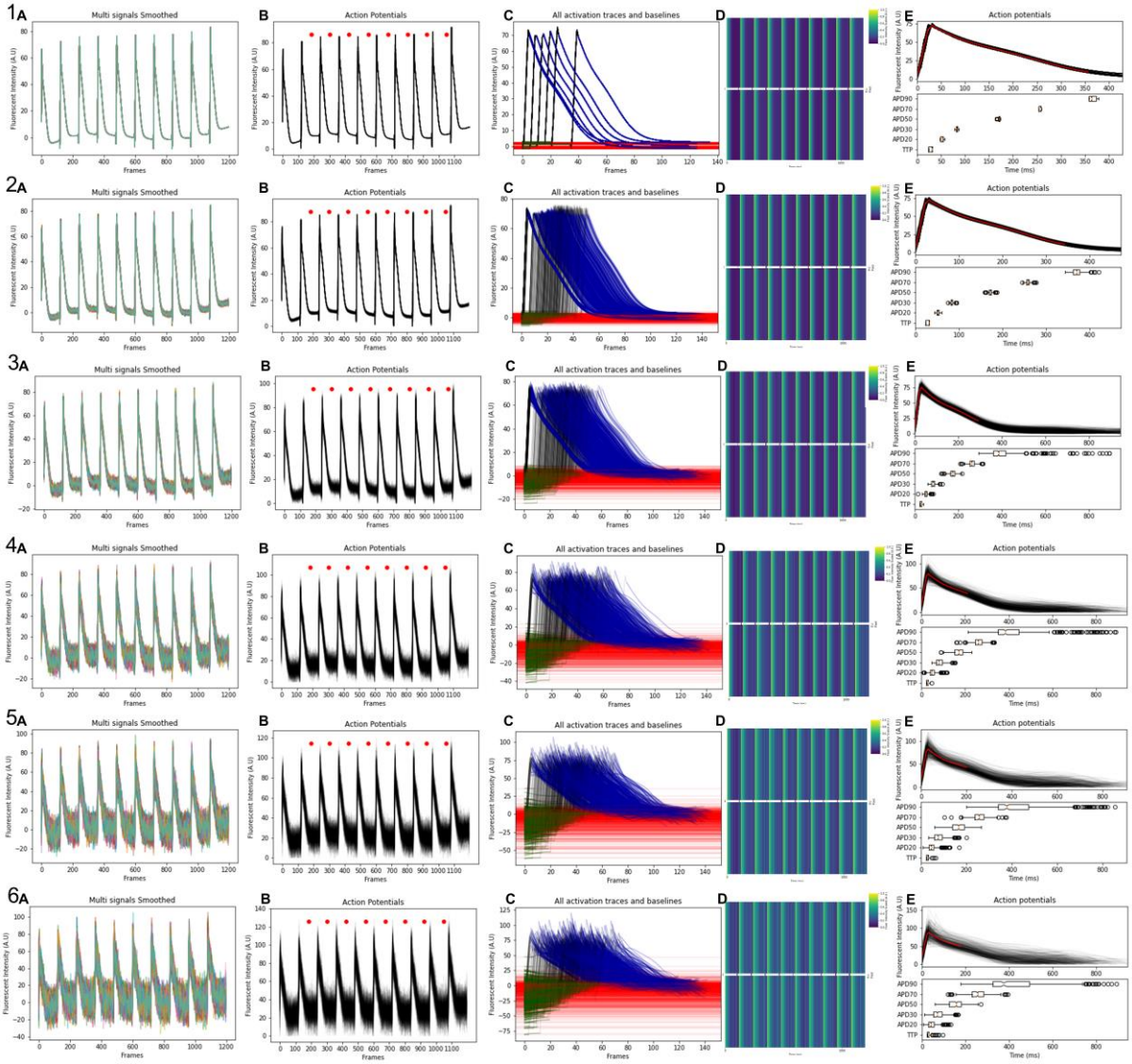

Figure 6-6. I quantified the measurement sensitivity to Gaussian noise.

A) Initial trace from Onal 2017 filtered by Savitzky-Golay filter. B) The trace segmented by the 'comb' of COSMAS. C) The sum of traces from 100 repeats of Gaussian noise added to each trace by the respective %, with the smoothed trace in blue, the baseline in red, and the pre-depolarisation trace in green. D) A heatmap of individual traces, enabling interactive quality control in a pixel-specific manner. E) The final output of traces, with the average trace plotted in red. The lower panel displays the distribution of the respective parameters on the y-axis against time on the x-axis. The boxplot is centred around the median represented by a vertical line in orange. The notches then describe the 95% CI. The limits of the box describe the IQR. The extended error bars then describe Q1 or Q3 + 1.5IQR. Observations beyond this are plotted as individual dots.

1) 1% Peak height added as Gaussian noise along trace.
2) 2% Peak height added as Gaussian noise along trace.
3) 5% Peak height added as Gaussian noise along trace.
4) 10% Peak height added as Gaussian noise along trace.
5) 15% Peak height added as Gaussian noise along trace.
6) 20% Peak height added as Gaussian noise along trace.

v. Validation and robustness to noise

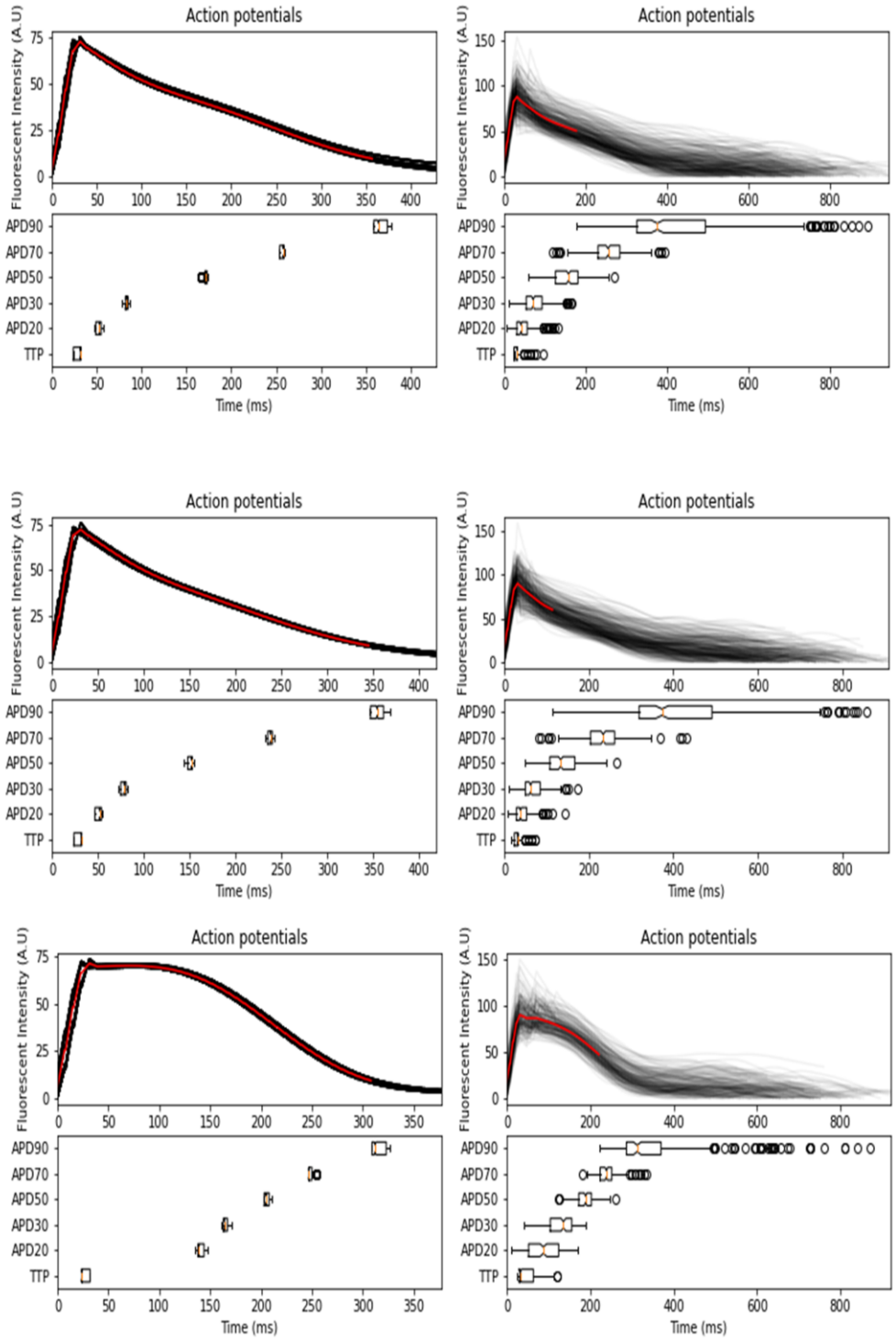

Figure 6-7. Even with extreme Gaussian noise, our data analysis pipeline was fairly accurate.

Each row represents a different computational model of the human atrial action potential.

The top row is Onal et al 2017. The middle row is Grandi et al 2011. The bottom row is Courtemanche et al 1998.

The left panel represents the respective 100 traces with no added noise. The right panel represents the 100 traces with 20% of peak height added as random Gaussian noise to each trace. The top plot within each panel represents all the traces overlaid, with the mean trace plotted in red. The bottom plot within each panel represents the respective parameters on the y-axis, and their times on the x. The boxplot is centred

around the median represented by a vertical line in orange. The notches then describe the 95% CI. The limits of the box describe the IQR. The extended error bars then describe Q1 or Q3 + 1.5IQR. Observations beyond this are plotted as individual dots.

I sought to validate my updated analytical methodology using computational action potential data. I generated data from 3 different computational models of the human atrial action potential, across both triangular and 'dome and spike' known atrial potential morphologies[385-387]. I first established that my updated methodology could accurately identify different parameters across the action potential, from TTP, through to different action potential durations. Thus, my additions to the filtering had not grossly affected the ability of the COSMAS[382] framework to measure different action potential parameters.

Next, I sought to quantify the sensitivity of the measurements to noise. I added Gaussian noise at varying degrees up to 20% of peak height across 100 simulations per model. For each model, every measurement was statistically significantly different across the different amounts of added noise. However, the median measurement was largely unaffected even at 20% noise across models. Measurement error was heavily model-dependent and parameter-dependent. For example, at 20% added noise, TTP was unaffected in 2 out 3 models, and only differed by 1 frame in the Courtemanche model. However, APD20 was the most affected in the Grandi model, with a median 6 frame error in measurement at 20% noise. However, APD90 had the most dispersion at the higher noise levels. Broadly, the measurement error remained within acceptable bounds even with extreme noise at 20% of the peak height. Whilst further validation is required to characterise the complete capabilities of this methodology, the measurement error was mostly resilient to even a high degree of noise.

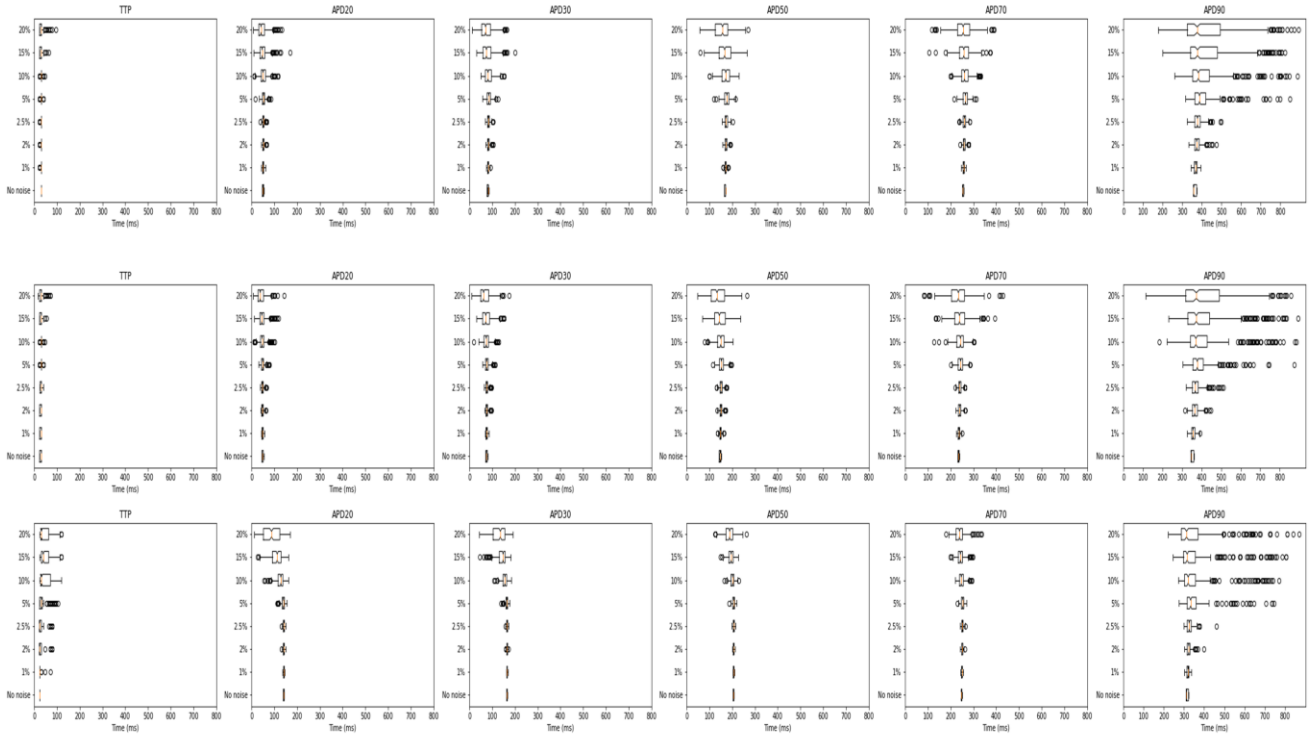

Figure 6-8. Even at high amounts of noise, the average measurement is mostly resistant across different action potential morphologies.

Each row represents a different computational model of the human atrial action potential.

The top row is Onal et al 2017. The middle row is Grandi et al 2011. The bottom row is Courtemanche et al 1998.

Each column represents a different parameter measured.

Each plot is the respective model and parameter, with the y-axis denoting increasing % of noise added, and the x-axis representing the time duration of that parameter in ms. The boxplot is centred around the median represented by a vertical line in orange. The notches then describe the 95% CI. The limits of the box describe the IQR. The extended error bars then describe Q1 or Q3 + 1.5IQR. Observations beyond this are plotted as individual dots.

Group	Parameter	Median at baseline (ms)	Difference at 20% added Gaussian noise from baseline median (frames/8 ms)	Degrees of freedom	H coefficient	Krusal-Wallis all noise level comparison P value	Benjamini-Hochberh adjusted p value
Onal et al 2017	TTP	32	0	7	76.56	6.93e-14	6.93e-14
	APD20	53	-2	7	241.60	1.70e-48	3.06e-48
	APD30	83	-2	7	182.82	4.95e-36	6.86e-36
	APD50	171	-2	7	219.88	7.00e-44	1.05e-43
	APD70	258	-1	7	253.96	3.97e-51	8.94e-51
	APD90	364	2	7	321.66	1.42e-65	5.11e-65
Grandi et al 2011	TTP	32	0	7	138.47	1.06e-26	1.19e-26
	APD20	52	-2	7	294.11	1.09e-59	3.28e-59
	APD30	79	-2	7	174.16	3.33e-34	4.28e-34
	APD50	152	-2	7	121.31	4.08e-23	4.32e-23
	APD70	238	0	7	162.06	1.18e-31	1.42e-31
	APD90	354	2	7	253.27	5.58e-51	1.12e-50
Courtemanche et al 1998	TTP	24	1	7	751.35	5.81e-158	3.49e-157
	APD20	139	-6	7	905.43	3.23e-191	5.81e-190
	APD30	164	-3	7	788.51	5.58e-166	5.02e-165
	APD50	205	-2	7	424.77	1.16e-87	5.20e-87
	APD70	247	0	7	272.25	5.04e-55	1.29e-54
	APD90	312	1	7	234.74	4.86e-47	7.96e-47

Table 6-1. Statistical results comparing baseline and added noise across computational models.

d. Optical analysis discussion

i. Re-establishing local use of hiPSC-AM protocol

Prior to optimising downstream assays, I first confirmed the reproducibility of the G2RA protocol to produce beating cardiomyocytes. The technique had previously been developed by Dr. Faizzan Ahmad, and then worked on locally by Dr. Yongcheng Jin. However, since then the technique had not been used locally, and the local knowledge of the technique had been lost. Alongside initial optimisation of hiPSC culture and fluorescent dye-based calcium handling experiments (data not shown), I wanted to confirm the structural aspects of hiPSC-CM production as well. Whilst additional co-staining in the immunofluorescence could have helped confirm the retained atrial-like structural properties of the hiPSC-AMs, I elected to focus on describing their functional properties, which had been less well-described locally in our earlier work than the structural aspects. I made this decision on the basis that functional properties of hiPSC-AMs, particularly with regards to the electrophysiological and pharmacological properties, would be downstream of the appropriate structure, and most important for ascertaining the putative impact of them as a useful model of native human atria.

ii. Producing a high-/mid-throughput dynamic electrophysiology recording set-up

I built on our existing electrophysiology set-up to produce a fully adapted set-up for the study of hiPSC-CM electrophysiology. I produced a set-up capable of dynamic electrical and pharmacological interrogation of hiPSC-CM function, whilst maintaining control of temperature and pH. This enabled me to optimise not only our fluorescent calcium dye experiments locally, but also our ability to record hiPSC-CM membrane potential, which had not successfully been done before by our group. I attempted several fluorescent potentiometric dyes prior to optimising FluoVolt (data not shown). Furthermore, I produced promising initial results in establishing our local technique for the single-cell patch clamp electrophysiology of hiPSC-CMs. After much optimisation (data not shown), I was able to briefly record traces consistent with whole-cell recordings in voltage clamp. However, further work is required to optimise this technique locally. In particular, the challenge of hiPSC-CM spontaneous activity added the additional challenge of attempting to record from beating cells.

iii. Establishing a reliable, accurate, and scalable solution for optical electrophysiological analysis of hiPSC-CMs

The most importance piece of work from this chapter relates to expanding on existing optical analysis workflows. After first attempting to use a range of existing optical analysis methods, I found that my results were either accurate but agonisingly slow to process, or were rapid but wildly inaccurate. Broadly, my adaptation of COSMAS enabled me to implement more rigorous automatic and manual quality control, with a greatly increased depth of output, without compromising on its speed. The use of COSMAS as a working basis enabled me to advance the specific functionalities I desired, without needing to completely re-validate the entire process, with COSMAS showing a very high correlation with leading open-source optical analysis software ElectroMap[383] for detecting activation times (R^2=0.99)[382]. Furthermore, I sought to quantify the sensitivity of the measurement to noise, and to quantify the action potential duration sensitivity to noise in particular, which is counterintuitively rarely done in most benchmarking of similar workstreams. Tomek et al did perform some noise sensitivity analysis in the original COSMAS work, but this was focused on median error in detecting the peak of the signal, which is the strongest signal-to-noise ratio section of all recordings[382]. Reassuring, even with my 20% Gaussian noise of peak height added, I achieved similar levels of robustness to noise as in their most comparable (±0.25 SD, μ=0, Gaussian noise added to a 0-1 normalised signal height

calcium transient) simulation. Tomek et al observed a c. 5 ms median error in detecting peak height[382], and I observed either 0 or 1 frames of error (1 frame = 8 ms) across my 3 models in detecting the time-to-peak, as the most comparable measure. Future work should focus on optimising the filters I used, and identifying the sensitivity of the final output to these in a systematic fashion alongside performing some benchmarking of extant optical analysis pipelines across ease-of-use, scalability, and accuracy to some ground truth dataset.

Chapter 7. Channel pharmacology of hiPSC-AMs

a. Introduction

This section is introduced in Chapter 1 A & C.

The cassette of ion transporters contributes greatly to the precise electrical activity of specific cell types[128,353]. In the heart, one of the most marked differences between the atria and other cardiomyocytes electrophysiologically is the shorter action potential duration of the atria, and their more triangular morphology[386]. This is primarily associated with the differential expression of a number of potassium channels in the atria such as I_{Kur}[455]. Attempts to understand the expression of different potassium channels as a confirmatory signal of atrial phenotypes in hiPSC-AMs has mostly relied on either transcriptomic work, or patch clamp work – both of which have limited interpretability for the contribution of potassium channels to the whole cell action potential in the context of hiPSC-CMs. This Chapter builds on the work of those who originally described these currents (I_{to}, I_{Kur}, and I_{Kr}) and their pharmacology in native atrial cardiomyocytes[150,323,455-462] alongside the seminal work by Feyen et al who performed similar TTX dose-response curves in hiPSC-CMs and the maturity/strength of their TTX-sensitive sodium currents[322].

b. Methods

THE METHODS USED FOR THE DATA IN THIS SECTION ARE PRESENTED IN CHAPTER 2B & C:

c. Results

i. 4-aminopyridine had a variable effect to prolong APD

I then sought to establish the specific electrophysiological profile of our hiPSC-AMs, particularly their atrial-specific potassium channel expression. In order to compare our hiPSC-AM model (G2RA) to existing models, I sought to use an adapted version of the commonly used retinoic acid-only method for producing hiPSC-AMs, where I applied retinoic acid from day 6 – 10 of the standard differentiation protocol (RA[6]). This reliably produced beating sheets of hiPSC-AMs (data not shown). Following preliminary experiments, I used a metabolic purification method to enrich the proportion of cardiomyocytes within my samples. I then assayed these cardiomyocytes between day 27 through to day 35 using potentiometric dyes (FluoVolt) and a dose-response to 4-aminopyridine – an I_{Kur} antagonist[463] (Baseline, 10 uM, 100 uM, 1 mM). At baseline, there was a significant difference between the G2RA and RA[6] groups across all parameters (TTP, APD20, APD30, APD50, APD70, APD90), with the G2RA group having shorter durations and a more triangular action potential morphology. Upon serial addition of 4-AP, both groups displayed a significant prolongation of all durations, apart from APD90. Yet, APD90 did display a significantly different response depending on the dose and the group ($p=0.007837$). This indicates that the two groups did not respond in the same way across doses. In general, the effect of increasing 4-AP dose only had a significant increase in APD from 100 μM and onwards. However, at G2RA, there was a trend for this to increase even at 10 μM, whereas RA[6] showed a trend to stay the same or decrease at 10 μM e.g. APD70 G2RA Baseline 114.4±3.52 ms to 10 μM 133.3±3.3 ms vs RA[6] 187.8±2.06 ms to 163.5±1.65 ms. This generally repeated itself at 100 μM. However, at 1 mM, the opposite appeared to occur and RA[6] now experienced a large prolongation of APD (e.g), but G2RA either stayed the same or decreased slightly. However, the G2RA group demonstrated a lot of variability, with some particularly prolonged APs at 100 μM or above. However, the overall effect was consistent across batches (n>=3) and wells (n>=10).

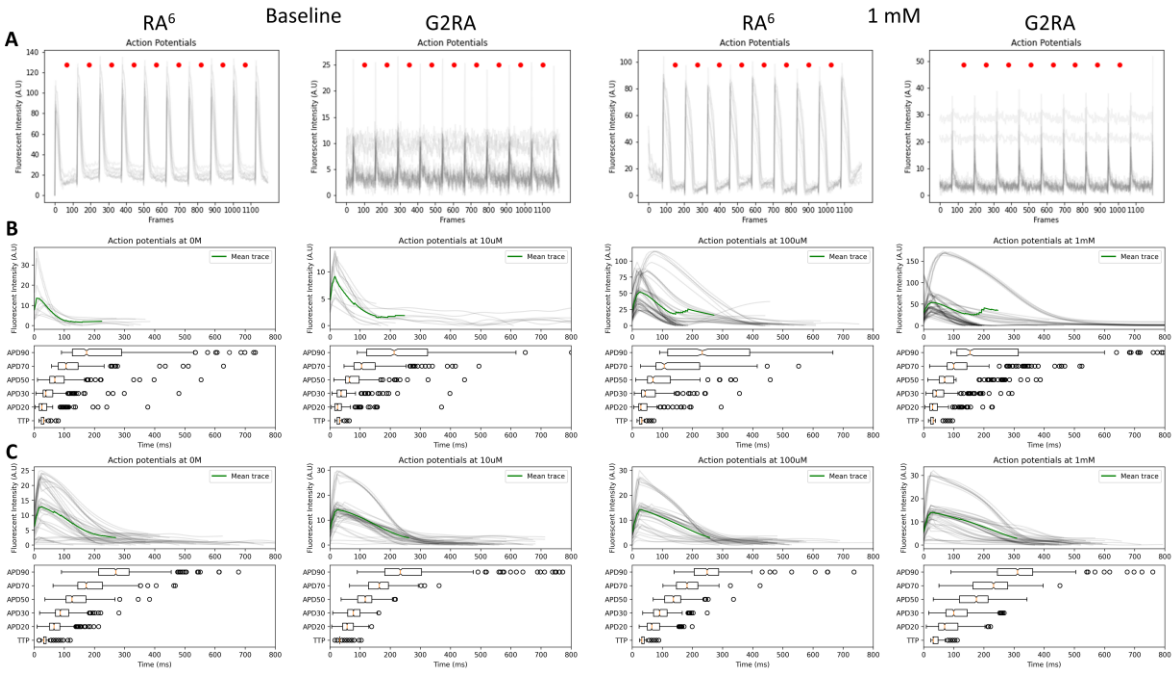

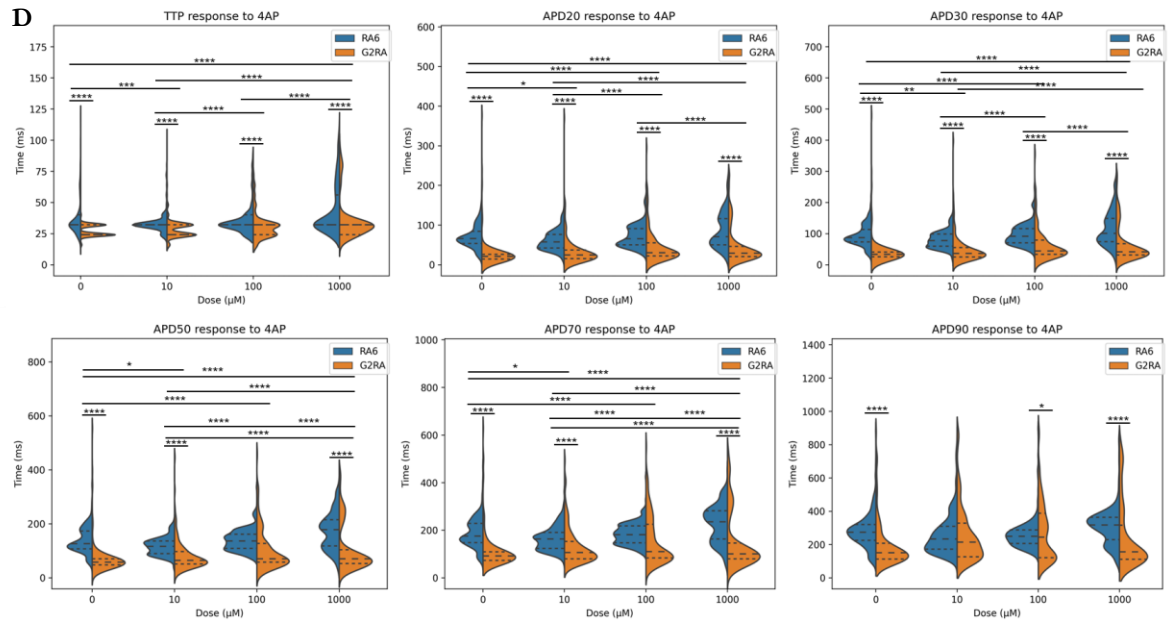

Figure 7-1. 4-AP had prolonged APD in a variable manner across hiPSC-AMs.

A) Representative traces demonstrating the different RA[6] and G2RA groups at baseline, and then at the addition of the maximal dose 1 mM.

B) G2RA responses to 4-AP: each column from left to right represents an increasing dose of 4-AP (Baseline, 10 μM, 100 μM, & 1 mM). The top plot in each panel represents the traces of all action potentials included in the summary statistics for the respective group and dose shown in the plot immediately below. Parameters are shown on the y-axis, with duration on the x-axis in ms. The boxplot is centred around the median represented by a vertical line in orange. The notches then describe the 95% CI. The limits of the box describe the IQR. The extended error bars then describe Q1 or Q3 + 1.5IQR. Observations beyond this are plotted as individual dots.

C) RA[6] responses to 4-AP: each column from left to right represents an increasing dose of 4-AP (Baseline, 10 μM, 100 μM, & 1 mM). The top plot in each panel represents the traces of all action potentials included in the summary statistics for the respective group and dose shown in the plot immediately below. Parameters are shown on the y-axis, with duration on the x-axis in ms. The boxplot is centred around the median represented by a vertical line in orange. The notches then describe the 95% CI. The limits of the box describe the IQR. The extended error bars then describe Q1 or Q3 + 1.5IQR. Observations beyond this are plotted as individual dots.

D) Split violin plots demonstrating each parameter's response to increasing concentrations of 4-AP. From left to right the plots represent: TTP, APD20, APD30, APD50, APD70, & APD90. Within each plot the y-axis displays time in ms, and the x-axis displays the increasing concentrations grouped from left to right. The violin plots at each concentration are split vertically to indicate either the RA[6] (blue), or G2RA (orange) distributions. The dashed line with small spaces indicates the median of each distribution, and the dashed lines either side indicate the first and third quartile. Comparisons were made using a two-way mixed effects ANOVA model, with Benjamini-Hochberg post-hoc p-value adjustment. Post-hoc t-tests were then performed where appropriate and FDR controlled by Benjamini-Hochberg adjustment.
p <= 0.05: *, p <= 0.005: **, p <= 0.0005: ***, and p <= 0.00005: ****.

Parameter	Batches (G2RA)	Wells (G2RA)	Batches (RA^6)	Wells (RA^6)	Source	Sum of Squares	DF1	DF2	Mean Square	F statistic	P-value	P Adj.
TTP	3	12	4	11	Group	1113.73	1	15	1113.73	36.54	0.000022	0.000101
					Dose	656.22	3	45	218.74	12.41	0.000005	0.000750
					Interaction	128.56	3	45	42.85	2.43	0.077429	0.081983
APD20	3	12	3	10	Group	19019.43	1	14	19019.43	42.39	0.000014	0.000095
					Dose	3965.46	3	42	1321.82	9.20	0.000085	0.000254
					Interaction	1404.23	3	42	468.08	3.26	0.030783	0.034631
APD30	3	12	3	10	Group	30848.46	1	14	30848.46	41.32	0.000016	0.000095
					Dose	7832.38	3	42	2610.79	11.27	0.000015	0.000095
					Interaction	2671.70	3	42	890.57	3.84	0.016110	0.020712
APD50	3	12	3	10	Group	44958.80	1	14	44958.80	31.56	0.000063	0.000228
					Dose	21578.33	3	42	7192.78	12.53	0.000005	0.000750
					Interaction	7378.06	3	42	2459.36	4.29	0.009996	0.013841
APD70	3	12	3	10	Group	46381.01	1	14	46381.01	19.43	0.000595	0.001191
					Dose	29159.85	3	42	9719.95	7.64	0.000346	0.010481
					Interaction	16734.13	3	42	5578.04	4.39	0.008971	0.013456
APD90	3	12	3	10	Group	19075.87	1	14	19075.87	6.85	0.020251	0.024301
					Dose	32276.89	3	42	10758.96	2.96	0.043179	0.125474
					Interaction	55369.09	3	42	18456.36	5.072	0.004354	0.007837

Table 7-1. Statistics describing the response of hiPSC-AMs to 4-AP.

Parameter	Group	Concentration of 4-AP (μM)	Median (ms)	IQR (ms)	Mean (ms)	SEM (ms)	CV (%)
TTP	G2RA	0	24	8	27.3	0.19	0.16
	G2RA	10	24	8	28.3	0.28	0.234
	G2RA	100	32	8	30.9	0.45	0.341
	G2RA	1000	32	8	35.3	0.7	0.463
	RA^6	0	32	8	36.8	0.5	0.399
	RA^6	10	32	0	33.7	0.31	0.275
	RA^6	100	32	8	35.7	0.42	0.344
	RA^6	1000	32	24	43	0.67	0.457
APD20	G2RA	0	21	12	29.7	1.86	1.54
	G2RA	10	24	22	35.9	1.74	1.195
	G2RA	100	30	33	46.7	1.82	0.962
	G2RA	1000	29	25.5	46.3	1.82	0.968
	RA^6	0	66	31	70	0.96	0.406
	RA^6	10	57	34	60.5	0.81	0.398
	RA^6	100	65	41	71.5	0.97	0.403
	RA^6	1000	70.5	66.2	84.7	1.5	0.525
APD30	G2RA	0	33	15	43.6	2.3	1.297
	G2RA	10	36	31	49.7	2	0.989
	G2RA	100	44	46	64.3	2.21	0.846
	G2RA	1000	41	36	65.4	2.38	0.895
	RA^6	0	87	40	93.6	1.16	0.366
	RA^6	10	77	39	80.1	0.91	0.335
	RA^6	100	91	46	95.3	1.1	0.342
	RA^6	1000	100.5	74.2	115	1.83	0.47
APD50	G2RA	0	57	23	72.5	2.76	0.935
	G2RA	10	64	46	83.4	2.42	0.714

	G2RA	100	70	70	104.4	3.11	0.732
	G2RA	1000	70	51	108.3	3.61	0.82
	RA[6]	0	126	66	137.3	1.55	0.333
	RA[6]	10	116	47	116.6	1.08	0.275
	RA[6]	100	136	53	138.3	1.3	0.278
	RA[6]	1000	177.5	97	171.1	2.24	0.388
APD70	G2RA	0	92	36	114.4	3.52	0.758
	G2RA	10	106	73	133.3	3.3	0.609
	G2RA	100	110	141	158.9	4.2	0.651
	G2RA	1000	100	67	155.6	4.94	0.782
	RA[6]	0	175	80	187.8	2.06	0.324
	RA[6]	10	163	67	163.5	1.65	0.298
	RA[6]	100	181	71	184	1.5	0.242
	RA[6]	1000	235	118	225.8	2.61	0.342
APD90	G2RA	0	150	94.5	199.6	5.9	0.728
	G2RA	10	214	202	255.8	6.81	0.656
	G2RA	100	244	267	272.6	7.27	0.656
	G2RA	1000	155	205	249.7	8.11	0.799
	RA[6]	0	274	95	278.1	3.4	0.361
	RA[6]	10	233	136	259.5	4.08	0.465
	RA[6]	100	249	81.5	257.5	2.89	0.332
	RA[6]	1000	317	134.8	309.1	3.83	0.367

Table 7-2. Summary statistics of hiPSC-AM response to 4-AP.

ii. Preliminary E-4031 results suggest a prolonging effect on APD

Next, I sought to ascertain the response of our hiPSC-AMs to less atrial-specific potassium channel inhibitors. I used E-4031, an I_{Kr} inhibitor, to examine the response of both G2RA and RA[6] groups to I_{Kr} inhibition – a classical pan-cardiomyocyte repolarising current. I observed that the two groups again had different parameters at baseline. However, with E-4031 increasing in dose from 0, 10 nM, 100 nM, to 1 uM, I observed that there was a trend for prolongation of the different repolarisation phases of the action potential only in the RA[6] group and not in the G2RA group. However, this only reached significance at 1 uM. Unfortunately, my data analysis pipeline failed to process the majority of these action potentials and thus a low n and N number, with somewhat unexpected action potential morphologies compared to the representative traces. Thus, whilst I observed a trend for a dose-dependent increase in action potential duration with E-4031, I could not verify this and repeat experiments are necessary to confirm this.

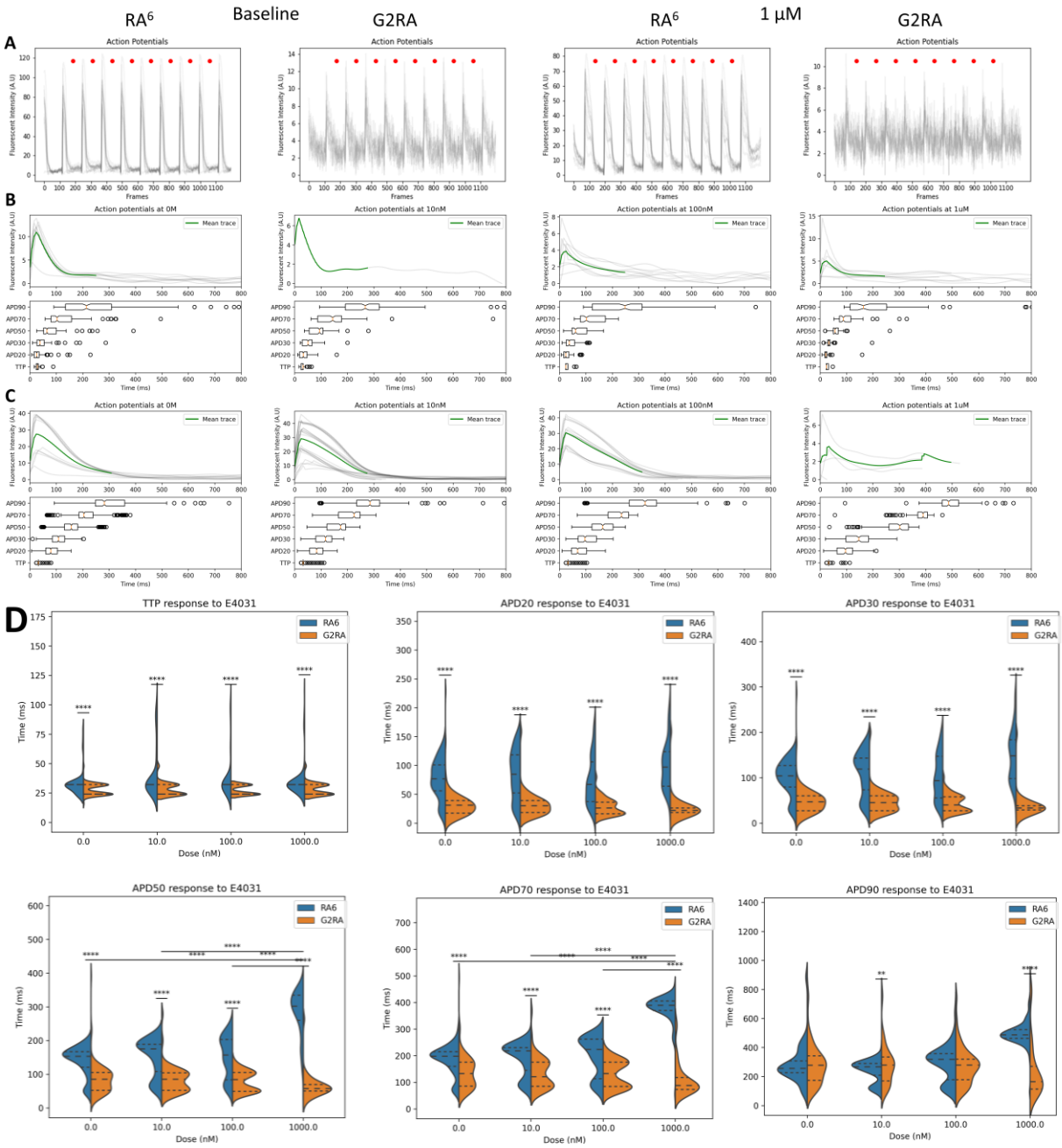

Figure 7-2. E-4031 had a trend to prolong APD across hiPSC-AMs.

A) Representative traces demonstrating the different RA[6] and G2RA groups at baseline, and then at the addition of the maximal dose 1 μM.

B) G2RA responses to E-4031: each column from left to right represents an increasing dose of E-4031 (Baseline, 10 nM, 100 nM, & 1 μM). The top plot in each panel represents the traces of all action potentials included in the summary statistics for the respective group and dose shown in the plot immediately below. Parameters are shown on the y-axis, with duration on the x-axis in ms. The boxplot is centred around the median represented by a vertical line in orange. The notches then describe the 95% CI. The limits of the box describe the IQR. The extended error bars then describe Q1 or Q3 + 1.5IQR. Observations beyond this are plotted as individual dots.

C) RA[6] responses to E-4031: each column from left to right represents an increasing dose of E-4031 (Baseline, 10 nM, 100 nM, & 1 μM). The top plot in each panel represents the traces of all action potentials included in the summary statistics for the respective group and dose shown in the plot immediately below. Parameters are shown on the y-axis, with duration on the x-axis in ms. The boxplot is centred around the median represented by a vertical line in orange. The notches then

describe the 95% CI. The limits of the box describe the IQR. The extended error bars then describe Q1 or Q3 + 1.5IQR. Observations beyond this are plotted as individual dots.

D) Split violin plots demonstrating each parameter's response to increasing concentrations of E-4031. From left to right the plots represent: TTP, APD20, APD30, APD50, APD70, & APD90. Within each plot the y-axis displays time in ms, and the x-axis displays the increasing concentrations grouped from left to right. The violin plots at each concentration are split vertically to indicate either the RA^6 (blue), or G2RA (orange) distributions. The dashed line with small spaces indicates the median of each distribution, and the dashed lines either side indicate the first and third quartile. Comparisons were made using a two-way mixed effects ANOVA model, with Benjamini-Hochberg post-hoc p-value adjustment. Post-hoc t-tests were then performed where appropriate and FDR controlled by Benjamini-Hochberg adjustment.
p <= 0.05: *, p <= 0.005: **, p <= 0.0005: ***, and p <= 0.00005: ****.

Parameter	Batches (G2RA)	Wells (G2RA)	Batches (RA^6)	Wells (RA^6)	Source	Sum of Squares	DF1	DF2	Mean Square	F statistic	P-value	P Adj.
TTP	1	4	1	4	Group	511.94	1	6	511.94	55.08	0.000308	0.000924
					Dose	95.73	3	18	31.91	2.33	0.108250	0.194589
					Interaction	79.95	3	18	26.65	1.95	0.157882	0.177618
APD20	1	4	1	4	Group	18176.46	1	6	18176.46	47.74	0.000455	0.001169
					Dose	1521.92	3	18	507.31	1.85	0.174886	0.264429
					Interaction	2306.07	3	18	768.69	2.80	0.069663	0.083596
APD30	1	4	1	4	Group	31685.73	1	6	31685.73	62.34	0.000219	0.00788
					Dose	4173.64	3	18	1391.21	2.83	0.067831	0.083596
					Interaction	7052.81	3	18	2359.94	4.78	0.012777	0.019165
APD50	1	4	1	4	Group	70678.60	1	6	70678.60	83.79	0.000096	0.000574
					Dose	25833.38	3	18	8611.13	9.40	0.000588	0.001323
					Interaction	41351.52	3	18	13783.84	15.04	0.000038	0.00574
APD70	1	4	1	4	Group	84217.41	1	6	84217.41	62.62	0.000216	0.00788
					Dose	47055.58	3	18	15685.19	8.51	0.000989	0.001978
					Interaction	74642.10	3	18	24880.70	13.49	0.000074	0.000574
APD90	1	4	1	4	Group	31660.46	1	6	31660.46	13.15	0.011020	0.018033
					Dose	62954.96	3	18	20984.99	3.08	0.053841	0.074550
					Interaction	107346.70	3	18	35782.23	5.25	0.008871	0.015968

Table 7-3. Statistics describing the response of hiPSC-AMs to E-4031.

Parameter	Group	Concentration of E-4031 (μM)	Median (ms)	IQR (ms)	Mean (ms)	SEM (ms)	CV (%)
TTP	G2RA	0	24	8	27.8	0.46	0.165
	G2RA	0.01	24	8	28.2	0.55	0.197
	G2RA	0.1	24	8	27.4	0.39	0.144
	G2RA	1	24	8	28.2	0.52	0.185
	RA^6	0	32	0	33.2	0.76	0.337
	RA^6	0.01	32	0	41	1.44	0.52
	RA^6	0.1	32	0	38.1	1.31	0.506
	RA^6	1	32	0	35.1	1.01	0.425
APD20	G2RA	0	31	22	32.4	2.56	0.806
	G2RA	0.01	30	21	31.8	2.15	0.69
	G2RA	0.1	26	20	28.4	1.4	0.503
	G2RA	1	22	8	26	2.38	0.933
	RA^6	0	76.5	45	76.2	2.25	0.44
	RA^6	0.01	84.5	66	82.7	2.82	0.507

	RA[6]	0.1	67	68.8	73.5	2.77	0.561
	RA[6]	1	97	59.8	100.3	2.8	0.415
APD30	G2RA	0	47	33	48.9	3.18	0.663
	G2RA	0.01	45	33	47.6	2.66	0.57
	G2RA	0.1	40	31	44	1.86	0.431
	G2RA	1	33	9	37.9	2.85	0.766
	RA[6]	0	104	20	74.3	2.16	0.193
	RA[6]	0.01	71	38	75	4.07	0.36
	RA[6]	0.1	86	24	90.6	3.27	0.239
	RA[6]	1	120	30	124.8	3.79	0.201
APD50	G2RA	0	85	53	85.4	4.53	0.541
	G2RA	0.01	85	52	84.7	4.04	0.486
	G2RA	0.1	84	56	78.8	2.88	0.373
	G2RA	1	57	19	64.5	3.78	0.598
	RA[6]	0	153	46.8	140.3	2.9	0.307
	RA[6]	0.01	175	80.8	148.7	3.71	0.371
	RA[6]	0.1	156.5	120	150.7	4.08	0.402
	RA[6]	1	302	74.5	280.9	4.62	0.245
APD70	G2RA	0	133	89	138.4	6.41	0.472
	G2RA	0.01	121	90	136.3	5.86	0.438
	G2RA	0.1	133	91	129.9	4.8	0.377
	G2RA	1	88	45	110.2	6.15	0.569
	RA[6]	0	153	46.8	140.3	2.9	0.307
	RA[6]	0.01	175	80.8	148.7	3.71	0.371
	RA[6]	0.1	156.5	120	150.7	4.08	0.402
	RA[6]	1	302	74.5	280.9	4.62	0.245
APD90	G2RA	0	197.5	55	185.1	3.6	0.289
	G2RA	0.01	218	85	186.6	4.17	0.333
	G2RA	0.1	223.5	149	200.1	4.86	0.361
	G2RA	1	389.5	36	378.5	3.36	0.132
	RA[6]	0	256	81.5	281.9	9.06	0.478
	RA[6]	0.01	267	81	239.5	4.98	0.309
	RA[6]	0.1	318	178.8	291.4	8.08	0.412
	RA[6]	1	487	60.8	495	5.02	0.151

Table 7-4. Summary statistics for hiPSC-AM response to E-4031.

iii. TTX demonstrated a minimal effect on action potential generation

I then sought to ascertain more about the depolarising currents responsible for the upstroke of the hiPSC-AM action potential. I used TTX to examine the sodium currents present at baseline, 100 nM, 1 uM, 10 uM and 100 uM. In both the RA[6] and G2RA groups, even with 100 uM TTX, cells continued to respond to field stimulation. I observed a slight trend to increase TTP in the RA[6] group, yet this did not reach significance. However, I observed a dose-dependent prolongation of the action potential duration, which others have used as a marker of TTX on hiPSC-CMs[322]. Yet, further experiments are required to increase the number of batches this was

performed on to further confirm this result. Additionally, I would use a fresh source of TTX.

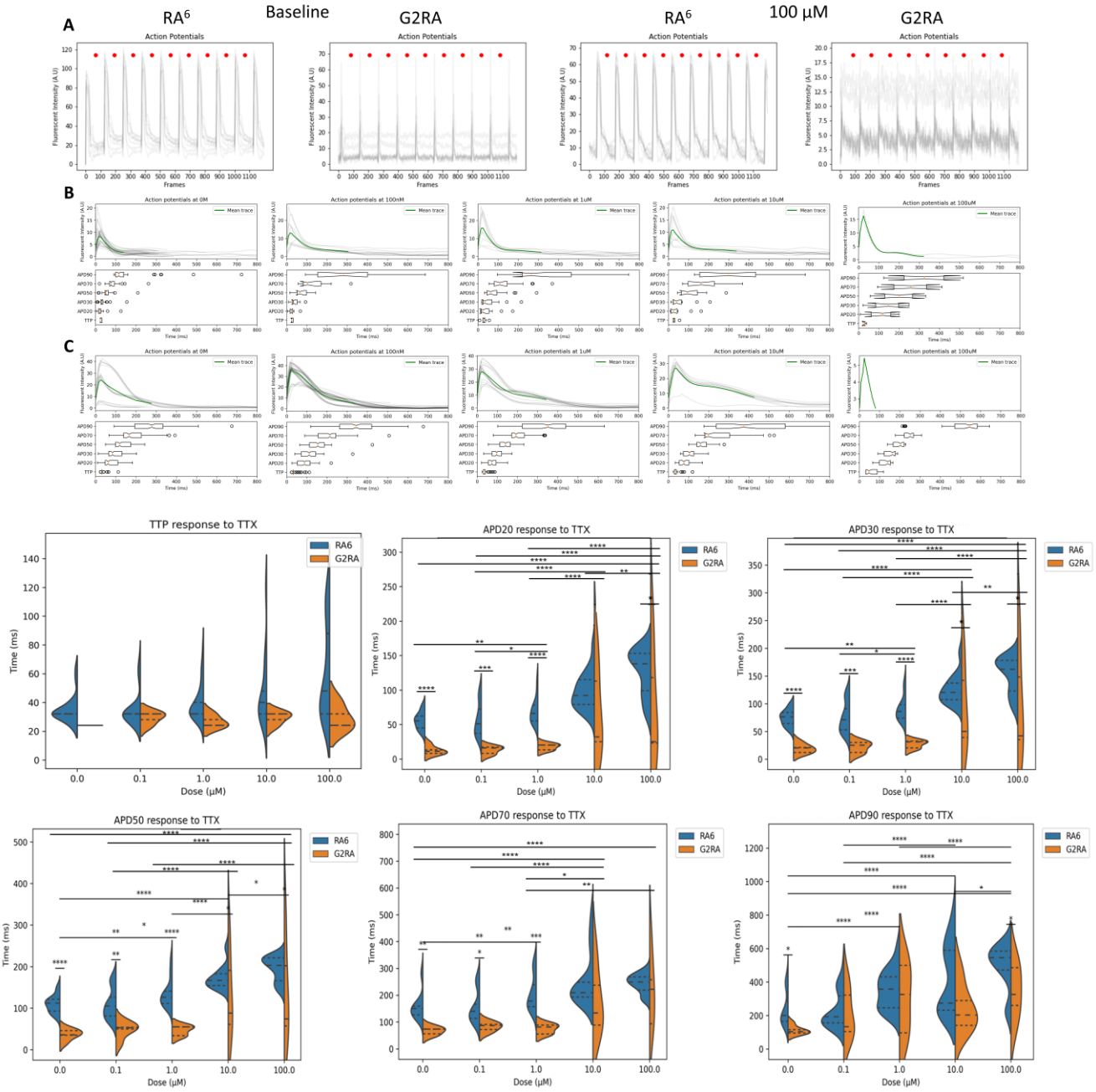

Figure 7-3. TTX had a trend to prolong APD across hiPSC-AMs.

A) Representative traces demonstrating the different RA^6 and G2RA groups at baseline, and then at the addition of the maximal dose 1 µM.

B) G2RA responses to TTX: each column from left to right represents an increasing dose of TTX (Baseline, 100 nM, 1 µM, 10 µM, 100 µM). The top plot in each panel represents the traces of all action potentials included in the summary statistics for the respective group and dose shown in the plot immediately below. Parameters are shown on the y-axis, with duration on the x-axis in ms. The boxplot is centred around the median represented by a vertical line in orange. The notches then describe the 95% CI. The limits of the box describe the IQR. The extended error bars then describe Q1 or Q3 + 1.5IQR. Observations beyond this are plotted as individual dots.

C) RA^6 responses to TTX: each column from left to right represents an increasing dose of TTX (Baseline, 100 nM, 1 µM, 10 µM, 100 µM). The top plot in each panel represents the traces of all action potentials included in the summary statistics for the respective group and dose shown in the plot immediately below.

Parameters are shown on the y-axis, with duration on the x-axis in ms. The boxplot is centred around the median represented by a vertical line in orange. The notches then describe the 95% CI. The limits of the box describe the IQR. The extended error bars then describe Q1 or Q3 + 1.5IQR. Observations beyond this are plotted as individual dots.

D) Split violin plots demonstrating each parameter's response to increasing concentrations of TTX. From left to right the plots represent: TTP, APD20, APD30, APD50, APD70, & APD90. Within each plot the y-axis displays time in ms, and the x-axis displays the increasing concentrations grouped from left to right. The violin plots at each concentration are split vertically to indicate either the RA[6] (blue), or G2RA (orange) distributions. The dashed line with small spaces indicates the median of each distribution, and the dashed lines either side indicate the first and third quartile. Comparisons were made using a repeated measures ANOVA for the dose effect, and a standard ANOVA for the group effect, with Benjamini-Hochberg post-hoc p-value adjustment. Post-hoc t-tests were then performed where appropriate and FDR controlled by Benjamini-Hochberg adjustment.
p <= 0.05: *, p <= 0.005: **, p <= 0.0005: ***, and p <= 0.00005: ****.

Parameter	Batches (G2RA)	Wells (G2RA)	Batches (RA[6])	Wells (RA[6])	Source	DF1	DF2	F statistic	P-value	P Adj.
TTP	1	1	1	1	Group	1	238	7.47	0.006732	0.008976
					Dose	4	4	1.60	0.330060	0.33006
APD20	1	1	1	1	Group	1	248	29.87	1.115864e-7	4.463455e-7
					Dose	4	4	39.36	0.001812	0.003623
APD30	1	1	1	1	Group	1	248	33.63	2.020321e-8	1.212192e-7
					Dose	4	4	39.55	1.794424-3	0.003623
APD50	1	1	1	1	Group	1	248	35.08	1.048838e-8	1.212192e-7
					Dose	4	4	21,54	5.731575e-3	0.008597
APD70	1	1	1	1	Group	1	248	23.41	0.000002	6.913844e-6
					Dose	4	4	8.87	0.028739	0.034487
APD90	1	1	1	1	Group	1	248	8.27	0.004388	0.007523
					Dose	4	4	7.95	0.034628	0.037776

Table 7-5. Statistics describing the response of hiPSC-AMs to TTX.

Parameter	Group	Concentration of TTX (μM)	Median (ms)	IQR (ms)	Mean (ms)	SEM (ms)	CV (%)
TTP	G2RA	0	24	0	24	0	0
	G2RA	0.1	32	4	29.3	2.67	0.129
	G2RA	1	24	4	26.7	2.67	0.141
	G2RA	10	32	4	29.3	2.67	0.129
	G2RA	100	24	8	29.3	5.33	0.257
	RA[6]	0	32	0	34.7	1.37	0.262
	RA[6]	0.1	32	0	35	1.75	0.331
	RA[6]	1	32	8	39.8	1.89	0.315
	RA[6]	10	40	16	46.9	3.61	0.51
	RA[6]	100	48	56	60.4	4.81	0.528
APD20	G2RA	0	11	5	12.4	2.86	0.461
	G2RA	0.1	16	9	12.8	2.63	0.412
	G2RA	1	20	7	17.6	2.16	0.245
	G2RA	10	32	88	69.8	29.05	0.832
	G2RA	100	25	95	74.8	36.86	0.985

	RA[6]	0	55	17	55.5	1.84	0.22
	RA[6]	0.1	51	35	57	3.54	0.412
	RA[6]	1	66	23	68.9	2.8	0.269
	RA[6]	10	92	36	97.6	3.84	0.261
	RA[6]	100	138	54	127.5	4.83	0.251
APD30	G2RA	0	20	9	19	3.9	0.41
	G2RA	0.1	25	18	21.4	4.59	0.429
	G2RA	1	31	12	26.8	3.22	0.24
	G2RA	10	50	103	92.8	35.11	0.757
	G2RA	100	42	113	99	43.78	0.884
	RA[6]	0	76	20	74.3	2.16	0.193
	RA[6]	0.1	71	38	75	4.07	0.36
	RA[6]	1	86	24	90.6	3.27	0.239
	RA[6]	10	120	30	124.8	3.79	0.201
	RA[6]	100	162	55	152.6	4.69	0.204
APD50	G2RA	0	36	11	36.6	5.9	0.322
	G2RA	0.1	53	4	48.2	8.93	0.371
	G2RA	1	55	21	46.8	5.44	0.233
	G2RA	10	88	130	135	45.55	0.675
	G2RA	100	74	145	144.2	54.28	0.753
	RA[6]	0	112	28	109.8	3.09	0.187
	RA[6]	0.1	105	45	110.3	5.43	0.326
	RA[6]	1	126	30	135.1	5.1	0.251
	RA[6]	10	167	29	173	4.15	0.159
	RA[6]	100	203	55	195.4	4.33	0.147
APD70	G2RA	0	73	17	67	7.19	0.215
	G2RA	0.1	87	19	82.4	8.24	0.2
	G2RA	1	81	33	74.6	8.26	0.222
	G2RA	10	133	149	179.6	55.46	0.618
	G2RA	100	222	165	214.4	60.53	0.565
	RA[6]	0	150	33	157.8	7.54	0.317
	RA[6]	0.1	140	52	155.6	8.93	0.38
	RA[6]	1	178	82	207.8	9.66	0.308
	RA[6]	10	209	55	252.6	14.35	0.377
	RA[6]	100	249	49	244.7	5.11	0.138
APD90	G2RA	0	103	20	112.6	11.75	0.209
	G2RA	0.1	133	219	213.2	65.42	0.614
	G2RA	1	325	403	305.4	91.61	0.6
	G2RA	10	203	149	245.8	62.14	0.506
	G2RA	100	326	226	342.6	72.95	0.426
	RA[6]	0	200	122	240	14.91	0.412
	RA[6]	0.1	192	161	226.8	15.75	0.461
	RA[6]	1	357	186	351.2	17.08	0.323
	RA[6]	10	273	358	415.5	30.11	0.481
	RA[6]	100	545	113	496.9	19.46	0.26

Table 7-6. Summary statistics of hiPSC-AM response to TTX.

d. Discussion

i. Baseline differences between G2RA and RA[6] hiPSC-AMs

Our earlier work had focused on ascertaining the difference between our G2RA hiPSC-AMs and their CMM-induced mixed/ventricular hiPSC-CM counterparts. I now sought to understand how our hiPSC-AMs compared to just the use of RA, the most commonly used method of producing hiPSC-AMs. I used RA between days 6 and 10 to enable comparison from the addition of GREMLIN-2 as this was not controlled for in our prior publication. However, many use RA between days 3-5 or 6 instead to derive their atrial-like phenotype[312-314,316,464].

I ascertain that reliably across biological and technical replicates, that our G2RA protocol generally induced a more triangular and shorter action potential than the RA[6] protocol e.g. in our 4-AP experiments at baseline with a mean APD90 of 199.6±5.9 ms in G2RA (N=3 n=12) vs 278.1±3.4 ms in RA[6] (N=3, n=10) with p=0.024. These APD90 values in our G2RA group were consistent with our earlier published results at 215±15 ms (n=7), and consistent with native human atria (170.1±63 ms)[331]. Furthermore, the relatively triangular morphology our our G2RA hiPSC-AM action potential is most consistent with more adult native atrial cardiomyocytes than neonatal atrial action potentials[331]. However, it is worth noting that there remains debate about the labile nature of native atrial action potentials even from the same heart. The more spike-and-dome morphology observed in the RA[6] protocol and the more prolonged APD90 is more consistent with certain reports of the human ventricular action potential (260±4 ms[465]). Whilst RA-treated hiPSC-AMs display a range of APD90 values from 89±4.5 ms[312], through to 247±37 ms[316], there is a striking resemblance between our results and those of Lee et al[464]. Lee et al observe that RA treatment of cardiac mesoderm (day 3-5) resulted in hiPSC-AMs with an APD90 of 189±18 ms, and an APD30 of 13.0±4.8 ms. However, when hiPSCs were already induced towards a ventricular fate, and then RA was added, a more mixed cellular phenotype was present with APD90 258±25 ms, and APD30 55±20 ms[464]. Our RA[6] group not only had a similar APD90 as this mixed group from Lee et al, but it also had a relatively more prolonged APD30 than our G2RA group (93.6±1.16 ms vs 43.6±2.3 ms), in the same manner as this RA-treated ventricular group from Lee et al[464]. It is tempting to speculate whether our relatively 'late' addition of RA between days 6 – 10, during cardiac progenitor proliferation and cardiomyocyte differentiation might be acting in a similar way to the RA treatment of already ventricularly-specified colonies in Lee et al, to produce a mixed phenotype in our RA[6], but with an atrial fate already primed and specified in G2RA group by the day 4-6 GREMLIN-2 treatment. We should further characterise this RA[6] group and the temporal sensitivity of RA signalling in inducing an atrial-like phenotype.

ii. Our hiPSC-AMs possess highly variable potassium currents

I used a range of different potassium channel antagonists to reveal their effects on the overall action potential morphology – 4-AP and E-4031. 4-AP demonstrated a dose-dependent effect to increase the action potential duration across all measured phases (APD20,30,50, and 70) apart from APD90, where the trend failed to reach significance. However, of particular interest is that generally G2RA experienced AP prolongation even from 10 μM, and then much more variable further increases between 100 μM to 1 mM, whereas RA[6] had the opposite and had only a weak response if any until 1 mM, where there was a large prolongation across the AP. 4-AP is well-established to be primarily an antagonist of I_{Kur} at low μM doses (e.g. EC_{50} 5.3 μM)[461], before also inhibiting I_{to} currents at higher μM – mM concentrations (e.g. EC_{50} 326 μM)[458]. My results might

indicate that I_{Kur} currents are present at relevant current densities in our G2RA group and not the RA^6 group. Certainly, this would be in line with the shorter action potential I observed in the G2RA group compared to the RA^6 group if the RA^6 group lacked sufficient expression of *KCNA5* to induce sufficient current density changes to I_{Kur} inhibition. Whereas our earlier findings highlighted the increased expression of *KCNA5* in our G2RA group relative to the CMM control, we lack any such information on our RA^6 control. However, as noted above, Lee et al demonstrate that in their ventricularly-specified hiPSCs then treated with RA, there was some induction of *KCNA5* expression, but significantly less than that in their RA-treated hiPSC-AM group[464]. We should confirm the expression of *KCNA5* in our RA^6 group, and the CMM group response to 4-AP, to best understand how our transcriptomic results best relate to our functional interrogation of channels. However, the G2RA-selective APD prolongation to low μM 4-AP is promising to suggest the expression of atrial-specific currents in this group. However, the highly variable response to 1 mM 4-AP, without much change from 100 μM, might be indicative of highly variable I_{to} current densities in our G2RA – with a lack of 4-AP sensitive I_{to} being previously reported as a sign of the immature human atria[459]. The opposite functional results in our RA^6 group suggest perhaps that this group has strong I_{to} current densities. My earlier work identified the particular sensitivity of my optical analysis pipeline to noise in measuring APD20 and APD30 (6 and 3 median frames error respectively with 20% noise) in spike-and-dome shaped action potentials like Courtemanche 1998 and our RA^6 group. Given the importance of I_{to} for APD20[457], my combined pipeline might provide particularly biased measurements for this unique combination – although this highlights the benefit of my approach to quantify measurement error across APDs. Future work with single-cell and single-channel electrophysiology is likely required to tease apart these differences with channel-specific confidence. Additionally, future work should focus on the use of more complex stimulation protocols, such as those used by Burashnikov et al[466] and Schaffer et al[467], to distinguish between the rapid reactivation kinetics of I_{Kur} from those of the less rapid kinetics of I_{to}.

4-AP has also been implicated in modulating I_{Kr}[460] and I sought to understand the relative contribution of this current to repolarisation in our hiPSC-AM models. However, despite E-4031 appearing to induce a dose-dependent shortening of the earlier portions of the action potential at 10 nM and 100 nM, followed by a prolongation of these same parameters at 1 μM – I am unable to reach any definitive conclusions. Unfortunately, these experiments were only performed in a small number of cases, and thus we lack robust repeats to conclusively report on the effects of E-4031 on our hiPSC-AMs. In particular, our G2RA hiPSC-AM signals were particularly weak for those recordings we were able to achieve. However, our RA^6 hiPSC-AMs certainly indicate that at 1 μM, E-4031 was able to prolong the action potential duration in at least a number of samples. However, these unfortunately were excluded by the QC metrics of optical analysis pipeline. Repeat experiments are required here to establish the reliability of this E-4031-dependent APD prolongation and optimise the specificity of the optical analysis' quality control.

Our earlier transcriptomic investigations suggested that our hiPSC-AMs did have higher expression of transcripts encoding specific subunits of I_{to}, I_{Kur}, and I_{Kr} - KCNE3, KCNA5, and KCNH2 respectively. However, this was against a CMM ventricular-like control hiPSC-CM population. Currently, despite promising initial results, further work is required to understand whether these currents are present at pertinent densities in our hiPSC-AMs. The use of both single-cell electrophysiology and combined exposure to 4-AP and E-4031, should aid in

discriminating their specific current densities and the functional coupling between the different currents that is implicated in both health and disease[463].

iii. Sodium channel blockade by TTX had minimal impact

Beyond describing solely the repolarisation phase of our hiPSC-AM action potentials, I sought to also describe the depolarisation phase and its pharmacology. TTX had minimal effect on TTP in either the G2RA or RA^6 groups. There was a trend for the RA^6 group to prolong the TTP at the highest doses of 10 – 100 μM TTX. However, this failed to reach significance and was only present in a small number of traces. Furthermore, in native cardiomyocytes, such doses of TTX would typically ablate the elicitation of an action potential by electrical stimulation. Certainly, others have demonstrated that 11 μM of TTX ablates this response in mature hiPSC-CMs. However, as in Feyen et al[322], we did observe a prolongation of APD with increasing TTX concentrations, which affected both the G2RA and RA^6 groups, with continued activity even at 100 μM TTX. Feyen et al cited the prior work of Sheng et al[468], which also identified hiPSC-CM resistance to even 100 μM TTX, and the presence of strong I_{CaL}, as evidence that hiPSC-CMs rely primarily on calcium currents for depolarisation. However, I would suggest that additional experiments are required to confirm this, such as a synergistic disproportionate effect of I_{CaL} inhibition in the presence of 100 μM TTX on upstroke velocity, and perhaps the use of TTX-resistant Na_V-specific cadmium ions[469] to distinguish if TTX-resistant Na_V currents are functionally important in hiPSC-CMs, as we know them to be in native human cardiomyocytes[470]. Nonetheless, this is perhaps an initial sign that our hiPSC-AMs lack the maturity observed by other groups with respect to the predominate currents mediating depolarisation despite scRNA-Seq suggesting G2RA expression of genes (SCN5A & SCN11A) encoding TTX-resistant $Na_{V1.5}$ and $Na_{V1.9}$ respectively.

Chapter 8. Neurohormonal pharmacology of hiPSC-AMs

a. Introduction

This section is introduced in Chapter 1A, B, & C.

If hiPSC-CMs are to be used as models of cardiac physiology and pathophysiology, then we should interrogate whether they are able to mirror the native response to neurotransmitter modulation – namely the two major neurotransmitters axes of the autonomic modulation of the heart: adrenergic and cholinergic. Both adrenergic and cholinergic stimuli are implicated in regulating the heart in health, and also contributing to pathogenesis[471,472]. However, whilst all cardiomyocyte subtypes are broadly described as responding to adrenergic stimuli, the response to cholinergic stimuli is much more marked in atrial cardiomyocytes and the CCS[320,473]. Furthermore, in previous work, we have observed that our hiPSC-AM protocol produced CMs with a I_{KACh} current density significantly closer to native human atrial cardiomyocytes than any other protocol[1]. However, this is separate from the observation that it may be significantly strong enough to appropriately modulate cardiomyocyte behaviour upon stimulation through shortened the cardiac action potential duration in simpler and more physiological experimental conditions. In a similar vein, our prior work had identified an increased calcium transient amplitude in response to adrenergic stimulus, but had not defined the dose response curve for this[1]. This chapter was the premise for subsequent work (not shown) that attempted to use the same doses of isoprenaline for the purpose of arrhythmogenesis in a model of cateholaminergic polymorphic ventricular tachycardia and thus purposefully veered into a supraphysiological high 10 μM dose to maximise sensitivity in the experiment, given the noted variability in adrenergic response seen in hiPSC-CMs compared to native tissue. Similarly, our high dose of 10 μM CCh was to ensure that we maximised sensitivity in determining any differences in response between our two differentiation protocols, as prior work had demonstrated much weaker responses in RA-only differentiation protocols at the level of I_{KACh} current density[1]. The well-recognised work of others provided the basis of using 10 μM isoprenaline and CCh in similar hiPSC-CM cultures and facilitates more easily interpretable comparison[312-315].

b. Methods

The methods used to produce the data in this section are presented in Chapter 2B & C:

c. Results

i. Response of hiPSC-AMs to β-adrenoceptor agonism

After having established preliminary evidence surrounding the channel-specific pharmacology of our hiPSC-AM protocol, I then sought to further characterise their neuropharmacological profile. I first started with isoprenaline, a β-adrenoceptor specific agonist – which activates the major signalling cascades associated with sympathetic stimulation of cardiomyocytes. Given the stability of cell cultures over prolonged experimental periods per well, with regular 1:1 pacing to field stimulation even after 1> hour of exposure in prior experiments (data not shown): I determined that they were suitable to subject to a multi-stage tachypacing and isoprenaline (ISO) dose-response protocol.

I first identified that counterintuitively, both the G2RA and RA^6 groups showed a decreased propensity for a 1:1 response coupling with pacing at higher frequencies from baseline to 10 uM ISO (n=7 (G2RA), 4 (RA^6). P.adj=0.049, F=8.61). The expected response is that ISO should increase the frequency at which cardiac tissue can be successfully paced with a 1:1 response.

To further understand whether the initial tachypacing protocol at baseline was causing insult to the cardiac tissue and potentially confounding the experiment, I compared calcium transient properties between baseline at 1 Hz, and then at 1 Hz pacing ≥30 seconds after cessation of 5 Hz pacing also still at baseline. There was a trend in the G2RA group for the distribution of results to include a prolonged calcium transient duration (CaTD) in the post-tachypacing group. However, this did not reach significance. Additionally, apart from significant differences in the TTP between groups, the other CaTD measurements were not significantly different between the G2RA and RA^6 groups. However, there was a trend for the RA^6 group to be more prolonged in the earlier portions (CaTD20-CaTD50) of the calcium transient compared to the G2RA group, as compared to the later CaTD90 distribution which is broadly indistinguishable.

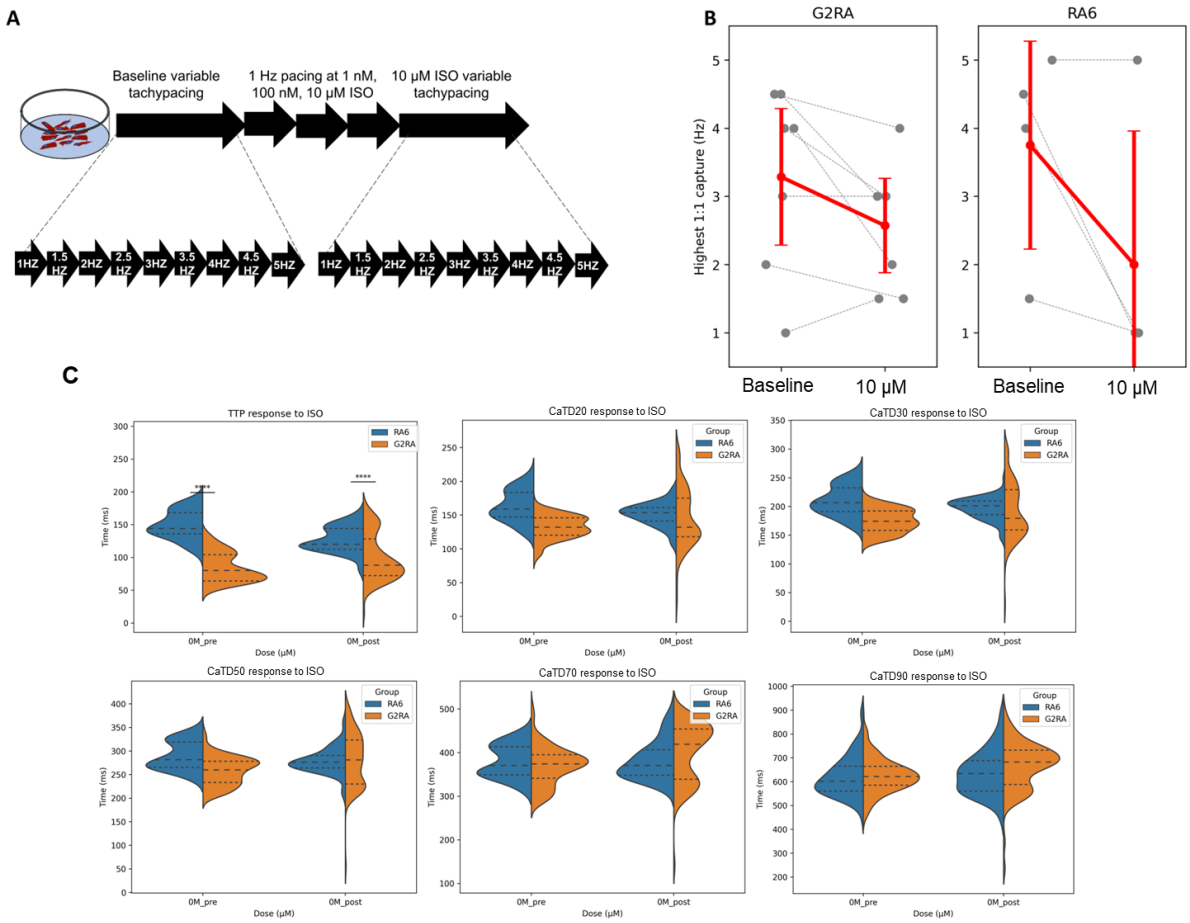

Figure 8-1. hiPSC-AMs were subjected to a tachypacing and β-adrenergic challenge.

A) Schematic diagram of tachypacing and ISO dose-response protocol.

B) G2RA and RA[6] fastest 1:1 coupling rate at baseline (pre-dose response), or 10 µM (post-dose response). The pacing frequencies are shown on the y-axis (Hz), with the pre or post categories shown on the x-axis. Observations are shown in grey, connected by a line between repeated measures from the same well from pre to post. The red line represents the mean, with errors bars as 95% CI.

C) Split violin plots demonstrating each parameter's response comparing baseline parameters before tachypacing to those after tachypacing, still at baseline. From left to right the plots represent: TTP, CaTD20, CaTD30, CaTD50, CaTD70, & CaTD90. Within each plot the y-axis displays time in ms, and the x-axis displays the increasing concentrations grouped from left to right. The violin plots at each concentration are split vertically to indicate either the RA[6] (blue), or G2RA (orange) distributions. The dashed line with small spaces indicates the median of each distribution, and the dashed lines either side indicate the first and third quartile. Comparisons were made using a two-way mixed effects ANOVA model, with Benjamini-Hochberg post-hoc p-value adjustment. Post-hoc t-tests were then performed where appropriate and FDR controlled by Benjamini-Hochberg adjustment.
p <= 0.05: *, p <= 0.005: **, p <= 0.0005: ***, and p <= 0.00005: ****.

I then sought to understand how the hiPSC-AMs responded to ISO in terms of changing CaTD measurements. TTP was significantly different between the G2RA and RA[6] groups at baseline and every dose of isoprenaline. However, there was only a slight trend for a decrease in TTP with increasing ISO concentration in the RA[6] group. However, this did not reach significance. Both CaTD20 and CaTD30 displayed similar response profiles, with no significant changes across doses. However, there was a significant difference between the G2RA and RA[6] groups after baseline. CaTD70 and CaTD90 did display a dose-dependent prolongation in both G2RA and RA[6] groups. Furthermore, with increasing ISO concentrations the G2RA had significantly

longer CaTD90 values than the RA[6] group, which became of a greater effect at the highest concentrations of ISO. This ISO-dependent prolongation of calcium transients is contrary to the canonical effect of ISO, which should be to shorten the calcium transient duration. We did observe a small number of ectopic beats in both groups, both at baseline and with ISO (data not shown).

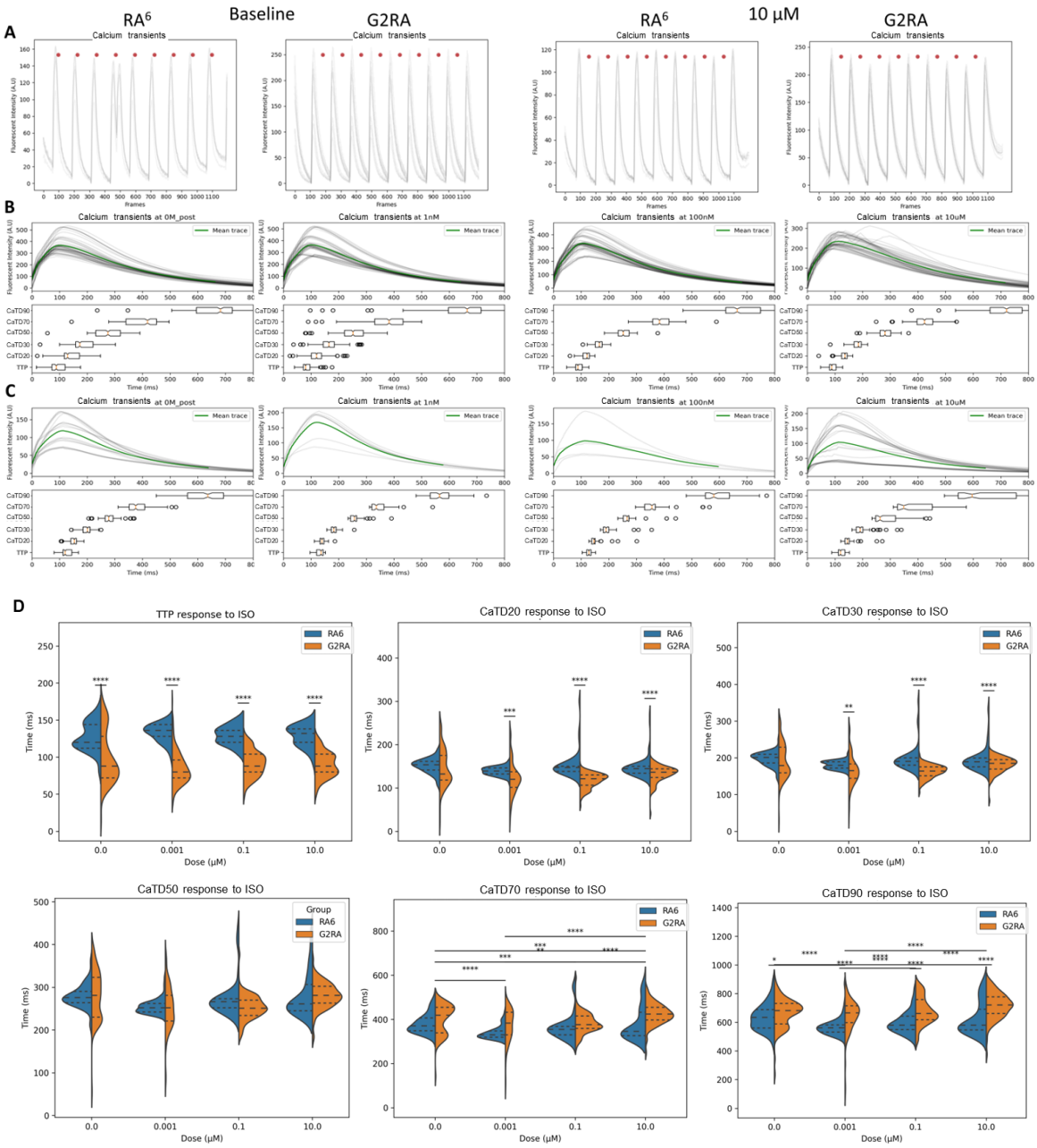

Figure 8-2. ISO counterintuitively prolonged CaTs across hiPSC-AMs.

A) Representative traces demonstrating the different RA[6] and G2RA groups at baseline, and then at the addition of the maximal dose 10 µM.

B) G2RA responses to ISO: each column from left to right represents an increasing dose of ISO (Baseline, 1 nM, 100 nM, & 10 µM). The top plot in each panel represents the traces of all calcium transients included in the summary statistics for the respective group and dose shown in the plot immediately below. Parameters are shown on the y-axis, with duration on the x-axis in ms. The boxplot is centred around the median represented by a vertical line in orange. The notches then describe the 95% CI. The limits of the

box describe the IQR. The extended error bars then describe Q1 or Q3 + 1.5IQR. Observations beyond this are plotted as individual dots.

C) RA[6] responses to ISO: each column from left to right represents an increasing dose of ISO (Baseline, 1 nM, 100 nM, & 10 μM). The top plot in each panel represents the traces of all calcium transients included in the summary statistics for the respective group and dose shown in the plot immediately below. Parameters are shown on the y-axis, with duration on the x-axis in ms. The boxplot is centred around the median represented by a vertical line in orange. The notches then describe the 95% CI. The limits of the box describe the IQR. The extended error bars then describe Q1 or Q3 + 1.5IQR. Observations beyond this are plotted as individual dots.

D) Split violin plots demonstrating each parameter's response to increasing concentrations of ISO. From left to right the plots represent: TTP, CaTD20, CaTD30, CaTD50, CaTD70, & CaTD90. Within each plot the y-axis displays time in ms, and the x-axis displays the increasing concentrations grouped from left to right. The violin plots at each concentration are split vertically to indicate either the RA[6] (blue), or G2RA (orange) distributions. The dashed line with small spaces indicates the median of each distribution, and the dashed lines either side indicate the first and third quartile. Comparisons were made using a two-way mixed effects ANOVA model, with Benjamini-Hochberg post-hoc p-value adjustment. Post-hoc t-tests were then performed where appropriate and FDR controlled by Benjamini-Hochberg adjustment.
p <= 0.05: *, p <= 0.005: **, p <= 0.0005: ***, and p <= 0.00005: ****.

Parameter	Batches (G2RA)	Wells (G2RA)	Batches (RA[6])	Wells (RA[6])	Source	Sum of squares	DF1	DF2	Mean of squares	F statistic	P-value (Group)	P Adj. (Group)
TTP	1	4	1	3	Group	10071.33	1	5	10071.33	102.86	0.000160	0.002876
					Dose	57.52	3	15	19.17	0.19	0.904778	0.981138
					Interaction	594.00	3	15	198.00	191	0.170863	0.256295
CaTD20	1	4	1	3	Group	2700.23	1	5	2700.23	23.96	0.004496	0.024212
					Dose	1150.55	3	15	383.52	2.00	0.157566	0.256295
					Interaction	487.40	3	15	162.47	0.85	0.489695	0.67804
CaTD30	1	4	1	3	Group	2570.03	1	5	2570.03	19.77	0.006725	0.024212
					Dose	2098.75	3	15	699.58	2.93	0.067779	0.152502
					Interaction	476.23	3	15	158.74	0.66	0.586543	0.754126
CaTD50	1	4	1	3	Group	718.50	1	5	718.50	4.04	0.100499	0.200806
					Dose	6247.93	3	15	2142.64	4.17	0.024761	0.063672
					Interaction	234.93	3	15	78.31	0.15	0.926630	0.981138
CaTD70	1	4	1	3	Group	2410.12	1	5	2410.12	3.72	0.111559	0.200806
					Dose	16810.58	3	15	5603.53	5.60	0.008859	0.026576
					Interaction	150.00	3	15	50.00	0.05	0.984668	0.984668
CaTD90	1	4	1	3	Group	23600.97	1	5	23600.97	23.08	0.004867	0.024212
					Dose	30860.14	3	15	10286.71	6.08	0.006443	0.024212
					Interaction	900.19	3	15	300.06	0.18	0.910121	0.981138

Table 8-1. Statistics for response of hiPSC-AMs to ISO.

Parameter	Group	Concentration of ISO (μM)	Median (ms)	IQR (ms)	Mean (ms)	SEM (ms)	CV (%)
TTP	G2RA	0	88	56	99.6	2.06	0.348
	G2RA	0.1	80	24	85.7	1.31	0.258
	G2RA	1	88	24	91.6	1.03	0.19
	G2RA	10	88	24	90.2	1.01	0.188
	RA[6]	0	120	32	127.5	2.1	0.15
	RA[6]	0.1	136	16	132.8	1.34	0.092
	RA[6]	1	128	16	129.3	1.38	0.097

	RA[6]	10	132	18	128.6	1.58	0.112
APD20	G2RA	0	132	57	145.8	2.58	0.298
	G2RA	0.1	120	36	123	2.26	0.309
	G2RA	1	121	24	116.5	1.02	0.148
	G2RA	10	136	20	131.9	1.14	0.145
	RA[6]	0	153.5	20	151	1.84	0.111
	RA[6]	0.1	139	14	138.7	1.05	0.069
	RA[6]	1	147	12	152.8	3.29	0.196
	RA[6]	10	144.5	16	146.2	2.48	0.154
APD30	G2RA	0	179	70	192	2.87	0.252
	G2RA	0.1	165	39	166.1	2.51	0.255
	G2RA	1	164	24	162.8	1.06	0.11
	G2RA	10	185	26	180.8	1.26	0.117
	RA[6]	0	201	23.5	196.6	2.02	0.094
	RA[6]	0.1	179.5	17.5	180.7	1.21	0.061
	RA[6]	1	190	20	198.4	3.93	0.18
	RA[6]	10	189	24	193.6	3.38	0.159
APD50	G2RA	0	281	93	281.2	3.38	0.203
	G2RA	0.1	252	60	252.5	3.14	0.21
	G2RA	1	251	36	253.1	1.65	0.11
	G2RA	10	281	39	280.5	1.79	0.107
	RA[6]	0	276	26.2	278.7	2.9	0.095
	RA[6]	0.1	252	20.2	255	1.83	0.066
	RA[6]	1	266	21	274.1	4.85	0.161
	RA[6]	10	261	61.5	280.7	5.53	0.18
APD70	G2RA	0	419	115	400.2	3.94	0.166
	G2RA	0.1	383	102	372.7	4.44	0.201
	G2RA	1	376	56	383	2.73	0.12
	G2RA	10	424	57	424.1	2.84	0.113
	RA[6]	0	370.5	58.2	381.3	4.75	0.113
	RA[6]	0.1	330	28.8	339.6	3.03	0.081
	RA[6]	1	355	38.2	364.6	6.4	0.16
	RA[6]	10	346	106.2	380	8.27	0.198
APD90	G2RA	0	682	144	665.3	5.99	0.152
	G2RA	0.1	665	118	641	7.1	0.187
	G2RA	1	661	140	680.7	5.6	0.139
	G2RA	10	721	116	715.5	5.35	0.126
	RA[6]	0	634	128.8	634.7	9.86	0.142
	RA[6]	0.1	561	50	567.2	6.25	0.1
	RA[6]	1	580	92.5	597.6	8.19	0.125
	RA[6]	10	579.5	145.5	626.4	12.33	0.179

Table 8-2. Summary statistics of hiPSC-AM response to ISO.

i. Response of hiPSC-AMs to muscarinic agonism

I then sought to understand the effects of activating the signalling cascades associated with parasympathetic stimulation in my hiPSC-AM groups. In a similar fashion as with ISO, I used carbamylcholine chloride, a cholinergic receptor agonist, with a dose-response and tachypacing protocol, with potentiometric dyes to study membrane voltage changes.

I first identified both the G2RA and RA[6] groups showed a decreased propensity for a 1:1 response coupling with pacing at higher frequencies from baseline to 10 uM CCh (n=4 (G2RA), 6 (RA[6]). P.adj=0.016). This is in line with the canonical expectation that CCh should increase the frequency at which cardiac tissue can be successfully paced with a 1:1 response.

To further understand whether the initial tachypacing protocol at baseline was causing insult to the cardiac tissue and potentially confounding the experiment, I compared action potential properties between baseline at 1 Hz, and then at 1 Hz pacing ≥30 seconds after cessation of the end of the tachypacing protocol at baseline. The action potentials were significantly shorter in the G2RA group against the RA[6] group at both baseline and after the tachypacing at baseline, across all repolarisation parameters (APD20,30,50,70,90) (N=1, n=4 (G2RA); N=1, n=8 (RA[6]), p.adj=0.0029 (APD20), 0.0039 (APD30), 0.0022 (APD50), 0.00062 (APD70), 0.000280 (APD90)), but not TTP (N=1, n=4 (G2RA); N=2, n=9 (RA[6]), p.adj=0.056). However, APD50 and APD70 appear to also display a tachypacing-dependent shortening across both groups (p.adj=0.0187 (APD50), 0.034 (APD70)). There is a trend for this in APD90 as well, particularly in the G2RA group. However, this does not reach significance. Thus, it appears that the tachypacing protocol might be affecting the hiPSC-derived cardiac tissue, although its functional importance remains unclear.

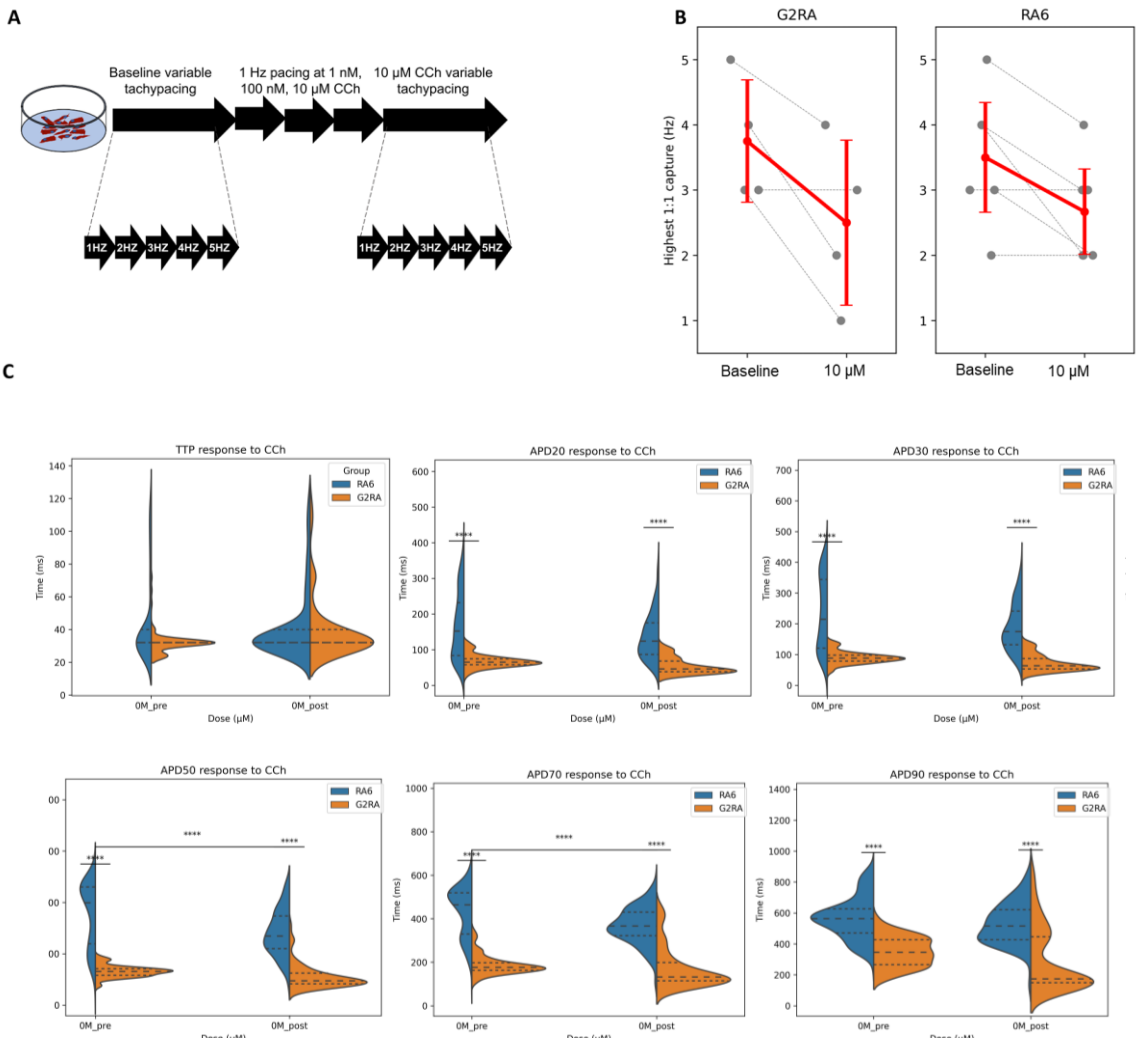

Figure 8-3. hiPSC-AMs were subjected to a tachypacing and cholinergic challenge.

A) Schematic diagram of tachypacing and CCh dose-response protocol.
B) G2RA and RA^6 fastest 1:1 coupling rate at baseline (pre-dose response), or 10 μM (post-dose response). The pacing frequencies are shown on the y-axis (Hz), with the pre or post categories shown on the x-axis. Observations are shown in grey, connected by a line between repeated measures from the same well from pre to post. The red line represents the mean, with errors bars as 95% CI.
C) Split violin plots demonstrating each parameter's response comparing baseline parameters before tachypacing to those after tachypacing, still at baseline. From left to right the plots represent: TTP, APD20, APD30, APD50, APD70, & APD90. Within each plot the y-axis displays time in ms, and the x-axis displays the increasing concentrations grouped from left to right. The violin plots at each concentration are split vertically to indicate either the RA^6 (blue), or G2RA (orange) distributions. The dashed line with small spaces indicates the median of each distribution, and the dashed lines either side indicate the first and third quartile. Comparisons were made using a two-way mixed effects ANOVA model, with Benjamini-Hochberg post-hoc p-value adjustment. Post-hoc t-tests were then performed where appropriate and FDR controlled by Benjamini-Hochberg adjustment. Further details provided in Table X.
p <= 0.05: *, p <= 0.005: **, p <= 0.0005: ***, and p <= 0.00005: ****.

I then sought to characterise any dose-dependent changes to action potential parameters with increasing CCh concentrations. TTP was not different at baseline between G2RA and RA^6 groups, nor was it affected by increasing concentrations of CCh (N=1, n=4 (G2RA); N=2, n=9 (RA^6), p.adj=0.50 (Group), 0.73 (Dose)). APD20, 30, 50 and 70 displayed the same response, with the G2RA significantly shorter than the RA^6 group at every concentration, but with a trend for a dose-dependent decrease in both groups. However, this trend did not reach significance. APD90 displayed a similar difference between groups at every concentration, but the dose-dependent decrease in APD90 reached significance (N=1, n=4 (G2RA); N=1, n=8 (RA^6), p.adj= 0.00043 (Group), 0.018 (Dose)). This APD90-specific decrease with CCh matches the canonical effect of CCh on atrial cardiomyocytes.

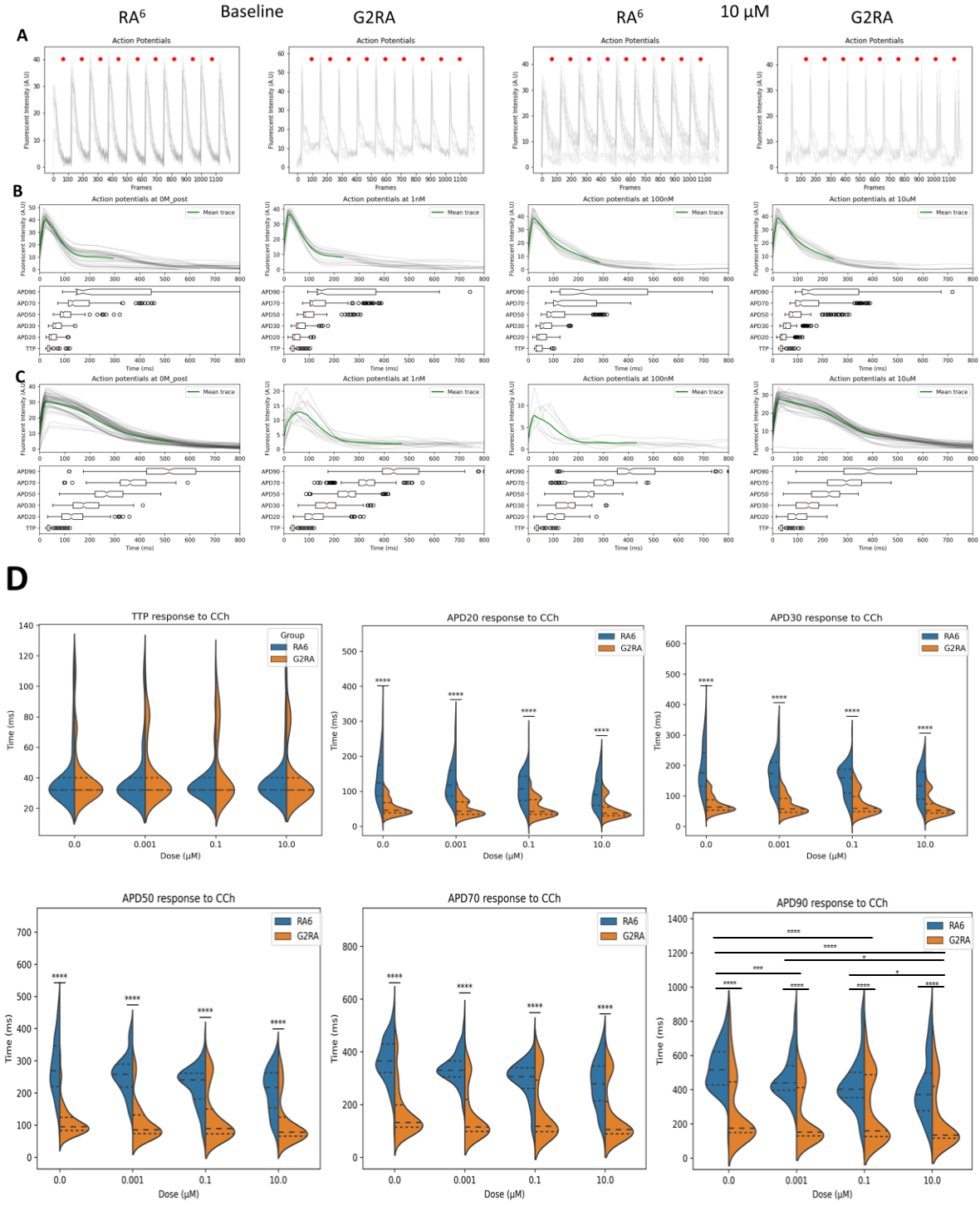

Figure 8-4. CCh shortened APD across hiPSC-AMs.

A) Representative traces demonstrating the different RA[6] and G2RA groups at baseline, and then at the addition of the maximal dose 10 μM.

B) G2RA responses to CCh: each column from left to right represents an increasing dose of CCh (Baseline, 1 nM, 100 nM, & 10 μM). The top plot in each panel represents the traces of all action potentials included in the summary statistics for the respective group and dose shown in the plot immediately below. Parameters are shown on the y-axis, with duration on the x-axis in ms. The boxplot is centred around the median represented by a vertical line in orange. The notches then describe the 95% CI. The limits of the box describe the IQR. The extended error bars then describe Q1 or Q3 + 1.5IQR. Observations beyond this are plotted as individual dots.

C) RA[6] responses to CCh: each column from left to right represents an increasing dose of CCh (Baseline, 1 nM, 100 nM, & 10 μM). The top plot in each panel represents the traces of all action potentials included in the summary statistics for the respective group and dose shown in the plot immediately below. Parameters are shown on the y-axis, with duration on the x-axis in ms. The boxplot is centred around the median represented by a vertical line in orange. The notches then describe the 95% CI. The limits of the box describe the IQR. The extended error bars then describe Q1 or Q3 + 1.5IQR. Observations beyond this are plotted as individual dots.

D) Split violin plots demonstrating each parameter's response to increasing concentrations of CCh. From left to right the plots represent: TTP, APD20, APD30, APD50, APD70, & APD90. Within each plot the y-axis displays time in ms, and the x-axis displays the increasing concentrations grouped from left to right. The violin plots at each concentration are split vertically to indicate either the RA[6] (blue), or G2RA (orange) distributions. The dashed line with small spaces indicates the median of each distribution, and the dashed lines either side indicate the first and third quartile. Comparisons were made using a two-way mixed effects ANOVA model, with Benjamini-Hochberg post-hoc p-value adjustment. Post-hoc t-tests were then performed where appropriate and FDR controlled by Benjamini-Hochberg adjustment. Further details are provided in Table X.
p <= 0.05: *, p <= 0.005: **, p <= 0.0005: ***, and p <= 0.00005: ****.

Parameter	Batches (G2RA)	Wells (G2RA)	Batches (RA[6])	Wells (RA[6])	Source	Sum of squares	DF1	DF2	Mean of squares	F statistic	P-value	P Adj.
TTP	1	4	2	9	Group	149.44	1	11	149.44	0.62	0.446101	0.501864
					Dose	97.97	3	33	32.66	0.43	0.733172	0.733172
					Interaction	165.08	3	33	55.03	0.72	0.544998	0.577057
APD20	1	4	1	8	Group	49628.47	1	10	49628.47	42.44	0.000068	0.000305
					Dose	4708.42	3	30	1569.47	3.49	0.027734	0.128497
					Interaction	1689.80	3	30	563.27	1.25	0.308538	0.396692
APD30	1	4	1	8	Group	97329.06	1	10	97329.06	43.46	0.000061	0.000305
					Dose	8145.66	3	30	2715.22	3.29	0.033951	0.137347
					Interaction	3438.83	3	30	1146.28	1.39	0.265012	0.366939
APD50	1	4	1	8	Group	191401.91	1	10	191401.91	44.74	0.000054	0.000305
					Dose	14062.92	3	30	4687.64	3.31	0.033273	0.142076
					Interaction	8864.92	3	30	2954.97	2.09	0.122846	0.20102
APD70	1	4	1	8	Group	284059.35	1	10	284059.35	49.86	0.000035	0.000305
					Dose	23929.03	3	30	7976.34	5.02	0.006154	0.057488
					Interaction	8840.70	3	30	2946.9	1.85	0.158800	0.2382
APD90	1	4	1	8	Group	504340.74	1	10	504340.74	36.91	0.000120	0.00043
					Dose	56025.34	3	30	18675.11	6.29	0.001927	0.018606
					Interaction	9809.65	3	30	3269.88	1.10	0.363735	0.436482

Table 8-3. Statistics of response of hiPSC-AMs to CCh.

Parameter	Group	Concentration of CCh (μM)	Median (ms)	IQR (ms)	Mean (ms)	SEM (ms)	CV (%)
TTP	G2RA	0	32	8	39.2	1.22	0.48
	G2RA	0.1	32	8	42.4	1.25	0.457
	G2RA	1	32	32	45.4	1.5	0.511
	G2RA	10	32	8	39.9	1.23	0.477
	RA[6]	0	32	8	41.5	1.39	0.51
	RA[6]	0.1	32	8	39.7	1.32	0.505
	RA[6]	1	32	8	37.7	1.02	0.41
	RA[6]	10	32	8	39.8	1.23	0.47

APD20	G2RA	0	45.5	29.5	54	1.46	0.42
	G2RA	0.1	43	35.8	51.9	1.53	0.457
	G2RA	1	42	42.2	52.9	1.71	0.501
	G2RA	10	37	25	47.5	1.67	0.545
	RA[6]	0	124	89	136.7	4.2	0.468
	RA[6]	0.1	117	73	128.3	3.54	0.421
	RA[6]	1	107	69	108.2	2.92	0.41
	RA[6]	10	90	70	96.6	2.98	0.47
APD30	G2RA	0	63	34	72	1.74	0.372
	G2RA	0.1	57	45.2	70.6	2.05	0.449
	G2RA	1	59	50.2	74.7	2.45	0.507
	G2RA	10	52	30.5	65.5	2.17	0.513
	RA[6]	0	175	109	189.2	5.06	0.407
	RA[6]	0.1	174	81	175.8	3.85	0.334
	RA[6]	1	159	78	149.3	3.45	0.352
	RA[6]	10	133	89	135.4	3.58	0.403
APD50	G2RA	0	94.5	41	110.8	3.13	0.437
	G2RA	0.1	85.5	57.8	112.7	4.14	0.567
	G2RA	1	89	76.5	127.2	5.19	0.631
	G2RA	10	78	58.8	112.5	4.72	0.649
	RA[6]	0	269	127	280.3	5.76	0.313
	RA[6]	0.1	258	71	257.5	4.03	0.239
	RA[6]	1	240	80	219.9	4.09	0.284
	RA[6]	10	217	109	205.3	4.57	0.339
APD70	G2RA	0	131.5	84.2	173.1	6.15	0.55
	G2RA	0.1	115	121.2	164.1	6.19	0.583
	G2RA	1	117	195.8	181.6	7.42	0.632
	G2RA	10	105	122	160	6.77	0.654
	RA[6]	0	366	108	366.8	5.57	0.231
	RA[6]	0.1	330	61	336.9	4.11	0.186
	RA[6]	1	306	78	292.2	4.86	0.253
	RA[6]	10	278	131	277.4	6.09	0.334
APD90	G2RA	0	173.5	296.8	295.2	13.14	0.688
	G2RA	0.1	151	281.2	246.7	10.35	0.649
	G2RA	1	158.5	362.2	287.2	12.48	0.672
	G2RA	10	133	304	245.8	11.78	0.741
	RA[6]	0	515	194	528.1	8.75	0.252
	RA[6]	0.1	438	142	475.6	8.61	0.276
	RA[6]	1	402	148	430.2	10.45	0.37
	RA[6]	10	370	219	408.7	11.8	0.44

Table 8-4. Summary statistics of hiPSC-AM response to CCh.

ii. hiPSC-AM subcellular effectors of neurohormonal signalling

The subcellular signalling cascades that mediate the effects of cell surface receptor ligation are poorly characterised in hiPSC-CMs. I sought to collaborate with Ms. Emily Akerman and Mr. Matt Read, of the R. Burton group (Department of Pharmacology, University of Oxford), to better characterise these signalling networks within my hiPSC-AMs.

We first observed that our G2RA hiPSC-AMs were LAMP2^{+}, and that the subcellular distribution was consistent with true positive staining of the lysosomal compartment. LAMP2 expression within our hiPSC-AMs indicates a likely functional lysosomal compartment with mature lysosomes.

We observed that our G2RA hiPSC-AMs at the single-cell level did respond to 100 nM ISO, with an increase in cytosolic cAMP concentrations, as measured by the increased EPAC-SH187 signal. However, of particular interest is that these signals were diminished by the addition of Ned-19. This indicates that NAADP-associated signalling is likely involved in the response to β-adrenergic stimulation in our hiPSC-AMs.

We then observed a similar increase in FRET signal to high-dose phenylephrine (30 μM), and TPC2-A1-N (30 μM) – an agonist of TPC2 channels that release non-canonical calcium stores, such as from lysosomes. Broadly, these results support the hypothesis that our hiPSC-AMs contain similar pathways as observed in rat and mouse atrial cardiomyocytes (data not shown), albeit at a much higher dose of PE, and increase cytosolic cAMP concentrations in response to liberation of internal calcium stores from both canonical and non-canonical stores.

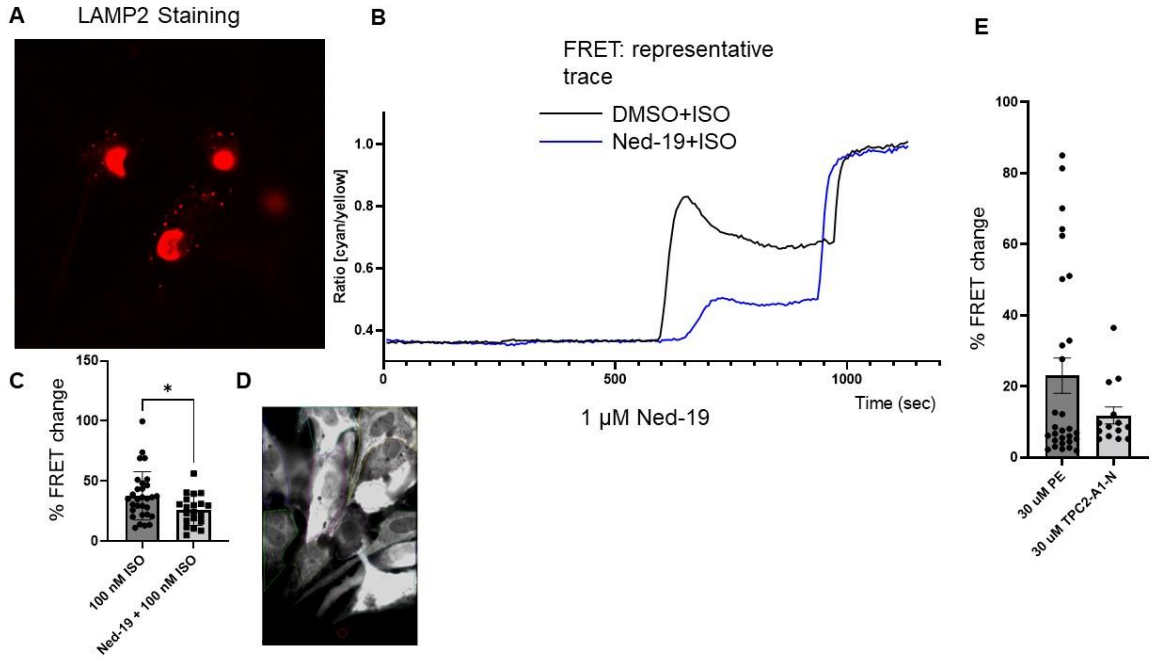

Figure 8-5. hiPSC-AMs display coordinated cellular canonical & non-canonical signalling domains.

A) hiPSC-AMs stained with anti-LAMP2 fluorescent antibodies.
B) A representative trace of FRET signalling using EPAC-SH187 cytosolic cAMP sensor + ISO. In blue is a representative trace when Ned-19 is added with ISO.
C) FRET signal change is significantly reduced when Ned-19 is added with ISO, compared to ISO alone, in hiPSC-AMs.
D) Representative image of hiPSC-AMs in FRET imaging set-up.
E) Phenylephrine and TPC2 agonists also induce increases in cytosolic FRET signal change.

d. Discussion

i. Our hiPSC-AM models displayed a mixed response to β-adrenoceptor agonism

Both our hiPSC-AM groups failed to display the expected behaviour with regards to β-adrenoceptor agonism by ISO. We had previously characterised our G2RA hiPSC-AM's counterintuitive prolongation of the calcium transient in response to ISO. However, I now demonstrated that this had the functional sequalae of ISO inducing a reduced propensity for coupling at faster pacing rates. The functional response to β-adrenoceptor agonism in hiPSC-CMs remains poorly characterised and highly variable across differentiation protocols – many only elicit a robust adrenergic response if some additional maturation protocol has been implemented. Within the scope of interpreting my results, it is tempting to implicate my earlier work implying discordant calcium handling networks in hiPSC-CMs. To prolong the calcium transient, ISO must be acting to reduce the relative efflux of calcium ions from the sarcoplasm, relative to its effect increasing the influx or buffering of calcium ions within the sarcoplasm. Whilst my earlier work was solely at the level of the transcriptome, and could only play a role in setting the relative ratios of the different proteins, it could be that these discordant networks become increasingly discordant with β-adrenoceptor agonism and give rise to this uncoupling between the expected positive inotropic and lusitropic effects downstream[474]. Alternatively, subcellular domains of cyclic nucleotide signalling downstream of β-adrenoceptor agonism might act to stimulate different fluxes in a manner different from native cardiomyocytes. Ultimately, further work should seek to characterise the subcellular cyclic nucleotide networks and how they differ across different hiPSC-CM models at the level of micro- and nano-domains.

ii. Muscarinic agonists induced a shortened APD

Our earlier results indicated that our G2RA hiPSC-AMs had increased expression of KCNJ3 which encodes a major subunit of the $K_{ir3.1}$ channel that gives rise to $I_{KACh.}$ We then observed that this corresponded with a near native I_{KACh} current density. However, these latest results indicate that this also translates to a dose-dependent shortening of the action potential specifically within the APD90 phase of repolarisation. Thus, whilst our M-cholinoceptor agonists had the expected effect, our β-adrenoceptor agonists did not. This might reflect a simpler mechanism of action, with activation of the I_{KACh} current sufficient to induce the action potential shortening, whereas the native effect of β-adrenoceptor agonists requires more complex coordinated effectors. Given the importance of the synergistic and antagonistic actions of the autonomic nervous system in both healthy and diseased arrhythmia, it is encouraging that our hiPSC-AMs at least demonstrate a response to both, even if the sympathomimetic response is somewhat aberrant.

iii. Subcellular ion fluxes and signalling domains

It is of interest to note that whereas the calcium transient was largely unaffected by the tachypacing protocol at baseline: the action potential was shortened by the tachypacing protocol. Whilst this appears subtle and inconsequential, it has ramifications for the presence and deficits of certain subcellular ion dynamics and signalling cascades, associated with this frequency-dependent shortening in native cardiomyocytes, in our hiPSC-AMs. There are a number of potential explanations for this that fit broadly into either increased outward currents (I_K) or reduced inwards currents (I_{Na} or I_{Ca})[475]. Currents depend on channels, the electrochemical gradients for pertinent ions, and the interactions between these channels and ions. The 30 second period between the cessation of the tachypacing and measurement of these APDs at 1 Hz rules out the effects of ion channel kinetics, which would be more pertinent at shorter time

periods (ms – s)[44]. Calmodulin-activated kinase II (CaMKII) is a kinase activated by tachypacing, with similar protein targets and stimulatory effects as PKA-mediated adrenergic signalling[476]. However, CaMKII is unlikely to be the cause of this APD shortening for two major reasons: the effects of CaMKII on altering APD are mostly reported to act to increase depolarising currents and CaMKII would be expected to modulate the calcium transient, which was not apparent here. Another option is the alteration of internal or external ion concentrations. For example, tachypacing is associated with increased $[K^+_e]$. However, $[K^+_e]$ increases from tachypacing are typically associated with the tortuosity of the extracellular spaces in native cardiac tissue, which is likely less applicable in our mono/oligo-cellular layers. Furthermore, these changes in $[K^+_e]$ have been well-characterised as contributing to frequency-dependent APD shortening[477]. However, over similar durations of tachypacing at 5 Hz, Atwell et al. reported that by 30 s after the tachypacing, the pacing-depolarisation of the resting membrane potential had largely resolved (as a proxy measure of $[K^+_e]$), yet similar conditions revealed a less than 10% recovery of APD. Thus, given the similarity in our experimental conditions, it appears unlikely that $[K^+_e]$ changes are the sole cause of my observed APD shortening. Changes to Na^+ and Ca^{2+} fluxes have been implicated by many to account for these frequency-dependent shortenings. The increase in $[Na^+_i]$ with tachypacing has been demonstrated[478] and implied to shorten the action potential via reductions in I_{NCX} across phases 2-3[479]. It is possible that this might be the case in my results. Mr. Matthew Read and I attempted to elicit confocal laser microscopy-based examination of single-cell high-spatial resolution fluorescent calcium imaging, with a goal to examine the subcellular calcium dynamics with field stimulation (data not shown). However, unfortunately, we have not yet overcome technical challenges associated with field stimulation on this set-up. Ultimately, the causal mechanism of frequency-dependent APD changes has not fully been elucidated even within native cardiomyocytes. However, that our hiPSC-AMs display this characteristic is a reassuring link to support co-ordinated subcellular ion fluxes similar to those found in native cardiomyocytes.

It was promising to see preliminary results supporting cellular cAMP responses similar to native cardiomyocytes, and the calcium-dependence of this signal. However, it was particularly interesting to see results implying the functional presence of non-canonical calcium release mechanisms in regulating cellular cAMP responses. Our earlier transcriptomic work identified that our G2RA hiPSC-AMs had particularly robust expression of a range of isoforms of PDE3,4,5,7,8, and 9. We measured cAMP, which is dependent on production as well as degradation. We are currently unable to confirm anything beyond these early promising results. However, the calcium-sensitivity of cAMP concentrations, as demonstrated by its inhibition by Ned-19, makes it tempting to speculate about the presence of calcium-sensitive adenylyl cyclases and/or perhaps calcium-sensitive PDEs. However, future work is required to repeat these initial experiments and further characterise the signalling pathways involved.

Chapter 9. Closing discussion, conclusions, and next steps

a. Addressing thesis aims, conclusions, and next steps

This thesis set out to address several questions that I will address in turn below each one as to whether this has been successful, and what lies next:

i. What is the cardiac expression of catecholaminergic biosynthetic genes and does it have any importance?

Whilst we had in previous work identified that cardiomyocytes expressed the final enzyme in the biosynthesis of catecholamines (PNMT)[3,338,339], it was not clear when this began or whether cardiomyocytes expressed the other upstream and downstream components for this to have any functional importance. This work characterised the expression of *Dbh* by cardiomyocytes and its functional importance for intracardiac conduction, alongside the presence of catecholaminergic vesicles in cardiomyocytes. *Dbh* represents an important catalytic step from dopamine to the stronger adrenergic agonist noradrenaline. However, whilst I did identify some cardiomyocytes expressing the upstream enzymes (*Th* etc. data not shown), and GO analysis did identify some difference in downstream synaptic vesicle-associated genes in Dbh^{+} cardiomyocytes compared to their Dbh^{-} counterparts (data not shown), it remains to be determined whether the source of these catecholamines is cardiomyocyte biosynthesis, from what stage of precursor, and what stimulus, if any, induces the release of these vesicles. The transcriptional comparison of Dbh^{+} cardiomyocytes compared to their Dbh^{-} counterparts was also likely limited by the probable 'drop-out' of *Dbh* expression, to result in a number of 'false negative' Dbh^{-} cardiomyocytes that might in fact express *Dbh* that was not detected. However, as with most tools, the best output is produced when used in a thoughtful manner adapted to scientific question at hand: thus, whilst I had success with scRNA-Seq as an initial hypothesis screening tool, there are many questions that remain outside of its current scope.

ii. Can we use scRNA-seq to produce actionable insights into atrial development and maturation, and how do these relate to hiPSC-AM differentiation?

This thesis demonstrated that scRNA-Seq enabled informatics-based approaches could faithfully reproduce known biology in terms of major transcription factors in networks involved in atrial development and perinatal maturation – such as *Nr2f2*, *Tbx20*, and *Ppargc1a*. However, these did not appear to translate across to explaining the apparently more mature phenotype of our G2RA-based hiPSC-AM differentiation protocol. Ultimately, the relationship between transcriptional abundance and phenotype remains only an approximation, and in particular the significance of different regulatory genes, such as transcription factors, is likely to be highly non-linear. Characterising these imprecise and non-linear relationships is likely to require systematic high-throughput approaches similar to a mutagenesis screen. Nonetheless, understanding these relationships with regards to differentiation and maturation is likely to yield promising signalling cascades for small-molecule promotion of chamber-specific and mature hiPSC-CMs.

iii. What is the relationship between calcium handling components at the level of the transcriptome?

It is easy to examine the absolute abundance of particular fluxes, proteins, and transcripts, and use this as a basis of describing complex multi-cellular life. However, the work of Riabiz et al, and my contribution in this thesis at the level of the transcriptome suggest that there is much complexity beyond absolute or even relative abundances, and that co-variance networks exist at the currently measured levels of fluxes and transcripts. This thesis demonstrates that correlation networks do emerge within transcriptomes of cardiomyocytes, and that this appears different between cell types that are understood to have different calcium handling properties. However, this thesis is unable to delve beyond this. As we improve methodological approaches to accurate and precise quantitative measurements from single-cells, such as the nascent field of single-cell proteomics, we should be able to better describe these co-variance networks at each level. However, the bigger challenge is likely to be understanding how these parameters co-vary between the different '-omic' levels. The now rarely used 'Patch-Seq' from neuroscience would enable linked single-cell recordings of action potentials and single-cell RNA sequencing that might provide sufficient information to adequately address the existing debate surrounding this relationship. However, given that sampling single-cell proteomes or transcriptomes is, nearly by definition, a destructive process, it will be a challenge to understand how we can best measure single-cell protein levels serially with recording both functional and transcriptomic information. Perhaps well-calibrated low-plex nanobody-based live-cell recordings in a similar fashion to current spatial transcriptomics/proteomics might allow for serial functional, protein, and then transcriptome sampling from single cells.

iv. Can we characterise our hiPSC-AMs further, with a particular focus on their wider pharmacology?

Following on from our published work which demonstrated a transcriptional and limited functional signature that appeared to be a vast improvement over other atrial-specific hiPSC differentiation protocols, I attempted to further characterise our G2RA model and its pharmacology. I also sought to use a RA[6] model as a control, to identify whether our addition of GREMLIN-2 was adding anything to the most widespread use of just RA – albeit it typically at an earlier point of differentiation. I established that our G2RA protocol appeared to induce stronger I_{Kur} currents, but much more variable I_{to} currents – with the opposite being true in our RA[6] group. I was unable to produce sufficient data on I_{Kr} and I_{Na} to conclude anything further beyond preliminary data. I also identified that our G2RA and RA[6] groups both displayed our previously reported ISO-induced prolongation of the calcium transient. However, I now reported, in line with our published work, that our G2RA hiPSC-AMs showed the expected APD90-selective shortening with increasing CCh concentrations, which was also true in my RA[6] group. I_{KACh} constitutive activation is strongly implicated in atrial fibrillation, and even if our G2RA model is limited in many domains, it may function as a useful tool for the high-throughput development of novel I_{KACh} antagonists.

"We must not forget that when radium when discovered no one knew that it would prove useful in hospitals. The work was one of pure science. And this is a proof that scientific work must not be considered from the point of view of the direct usefulness of it. It must be done for itself, for the beauty of science, and then there is always the chance that a scientific discovery may become, like the radium, a benefit to humanity." - *Marie Curie 1921.*

Publications, awards, and teaching

Publications:

Sun*, T., Grassam-Rowe*, A., Pu*, Z., Li, Y., Ren, H., An, Y., Guo, X., Hu, W., Liu, Y., Zheng, Y. and Liu, Z., 2023. Dbh+ catecholaminergic cardiomyocytes contribute to the structure and function of the cardiac conduction system in murine heart. Nature Communications, 14(1), p.7801. *Co-first author - contributed equally.

Grassam-Rowe, A. and Lei, M., 2023. Unveiling the neural remodelling landscape in failure heart: A new frontier in cardiac arrhythmogenesis research. Journal of Molecular and Cellular Cardiology Plus, p.100045.

He, Y., Grassam-Rowe, A., Lei, M. and Bae, J.S., 2023. Targeting p21-activated kinase 1 for development of a novel anti-arrhythmic drug class. Philosophical Transactions of the Royal Society B, 378(1879), p.20220285.

Ahmad*, F.S., Jin*, Y., Grassam-Rowe*, A., Zhou, Y., Yuan, M., Fan, X., Zhou, R., Mu-U-Min, R., O'Shea, C., Ibrahim, A.M. and Hyder, W., 2023. Generation of cardiomyocytes from human-induced pluripotent stem cells resembling atrial cells with ability to respond to adrenoceptor agonists. Philosophical Transactions of the Royal Society B, 378(1879), p.20220312. *Co-first author.

Awards:

Medical Sciences Division, University of Oxford – Commendation: Teaching Excellence Awards

Teaching:

Teaching Assistant – Laboratory Practicals (BM1 & MSc): Department of Pharmacology

Sabbatical cover – Cardiovascular Pharmacology Seminars (BM1): Department of Pharmacology

Tutor – Physiology & Pharmacology (BM1): The Queen's College, University of Oxford

Invited Judge – Pharmacology Research Symposium 2024, Department of Pharmacology

References

1 Ahmad, F. S. *et al.* Generation of cardiomyocytes from human-induced pluripotent stem cells resembling atrial cells with ability to respond to adrenoceptor agonists. *Philosophical Transactions of the Royal Society B* **378**, 20220312 (2023).

2 Sun, T. *et al.* Dbh+ catecholaminergic cardiomyocytes contribute to the structure and function of the cardiac conduction system in murine heart. *Nature communications* **14**, 7801 (2023).

3 Grassam-Rowe, A., Ou, X. & Lei, M. Novel cardiac cell subpopulations: Pnmt-derived cardiomyocytes. *Open Biology* **10**, 200095 (2020). https://doi.org/doi:10.1098/rsob.200095

4 Mitchell, P. Chemiosmotic coupling in oxidative and photosynthetic phosphorylation. *Biological Reviews* **41**, 445-501 (1966).

5 Mitchell, P. Coupling of phosphorylation to electron and hydrogen transfer by a chemi-osmotic type of mechanism. *Nature* **191**, 144-148 (1961).

6 Shampo, M. A., Kyle, R. A. & Steensma, D. P. Paul D. Boyer—Nobel prize for work on ATP synthase. *Mayo Clin Proc* **86**, e51 (2011). https://doi.org/10.4065/mcp.2011.0615

7 Prebble, J. N. Contrasting Approaches to a Biological Problem: Paul Boyer, Peter Mitchell and the Mechanism of the ATP Synthase, 1961–1985. *Journal of the History of Biology* **46**, 699-737 (2013). https://doi.org/10.1007/s10739-012-9343-7

8 Pearce, J. M. S. Malpighi and the Discovery of Capillaries. *European Neurology* **58**, 253-255 (2007). https://doi.org/10.1159/000107974

9 Comtor Jr, J. Harvey's 1651 perfusion of the pulmonary circulation of man. *Circulation* **65**, 1-3 (1982).

10 Tubbs, R. S., Linganna, S. & Loukas, M. Matteo Realdo Colombo (c. 1516–1559): the anatomist and surgeon. *The American Surgeon* **74**, 84-86 (2008).

11 Harvey, W. *On the Motion of the Heart and Blood in Animals*. (G. Bell and Sons, 1889).

12 Harvey, W. De Motu Cordis. (1628).

13 AIRD, W. C. Discovery of the cardiovascular system: from Galen to William Harvey. *Journal of Thrombosis and Haemostasis* **9**, 118-129 (2011). https://doi.org/https://doi.org/10.1111/j.1538-7836.2011.04312.x

14 Siegel, R. E. Why Galen and Harvey did not compare the heart to a pump. *The American Journal of Cardiology* **20**, 117-121 (1967). https://doi.org/https://doi.org/10.1016/0002-9149(67)90116-6

15 Ball, J. M. *Andreas Vesalius: the reformer of anatomy*. (Medical Science Press, 1910).

16 Loukas, M. *et al.* History of cardiac anatomy: A comprehensive review from the egyptians to today. *Clinical Anatomy* **29**, 270-284 (2016). https://doi.org/https://doi.org/10.1002/ca.22705

17 Davis, I. M. "Round, red globules floating in a crystalline fluid" – Antoni van Leeuwenhoek's observations of red blood cells and hemocytes. *Micron* **157**, 103249 (2022). https://doi.org/https://doi.org/10.1016/j.micron.2022.103249

18 His, W. (Basel: Schweighauser, 1865).

19 Hwa, C. & Aird, W. C. The history of the capillary wall: doctors, discoveries, and debates. *American Journal of Physiology-Heart and Circulatory Physiology* **293**, H2667-H2679 (2007). https://doi.org/10.1152/ajpheart.00704.2007

20 Katz, A. M. Evolving concepts of heart failure: Cooling furnace, malfunctioning pump, enlarging muscle—Part I. *Journal of Cardiac Failure* **3**, 319-334 (1997). https://doi.org/https://doi.org/10.1016/S1071-9164(97)90032-4

21 Hales, S. Statistical essays containing haemostaticks;or an account of some hydraulic and hydrostaticalexperiments made on the blood and blood pressure ofanimals. *London: Innys and Manby* (1933).

22 Howell, W. H., Donaldson, F. & Foster, M. Experiments upon the heart of the dog with reference to the maximum volume of blood sent out by the left ventricle in a single beat, and the influence of variations in venous pressure, arterial pressure, and pulse rate upon the work done by the heart. *Proceedings of the Royal Society of London* **35**, 271-274 (1997). https://doi.org/10.1098/rspl.1883.0046

23 Howell, W. H. & Foster, M. VI. Experiments upon the heart of the dog with reference to the maximum volume of blood sent out by the left ventricle in a single beat and the influence of variations in venous pressure, arterial pressure, and pulse-rate upon the work done by the heart. *Philosophical Transactions of the Royal Society of London* **175**, 139-160 (1884). https://doi.org/doi:10.1098/rstl.1884.0007

24 Kuhtz-Buschbeck, J. P., Drake-Holland, A., Noble, M. I. M., Lohff, B. & Schaefer, J. Rediscovery of Otto Frank's contribution to science. *Journal of Molecular and Cellular*

Cardiology **119**, 96-103 (2018). https://doi.org/https://doi.org/10.1016/j.yjmcc.2018.04.017

25 Patterson, S., Piper, H. & Starling, E. The regulation of the ventricles. *J Physiol (Lond)* **48**, 465-513 (1914).

26 Patterson, S. & Starling, E. On the mechanical factors which determine the output of the ventricles. *The Journal of physiology* **48**, 357 (1914).

27 Kuijpers, P. History in medicine: the road to clinical electrophysiology. *E-Journal of Cardiology Practice December* **21** (2021).

28 Kuhtz-Buschbeck, J. P., Schaefer, J., Wilder, N. & Wolze, W. T. The origin of the heartbeat and theories of muscle contraction. Physiological concepts and conflicts in the 19th century. *Progress in Biophysics and Molecular Biology* **159**, 3-9 (2021). https://doi.org/https://doi.org/10.1016/j.pbiomolbio.2020.05.009

29 Weber, E. Muskelbewegung. *Handworterbuch der Physiologie* (1846).

30 Müller, J. *Handbuch der physiologie des menschen*. Vol. 1 (J. Hölscher, 1838).

31 Legallois, C. J. J. & Le Gallois, J. J. C. *Expériences sur le principe de la vie: notamment sur celui des mouvemens du coeurs, et sur la siège de ce principe: ornées d'une planche gravée*. (d'Hautel, 1812).

32 Galvani, L. *Opere edite ed inedite del professore Luigi Galvani*. (Dall'Olmo, 1841).

33 Matteucci, C. Sur un phenomene physiologique produit par les muscles en contraction. *Ann Chim Phys.* **6**, 339-341 (1842).

34 Kolliker, A. V. Croonian lecture-On the termination of nerves in muscles, as observed in the frog; and on the disposition of the nerves in the frog's heart. *Proceedings of the Royal Society of London*, 65-84 (1863).

35 Burdon-Sanderson, J. On the time-relations of the excitatory process in the ventricle of the heart of the frog. *The Journal of Physiology* **2**, 384 (1880).

36 Einthoven, W. in *KNAW proceedings*. 107-115.

37 Huxley, H. E. Electron microscope studies of the organisation of the filaments in striated muscle. *Biochimica et Biophysica Acta* **12**, 387-394 (1953). https://doi.org/https://doi.org/10.1016/0006-3002(53)90156-5

38 Frampton, J. E., Orchard, C. H. & Boyett, M. R. Diastolic, systolic and sarcoplasmic reticulum [Ca2+] during inotropic interventions in isolated rat myocytes. *The Journal of Physiology* **437**, 351-375 (1991). https://doi.org/https://doi.org/10.1113/jphysiol.1991.sp018600

39 Tian, J., Gong, X. & Xie, Z. Signal-transducing function of Na+-K+-ATPase is essential for ouabain's effect on [Ca2+]i in rat cardiac myocytes. *American Journal of Physiology-Heart and Circulatory Physiology* **281**, H1899-H1907 (2001). https://doi.org/10.1152/ajpheart.2001.281.5.H1899

40 Vahl, C. F., Bonz, A., Timek, T. & Hagl, S. Intracellular calcium transient of working human myocardium of seven patients transplanted for congestive heart failure. *Circulation Research* **74**, 952-958 (1994). https://doi.org/doi:10.1161/01.RES.74.5.952

41 Piacentino, V. *et al.* Cellular Basis of Abnormal Calcium Transients of Failing Human Ventricular Myocytes. *Circulation Research* **92**, 651-658 (2003). https://doi.org/doi:10.1161/01.RES.0000062469.83985.9B

42 Ringer, S. A further Contribution regarding the influence of the different Constituents of the Blood on the Contraction of the Heart. *J Physiol* **4**, 29-42.23 (1883). https://doi.org/10.1113/jphysiol.1883.sp000120

43 Miller, D. J. Sydney Ringer; physiological saline, calcium and the contraction of the heart. *J Physiol* **555**, 585-587 (2004). https://doi.org/10.1113/jphysiol.2004.060731

44 Eisner, D. A., Dibb, K. M. & Trafford, A. W. The mechanism and significance of the slow changes of ventricular action potential duration following a change of heart rate. *Experimental Physiology* **94**, 520-528 (2009). https://doi.org/https://doi.org/10.1113/expphysiol.2008.044008

45 Díaz, M. E., O'Neill, S. C. & Eisner, D. A. Sarcoplasmic Reticulum Calcium Content Fluctuation Is the Key to Cardiac Alternans. *Circulation Research* **94**, 650-656 (2004). https://doi.org/doi:10.1161/01.RES.0000119923.64774.72

46 Trafford, A. W., Díaz, M. E., Sibbring, G. C. & Eisner, D. A. Modulation of CICR has no maintained effect on systolic Ca2+: simultaneous measurements of sarcoplasmic reticulum and sarcolemmal Ca2+ fluxes in rat ventricular myocytes. *The Journal of Physiology* **522**, 259-270 (2000). https://doi.org/https://doi.org/10.1111/j.1469-7793.2000.t01-2-00259.x

47 Lindner, M., Erdmann, E. & Beuckelmann, D. J. Calcium Content of the Sarcoplasmic Reticulum in Isolated Ventricular Myocytes from Patients with Terminal Heart Failure. *Journal of Molecular and Cellular Cardiology* **30**, 743-749 (1998). https://doi.org/https://doi.org/10.1006/jmcc.1997.0626

48 Nimer, L. R., Needleman, D. H., Hamilton, S. L., Krall, J. & Movsesian, M. A. Effect of Ryanodine on Sarcoplasmic Reticulum Ca²⁺ Accumulation in Nonfailing and Failing Human Myocardium. *Circulation* **92**, 2504-2510 (1995). https://doi.org/doi:10.1161/01.CIR.92.9.2504

49 Marx, S. O. *et al.* Coupled Gating Between Cardiac Calcium Release Channels (Ryanodine Receptors). *Circulation Research* **88**, 1151-1158 (2001). https://doi.org/doi:10.1161/hh1101.091268

50 Ondrias, K., Brillantes, A.-M. B., Scott, A., Ehrlich, B. E. & Marks, A. R. Single channel properties and calcium conductance of the cloned expressed ryanodine receptor/calcium-release channel. *Society of General Physiologists Series* **51**, 29-46 (1996).

51 Cleemann, L., Wang, W. & Morad, M. Two-dimensional confocal images of organization, density, and gating of focal Ca²⁺ release sites in rat cardiac myocytes. *Proceedings of the National Academy of Sciences* **95**, 10984-10989 (1998). https://doi.org/doi:10.1073/pnas.95.18.10984

52 Fabiato, A. Calcium-induced release of calcium from the cardiac sarcoplasmic reticulum. *American Journal of Physiology-Cell Physiology* **245**, C1-C14 (1983). https://doi.org/10.1152/ajpcell.1983.245.1.C1

53 Franzini-Armstrong, C. Architecture and regulation of the Ca2+ delivery system in muscle cells. *Applied Physiology, Nutrition, and Metabolism* **34**, 323-327 (2009).

54 Hayashi, T. *et al.* Three-dimensional electron microscopy reveals new details of membrane systems for Ca2+ signaling in the heart. *Journal of Cell Science* **122**, 1005-1013 (2009). https://doi.org/10.1242/jcs.028175

55 Noble, D. A modification of the Hodgkin—Huxley equations applicable to Purkinje fibre action and pacemaker potentials. *The Journal of physiology* **160**, 317 (1962).

56 DiFrancesco, D. & Noble, D. I984 A model of cardiac electrical activity incorporating ionic pumps and concentration changes. *Phil. Trans. R. Soc. Lond. B (In the press.)*

57 Luo, C.-H. & Rudy, Y. A dynamic model of the cardiac ventricular action potential. II. Afterdepolarizations, triggered activity, and potentiation. *Circulation research* **74**, 1097-1113 (1994).

58 Winslow, R. L., Varghese, A., Noble, D., Adlakha, C. & Hoythya, A. Generation and propagation of ectopic beats induced by spatially localized Na–K pump inhibition in atrial network models. *Proceedings of the Royal Society of London. Series B: Biological Sciences* **254**, 55-61 (1993).

59 Hooks, D. A. *et al.* Cardiac microstructure: implications for electrical propagation and defibrillation in the heart. *Circulation research* **91**, 331-338 (2002).

60 Niederer, S. A., Lumens, J. & Trayanova, N. A. Computational models in cardiology. *Nature Reviews Cardiology* **16**, 100-111 (2019). https://doi.org/10.1038/s41569-018-0104-y

61 Britton, O. J. *et al.* Experimentally calibrated population of models predicts and explains intersubject variability in cardiac cellular electrophysiology. *Proceedings of the National*

Academy of Sciences **110**, E2098-E2105 (2013). https://doi.org/doi:10.1073/pnas.1304382110

62 Muszkiewicz, A. *et al.* Variability in cardiac electrophysiology: Using experimentally-calibrated populations of models to move beyond the single virtual physiological human paradigm. *Progress in Biophysics and Molecular Biology* **120**, 115-127 (2016). https://doi.org/https://doi.org/10.1016/j.pbiomolbio.2015.12.002

63 Romero, L., Pueyo, E., Fink, M. & Rodríguez, B. Impact of ionic current variability on human ventricular cellular electrophysiology. *American Journal of Physiology-Heart and Circulatory Physiology* **297**, H1436-H1445 (2009). https://doi.org/10.1152/ajpheart.00263.2009

64 Groenendaal, W. *et al.* Cell-specific cardiac electrophysiology models. *PLoS computational biology* **11**, e1004242 (2015).

65 Temporal, S. *et al.* Neuromodulation independently determines correlated channel expression and conductance levels in motor neurons of the stomatogastric ganglion. *J Neurophysiol* **107**, 718-727 (2012). https://doi.org/10.1152/jn.00622.2011

66 Riabiz, M. *et al.* Optimal Thinning of MCMC Output. *Journal of the Royal Statistical Society Series B: Statistical Methodology* **84**, 1059-1081 (2022). https://doi.org/10.1111/rssb.12503

67 Hinch, R., Greenstein, J., Tanskanen, A., Xu, L. & Winslow, R. A simplified local control model of calcium-induced calcium release in cardiac ventricular myocytes. *Biophysical journal* **87**, 3723-3736 (2004).

68 Ballouz, S. *et al.* Co-expression of calcium and hERG potassium channels reduces the incidence of proarrhythmic events. *Cardiovasc Res* **117**, 2216-2227 (2021). https://doi.org/10.1093/cvr/cvaa280

69 Banyasz, T., Horvath, B., Jian, Z., Izu, L. T. & Chen-Izu, Y. Sequential dissection of multiple ionic currents in single cardiac myocytes under action potential-clamp. *J Mol Cell Cardiol* **50**, 578-581 (2011). https://doi.org/10.1016/j.yjmcc.2010.12.020

70 Harary, I. & Farley, B. In vitro studies on single beating rat heart cells: I. Growth and organization. *Experimental Cell Research* **29**, 451-465 (1963). https://doi.org/https://doi.org/10.1016/S0014-4827(63)80008-7

71 Carrel, A. On the permanent life of tissues outside of the organism. *The Journal of experimental medicine* **15**, 516 (1912).

72 Walklate, J. *et al.* Alpha and beta myosin isoforms and human atrial and ventricular contraction. *Cellular and Molecular Life Sciences* **78**, 7309-7337 (2021). https://doi.org/10.1007/s00018-021-03971-y

73 Johnson, C. A. *et al.* The ATPase cycle of human muscle myosin II isoforms: Adaptation of a single mechanochemical cycle for different physiological roles. *Journal of Biological Chemistry* **294**, 14267-14278 (2019). https://doi.org/10.1074/jbc.RA119.009825

74 Piroddi, N. *et al.* Tension generation and relaxation in single myofibrils from human atrial and ventricular myocardium. *Pflügers Archiv - European Journal of Physiology* **454**, 63-73 (2007). https://doi.org/10.1007/s00424-006-0181-3

75 Narolska, N. A. *et al.* Myosin heavy chain composition and the economy of contraction in healthy and diseased human myocardium. *Journal of Muscle Research & Cell Motility* **26**, 39-48 (2005). https://doi.org/10.1007/s10974-005-9005-x

76 Narolska, N. A. *et al.* Myocardial contraction is 5-fold more economical in ventricular than in atrial human tissue. *Cardiovascular Research* **65**, 221-229 (2005). https://doi.org/10.1016/j.cardiores.2004.09.029

77 Walden, A., Dibb, K. & Trafford, A. Differences in intracellular calcium homeostasis between atrial and ventricular myocytes. *Journal of molecular and cellular cardiology* **46**, 463-473 (2009).

78 Hodgkin, A. L. & Huxley, A. F. A quantitative description of membrane current and its application to conduction and excitation in nerve. *J Physiol* **117**, 500-544 (1952). https://doi.org/10.1113/jphysiol.1952.sp004764
79 Hodgkin, A. L., Huxley, A. F. & Katz, B. Measurement of current-voltage relations in the membrane of the giant axon of Loligo. *The Journal of physiology* **116**, 424 (1952).
80 Woodbury, L., Woodbury, J. & HECHT, H. H. Membrane resting and action potentials of single cardiac muscle fibers. *Circulation* **1**, 264-266 (1950).
81 Draper, M. H. & Weidmann, S. Cardiac resting and action potentials recorded with an intracellular electrode. *The Journal of physiology* **115**, 74 (1951).
82 Reuter, H. Strom-spannungsbeziehungen von purkinje-fasern bei verschiedenen extracellulären calcium-Konzentrationen und unter adrenalineinwirkung. *Pflüger's Archiv für die gesamte Physiologie des Menschen und der Tiere* **287**, 357-367 (1966).
83 Reuter, H. & Seitz, N. The dependence of calcium efflux from cardiac muscle on temperature and external ion composition. *The Journal of physiology* **195**, 451-470 (1968).
84 January, C. T. & Fozzard, H. A. The effects of membrane potential, extracellular potassium, and tetrodotoxin on the intracellular sodium ion activity of sheep cardiac muscle. *Circulation Research* **54**, 652-665 (1984). https://doi.org/doi:10.1161/01.RES.54.6.652
85 Terracciano, C. M., Tweedie, D. & MacLeod, K. T. The effects of changes to action potential duration on the calcium content of the sarcoplasmic reticulum in isolated guinea-pig ventricular myocytes. *Pflugers Arch* **433**, 542-544 (1997). https://doi.org/10.1007/s004240050312
86 Willius, F. A. & Dry, T. J. A history of the heart and the circulation. (1948).
87 Silverman, M. E., Grove, D. & Upshaw Jr, C. B. Why does the heart beat? The discovery of the electrical system of the heart. *Circulation* **113**, 2775-2781 (2006).
88 Tawara, S. *Das Reizleitungssystem des Säugetierherzens: eine anatomisch-histologische Studie über das Atrioventrikularbündel und die Purkinjeschen Fäden*. (Fischer, 1906).
89 Silverman, M. E. & Upshaw, C. B. Walter Gaskell and the understanding of atrioventricular conduction and block. *Journal of the American college of cardiology* **39**, 1574-1580 (2002).
90 Gaskell, W. The contraction of cardiac muscle. *Textbook of physiology* **2**, 169 (1900).
91 Gaskell, W. H. On the innervation of the heart, with especial reference to the heart of the tortoise. *The Journal of Physiology* **4**, 43 (1883).
92 Bast, T. H., Gardner, W. D. & His, W. Wilhelm His, Jr. and the bundle of His. *Journal of the History of Medicine and Allied Sciences* **4**, 170-187 (1949).
93 HIS, W. The story of the atrioventricular bundle with remarks concerning embryonic heart activity. *Journal of the history of medicine and allied sciences* **4**, 319-333 (1949).
94 Lewis, T. ON THE ELECTRO-CARDIOGRAPHIC CURVES YIELDED BY ECTOPIC BEATS ARISING IN THE WALLS OF THE AURICLES AND VENTRICLES. *Br Med J* **1**, 750 (1910). https://doi.org/10.1136/bmj.1.2569.750
95 MONFREDI, O., DOBRZYNSKI, H., MONDAL, T., BOYETT, M. R. & MORRIS, G. M. The Anatomy and Physiology of the Sinoatrial Node—A Contemporary Review. *Pacing and Clinical Electrophysiology* **33**, 1392-1406 (2010). https://doi.org/https://doi.org/10.1111/j.1540-8159.2010.02838.x
96 WATANABE, Y. & DREIFUS, L. S. Sites of Impulse Formation within the Atrioventricular Junction of the Rabbit. *Circulation Research* **22**, 717-727 (1968). https://doi.org/doi:10.1161/01.RES.22.6.717
97 Keith, A. The sino-auricular node: a historical note. *British Heart Journal* **4**, 77 (1942).
98 Keith, A. & Flack, M. The form and nature of the muscular connections between the primary divisions of the vertebrate heart. *Journal of anatomy and physiology* **41**, 172 (1907).

99 Lewis, T. The excitation wave in the heart. *Lewis T. Lectures on the Heart. New York, NY: Paul B. Hoeber*, 3-31 (1915).

100 Brennan Jaclyn, A. *et al.* Evidence of Superior and Inferior Sinoatrial Nodes in the Mammalian Heart. *JACC: Clinical Electrophysiology* **6**, 1827-1840 (2020). https://doi.org/10.1016/j.jacep.2020.09.012

101 Boineau, J. P. *et al.* Demonstration of a widely distributed atrial pacemaker complex in the human heart. *Circulation* **77**, 1221-1237 (1988). https://doi.org/10.1161/01.CIR.77.6.1221

102 Sano, T. & Iida, Y. The sino-atrial connection and wandering pacemaker. *Journal of Electrocardiology* **1**, 147-153 (1968). https://doi.org/https://doi.org/10.1016/S0022-0736(68)80021-4

103 Bleeker, W. K., Mackaay, A., Masson-Pévet, M., Bouman, L. N. & Becker, A. E. Functional and morphological organization of the rabbit sinus node. *Circulation research* **46**, 11-22 (1980).

104 DiFrancesco, D. The pacemaker current (I f) plays an important role in regulating SA node pacemaker activity. *Cardiovascular research* **30**, 307-308 (1995).

105 Shi, W. *et al.* Distribution and prevalence of hyperpolarization-activated cation channel (HCN) mRNA expression in cardiac tissues. *Circulation research* **85**, e1-e6 (1999).

106 Lei, M., Wu, L., Terrar, D. A. & Huang, C. L.-H. Modernized classification of cardiac antiarrhythmic drugs. *Circulation* **138**, 1879-1896 (2018).

107 Baruscotti, M. *et al.* Deep bradycardia and heart block caused by inducible cardiac-specific knockout of the pacemaker channel gene Hcn4. *Proceedings of the National Academy of Sciences* **108**, 1705-1710 (2011).

108 Herrmann, S., Stieber, J., Stöckl, G., Hofmann, F. & Ludwig, A. HCN4 provides a 'depolarization reserve' and is not required for heart rate acceleration in mice. *The EMBO Journal* **26**, 4423-4432-4432 (2007). https://doi.org/https://doi.org/10.1038/sj.emboj.7601868

109 He, Y., Grassam-Rowe, A., Lei, M. & Bae, J. S. Targeting p21-activated kinase 1 for development of a novel anti-arrhythmic drug class. *Philosophical Transactions of the Royal Society B* **378**, 20220285 (2023).

110 Bogdanov, K. Y., Vinogradova, T. M. & Lakatta, E. G. Sinoatrial Nodal Cell Ryanodine Receptor and Na⁺-Ca²⁺ Exchanger. *Circulation Research* **88**, 1254-1258 (2001). https://doi.org/doi:10.1161/hh1201.092095

111 Torrente, A. G. *et al.* L-type Cav1. 3 channels regulate ryanodine receptor-dependent Ca2+ release during sino-atrial node pacemaker activity. *Cardiovascular Research* **109**, 451-461 (2016).

112 Maltsev, V. A. & Lakatta, E. G. Dynamic interactions of an intracellular Ca2+ clock and membrane ion channel clock underlie robust initiation and regulation of cardiac pacemaker function. *Cardiovascular Research* **77**, 274-284 (2007). https://doi.org/10.1093/cvr/cvm058

113 Maltsev, V. A. & Lakatta, E. G. Normal heart rhythm is initiated and regulated by an intracellular calcium clock within pacemaker cells. *Heart, Lung and Circulation* **16**, 335-348 (2007).

114 Sirenko, S. *et al.* Sarcoplasmic reticulum Ca2+ cycling protein phosphorylation in a physiologic Ca2+ milieu unleashes a high-power, rhythmic Ca2+ clock in ventricular myocytes: relevance to arrhythmias and bio-pacemaker design. *Journal of molecular and cellular cardiology* **66**, 106-115 (2014).

115 Vinogradova, T. M. *et al.* Constitutive phosphodiesterase activity restricts spontaneous beating rate of cardiac pacemaker cells by suppressing local Ca2+ releases. *Circulation research* **102**, 761-769 (2008).

116 Masson-Pévet, M., Bleeker, W. K., Mackaay, A. J. C., Bouman, L. N. & Houtkooper, J. M. Sinus node and atrium cells from the rabbit heart: A quantitative electron microscopic description after electrophysiological localization. *Journal of Molecular and Cellular Cardiology* **11**, 561-568 (1979). https://doi.org/10.1016/0022-2828(79)90430-9

117 JAMES, T. N., SHERF, L., FINE, G. & MORALES, A. R. Comparative Ultrastructure of the Sinus Node in Man and Dog. *Circulation* **34**, 139-163 (1966). https://doi.org/doi:10.1161/01.CIR.34.1.139

118 Kodama, I. *et al.* Regional differences in the role of the Ca2+ and Na+ currents in pacemaker activity in the sinoatrial node. *Am J Physiol* **272**, H2793-2806 (1997). https://doi.org/10.1152/ajpheart.1997.272.6.H2793

119 Mangoni, M. E. *et al.* Voltage-dependent calcium channels and cardiac pacemaker activity: from ionic currents to genes. *Progress in biophysics and molecular biology* **90**, 38-63 (2006).

120 Kim, M. S. *et al.* Heterogeneity of calcium clock functions in dormant, dysrhythmically and rhythmically firing single pacemaker cells isolated from SA node. *Cell Calcium* **74**, 168-179 (2018). https://doi.org/https://doi.org/10.1016/j.ceca.2018.07.002

121 Munk, A. A., Adjemian, R. A., Zhao, J., Ogbaghebriel, A. & Shrier, A. Electrophysiological properties of morphologically distinct cells isolated from the rabbit atrioventricular node. *The Journal of Physiology* **493**, 801-818 (1996). https://doi.org/https://doi.org/10.1113/jphysiol.1996.sp021424

122 ANDERSON, R. H. *et al.* A Combined Morphological and Electrophysiological Study of the Atrioventricular Node of the Rabbit Heart. *Circulation Research* **35**, 909-922 (1974). https://doi.org/doi:10.1161/01.RES.35.6.909

123 George, S. A. *et al.* At the Atrioventricular Crossroads: Dual Pathway Electrophysiology in the Atrioventricular Node and its Underlying Heterogeneities. *Arrhythm Electrophysiol Rev* **6**, 179-185 (2017). https://doi.org/10.15420/aer.2017.30.1

124 Fedorov, V. V. *et al.* Anatomic localization and autonomic modulation of atrioventricular junctional rhythm in failing human hearts. *Circ Arrhythm Electrophysiol* **4**, 515-525 (2011). https://doi.org/10.1161/circep.111.962258

125 CARVALHO, A. P. D. & ALMEIDA, D. F. D. Spread of Activity Through the Atrioventricular Node. *Circulation Research* **8**, 801-809 (1960). https://doi.org/doi:10.1161/01.RES.8.4.801

126 McGuire, M. A. *et al.* Atrioventricular junctional tissue. Discrepancy between histological and electrophysiological characteristics. *Circulation* **94**, 571-577 (1996). https://doi.org/10.1161/01.cir.94.3.571

127 Kreuzberg, M. M. *et al.* Connexin30.2 containing gap junction channels decelerate impulse propagation through the atrioventricular node. *Proc Natl Acad Sci U S A* **103**, 5959-5964 (2006). https://doi.org/10.1073/pnas.0508512103

128 Greener, I. D. *et al.* Molecular architecture of the human specialised atrioventricular conduction axis. *J Mol Cell Cardiol* **50**, 642-651 (2011). https://doi.org/10.1016/j.yjmcc.2010.12.017

129 Temple, I. P., Inada, S., Dobrzynski, H. & Boyett, M. R. Connexins and the atrioventricular node. *Heart Rhythm* **10**, 297-304 (2013). https://doi.org/10.1016/j.hrthm.2012.10.020

130 Unudurthi, S. D., Wolf, R. M. & Hund, T. J. Role of sinoatrial node architecture in maintaining a balanced source-sink relationship and synchronous cardiac pacemaking. *Frontiers in Physiology* **5** (2014). https://doi.org/10.3389/fphys.2014.00446

131 Verheijck, E. E. *et al.* Electrophysiological features of the mouse sinoatrial node in relation to connexin distribution. *Cardiovascular Research* **52**, 40-50 (2001). https://doi.org/10.1016/S0008-6363(01)00364-9

132 Shimada, T., Kawazato, H., Yasuda, A., Ono, N. & Sueda, K. Cytoarchitecture and intercalated disks of the working myocardium and the conduction system in the mammalian heart. *Anat Rec A Discov Mol Cell Evol Biol* **280**, 940-951 (2004). https://doi.org/10.1002/ar.a.20109

133 Miquerol, L. *et al.* Architectural and functional asymmetry of the His-Purkinje system of the murine heart. *Cardiovasc Res* **63**, 77-86 (2004). https://doi.org/10.1016/j.cardiores.2004.03.007

134 Atkinson, A. *et al.* Anatomical and molecular mapping of the left and right ventricular His-Purkinje conduction networks. *J Mol Cell Cardiol* **51**, 689-701 (2011). https://doi.org/10.1016/j.yjmcc.2011.05.020

135 Gaborit, N. *et al.* Regional and tissue specific transcript signatures of ion channel genes in the non-diseased human heart. *J Physiol* **582**, 675-693 (2007). https://doi.org/10.1113/jphysiol.2006.126714

136 Huang, S. *et al.* Restitution characteristics of His bundle and working myocardium in isolated rabbit hearts. *PLOS ONE* **12**, e0186880 (2017). https://doi.org/10.1371/journal.pone.0186880

137 Colatsky, T. J. Voltage clamp measurements of sodium channel properties in rabbit cardiac Purkinje fibres. *The Journal of Physiology* **305**, 215-234 (1980). https://doi.org/https://doi.org/10.1113/jphysiol.1980.sp013359

138 Colatsky, T. J. & Tsien, R. W. Sodium channels in rabbit cardiac Purkinje fibres. *Nature* **278**, 265-268 (1979). https://doi.org/10.1038/278265a0

139 Wiedmann, R. T., Tan, R. C. & Joyner, R. W. Discontinuous conduction at Purkinje-ventricular muscle junction. *American Journal of Physiology-Heart and Circulatory Physiology* **271**, H1507-H1516 (1996).

140 Walton, M. K. & Fozzard, H. A. Experimental study of the conducted action potential in cardiac Purkinje strands. *Biophys J* **44**, 1-8 (1983). https://doi.org/10.1016/s0006-3495(83)84272-6

141 Ruskin, J., McHale, P. A., Harley, A. & Greenfield, J. C., Jr. Pressure-flow studies in man: effect of atrial systole on left ventricular function. *The Journal of Clinical Investigation* **49**, 472-478 (1970). https://doi.org/10.1172/JCI106256

142 Nagano, T. *et al.* Diastolic compliance of the left atrium in man: A determinant of preload of the left ventricle. *Heart and Vessels* **5**, 25-32 (1989). https://doi.org/10.1007/BF02058355

143 Mulder, B. J. M. & van der Wall, E. E. Size and function of the atria. *The International Journal of Cardiovascular Imaging* **24**, 713-716 (2008). https://doi.org/10.1007/s10554-008-9323-3

144 Matsuda, Y. *et al.* Change of left atrial systolic pressure waveform in relation to left ventricular end-diastolic pressure. *Circulation* **82**, 1659-1667 (1990). https://doi.org/doi:10.1161/01.CIR.82.5.1659

145 MORRIS, J. J., ENTMAN, M., NORTH, W. C., KONG, Y. & MCINTOSH, H. The Changes in Cardiac Output with Reversion of Atrial Fibrillation to Sinus Rhythm. *Circulation* **31**, 670-678 (1965). https://doi.org/doi:10.1161/01.CIR.31.5.670

146 Mukharji, J. *et al.* Comparison of atrial contribution to cardiac hemodynamics in patients with normal and severely compromised cardiac function. *Clinical Cardiology* **13**, 639-643 (1990). https://doi.org/https://doi.org/10.1002/clc.4960130910

147 Kirk, M. M. *et al.* Role of the Transverse-Axial Tubule System in Generating Calcium Sparks and Calcium Transients in Rat Atrial Myocytes. *The Journal of Physiology* **547**, 441-451 (2003). https://doi.org/https://doi.org/10.1113/jphysiol.2002.034355

148 Smyrnias, I. *et al.* Comparison of the T-tubule system in adult rat ventricular and atrial myocytes, and its role in excitation–contraction coupling and inotropic stimulation. *Cell Calcium* **47**, 210-223 (2010). https://doi.org/https://doi.org/10.1016/j.ceca.2009.10.001

149 Hatem, S. N. *et al.* Different Compartments of Sarcoplasmic Reticulum Participate in the Excitation-Contraction Coupling Process in Human Atrial Myocytes. *Circulation Research* **80**, 345-353 (1997). https://doi.org/doi:10.1161/01.RES.80.3.345

150 Hatem, S. N. *et al.* Differential regulation of voltage-activated potassium currents in cultured human atrial myocytes. *American Journal of Physiology-Heart and Circulatory Physiology* **271**, H1609-H1619 (1996). https://doi.org/10.1152/ajpheart.1996.271.4.H1609

151 Bootman, M. D., Higazi, D. R., Coombes, S. & Roderick, H. L. Calcium signalling during excitation-contraction coupling in mammalian atrial myocytes. *Journal of Cell Science* **119**, 3915-3925 (2006). https://doi.org/10.1242/jcs.03223

152 Mackenzie, L., Roderick, H. L., Berridge, M. J., Conway, S. J. & Bootman, M. D. The spatial pattern of atrial cardiomyocyte calcium signalling modulates contraction. *Journal of Cell Science* **117**, 6327-6337 (2004). https://doi.org/10.1242/jcs.01559

153 Delorme, B. *et al.* Developmental regulation of connexin 40 gene expression in mouse heart correlates with the differentiation of the conduction system. *Developmental Dynamics* **204**, 358-371 (1995).

154 Hagendorff, A., Schumacher, B., Kirchhoff, S., Lüderitz, B. & Willecke, K. Conduction Disturbances and Increased Atrial Vulnerability in Connexin40-Deficient Mice Analyzed by Transesophageal Stimulation. *Circulation* **99**, 1508-1515 (1999). https://doi.org/doi:10.1161/01.CIR.99.11.1508

155 Schram, G., Pourrier, M., Melnyk, P. & Nattel, S. Differential Distribution of Cardiac Ion Channel Expression as a Basis for Regional Specialization in Electrical Function. *Circulation Research* **90**, 939-950 (2002). https://doi.org/doi:10.1161/01.RES.0000018627.89528.6F

156 Malliani, A., Recordati, G. & Schwartz, P. Nervous activity of afferent cardiac sympathetic fibres with atrial and ventricular endings. *The Journal of physiology* **229**, 457-469 (1973).

157 Bezold, V. Zur Physiologie der Herzbewegungen. (1858).

158 Von Bezold, A. H. L. Über die physiologischen Wirkungen des essigsauren Veratrins. II: Von der Wirkung des Veratrins auf den Kreislauf. Untersuchungen aus den physiologischen Laboratorienzu Würzburg. (1867).

159 Weber, E. Ueber Eduard Weber's Entdeckungen in der Lehre von der Muskelcontraction. (1846).

160 Henderson, V. & Roepke, M. Drugs affecting parasympathetic nerves. *Physiological Reviews* **17**, 373-407 (1937).

161 Gaskell, W. On the tonicity of the heart and blood vessels. *The Journal of physiology* **3**, 48 (1880).

162 Gaskell, W. H. On the structure, distribution and function of the nerves which innervate the visceral and vascular systems. *The Journal of physiology* **7**, 1 (1886).

163 Langley, J. N. The arrangement of the sympathetic nervous system, based chiefly on observations upon pilo-motor nerves. *The Journal of physiology* **15**, 176 (1893).

164 Langley, J. N. & Dickinson, W. L. III. On the local paralysis of peripheral ganglia, and on the connexion of different classes of nerve fibres with them. *Proceedings of the Royal Society of London* **46**, 423-431 (1890).

165 Dale, H. H. in *Cold Spring Harbor Symposia on Quantitative Biology*. 143-149 (Cold Spring Harbor Laboratory Press).

166 Dale, H. H. The action of certain esters and ethers of choline, and their relation to muscarine. *Journal of Pharmacology and Experimental Therapeutics* **6**, 147-190 (1914).

167 Elliott, T. R. The action of adrenalin. *The Journal of physiology* **32**, 401 (1905).

168 Leenen, F. H. H. Functional Significance of B1- Versus B2-Receptors for Cardiac Inotropic and Chronotropic Responses in Man. *Clinical and Experimental Hypertension. Part A: Theory and Practice* **11**, 43-58 (1989). https://doi.org/10.3109/10641968909045411

169 Motomura, S. & Hashimoto, K. Beta 2-adrenoceptor-mediated positive dromotropic effects on atrioventricular node of dogs. *American Journal of Physiology-Heart and Circulatory Physiology* **262**, H123-H129 (1992). https://doi.org/10.1152/ajpheart.1992.262.1.H123

170 Reddy, Y. S. Phosphorylation of cardiac regulatory proteins by cyclic AMP-dependent protein kinase. *Am J Physiol* **231**, 1330-1336 (1976). https://doi.org/10.1152/ajplegacy.1976.231.5.1330

171 Sutherland, E. W. & Rail, T. Formation of Adenosine-3', 5'-Phosphate (Cyclic Adenylate) and its Relation to the Action of Several Neurohormones or Hormones. *European Journal of Endocrinology* **34**, S171-S174 (1960).

172 Kingwell, B. A. *et al.* Heart rate spectral analysis, cardiac norepinephrine spillover, and muscle sympathetic nerve activity during human sympathetic nervous activation and failure. *Circulation* **90**, 234-240 (1994).

173 Burgoyne, R. D. Mechanisms of secretion from adrenal chromaffin cells. *Biochimica et Biophysica Acta (BBA)-Reviews on Biomembranes* **779**, 201-216 (1984).

174 Axelrod, J. Purification and properties of phenylethanolamine-N-methyl transferase. *Journal of Biological Chemistry* **237**, 1657-1660 (1962).

175 Papka, R. E. A study of catecholamine-containing cells in the hearts of fetal and postnatal rabbits by fluorescence and electron microscopy. *Cell and Tissue Research* **154**, 471-484 (1974).

176 Ignarro, L. J. & Shideman, F. The requirement of sympathetic innervation for the active transport of norepinephrine by the heart. *Journal of Pharmacology and Experimental Therapeutics* **159**, 59-65 (1968).

177 Ignarro, L. J. & Shideman, F. Appearance and concentrations of catecholamines and their biosynthesis in the embryonic and developing chick. *Journal of Pharmacology and Experimental Therapeutics* **159**, 38-48 (1968).

178 Ignarro, L. J. & Shideman, F. Norepinephrine and epinephrine in the embryo and embryonic heart of the chick: uptake and subcellular distribution. *Journal of Pharmacology and Experimental Therapeutics* **159**, 49-58 (1968).

179 Ebert, S. N., Baden, J. M., Mathers, L. H., Siddall, B. J. & Wong, D. L. Expression of phenylethanolamine n-methyltransferase in the embryonic rat heart. *J Mol Cell Cardiol* **28**, 1653-1658 (1996). https://doi.org/10.1006/jmcc.1996.0155

180 Ebert, S. N. & Thompson, R. P. Embryonic epinephrine synthesis in the rat heart before innervation: association with pacemaking and conduction tissue development. *Circulation research* **88**, 117-124 (2001).

181 Huang, M.-H. *et al.* Neuroendocrine properties of intrinsic cardiac adrenergic cells in fetal rat heart. *American Journal of Physiology-Heart and Circulatory Physiology* **288**, H497-H503 (2005).

182 Huang, M.-H. *et al.* An intrinsic adrenergic system in mammalian heart. *The Journal of clinical investigation* **98**, 1298-1303 (1996).

183 Natarajan, A. R., Rong, Q., Katchman, A. N. & Ebert, S. N. Intrinsic cardiac catecholamines help maintain beating activity in neonatal rat cardiomyocyte cultures. *Pediatr Res* **56**, 411-417 (2004). https://doi.org/10.1203/01.Pdr.0000136279.80897.4c

184 Baker, C. *et al.* Adrenergic deficiency leads to impaired electrical conduction and increased arrhythmic potential in the embryonic mouse heart. *Biochem Biophys Res Commun* **423**, 536-541 (2012). https://doi.org/10.1016/j.bbrc.2012.05.163

185 Hall, E. K. Acetylcholine and epinephrine effects on the embryonic rat heart. *J Cell Comp Physiol* **49**, 187-200 (1957). https://doi.org/10.1002/jcp.1030490203

186 Markowitz, C. Response of explanted embryonic cardiac tissue to epinephrine and acetylcholine. *American Journal of Physiology-Legacy Content* **97**, 271-275 (1931).

187 Zhou, Q.-Y., Quaife, C. J. & Palmiter, R. D. Targeted disruption of the tyrosine hydroxylase gene reveals that catecholamines are required for mouse fetal development. *Nature* **374**, 640-643 (1995).
188 Thomas, S. A., Marck, B. T., Palmiter, R. D. & Matsumoto, A. M. Restoration of norepinephrine and reversal of phenotypes in mice lacking dopamine β-hydroxylase. *Journal of neurochemistry* **70**, 2468-2476 (1998).
189 Thomas, S. A., Matsumoto, A. M. & Palmiter, R. D. Noradrenaline is essential for mouse fetal development. *Nature* **374**, 643-646 (1995). https://doi.org/10.1038/374643a0
190 Thomas, S. A., Marck, B. T., Palmiter, R. D. & Matsumoto, A. M. Restoration of norepinephrine and reversal of phenotypes in mice lacking dopamine beta-hydroxylase. *J Neurochem* **70**, 2468-2476 (1998). https://doi.org/10.1046/j.1471-4159.1998.70062468.x
191 Kobayashi, K. *et al.* Targeted disruption of the tyrosine hydroxylase locus results in severe catecholamine depletion and perinatal lethality in mice. *Journal of Biological Chemistry* **270**, 27235-27243 (1995).
192 MOORE, G. E. & Parratt, J. Effect of noradrenaline and isoprenaline on blood flow in the acutely ischaemic myocardium. *Cardiovascular Research* **7**, 446-457 (1973).
193 Shanks, R. & Dunlop, D. Effect of propranolol on arrhythmias following coronary artery occlusion in dogs. *Cardiovascular Research* **1**, 34-41 (1967).
194 Morisco, C., Zebrowski, D. C., Vatner, D. E., Vatner, S. F. & Sadoshima, J. β-Adrenergic cardiac hypertrophy is mediated primarily by the β1-subtype in the rat heart. *Journal of molecular and cellular cardiology* **33**, 561-573 (2001).
195 Engelhardt, S., Hein, L., Wiesmann, F. & Lohse, M. J. Progressive hypertrophy and heart failure in β1-adrenergic receptor transgenic mice. *Proceedings of the National Academy of Sciences* **96**, 7059-7064 (1999).
196 Pimenov, O. Y. *et al.* Myocardial α2-adrenoceptors as therapeutic targets to prevent cardiac hypertrophy and heart failure. *Biophysics* **64**, 738-750 (2019).
197 Shimizu, K. & McGrath, B. P. Sympathetic dysfunction in heart failure. *Baillière's Clinical Endocrinology and Metabolism* **7**, 439-463 (1993). https://doi.org/https://doi.org/10.1016/S0950-351X(05)80183-1
198 Lysholm, E., Nylin, G. & Quarnà, K. The Relation between the Heart Volume and Stroke Volume under Physiological and Pathological Conditions. *Acta Radiologica* **os-15**, 237-257 (1934). https://doi.org/10.1177/028418513401500305
199 Dodge, H. T. & Baxley, W. A. Hemodynamic aspects of heart failure∗. *The American Journal of Cardiology* **22**, 24-34 (1968). https://doi.org/https://doi.org/10.1016/0002-9149(68)90243-9
200 Rasmussen, S. *et al.* Stroke volume calculated from the mitral valve echogram in patients with and without ventricular dyssynergy. *Circulation* **58**, 125-133 (1978). https://doi.org/doi:10.1161/01.CIR.58.1.125
201 Mangrum, J. M. & DiMarco, J. P. The Evaluation and Management of Bradycardia. *New England Journal of Medicine* **342**, 703-709 (2000). https://doi.org/10.1056/nejm200003093421006
202 Lombardi, F. Rate-dependent left ventricular filling time: A critical factor for adequate cardiac output. *Heart Rhythm* **18**, 1113-1114 (2021). https://doi.org/10.1016/j.hrthm.2021.03.025
203 熊田, 衛., 東, 健. & 松田, 幸. THE CARDIAC OUTPUT-HEART RATE RELATIONSHIP UNDER DIFFERENT CONDITIONS. *The Japanese Journal of Physiology* **17**, 538-555 (1967). https://doi.org/10.2170/jjphysiol.17.538
204 Samie, F. H. & Jalife, J. Mechanisms underlying ventricular tachycardia and its transition to ventricular fibrillation in the structurally normal heart. *Cardiovascular Research* **50**, 242-250 (2001). https://doi.org/10.1016/s0008-6363(00)00289-3

205 Lippi, G., Sanchis-Gomar, F. & Cervellin, G. Global epidemiology of atrial fibrillation: an increasing epidemic and public health challenge. *International Journal of Stroke* **16**, 217-221 (2021).
206 Mou, L. *et al.* Lifetime risk of atrial fibrillation by race and socioeconomic status: ARIC study (Atherosclerosis Risk in Communities). *Circulation: Arrhythmia and Electrophysiology* **11**, e006350 (2018).
207 Cluitmans, M. J. *et al.* The circle of reentry: Characteristics of trigger-substrate interaction leading to sudden cardiac arrest. *Frontiers in cardiovascular medicine* **10**, 1121517 (2023).
208 Colman, M. A. Arrhythmia mechanisms and spontaneous calcium release: Bi-directional coupling between re-entrant and focal excitation. *PLoS Comput Biol* **15**, e1007260 (2019). https://doi.org/10.1371/journal.pcbi.1007260
209 Merchant, F. M. & Armoundas, A. A. Role of substrate and triggers in the genesis of cardiac alternans, from the myocyte to the whole heart: implications for therapy. *Circulation* **125**, 539-549 (2012).
210 Nogami, A. Mapping and ablating ventricular premature contractions that trigger ventricular fibrillation: trigger elimination and substrate modification. *Journal of cardiovascular electrophysiology* **26**, 110-115 (2015).
211 Voigt, N. *et al.* Cellular and molecular mechanisms of atrial arrhythmogenesis in patients with paroxysmal atrial fibrillation. *Circulation* **129**, 145-156 (2014). https://doi.org/10.1161/circulationaha.113.006641
212 Wit, A. L. Afterdepolarizations and triggered activity as a mechanism for clinical arrhythmias. *Pacing and Clinical Electrophysiology* **41**, 883-896 (2018).
213 Verkerk, A. O. *et al.* Ionic mechanism of delayed afterdepolarizations in ventricular cells isolated from human end-stage failing hearts. *Circulation* **104**, 2728-2733 (2001).
214 Priori, S. G. & Corr, P. B. Mechanisms underlying early and delayed afterdepolarizations induced by catecholamines. *American Journal of Physiology-Heart and Circulatory Physiology* **258**, H1796-H1805 (1990).
215 Walfridsson, U., Strömberg, A., Janzon, M. & Walfridsson, H. Wolff-Parkinson-White syndrome and atrioventricular nodal re-entry tachycardia in a Swedish population: Consequences on health-related quality of life. *Pacing and clinical electrophysiology* **32**, 1299-1306 (2009).
216 Saffitz, J. E., Schuessler, R. B. & Yamada, K. A. Mechanisms of remodeling of gap junction distributions and the development of anatomic substrates of arrhythmias. *Cardiovascular Research* **42**, 309-317 (1999). https://doi.org/10.1016/s0008-6363(99)00023-1
217 Gardner, P., Ursell, P., Fenoglio Jr, J. & Wit, A. Electrophysiologic and anatomic basis for fractionated electrograms recorded from healed myocardial infarcts. *Circulation* **72**, 596-611 (1985).
218 Ursell, P. C., Gardner, P. I., Albala, A., Fenoglio Jr, J. J. & Wit, A. L. Structural and electrophysiological changes in the epicardial border zone of canine myocardial infarcts during infarct healing. *Circulation Research* **56**, 436-451 (1985).
219 Lawson, B. A. *et al.* Variability in electrophysiological properties and conducting obstacles controls re-entry risk in heterogeneous ischaemic tissue. *Philosophical Transactions of the Royal Society A* **378**, 20190341 (2020).
220 El-Sherif, N., Scherlag, B. J., Lazzara, R. & Hope, R. R. Re-entrant ventricular arrhythmias in the late myocardial infarction period. 1. Conduction characteristics in the infarction zone. *Circulation* **55**, 686-702 (1977). https://doi.org/10.1161/01.CIR.55.5.686
221 Wijesurendra, R. S. & Casadei, B. Mechanisms of atrial fibrillation. *Heart* **105**, 1860-1867 (2019).
222 Ng, G. A. *et al.* Sympathetic nerve stimulation produces spatial heterogeneities of action potential restitution. *Heart rhythm* **6**, 696-706 (2009).

223 Ajijola, O. A. *et al.* Sympathetic modulation of electrical activation in normal and infarcted myocardium: implications for arrhythmogenesis. *American Journal of Physiology-Heart and Circulatory Physiology* **312**, H608-H621 (2017).

224 Rajendran, P. S. *et al.* Myocardial infarction induces structural and functional remodelling of the intrinsic cardiac nervous system. *J Physiol* **594**, 321-341 (2016). https://doi.org/10.1113/jp271165

225 Fernández-Velasco, M. *et al.* Increased Ca2+ sensitivity of the ryanodine receptor mutant RyR2R4496C underlies catecholaminergic polymorphic ventricular tachycardia. *Circulation research* **104**, 201-209 (2009).

226 Paavola, J. *et al.* Mutant ryanodine receptors in catecholaminergic polymorphic ventricular tachycardia generate delayed afterdepolarizations due to increased propensity to Ca2+ waves. *European heart journal* **28**, 1135-1142 (2007).

227 Priori, S. G. *et al.* Clinical and molecular characterization of patients with catecholaminergic polymorphic ventricular tachycardia. *Circulation* **106**, 69-74 (2002).

228 Laitinen, P. i. J. *et al.* Mutations of the cardiac ryanodine receptor (RyR2) gene in familial polymorphic ventricular tachycardia. *Circulation* **103**, 485-490 (2001).

229 Haissaguerre, M. *et al.* Spontaneous initiation of atrial fibrillation by ectopic beats originating in the pulmonary veins. *New England Journal of Medicine* **339**, 659-666 (1998).

230 Cox, J. L. *et al.* The surgical treatment of atrial fibrillation: III. Development of a definitive surgical procedure. *The Journal of thoracic and cardiovascular surgery* **101**, 569-583 (1991).

231 Calvo, D., Filgueiras-Rama, D. & Jalife, J. Mechanisms and drug development in atrial fibrillation. *Pharmacological Reviews* **70**, 505-525 (2018).

232 Verma, A. *et al.* Approaches to catheter ablation for persistent atrial fibrillation. *New England Journal of Medicine* **372**, 1812-1822 (2015).

233 Macle, L. *et al.* Adenosine-guided pulmonary vein isolation for the treatment of paroxysmal atrial fibrillation: an international, multicentre, randomised superiority trial. *The Lancet* **386**, 672-679 (2015).

234 Heijman, J., Guichard, J.-B., Dobrev, D. & Nattel, S. Translational challenges in atrial fibrillation. *Circulation research* **122**, 752-773 (2018).

235 Valembois, L. *et al.* Antiarrhythmics for maintaining sinus rhythm after cardioversion of atrial fibrillation. *Cochrane Database of Systematic Reviews* (2019).

236 Lafuente-Lafuente, C., Valembois, L., Bergmann, J. F. & Belmin, J. Antiarrhythmics for maintaining sinus rhythm after cardioversion of atrial fibrillation. *Cochrane Database of Systematic Reviews* (2015).

237 Boiani, M. & Schöler, H. R. Regulatory networks in embryo-derived pluripotent stem cells. *Nature Reviews Molecular Cell Biology* **6**, 872-881 (2005). https://doi.org/10.1038/nrm1744

238 Rawles, M. E. The heart-forming areas of the early chick blastoderm. *Physiological Zoology* **16**, 22-43 (1943).

239 Tam, P. P., Parameswaran, M., Kinder, S. J. & Weinberger, R. P. The allocation of epiblast cells to the embryonic heart and other mesodermal lineages: the role of ingression and tissue movement during gastrulation. *Development* **124**, 1631-1642 (1997).

240 Sugi, Y. & Lough, J. Activin-A and FGF-2 mimic the inductive effects of anterior endoderm on terminal cardiac myogenesis in vitro. *Developmental biology* **168**, 567-574 (1995).

241 Monzen, K. *et al.* Bone morphogenetic proteins induce cardiomyocyte differentiation through the mitogen-activated protein kinase kinase kinase TAK1 and cardiac transcription factors Csx/Nkx-2.5 and GATA-4. *Molecular and cellular biology* **19**, 7096-7105 (1999).

242 Shi, Y., Katsev, S., Cai, C. & Evans, S. BMP signaling is required for heart formation in vertebrates. *Developmental biology* **224**, 226-237 (2000).
243 Kelly, R. G., Brown, N. A. & Buckingham, M. E. The arterial pole of the mouse heart forms from Fgf10-expressing cells in pharyngeal mesoderm. *Developmental cell* **1**, 435-440 (2001).
244 Cai, C.-L. *et al.* Isl1 identifies a cardiac progenitor population that proliferates prior to differentiation and contributes a majority of cells to the heart. *Developmental cell* **5**, 877-889 (2003).
245 Yuan, S. & Schoenwolf, G. C. Islet-1 marks the early heart rudiments and is asymmetrically expressed during early rotation of the foregut in the chick embryo. *The Anatomical Record: An Official Publication of the American Association of Anatomists* **260**, 204-207 (2000).
246 Waldo, K. L. *et al.* Conotruncal myocardium arises from a secondary heart field. (2001).
247 De la Cruz, M., Gomez, C. S., Arteaga, M. M. & Argüello, C. Experimental study of the development of the truncus and the conus in the chick embryo. *Journal of anatomy* **123**, 661 (1977).
248 Rana, M. S. *et al.* Tbx1 coordinates addition of posterior second heart field progenitor cells to the arterial and venous poles of the heart. *Circulation research* **115**, 790-799 (2014).
249 Galli, D. *et al.* Atrial myocardium derives from the posterior region of the second heart field, which acquires left-right identity as Pitx2c is expressed. (2008).
250 Domínguez, J. N., Meilhac, S. M., Bland, Y. S., Buckingham, M. E. & Brown, N. A. Asymmetric Fate of the Posterior Part of the Second Heart Field Results in Unexpected Left/Right Contributions to Both Poles of the Heart. *Circulation Research* **111**, 1323-1335 (2012). https://doi.org/doi:10.1161/CIRCRESAHA.112.271247
251 Mommersteeg, M. T. M. *et al.* Molecular Pathway for the Localized Formation of the Sinoatrial Node. *Circulation Research* **100**, 354-362 (2007). https://doi.org/doi:10.1161/01.RES.0000258019.74591.b3
252 Mohan, R. A., Boukens, B. J. & Christoffels, V. M. Developmental Origin of the Cardiac Conduction System: Insight from Lineage Tracing. *Pediatric Cardiology* **39**, 1107-1114 (2018). https://doi.org/10.1007/s00246-018-1906-8
253 Liang, X. *et al.* HCN4 dynamically marks the first heart field and conduction system precursors. *Circulation research* **113**, 399-407 (2013).
254 Bakker, M. L., Moorman, A. F. M. & Christoffels, V. M. The Atrioventricular Node: Origin, Development, and Genetic Program. *Trends in Cardiovascular Medicine* **20**, 164-171 (2010). https://doi.org/https://doi.org/10.1016/j.tcm.2011.02.001
255 Hoogaars, W. M. *et al.* The transcriptional repressor Tbx3 delineates the developing central conduction system of the heart. *Cardiovascular research* **62**, 489-499 (2004).
256 David, R. *et al.* Induction of MesP1 by Brachyury (T) generates the common multipotent cardiovascular stem cell. *Cardiovascular research* **92**, 115-122 (2011).
257 Tanaka, M., Chen, Z., Bartunkova, S., Yamasaki, N. & Izumo, S. The cardiac homeobox gene Csx/Nkx2. 5 lies genetically upstream of multiple genes essential for heart development. *Development* **126**, 1269-1280 (1999).
258 Ghosh, T. K. *et al.* Physical interaction between TBX5 and MEF2C is required for early heart development. *Molecular and cellular biology* **29**, 2205-2218 (2009).
259 Dodou, E., Verzi, M. P., Anderson, J. P., Xu, S.-M. & Black, B. L. Mef2c is a direct transcriptional target of ISL1 and GATA factors in the anterior heart field during mouse embryonic development. (2004).
260 Garcia-Frigola, C., Shi, Y. & Evans, S. M. Expression of the hyperpolarization-activated cyclic nucleotide-gated cation channel HCN4 during mouse heart development. *Gene Expression Patterns* **3**, 777-783 (2003).
261 Ilagan, R. *et al.* Fgf8 is required for anterior heart field development. (2006).

262 Vega-Hernández, M., Kovacs, A., De Langhe, S. & Ornitz, D. M. FGF10/FGFR2b signaling is essential for cardiac fibroblast development and growth of the myocardium. *Development* **138**, 3331-3340 (2011).

263 Kitamura, K. *et al.* Mouse Pitx2 deficiency leads to anomalies of the ventral body wall, heart, extra-and periocular mesoderm and right pulmonary isomerism. *Development* **126**, 5749-5758 (1999).

264 McFadden, D. G. *et al.* The Hand1 and Hand2 transcription factors regulate expansion of the embryonic cardiac ventricles in a gene dosage-dependent manner. (2005).

265 Anderson, D. J. *et al.* NKX2-5 regulates human cardiomyogenesis via a HEY2 dependent transcriptional network. *Nature Communications* **9**, 1373 (2018). https://doi.org/10.1038/s41467-018-03714-x

266 Asp, M. *et al.* A Spatiotemporal Organ-Wide Gene Expression and Cell Atlas of the Developing Human Heart. *Cell* **179**, 1647-1660.e1619 (2019). https://doi.org/https://doi.org/10.1016/j.cell.2019.11.025

267 Churko, J. M. *et al.* Defining human cardiac transcription factor hierarchies using integrated single-cell heterogeneity analysis. *Nature Communications* **9**, 4906 (2018). https://doi.org/10.1038/s41467-018-07333-4

268 De Bono, C. *et al.* T-box genes and retinoic acid signaling regulate the segregation of arterial and venous pole progenitor cells in the murine second heart field. *Hum Mol Genet* **27**, 3747-3760 (2018). https://doi.org/10.1093/hmg/ddy266

269 de Soysa, T. Y. *et al.* Single-cell analysis of cardiogenesis reveals basis for organ-level developmental defects. *Nature* **572**, 120-124 (2019). https://doi.org/10.1038/s41586-019-1414-x

270 DeLaughter, D. M. *et al.* Single-Cell Resolution of Temporal Gene Expression during Heart Development. *Developmental Cell* **39**, 480-490 (2016). https://doi.org/https://doi.org/10.1016/j.devcel.2016.10.001

271 Gonzalez, D. M. *et al.* Dissecting mechanisms of chamber-specific cardiac differentiation and its perturbation following retinoic acid exposure. *Development* **149** (2022). https://doi.org/10.1242/dev.200557

272 Koenig, A. L. *et al.* Single-cell transcriptomics reveals cell-type-specific diversification in human heart failure. *Nature Cardiovascular Research* **1**, 263-280 (2022). https://doi.org/10.1038/s44161-022-00028-6

273 Li, G. *et al.* Single cell expression analysis reveals anatomical and cell cycle-dependent transcriptional shifts during heart development. *Development* **146**, dev173476 (2019).

274 Mantri, M. *et al.* Spatiotemporal single-cell RNA sequencing of developing chicken hearts identifies interplay between cellular differentiation and morphogenesis. *Nature Communications* **12**, 1771 (2021). https://doi.org/10.1038/s41467-021-21892-z

275 Moskowitz, I. P. *et al.* A molecular pathway including Id2, Tbx5, and Nkx2-5 required for cardiac conduction system development. *Cell* **129**, 1365-1376 (2007). https://doi.org/10.1016/j.cell.2007.04.036

276 Padula, S. L., Velayutham, N. & Yutzey, K. E. Transcriptional Regulation of Postnatal Cardiomyocyte Maturation and Regeneration. *Int J Mol Sci* **22** (2021). https://doi.org/10.3390/ijms22063288

277 Skelly, D. A. *et al.* Single-Cell Transcriptional Profiling Reveals Cellular Diversity and Intercommunication in the Mouse Heart. *Cell Reports* **22**, 600-610 (2018). https://doi.org/https://doi.org/10.1016/j.celrep.2017.12.072

278 van Eif, V. W. W., Devalla, H. D., Boink, G. J. J. & Christoffels, V. M. Transcriptional regulation of the cardiac conduction system. *Nat Rev Cardiol* **15**, 617-630 (2018). https://doi.org/10.1038/s41569-018-0031-y

279 van Eif, V. W. W., Stefanovic, S., Mohan, R. A. & Christoffels, V. M. Gradual differentiation and confinement of the cardiac conduction system as indicated by marker

gene expression. *Biochimica et Biophysica Acta (BBA) - Molecular Cell Research* **1867**, 118509 (2020). https://doi.org/https://doi.org/10.1016/j.bbamcr.2019.07.004

280 Ryckebusch, L. *et al.* Retinoic acid deficiency alters second heart field formation. *Proc Natl Acad Sci U S A* **105**, 2913-2918 (2008). https://doi.org/10.1073/pnas.0712344105

281 Wiesinger, A., Boink, G. J. J., Christoffels, V. M. & Devalla, H. D. Retinoic acid signaling in heart development: Application in the differentiation of cardiovascular lineages from human pluripotent stem cells. *Stem Cell Reports* **16**, 2589-2606 (2021). https://doi.org/10.1016/j.stemcr.2021.09.010

282 Niederreither, K. *et al.* Embryonic retinoic acid synthesis is essential for heart morphogenesis in the mouse. *Development* **128**, 1019-1031 (2001). https://doi.org/10.1242/dev.128.7.1019

283 Keegan, B. R., Feldman, J. L., Begemann, G., Ingham, P. W. & Yelon, D. Retinoic Acid Signaling Restricts the Cardiac Progenitor Pool. *Science* **307**, 247-249 (2005). https://doi.org/doi:10.1126/science.1101573

284 Gonzalez, D. M. *et al.* Dissecting mechanisms of chamber-specific cardiac differentiation and its perturbation following retinoic acid exposure. *Development* **149**, dev200557 (2022).

285 Duong, T. B., Holowiecki, A. & Waxman, J. S. Retinoic acid signaling restricts the size of the first heart field within the anterior lateral plate mesoderm. *Developmental Biology* **473**, 119-129 (2021). https://doi.org/https://doi.org/10.1016/j.ydbio.2021.02.005

286 Breckenridge, R. A., Mohun, T. J. & Amaya, E. A role for BMP signalling in heart looping morphogenesis in Xenopus. *Developmental biology* **232**, 191-203 (2001).

287 Chen, H. *et al.* BMP10 is essential for maintaining cardiac growth during murine cardiogenesis. (2004).

288 Chocron, S., Verhoeven, M. C., Rentzsch, F., Hammerschmidt, M. & Bakkers, J. Zebrafish Bmp4 regulates left–right asymmetry at two distinct developmental time points. *Developmental biology* **305**, 577-588 (2007).

289 de Pater, E. *et al.* Bmp signaling exerts opposite effects on cardiac differentiation. *Circulation research* **110**, 578-587 (2012).

290 Kim, R. Y., Robertson, E. J. & Solloway, M. J. Bmp6 and Bmp7 are required for cushion formation and septation in the developing mouse heart. *Developmental biology* **235**, 449-466 (2001).

291 McCulley, D. J., Kang, J. O., Martin, J. F. & Black, B. L. BMP4 is required in the anterior heart field and its derivatives for endocardial cushion remodeling, outflow tract septation, and semilunar valve development. *Developmental dynamics: an official publication of the American Association of Anatomists* **237**, 3200-3209 (2008).

292 Tanwar, V. *et al.* Gremlin 2 Promotes Differentiation of Embryonic Stem Cells to Atrial Fate by Activation of the JNK Signaling Pathway. *Stem Cells* **32**, 1774-1788 (2014). https://doi.org/10.1002/stem.1703

293 Zhang, H. & Bradley, A. Mice deficient for BMP2 are nonviable and have defects in amnion/chorion and cardiac development. *Development* **122**, 2977-2986 (1996).

294 Choi, M., Stottmann, R. W., Yang, Y.-P., Meyers, E. N. & Klingensmith, J. The bone morphogenetic protein antagonist noggin regulates mammalian cardiac morphogenesis. *Circulation research* **100**, 220-228 (2007).

295 Müller, I. I. *et al.* Functional modeling in zebrafish demonstrates that the atrial-fibrillation-associated gene GREM2 regulates cardiac laterality, cardiomyocyte differentiation and atrial rhythm. *Disease Models & Mechanisms* **6**, 332-341 (2013). https://doi.org/10.1242/dmm.010488

296 Li, W. *et al.* Gremlin2 Regulates the Differentiation and Function of Cardiac Progenitor Cells via the Notch Signaling Pathway. *Cellular Physiology and Biochemistry* **47**, 579-589 (2018). https://doi.org/10.1159/000490012

297 Gurdon, J. B. The developmental capacity of nuclei taken from intestinal epithelium cells of feeding tadpoles. *Development* **10**, 622-640 (1962).
298 Takahashi, K. & Yamanaka, S. Induction of pluripotent stem cells from mouse embryonic and adult fibroblast cultures by defined factors. *cell* **126**, 663-676 (2006).
299 Gai, H. *et al.* Generation and characterization of functional cardiomyocytes using induced pluripotent stem cells derived from human fibroblasts. *Cell biology international* **33**, 1184-1193 (2009).
300 Yokoo, N. *et al.* The effects of cardioactive drugs on cardiomyocytes derived from human induced pluripotent stem cells. *Biochemical and Biophysical Research Communications* **387**, 482-488 (2009). https://doi.org/https://doi.org/10.1016/j.bbrc.2009.07.052
301 Zhang, J. *et al.* Functional Cardiomyocytes Derived From Human Induced Pluripotent Stem Cells. *Circulation Research* **104**, e30-e41 (2009). https://doi.org/doi:10.1161/CIRCRESAHA.108.192237
302 Kattman, S. J. *et al.* Stage-Specific Optimization of Activin/Nodal and BMP Signaling Promotes Cardiac Differentiation of Mouse and Human Pluripotent Stem Cell Lines. *Cell Stem Cell* **8**, 228-240 (2011). https://doi.org/10.1016/j.stem.2010.12.008
303 Ren, Y. *et al.* Small molecule Wnt inhibitors enhance the efficiency of BMP-4-directed cardiac differentiation of human pluripotent stem cells. *Journal of Molecular and Cellular Cardiology* **51**, 280-287 (2011). https://doi.org/https://doi.org/10.1016/j.yjmcc.2011.04.012
304 Itzhaki, I. *et al.* Modelling the long QT syndrome with induced pluripotent stem cells. *Nature* **471**, 225-229 (2011). https://doi.org/10.1038/nature09747
305 Carvajal-Vergara, X. *et al.* Patient-specific induced pluripotent stem-cell-derived models of LEOPARD syndrome. *Nature* **465**, 808-812 (2010).
306 Moretti, A. *et al.* Patient-specific induced pluripotent stem-cell models for long-QT syndrome. *New England Journal of Medicine* **363**, 1397-1409 (2010). https://doi.org/10.1056/NEJMoa0908679
307 Kehat, I. *et al.* Human embryonic stem cells can differentiate into myocytes with structural and functional properties of cardiomyocytes. *The Journal of Clinical Investigation* **108**, 407-414 (2001). https://doi.org/10.1172/JCI12131
308 Lian, X. *et al.* Robust cardiomyocyte differentiation from human pluripotent stem cells via temporal modulation of canonical Wnt signaling. *Proceedings of the National Academy of Sciences* **109**, E1848-E1857 (2012). https://doi.org/doi:10.1073/pnas.1200250109
309 Zhao, Q., Sun, Q., Zhou, L., Liu, K. & Jiao, K. Complex Regulation of Mitochondrial Function During Cardiac Development. *Journal of the American Heart Association* **8**, e012731 (2019). https://doi.org/doi:10.1161/JAHA.119.012731
310 Ueno, S. *et al.* Biphasic role for Wnt/β-catenin signaling in cardiac specification in zebrafish and embryonic stem cells. *Proceedings of the National Academy of Sciences* **104**, 9685-9690 (2007). https://doi.org/doi:10.1073/pnas.0702859104
311 Zhao, M., Tang, Y., Zhou, Y. & Zhang, J. Deciphering Role of Wnt Signalling in Cardiac Mesoderm and Cardiomyocyte Differentiation from Human iPSCs: Four-dimensional control of Wnt pathway for hiPSC-CMs differentiation. *Scientific Reports* **9**, 19389 (2019). https://doi.org/10.1038/s41598-019-55620-x
312 Argenziano, M. *et al.* Electrophysiologic characterization of calcium handling in human induced pluripotent stem cell-derived atrial cardiomyocytes. *Stem cell reports* **10**, 1867-1878 (2018).
313 Cyganek, L. *et al.* Deep phenotyping of human induced pluripotent stem cell–derived atrial and ventricular cardiomyocytes. *JCI insight* **3** (2018).
314 Devalla, H. D. *et al.* Atrial-like cardiomyocytes from human pluripotent stem cells are a robust preclinical model for assessing atrial-selective pharmacology. *EMBO molecular medicine* **7**, 394-410 (2015).

315 Goldfracht, I. *et al.* Generating ring-shaped engineered heart tissues from ventricular and atrial human pluripotent stem cell-derived cardiomyocytes. *Nature communications* **11**, 75 (2020).
316 Laksman, Z. *et al.* Modeling atrial fibrillation using human embryonic stem cell-derived atrial tissue. *Scientific reports* **7**, 5268 (2017).
317 Li, J. *et al.* Molecular and electrophysiological evaluation of human cardiomyocyte subtypes to facilitate generation of composite cardiac models. *Journal of Tissue Engineering* **13**, 20417314221127908 (2022).
318 Pei, F. *et al.* Chemical-defined and albumin-free generation of human atrial and ventricular myocytes from human pluripotent stem cells. *Stem cell research* **19**, 94-103 (2017).
319 Bolger, A. P. *et al.* Neurohormonal Activation and the Chronic Heart Failure Syndrome in Adults With Congenital Heart Disease. *Circulation* **106**, 92-99 (2002). https://doi.org/doi:10.1161/01.CIR.0000020009.30736.3F
320 Bosch, R. F. *et al.* Ionic mechanisms of electrical remodeling in human atrial fibrillation. *Cardiovascular research* **44**, 121-131 (1999).
321 Biendarra-Tiegs, S. M. *et al.* Single-cell RNA-sequencing and optical electrophysiology of human induced pluripotent stem cell-derived cardiomyocytes reveal discordance between cardiac subtype-associated gene expression patterns and electrophysiological phenotypes. *Stem cells and development* **28**, 659-673 (2019).
322 Feyen, D. A. M. *et al.* Metabolic Maturation Media Improve Physiological Function of Human iPSC-Derived Cardiomyocytes. *Cell Rep* **32**, 107925 (2020). https://doi.org/10.1016/j.celrep.2020.107925
323 Amos, G. J. *et al.* Differences between outward currents of human atrial and subepicardial ventricular myocytes. *The Journal of Physiology* **491**, 31-50 (1996). https://doi.org/https://doi.org/10.1113/jphysiol.1996.sp021194
324 Bénardeau, A. *et al.* Primary Culture of Human Atrial Myocytes is Associated with the Appearance of Structural and Functional Characteristics of Immature Myocardium. *Journal of Molecular and Cellular Cardiology* **29**, 1307-1320 (1997). https://doi.org/https://doi.org/10.1006/jmcc.1996.0366
325 Cui, Y. *et al.* Single-Cell Transcriptome Analysis Maps the Developmental Track of the Human Heart. *Cell Reports* **26**, 1934-1950.e1935 (2019). https://doi.org/https://doi.org/10.1016/j.celrep.2019.01.079
326 Dobrev, D. *et al.* Molecular basis of downregulation of G-protein–coupled inward rectifying K+ current (IK, ACh) in chronic human atrial fibrillation: Decrease in Girk4 mRNA correlates with reduced IK, ACh and muscarinic receptor–mediated shortening of action potentials. *Circulation* **104**, 2551-2557 (2001).
327 Grandi, E. *et al.* Human atrial action potential and Ca2+ model: sinus rhythm and chronic atrial fibrillation. *Circulation research* **109**, 1055-1066 (2011).
328 Jeevaratnam, K., Chadda, K. R., Huang, C. L.-H. & Camm, A. J. Cardiac Potassium Channels: Physiological Insights for Targeted Therapy. *Journal of Cardiovascular Pharmacology and Therapeutics* **23**, 119-129 (2018). https://doi.org/10.1177/1074248417729880
329 Pandit, S. V. in *Cardiac Electrophysiology: From Cell to Bedside (Seventh Edition)* (eds Douglas P. Zipes, José Jalife, & William G. Stevenson) 293-303 (Elsevier, 2018).
330 Wang, L. *et al.* Single-cell reconstruction of the adult human heart during heart failure and recovery reveals the cellular landscape underlying cardiac function. *Nature Cell Biology* **22**, 108-119 (2020). https://doi.org/10.1038/s41556-019-0446-7
331 Wang, Y. *et al.* Differences in transient outward current properties between neonatal and adult human atrial myocytes. *Journal of Molecular and Cellular Cardiology* **35**, 1083-1092 (2003). https://doi.org/https://doi.org/10.1016/S0022-2828(03)00200-1

332 Tanwar, V. *et al.* Gremlin 2 promotes differentiation of embryonic stem cells to atrial fate by activation of the JNK signaling pathway. *Stem Cells* **32**, 1774-1788 (2014).

333 Bylund, J. B. & Hatzopoulos, A. K. Differentiation of atrial cardiomyocytes from pluripotent stem cells using the BMP antagonist Grem2. *JoVE (Journal of Visualized Experiments)*, e53919 (2016).

334 Rocha-Resende, C. *et al.* Non-neuronal cholinergic machinery present in cardiomyocytes offsets hypertrophic signals. *Journal of Molecular and Cellular Cardiology* **53**, 206-216 (2012). https://doi.org/https://doi.org/10.1016/j.yjmcc.2012.05.003

335 Roy, A. *et al.* Cardiomyocyte-secreted acetylcholine is required for maintenance of homeostasis in the heart. *Faseb j* **27**, 5072-5082 (2013). https://doi.org/10.1096/fj.13-238279

336 Roy, A. *et al.* Cardiac acetylcholine inhibits ventricular remodeling and dysfunction under pathologic conditions. *The FASEB Journal* **30**, 688 (2016).

337 Grassam-Rowe, A., Ou, X. & Lei, M. Novel cardiac cell subpopulations: Pnmt-derived cardiomyocytes. *Open Biol* **10**, 200095 (2020). https://doi.org/10.1098/rsob.200095

338 Wang, Y. *et al.* Optogenetic Control of Heart Rhythm by Selective Stimulation of Cardiomyocytes Derived from Pnmt(+) Cells in Murine Heart. *Sci Rep* **7**, 40687 (2017). https://doi.org/10.1038/srep40687

339 Ni, H. *et al.* Three-dimensional image reconstruction of distribution of Pnmt+ cell-derived cells in murine heart. *Scientific Data* **4**, 170134 (2017). https://doi.org/10.1038/sdata.2017.134

340 Wang, L., Wada, Y., Ballan, N., Gepstein, L. & Knollmann, B. C. Thyroid and Dexamethasone Treatment Enhances the Expression of Repolarizing Potassium Currents and Improve Electrophysiological Maturation of Human IPSC-Derived Cardiomyocytes. *Biophysical Journal* **120**, 331a-332a (2021). https://doi.org/10.1016/j.bpj.2020.11.2084

341 Deng, Q., Ramsköld, D., Reinius, B. & Sandberg, R. Single-Cell RNA-Seq Reveals Dynamic, Random Monoallelic Gene Expression in Mammalian Cells. *Science* **343**, 193-196 (2014). https://doi.org/doi:10.1126/science.1245316

342 Guo, G. *et al.* Resolution of cell fate decisions revealed by single-cell gene expression analysis from zygote to blastocyst. *Developmental cell* **18**, 675-685 (2010).

343 Subkhankulova, T., Yano, K., Robinson, H. & Livesey, F. Grouping and classifying electrophysiologically-defined classes of neocortical neurons by single cell, whole-genome expression profiling. *Frontiers in Molecular Neuroscience* **3** (2010). https://doi.org/10.3389/fnmol.2010.00010

344 Zeisel, A. *et al.* Cell types in the mouse cortex and hippocampus revealed by single-cell RNA-seq. *Science* **347**, 1138-1142 (2015).

345 Han, A., Glanville, J., Hansmann, L. & Davis, M. M. Linking T-cell receptor sequence to functional phenotype at the single-cell level. *Nature Biotechnology* **32**, 684-692 (2014). https://doi.org/10.1038/nbt.2938

346 Shalek, A. K. *et al.* Single-cell transcriptomics reveals bimodality in expression and splicing in immune cells. *Nature* **498**, 236-240 (2013). https://doi.org/10.1038/nature12172

347 Shalek, A. K. *et al.* Single-cell RNA-seq reveals dynamic paracrine control of cellular variation. *Nature* **510**, 363-369 (2014). https://doi.org/10.1038/nature13437

348 Goodyer, W. R. *et al.* Transcriptomic Profiling of the Developing Cardiac Conduction System at Single-Cell Resolution. *Circulation Research* **125**, 379-397 (2019). https://doi.org/doi:10.1161/CIRCRESAHA.118.314578

349 Friedman, C. E. *et al.* Single-Cell Transcriptomic Analysis of Cardiac Differentiation from Human PSCs Reveals HOPX-Dependent Cardiomyocyte Maturation. *Cell Stem Cell* **23**, 586-598.e588 (2018). https://doi.org/10.1016/j.stem.2018.09.009

350 Goodyer, W. R. *et al.* In vivo visualization and molecular targeting of the cardiac conduction system. *The Journal of Clinical Investigation* (2022). https://doi.org/10.1172/JCI156955

351 Chandler, N. J. *et al.* Molecular Architecture of the Human Sinus Node. *Circulation* **119**, 1562-1575 (2009). https://doi.org/doi:10.1161/CIRCULATIONAHA.108.804369

352 Weber, N. *et al.* Advanced Single-Cell Mapping Reveals that in hESC Cardiomyocytes Contraction Kinetics and Action Potential Are Independent of Myosin Isoform. *Stem Cell Reports* **14**, 788-802 (2020). https://doi.org/10.1016/j.stemcr.2020.03.015

353 Chandler, N. J. *et al.* Molecular architecture of the human sinus node: insights into the function of the cardiac pacemaker. *Circulation* **119**, 1562-1575 (2009).

354 Linscheid, N. *et al.* Quantitative proteomics and single-nucleus transcriptomics of the sinus node elucidates the foundation of cardiac pacemaking. *Nature communications* **10**, 2889 (2019).

355 Itzhaki, I. *et al.* Calcium Handling in Human Induced Pluripotent Stem Cell Derived Cardiomyocytes. *PLOS ONE* **6**, e18037 (2011). https://doi.org/10.1371/journal.pone.0018037

356 Liu, W. *et al.* Pak1 as a novel therapeutic target for antihypertrophic treatment in the heart. *Circulation* **124**, 2702-2715 (2011).

357 Murphy, S. A. *et al.* PGC1/PPAR drive cardiomyocyte maturation at single cell level via YAP1 and SF3B2. *Nature Communications* **12**, 1648 (2021). https://doi.org/10.1038/s41467-021-21957-z

358 Nelson, M. E., Riva, S. G. & Cvejic, A. SMaSH: A scalable, general marker gene identification framework for single-cell RNA sequencing and Spatial Transcriptomics. *bioRxiv*, 2021.2004.2008.438978 (2021). https://doi.org/10.1101/2021.04.08.438978

359 Galow, A.-M. *et al.* Quality control in scRNA-Seq can discriminate pacemaker cells: the mtRNA bias. *Cellular and Molecular Life Sciences* (2021). https://doi.org/10.1007/s00018-021-03916-5

360 Hafemeister, C. & Satija, R. Normalization and variance stabilization of single-cell RNA-seq data using regularized negative binomial regression. *Genome Biology* **20**, 296 (2019). https://doi.org/10.1186/s13059-019-1874-1

361 Tran, H. T. N. *et al.* A benchmark of batch-effect correction methods for single-cell RNA sequencing data. *Genome Biology* **21**, 12 (2020). https://doi.org/10.1186/s13059-019-1850-9

362 Nygaard, V., Rødland, E. A. & Hovig, E. Methods that remove batch effects while retaining group differences may lead to exaggerated confidence in downstream analyses. *Biostatistics* **17**, 29-39 (2016). https://doi.org/10.1093/biostatistics/kxv027

363 Satija, R., Farrell, J. A., Gennert, D., Schier, A. F. & Regev, A. Spatial reconstruction of single-cell gene expression data. *Nat Biotechnol* **33**, 495-502 (2015). https://doi.org/10.1038/nbt.3192

364 Moon, K. R. *et al.* Visualizing structure and transitions in high-dimensional biological data. *Nature Biotechnology* **37**, 1482-1492 (2019). https://doi.org/10.1038/s41587-019-0336-3

365 McDavid, A. *et al.* Data exploration, quality control and testing in single-cell qPCR-based gene expression experiments. *Bioinformatics* **29**, 461-467 (2013).

366 Dijk, D. v. *et al.* MAGIC: A diffusion-based imputation method reveals gene-gene interactions in single-cell RNA-sequencing data. *BioRxiv*, 111591 (2017).

367 Aibar, S. *et al.* SCENIC: single-cell regulatory network inference and clustering. *Nature methods* **14**, 1083-1086 (2017).

368 Kohl, M., Wiese, S. & Warscheid, B. Cytoscape: software for visualization and analysis of biological networks. *Data mining in proteomics: from standards to applications*, 291-303 (2011).

369 Brionne, A., Juanchich, A. & Hennequet-Antier, C. ViSEAGO: a Bioconductor package for clustering biological functions using Gene Ontology and semantic similarity. *BioData Mining* **12**, 16 (2019). https://doi.org/10.1186/s13040-019-0204-1

370 Davis, S. & Meltzer, P. S. GEOquery: a bridge between the Gene Expression Omnibus (GEO) and BioConductor. *Bioinformatics* **23**, 1846-1847 (2007).

371 Chen, A. *et al.* Spatiotemporal transcriptomic atlas of mouse organogenesis using DNA nanoball-patterned arrays. *Cell* **185**, 1777-1792.e1721 (2022). https://doi.org/https://doi.org/10.1016/j.cell.2022.04.003

372 Wei, X. *et al.* Single-cell Stereo-seq reveals induced progenitor cells involved in axolotl brain regeneration. *Science* **377**, eabp9444 (2022). https://doi.org/doi:10.1126/science.abp9444

373 Liang, D. *et al.* Cellular and molecular landscape of mammalian sinoatrial node revealed by single-cell RNA sequencing. *Nature Communications* **12**, 287 (2021). https://doi.org/10.1038/s41467-020-20448-x

374 Cable, D. M. *et al.* Robust decomposition of cell type mixtures in spatial transcriptomics. *Nature biotechnology* **40**, 517-526 (2022).

375 Grün, D. *et al.* Single-cell messenger RNA sequencing reveals rare intestinal cell types. *Nature* **525**, 251-255 (2015).

376 Wilkinson, L. (Oxford University Press, 2011).

377 Gu, Z., Eils, R. & Schlesner, M. Complex heatmaps reveal patterns and correlations in multidimensional genomic data. *Bioinformatics* **32**, 2847-2849 (2016).

378 Yu, G., Wang, L.-G., Han, Y. & He, Q.-Y. clusterProfiler: an R package for comparing biological themes among gene clusters. *Omics: a journal of integrative biology* **16**, 284-287 (2012).

379 Tohyama, S. *et al.* Distinct metabolic flow enables large-scale purification of mouse and human pluripotent stem cell-derived cardiomyocytes. *Cell stem cell* **12**, 127-137 (2013).

380 Peters, M. C. *et al.* Metabolic Maturation Increases Susceptibility to Hypoxia-induced Damage in Human iPSC-derived Cardiomyocytes. *Stem Cells Translational Medicine* **11**, 1040-1051 (2022). https://doi.org/10.1093/stcltm/szac061

381 Fuerstenau-Sharp, M. *et al.* Generation of Highly Purified Human Cardiomyocytes from Peripheral Blood Mononuclear Cell-Derived Induced Pluripotent Stem Cells. *PLOS ONE* **10**, e0126596 (2015). https://doi.org/10.1371/journal.pone.0126596

382 Tomek, J., Wang, Z. J., Burton, R.-A. B., Herring, N. & Bub, G. COSMAS: a lightweight toolbox for cardiac optical mapping analysis. *Scientific Reports* **11**, 9147 (2021). https://doi.org/10.1038/s41598-021-87402-9

383 O'Shea, C. *et al.* ElectroMap: high-throughput open-source software for analysis and mapping of cardiac electrophysiology. *Scientific reports* **9**, 1389 (2019).

384 Onal, B., Gratz, D. & Hund, T. LongQt: A cardiac electrophysiology simulation platform. *MethodsX* **3**, 589-599 (2016).

385 Courtemanche, M., Ramirez, R. J. & Nattel, S. Ionic mechanisms underlying human atrial action potential properties: insights from a mathematical model. *American Journal of Physiology-Heart and Circulatory Physiology* **275**, H301-H321 (1998).

386 Grandi, E. *et al.* Human atrial action potential and Ca2+ model: sinus rhythm and chronic atrial fibrillation. *Circ Res* **109**, 1055-1066 (2011). https://doi.org/10.1161/circresaha.111.253955

387 Onal, B., Gratz, D. & Hund, T. J. Ca2+/calmodulin-dependent kinase II-dependent regulation of atrial myocyte late Na+ current, Ca2+ cycling, and excitability: a mathematical modeling study. *American Journal of Physiology-Heart and Circulatory Physiology* **313**, H1227-H1239 (2017).

388 Koschinski, A. & Zaccolo, M. in *cAMP Signaling: Methods and Protocols* 141-165 (Springer, 2022).

389 Ebert, S. N. & Taylor, D. G. Catecholamines and development of cardiac pacemaking: An intrinsically intimate relationship. *Cardiovascular Research* **72**, 364-374 (2006). https://doi.org/10.1016/j.cardiores.2006.08.013

390 Lescroart, F. *et al.* Defining the earliest step of cardiovascular lineage segregation by single-cell RNA-seq. *Science* **359**, 1177-1181 (2018). https://doi.org/doi:10.1126/science.aao4174

391 Goodyer, W. R. & Wu, S. M. Fates Aligned: Origins and Mechanisms of Ventricular Conduction System and Ventricular Wall Development. *Pediatric cardiology* **39**, 1090-1098 (2018). https://doi.org/10.1007/s00246-018-1869-9

392 Xiong, H. *et al.* Single-Cell Transcriptomics Reveals Chemotaxis-Mediated Intraorgan Crosstalk During Cardiogenesis. *Circulation Research* **125**, 398-410 (2019). https://doi.org/doi:10.1161/CIRCRESAHA.119.315243

393 Kanter, H. L., Laing, J. G., Beau, S. L., Beyer, E. C. & Saffitz, J. E. Distinct patterns of connexin expression in canine Purkinje fibers and ventricular muscle. *Circulation Research* **72**, 1124-1131 (1993). https://doi.org/doi:10.1161/01.RES.72.5.1124

394 Miquerol, L. *et al.* Architectural and functional asymmetry of the His–Purkinje system of the murine heart. *Cardiovascular Research* **63**, 77-86 (2004). https://doi.org/10.1016/j.cardiores.2004.03.007

395 Zaglia, T. *et al.* Optogenetic determination of the myocardial requirements for extrasystoles by cell type-specific targeting of ChannelRhodopsin-2. *Proceedings of the National Academy of Sciences* **112**, E4495-E4504 (2015). https://doi.org/10.1073/pnas.1509380112

396 Ng, W. A., Grupp, I. L., Subramaniam, A. & Robbins, J. Cardiac myosin heavy chain mRNA expression and myocardial function in the mouse heart. *Circulation Research* **68**, 1742-1750 (1991). https://doi.org/doi:10.1161/01.RES.68.6.1742

397 Surawicz, B. Role of potassium channels in cycle length dependent regulation of action potential duration in mammalian cardiac Purkinje and ventricular muscle fibres. *Cardiovascular Research* **26**, 1021-1029 (1992). https://doi.org/10.1093/cvr/26.11.1021

398 Cha, Y. *et al.* Effects of chemical subendocardial ablation on activation rate gradient during ventricular fibrillation. *American Journal of Physiology-Heart and Circulatory Physiology* **269**, H1998-H2009 (1995).

399 Takahashi, N. *et al.* Vascular Endothelial Growth Factor Induces Activation and Subcellular Translocation of Focal Adhesion Kinase (p125^{FAK}) in Cultured Rat Cardiac Myocytes. *Circulation Research* **84**, 1194-1202 (1999). https://doi.org/doi:10.1161/01.RES.84.10.1194

400 Saunders, V., Dewing, J. M., Sanchez-Elsner, T. & Wilson, D. I. Expression and localisation of thymosin beta-4 in the developing human early fetal heart. *PLoS One* **13**, e0207248 (2018). https://doi.org/10.1371/journal.pone.0207248

401 Bock-Marquette, I. *et al.* Thymosin beta-4 denotes new directions towards developing prosperous anti-aging regenerative therapies. *International Immunopharmacology* **116**, 109741 (2023). https://doi.org/https://doi.org/10.1016/j.intimp.2023.109741

402 Bock-Marquette, I., Saxena, A., White, M. D., Michael DiMaio, J. & Srivastava, D. Thymosin β4 activates integrin-linked kinase and promotes cardiac cell migration, survival and cardiac repair. *Nature* **432**, 466-472 (2004). https://doi.org/10.1038/nature03000

403 Liu, G. K.-M. Transforming Human Interactions with AI via Reinforcement Learning with Human Feedback (RLHF). (2023).

404 Oikawa, S. *et al.* Non-neuronal cardiac acetylcholine system playing indispensable roles in cardiac homeostasis confers resiliency to the heart. *The Journal of Physiological Sciences* **71** (2021). https://doi.org/10.1186/s12576-020-00787-6

405 Basavarajaiah, S., Shah, A. & Sharma, S. Sudden cardiac death in young athletes. *Heart* **93**, 287-289 (2007). https://doi.org/10.1136/hrt.2006.100107

406 Zoccarato, A. & Zaccolo, M. in *Microdomains in the Cardiovascular System* (eds Viacheslav Nikolaev & Manuela Zaccolo) 117-141 (Springer International Publishing, 2017).

407 Swoap, S. J., Weinshenker, D., Palmiter, R. D. & Garber, G. Dbh(-/-) mice are hypotensive, have altered circadian rhythms, and have abnormal responses to dieting and stress. *American Journal of Physiology-Regulatory, Integrative and Comparative Physiology* **286**, R108-R113 (2004). https://doi.org/10.1152/ajpregu.00405.2003

408 Wassenberg, T. *et al.* Clinical presentation and long-term follow-up of dopamine beta hydroxylase deficiency. *J Inherit Metab Dis* **44**, 554-565 (2021). https://doi.org/10.1002/jimd.12321

409 Hsu, J. *et al.* Whole Genome Expression Differences in Human Left and Right Atria Ascertained by RNA Sequencing. *Circulation: Cardiovascular Genetics* **5**, 327-335 (2012). https://doi.org/10.1161/CIRCGENETICS.111.961631

410 Wu, S.-p. *et al.* Atrial identity is determined by a COUP-TFII regulatory network. *Developmental cell* **25**, 417-426 (2013).

411 Cui, Y. *et al.* Single-cell transcriptome analysis maps the developmental track of the human heart. *Cell reports* **26**, 1934-1950. e1935 (2019).

412 Goodyer, W. R. *et al.* Transcriptomic profiling of the developing cardiac conduction system at single-cell resolution. *Circulation research* **125**, 379-397 (2019).

413 Street, K. *Trajectory Inference and Analysis in Single-Cell Genomics*. (University of California, Berkeley, 2018).

414 Giles, W. & Imaizumi, Y. Comparison of potassium currents in rabbit atrial and ventricular cells. *The Journal of physiology* **405**, 123-145 (1988).

415 Franco, D. *et al.* Divergent expression of delayed rectifier K+ channel subunits during mouse heart development. *Cardiovascular research* **52**, 65-75 (2001).

416 Dixon, J. E. & McKinnon, D. Quantitative analysis of potassium channel mRNA expression in atrial and ventricular muscle of rats. *Circulation research* **75**, 252-260 (1994).

417 Wickramasinghe, N. M. *et al.* PPARdelta activation induces metabolic and contractile maturation of human pluripotent stem cell-derived cardiomyocytes. *Cell Stem Cell* **29**, 559-576. e557 (2022).

418 Poon, E. *et al.* Proteomic analysis of human pluripotent stem Cell–Derived, fetal, and adult ventricular cardiomyocytes reveals pathways crucial for cardiac metabolism and maturation. *Circulation: Cardiovascular Genetics* **8**, 427-436 (2015).

419 Leimeister, C., Externbrink, A., Klamt, B. & Gessler, M. Hey genes: a novel subfamily of hairy-and Enhancer of split related genes specifically expressed during mouse embryogenesis. *Mechanisms of development* **85**, 173-177 (1999).

420 Huang, C. *et al.* Embryonic atrial function is essential for mouse embryogenesis, cardiac morphogenesis and angiogenesis. (2003).

421 Minamisawa, S. *et al.* Atrial chamber-specific expression of sarcolipin is regulated during development and hypertrophic remodeling. *Journal of Biological Chemistry* **278**, 9570-9575 (2003).

422 Diman, N. Y.-G. *et al.* A retinoic acid responsive Hoxa3 transgene expressed in embryonic pharyngeal endoderm, cardiac neural crest and a subdomain of the second heart field. *PLoS One* **6**, e27624 (2011).

423 Feng, J., Xu, D., Wang, Z. & Nattel, S. Ultrarapid delayed rectifier current inactivation in human atrial myocytes: properties and consequences. *American Journal of Physiology-Heart and Circulatory Physiology* **275**, H1717-H1725 (1998).

424 Fedida, D. *et al.* Identity of a novel delayed rectifier current from human heart with a cloned K+ channel current. *Circulation research* **73**, 210-216 (1993).

425 Krapivinsky, G. *et al.* The G-protein-gated atrial K+ channel IKAch is a heteromultimer of two inwardly rectifying K+-channel proteins. *Nature* **374**, 135-141 (1995). https://doi.org/10.1038/374135a0

426 Curran, M. E. *et al.* A molecular basis for cardiac arrhythmia: HERG mutations cause long QT syndrome. *Cell* **80**, 795-803 (1995).

427 Plaster, N. M. *et al.* Mutations in Kir2.1 Cause the Developmental and Episodic Electrical Phenotypes of Andersen's Syndrome. *Cell* **105**, 511-519 (2001). https://doi.org/10.1016/S0092-8674(01)00342-7

428 Dhamoon, A. S. & Jalife, J. The inward rectifier current (IK1) controls cardiac excitability and is involved in arrhythmogenesis. *Heart Rhythm* **2**, 316-324 (2005). https://doi.org/https://doi.org/10.1016/j.hrthm.2004.11.012

429 Paulin, D. & Li, Z. Desmin: a major intermediate filament protein essential for the structural integrity and function of muscle. *Experimental cell research* **301**, 1-7 (2004).

430 Lapidos, K. A., Kakkar, R. & McNally, E. M. The dystrophin glycoprotein complex: signaling strength and integrity for the sarcolemma. *Circulation research* **94**, 1023-1031 (2004).

431 George, C. H., Sorathia, R., Bertrand, B. M. & Lai, F. A. In situ modulation of the human cardiac ryanodine receptor (hRyR2) by FKBP12. 6. *Biochemical Journal* **370**, 579-589 (2003).

432 Chopra, N. *et al.* Ablation of triadin causes loss of cardiac Ca2+ release units, impaired excitation–contraction coupling, and cardiac arrhythmias. *Proceedings of the National Academy of Sciences* **106**, 7636-7641 (2009).

433 Gorza, L., Vettore, S., Tessaro, A., Sorrentino, V. & Vitadello, M. Regional and Age-related Differences in mRNA Composition of Intracellular Ca2+-release Channels of Rat Cardiac Myocytes. *Journal of Molecular and Cellular Cardiology* **29**, 1023-1036 (1997). https://doi.org/https://doi.org/10.1006/jmcc.1996.0346

434 Catterall, W. A., Perez-Reyes, E., Snutch, T. P. & Striessnig, J. International Union of Pharmacology. XLVIII. Nomenclature and structure-function relationships of voltage-gated calcium channels. *Pharmacological reviews* **57**, 411-425 (2005).

435 Perez-Reyes, E. Molecular physiology of low-voltage-activated t-type calcium channels. *Physiological reviews* **83**, 117-161 (2003).

436 Niwa, N. *et al.* Cav3.2 subunit underlies the functional T-type Ca2+ channel in murine hearts during the embryonic period. *American Journal of Physiology-Heart and Circulatory Physiology* **286**, H2257-H2263 (2004). https://doi.org/10.1152/ajpheart.01043.2003

437 Pacanowski, M. A. & Johnson, J. A. PharmGKB submission update: IX. ADRB1 gene summary. *Pharmacological reviews* **59**, 2-4 (2007).

438 Wechsler, J. *et al.* Isoforms of cyclic nucleotide phosphodiesterase PDE3A in cardiac myocytes. *Journal of Biological Chemistry* **277**, 38072-38078 (2002).

439 Hammer, R. & Giachetti, A. Muscarinic receptor subtypes: M1 and M2 biochemical and functional characterization. *Life sciences* **31**, 2991-2998 (1982).

440 Hakim, P. *et al.* Scn3b knockout mice exhibit abnormal ventricular electrophysiological properties. *Progress in biophysics and molecular biology* **98**, 251-266 (2008).

441 Dib-Hajj, S. D., Tyrrell, L. & Waxman, S. G. Structure of the sodium channel gene SCN11A: evidence for intron-to-exon conversion model and implications for gene evolution. *Molecular neurobiology* **26**, 235-250 (2002).

442 Abriel, H. Cardiac sodium channel Nav1. 5 and interacting proteins: physiology and pathophysiology. *Journal of molecular and cellular cardiology* **48**, 2-11 (2010).

443 Sullivan, R. *et al.* Structure, sequence and expression of the mouse Cx43 gene encoding connexin 43. *Gene* **130**, 191-199 (1993).

444 Hennemann, H. *et al.* Molecular cloning and functional expression of mouse connexin40, a second gap junction gene preferentially expressed in lung. *The Journal of cell biology* **117**, 1299-1310 (1992).
445 Davis, L. M., Rodefeld, M. E., Green, K., Beyer, E. C. & Saffitz, J. E. Gap junction protein phenotypes of the human heart and conduction system. *Journal of cardiovascular electrophysiology* **6**, 813-822 (1995).
446 Batista, M. R. *et al.* Balanced Notch-Wnt signaling interplay is required for mouse embryo and fetal development. *Reproduction* **161**, 385-398 (2021). https://doi.org/10.1530/rep-20-0435
447 Katoh, M. & Katoh, M. Notch ligand, JAG1, is evolutionarily conserved target of canonical WNT signaling pathway in progenitor cells. *International journal of molecular medicine* **17**, 681-685 (2006).
448 Tian, Y. *et al.* Characterization and in vivo pharmacological rescue of a Wnt2-Gata6 pathway required for cardiac inflow tract development. *Developmental cell* **18**, 275-287 (2010).
449 Schiebinger, G. *et al.* Optimal-transport analysis of single-cell gene expression identifies developmental trajectories in reprogramming. *Cell* **176**, 928-943. e922 (2019).
450 Justus, D. E. *et al.* Discoidin domain receptors in cardiac development. *Discoidin Domain Receptors in Health and Disease*, 331-347 (2016).
451 Gardner, R. T. *et al.* Targeting protein tyrosine phosphatase σ after myocardial infarction restores cardiac sympathetic innervation and prevents arrhythmias. *Nature Communications* **6**, 6235 (2015). https://doi.org/10.1038/ncomms7235
452 Terrar, D. A. Calcium flux balance across cell membranes in the heart: important unanswered questions with implications for the role of ryanodine receptors. *The Journal of Physiology* (2024).
453 Seibertz, F. & Voigt, N. High-throughput methods for cardiac cellular electrophysiology studies: the road to personalized medicine. *American Journal of Physiology-Heart and Circulatory Physiology* **326**, H938-H949 (2024).
454 Clark, A. P. *et al.* Leak current, even with gigaohm seals, can cause misinterpretation of stem cell-derived cardiomyocyte action potential recordings. *Europace* **25**, euad243 (2023).
455 Wettwer, E. *et al.* Role of I_{Kur} in Controlling Action Potential Shape and Contractility in the Human Atrium. *Circulation* **110**, 2299-2306 (2004). https://doi.org/doi:10.1161/01.CIR.0000145155.60288.71
456 Brandt, M. C., Priebe, L., Böhle, T., Südkamp, M. & Beuckelmann, D. J. The Ultrarapid and the Transient Outward K+Current in Human Atrial Fibrillation. Their Possible Role in Postoperative Atrial Fibrillation. *Journal of Molecular and Cellular Cardiology* **32**, 1885-1896 (2000). https://doi.org/https://doi.org/10.1006/jmcc.2000.1221
457 Golovko, V., Gonotkov, M. & Lebedeva, E. Effects of 4-aminopyridine on action potentials generation in mouse sinoauricular node strips. *Physiological Reports* **3**, e12447 (2015). https://doi.org/https://doi.org/10.14814/phy2.12447
458 Lei, M., Honjo, H., Kodama, I. & Boyett, M. R. Characterisation of the transient outward K+ current in rabbit sinoatrial node cells. *Cardiovasc Res* **46**, 433-441 (2000). https://doi.org/10.1016/s0008-6363(00)00036-5
459 Mansourati, J. & Grand, B. L. Transient outward current in young and adult diseased human atria. *American Journal of Physiology-Heart and Circulatory Physiology* **265**, H1466-H1470 (1993). https://doi.org/10.1152/ajpheart.1993.265.4.H1466
460 Mitcheson, J. S. & Hancox, J. C. Characteristics of a transient outward current (sensitive to 4-aminopyridine) in Ca2+-tolerant myocytes isolated from the rabbit atrioventricular node. *Pflügers Archiv* **438**, 68-78 (1999). https://doi.org/10.1007/s004240050881

461 Yue, L., Feng, J., Li, G. R. & Nattel, S. Characterization of an ultrarapid delayed rectifier potassium channel involved in canine atrial repolarization. *The Journal of Physiology* **496**, 647-662 (1996). https://doi.org/https://doi.org/10.1113/jphysiol.1996.sp021716

462 Mitcheson, J. S. & Hancox, J. C. An investigation of the role played by the E-4031-sensitive (rapid delayed rectifier) potassium current in isolated rabbit atrioventricular nodal and ventricular myocytes. *Pflügers Archiv* **438**, 843-850 (1999).

463 Wettwer, E. *et al.* Role of I Kur in controlling action potential shape and contractility in the human atrium: influence of chronic atrial fibrillation. *Circulation* **110**, 2299-2306 (2004).

464 Lee, J. H., Protze, S. I., Laksman, Z., Backx, P. H. & Keller, G. M. Human pluripotent stem cell-derived atrial and ventricular cardiomyocytes develop from distinct mesoderm populations. *Cell stem cell* **21**, 179-194. e174 (2017).

465 Taggart, P., Sutton, P. M. I., Boyett, M. R., Lab, M. & Swanton, H. Human Ventricular Action Potential Duration During Short and Long Cycles. *Circulation* **94**, 2526-2534 (1996). https://doi.org/doi:10.1161/01.CIR.94.10.2526

466 Burashnikov, A., Mannava, S. & Antzelevitch, C. Transmembrane action potential heterogeneity in the canine isolated arterially perfused right atrium: effect of I Kr and I Kur/I to block. *American Journal of Physiology-Heart and Circulatory Physiology* **286**, H2393-H2400 (2004).

467 Schaffer, P. *et al.* Estimation of outward currents in isolated human atrial myocytes using inactivation time course analysis. *Pflügers Archiv* **436**, 457-468 (1998). https://doi.org/10.1007/s004240050657

468 Sheng, X. *et al.* Human Pluripotent Stem Cell-Derived Cardiomyocytes: Response to TTX and Lidocain Reveals Strong Cell to Cell Variability. *PLOS ONE* **7**, e45963 (2012). https://doi.org/10.1371/journal.pone.0045963

469 Scornik, F. S. *et al.* Functional expression of "cardiac-type" Nav1.5 sodium channel in canine intracardiac ganglia. *Heart Rhythm* **3**, 842-850 (2006). https://doi.org/https://doi.org/10.1016/j.hrthm.2006.03.021

470 Lei, M. *et al.* Requirement of neuronal- and cardiac-type sodium channels for murine sinoatrial node pacemaking. *The Journal of Physiology* **559**, 835-848 (2004). https://doi.org/https://doi.org/10.1113/jphysiol.2004.068643

471 Herring, N., Kalla, M. & Paterson, D. J. The autonomic nervous system and cardiac arrhythmias: current concepts and emerging therapies. *Nat Rev Cardiol* **16**, 707-726 (2019). https://doi.org/10.1038/s41569-019-0221-2

472 Kalla, M., Herring, N. & Paterson, D. J. Cardiac sympatho-vagal balance and ventricular arrhythmia. *Autonomic Neuroscience* **199**, 29-37 (2016).

473 Bolger, A. P. *et al.* Neurohormonal activation and the chronic heart failure syndrome in adults with congenital heart disease. *Circulation* **106**, 92-99 (2002).

474 Katz, A. M. Interplay between inotropic and lusitropic effects of cyclic adenosine monophosphate on the myocardial cell. *Circulation* **82**, I7-11 (1990).

475 CARMELIET, E. Action Potential Duration, Rate of Stimulation, and Intracellular Sodium. *Journal of Cardiovascular Electrophysiology* **17**, S2-S7 (2006). https://doi.org/https://doi.org/10.1111/j.1540-8167.2006.00378.x

476 Bassani, R. A., Mattiazzi, A. & Bers, D. M. CaMKII is responsible for activity-dependent acceleration of relaxation in rat ventricular myocytes. *American Journal of Physiology-Heart and Circulatory Physiology* **268**, H703-H712 (1995). https://doi.org/10.1152/ajpheart.1995.268.2.H703

477 Attwell, D., Cohen, I. & Eisner, D. A. The effects of heart rate on the action potential of guinea-pig and human ventricular muscle. *The Journal of Physiology* **313**, 439-461 (1981). https://doi.org/https://doi.org/10.1113/jphysiol.1981.sp013675

478 Kaila, K. & VAUGHANJONES, R. in *JOURNAL OF PHYSIOLOGY-LONDON*. P171-P171 (CAMBRIDGE UNIV PRESS 40 WEST 20TH STREET, NEW YORK, NY 10011-4211).

479 Carmeliet, E. Intracellular Ca2+ concentration and rate adaptation of the cardiac action potential. *Cell Calcium* **35**, 557-573 (2004). https://doi.org/https://doi.org/10.1016/j.ceca.2004.01.010